

2015 | Faculty of Sciences

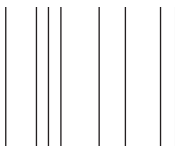
DOCTORAL DISSERTATION

# Chemical solution deposition of oxides for energy storage applications: the breakthrough in coating high aspect ratio 3D structures

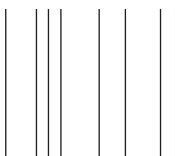
Doctoral dissertation submitted to obtain the degree of  
doctor of Science: Chemistry, to be defended by

**Sven Gielis**

Promoter: Prof. Dr Marlies K. Van Bael | UHasselt  
Co-promoters: Prof. Dr An Hardy | UHasselt  
Prof. Dr Philippe M. Vereecken | KU Leuven



D/2015/2451/73



Supported by



*Chairman*

Prof. Dr Ken Haenen, UHasselt

*Promoter*

Prof. Dr Marlies K. Van Bael, UHasselt

*Co-promoters*

Prof. Dr An Hardy, UHasselt

Prof. Dr Philippe M. Vereecken, KU Leuven / imec

*Members of the jury*

Prof. Dr Stefan De Gendt, KU Leuven / imec

Prof. Dr Christophe Detavernier, UGent

Prof. Dr Peter H. L. Notten, TU/Eindhoven

Dr Sandeep Unnikrishnan, TNO / Holst Centre



*"Eureka! I have found it!"*

Archimedes



# ACKNOWLEDGMENTS

This section gives me the possibility to thank all people who have directly and/or indirectly contributed to this PhD thesis. It very difficult to express feelings or thanks via the use of words. I will try it, but allow me to do in the language I know the best: Dutch.

Je kan een doctoraat eigenlijk het best vergelijken met een opeenvolging van *road trips*, één van mijn passies. Je maakt een planning, bereidt alles voor zodat het allemaal zo goed mogelijk verloopt. Uiteindelijk heb je een "Eureka"-moment als het zover is, als je het doel bereikt hebt (bijvoorbeeld een prachtig uitzicht over Arches NP). Tijdens *road trips* loopt er al wel eens iets fout, bijvoorbeeld het niet vinden van je gereserveerde *bed and breakfast*, het rijden over een slang, ... Maar het komt uiteindelijk altijd goed en die beslommeringen ben je nadien dan ook weer snel vergeten. Zo is een doctoraat ook, ik ben aan het einde gekomen van een groot avontuur, een lange tocht met hoogte-en dieptepunten, maar uiteindelijk ook met een doctoraatsthesis ... en dat is toch een beetje kicken. Net als tijdens *road trips* heb je nood aan metgezellen, want met twee of meer is altijd fijner dan alleen. Bovendien maken deze personen de voorbereiding en de route er naartoe een pak lichter. Zo is dat ook tijdens een doctoraat, daarom dat deze sectie misschien wel het belangrijkste deel van de thesis is.

Als je een dankwoord schrijft, schuilt er altijd een gevaar dat je iemand vergeet. Daarom dat ik wil beginnen met een algemene dankbetuiging: dank aan iedereen die direct en/of indirect heeft bijgedragen!

Mijn eerste persoonlijke bedanking gaat uit naar mijn promotor: prof. dr. Marlies Van Bael. Bedankt om me de mogelijkheid te geven om terug te keren naar de UHasselt om een doctoraat te starten, voor het vertrouwen en de diverse wetenschappelijke discussies de afgelopen jaren. Kortom, dank je wel voor de ruimte om me te vormen tot de wetenschapper die ik nu ben. Mijn co-promotor aan de Universiteit Hasselt, prof. dr. An Hardy, verdient ook een dankjewel. Ik ben er immers van overtuigd dat je kritische blik gedurende de voorbije jaren veel heeft bijgedragen tot de kwaliteit van dit werk.

Eveneens wil ik mijn andere co-promotor, prof. dr. Philippe Vereecken, graag oprecht bedanken. Ik ben er me van bewust dat de samenwerking met *imec* mij mogelijkheden heeft gegeven waar andere soms alleen maar van kunnen dromen. Verder hebben de talrijke meetings met jou op *imec* en met de mensen van *Toyota* mij alert en wakker gehouden.

Als ik over *imec* spreek, dan mag ik prof. dr. Stefan De Gendt absoluut niet vergeten. Mijn werk aldaar begon immers tijdens mijn eerste master chemie onder jouw vleugels. Dank je wel dat de je me destijds de kans gegeven hebt en bedankt voor je analytische kijk op de zaken en diverse tips de voorbije jaren.

De leden van de jury wil ik heel graag bedanken voor hun bereidwilligheid bij het evalueren van mijn werk.

Toffe collega's maken het werk niet alleen lichter, ze zorgen ook voor een goede sfeer waardoor de (voorbereiding op de) *road trip* plezanter wordt (denk aan de metgezellen). In een onderzoeksgroep met veel doctoraatsstudenten is het een komen en gaan van collega's.

Toen ik aan mijn doctoraat begon, was Ken net zijn thesis aan het afwerken. Ik herinner mij nog dat ik toen dacht: dat is voor later, Sven. Maar het was sneller mijn tijd dan ik op dat moment kon vermoeden. Ken, ik heb je leren kennen als een stille, maar warme persoonlijkheid. Wat ik mij bovendien altijd zal herinneren is de erbarmelijk stinkende rioolgeur in de badkamer van een gehuurd huisje tijdens de befaamde Balkan-trip ;-)

Christopher, ook jij was van de partij tijdens de Balkan-trip. Ik herinner me nog goed dat we kamer deelden in dat fantastische hostel in Dubrovnik ;-). Voor alle duidelijkheid: ik heb erg genoten van die reis :-)

Alexander, jij was de 3<sup>e</sup> persoon die reeds geruime tijd aanwezig was in de groep en was tevens aanwezig tijdens de reis. Jij bent vaak erg opgewekt (wat erg aanstekelijk werkt), oprecht recht uit en bovendien iemand die bijna letterlijk alles laat vallen wanneer iemand je iets vraagt. Bedankt daarvoor.

Wie Alexander zegt, denkt natuurlijk ook aan zijn partner. Nikolina, jij bent één van de personen geweest die mij goed heeft opgevangen toen ik aan de UHasselt startte en die mij wegwijs heeft gemaakt in multiferroïciteit. Bovendien stond je altijd klaar voor een babbel, bedankt voor de vriendschap. En als ik nog eens terug kijk aan de tijd in Novi Sad. Ik heb de eer gehad om er twee keer door jou gegidst te worden: één keer tijdens de Balkan-trip en één keer tijdens mijn eerste conferentie aldaar. Dank je wel!

Linny, Lize, bedankt voor de mooie *Clouseau* en musical-momenten (samen met Christopher), die avonden waren onvergetelijk!

Stan, jij was vaak op het *VITO*, maar de momenten dat we elkaar tegenkwamen waren altijd zeer aangenaam.

Daan, jij bent ook nog iemand van de *oude garde*. Jij had de kwaliteiten om Anke uit haar kot te lokken, zoals we in het *Vlaams* zeggen. De gesprekken tussen jou en haar zijn legendarisch. Dank je wel voor de animo :-)

Anke (en Tim!), bedankt voor de leuke gesprekken ('s morgens vroeg) op de bureau en ook daarbuiten. Bianca en ik genieten daar steeds met volle teugen van, alsook van onze leuke pokeravonden en gezellige onderonsjes.

Nu we bij jouw generatie zijn aangekomen, mag Nick natuurlijk niet ontbreken in het lijstje. Ik ben je steeds gevolgd tijdens mijn professionele loopbaan (van UHasselt via *imec* terug naar UHasselt), maar nu beloof ik om je niet meer te volgen ;-)

Dank je wel voor de voorbije jaren.

Bertie en Kevin, leeftijdsgenoten van Nick, bedankt voor de leuke gesprekken en vooral aan Kevin: bedankt voor de mobiele verwarming die ik van jou "geërfd" heb. Die is nog goed van pas gekomen. Ik heb deze alweer doorgegeven :-)

Andrius en Giedrius, de twee Litouwers van onze groep, bedankt voor jullie ongedwongen attitude en de fijne samenwerking.

Hanne, jij bent samen met mij aan het avontuur begonnen aan de UHasselt in 2005 (bachelor). Nu zijn onze wegen gescheiden, het ga je goed.

Nu ben ik aanbeland bij de *nieuwe garde* van de groep, vanaf dat moment begon ik mij oud te voelen ;-)

Laat me beginnen bij Thomas. Heel hard bedankt voor de talrijke leuke gesprekken die ik met jou gehad heb en bovendien bedankt om me de wereld van Android en VOIP bij te brengen. Dankzij jou bel ik nu zo goed als gratis tijdens mijn reizen vanuit de VS :-)

Maarten, je bent samen met Thomas begonnen aan het doctoraatsavontuur, dank je wel voor de gesprekken over de wereldpolitiek en de koers van goud, alsook alle hilarische momenten en nieuwtjes ;-)

De personen met wie ik de laatste periode aan de UHasselt nauw heb samengewerkt zijn Jonathan en Giulia, respectievelijk de vaste elektrolyt/spray coat en cathode/spray coat specialisten van de groep. Super hard bedankt voor de -wat mij betreft- uitstekende samenwerking. Jonathan, bedankt ook om mee te helpen aan de versterking van het patent. *Btw*, we moeten nog eens een *kapsalon* gaan eten ;-)

Wouter en Gilles, twee personen die tijdens mijn eerste jaar stage liepen in onze groep, Gilles deels onder mijn vleugels. Het deed me plezier om jullie beiden twee jaar later terug te zien. Twee zeer goede onderzoekers en vooral aangename collega's.

Boaz, hoe kan ik jou het best omschrijven? Assertief, maar eerlijk en oprecht. Trouwens dank je wel om me de wereld van de *NBA* te leren kennen. Nadien ben ik zelfs nog naar de openingsmatch van de *LA Lakers* gaan kijken :-P

Dries, buurman of toch bijna. Ik kon je droge humor wel smaken, je bier allerm minst, maar dat heeft niets te maken met je brouwkwaliteiten. Alcohol is gewoon niet aan mij besteed.

Fulya, Aleksander, my time with you was quite short. But based on what I have seen, I know for sure that you will be very good researchers. Take care!

Last but not least, de jonkie van onze groep, Bjorn. De tijd was te kort om jou erg goed te leren kennen, maar ik wens jou alle succes toe de komende jaren.

Gedurende mijn doctoraat heb ik het genoeg gehad om te mogen samenwerken met drie thesisstudenten. Ook zij hebben een belangrijke rol gespeeld voor mij en mogen dus zeker niet vergeten worden. Gilles (opnieuw), Koen en Ben, bedankt en succes met jullie verdere loopbaan.

Uiteraard mag ik de personen uit andere groepen aan de UHasselt, met wie ik samenwerkte, niet vergeten.

Guy, dank je wel om de TGA toestellen steeds werkende te houden.

Elsy en Greet, bedankt voor de vele ICP-AES metingen, deze voerden jullie steeds erg snel en vooral met de glimlach uit.

Ivo, bedankt voor de leuke sfeer en nodige luchtige grapjes in het labo.

Jens, dank je wel voor de fijne momenten. PS: nu is mijn onderzoek niet meer geheim en kan je hierin alles lezen ;-)

David en Pieter, mijn ex-studiegenoten en mede-doctoraatsstudenten, bedankt voor de leuke gesprekken in de wandelgangen.

Hilde, Eugene en Rita, bedankt bij de begeleiding van de studentenpractica. Verder ben ik prof. dr. Jan D'Haen en Bart Ruttens dankbaar voor XRD en SEM en de bijhorende kritische discussies.

Een groot deel van bovengenoemde collega's zijn net als mij lid van de werkgroep van *Jong-KVCCV*. Ik wil deze hele groep in het bijzonder bedanken voor de plezierige sfeer tijdens de vergaderingen, lezingen, congressen en andere activiteiten.

Tijdens mijn doctoraat heb ik eveneens het genoegen gehad om te mogen samenwerken met personen van andere instituten.

Eerst en vooral zou ik de *imec* collega's willen bedanken en dan denk ik in het bijzonder aan Brecht, Maarten en Sébastien. Bedankt voor de fijne samenwerking. Daarmee samenhangend, zou ik alle collega's van het *SoS-Lion* project willen bedanken en in het bijzonder Felix en prof. dr. Christophe Detavernier voor de in-situ XRD metingen.

Furthermore, I would like to thank Maksim Ivanov and prof. dr. Juras Banys from Vilnius University for the nice collaboration.

Dr. Sandeep Unnikrishnan, Ahmed Salem, Arjan Langen and colleagues from *TNO/Holst*, many thanks for the help in upscaling the (upcoming) patented 3D coating process.

*Last but not least* zou ik mijn naasten willen bedanken voor hun steun en geduld de voorbije jaren.

Eerst en vooral bedank ik mijn ouders voor de kans die ik heb gekregen om te mogen studeren en voor jullie onvoorwaardelijke steun. Ik kon steeds op jullie rekenen als het eens wat moeilijker ging, jullie stonden altijd klaar voor mij met gepaste raad en daad en een toffe *break*. Jullie zijn dan ook erg belangrijk voor mij. Vanaf heden zijn jullie eindelijk verlost van de bekommernissen van studenten in huis :-)

Ook mijn broer Steven, mijn schoonzus Katrien en hun lieve kinderen wil ik bedanken. Bedankt voor de leuke momenten en vooral bedankt, broer, om vaak te informeren naar mijn doctoraat als we eens onder ons tweeën waren.

Verder zou ik ook mijn schoonouders en schoonbroer Kevin en partner (Birgit) willen bedanken. Het zijn de leuke momenten en uitstapjes die me de kracht gaven om dit tot een goed einde te brengen. Eveneens hebben mijn favoriete honden, Gloria en Dexter, me afleiding bezorgd wanneer ik het nodig had en dit met hun wandelingen en speelmomenten.

Tot slot, mijn liefje, Bianca. Bedankt voor je steun en liefde. Ik heb jou leren kennen tijdens het begin van mijn doctoraat en je bent uitgegroeid tot de belangrijkste factor in mijn leven. Je hebt mij doorheen moeilijke momenten geholpen. Dit via onze passie *reizen*, maar ook door mij blijvend te motiveren, op te peppen en op tijd en stond eens achter mijn veren te zitten. Ik hou ontzettend veel van jou en de toekomst lacht ons toe <3

Hartelijk bedankt, allemaal!

Sven



# LIST OF ABBREVIATIONS

3D	three-dimensional
ALD	atomic layer deposition
APM	ammonia peroxide mixture
CSD	chemical solution deposition
DSC	differential scanning calorimetry
DTG	differential thermal gravimetric Analysis
EIS	electrochemical impedance spectroscopy
ERD	elastic recoil detection
FTIR	Fourier transform infrared spectroscopy
GATR	grazing-angle attenuated total reflectance
h-LuFeO <sub>3</sub>	hexagonal LuFeO <sub>3</sub>
HT-XRD	High Temperature - X-Ray Diffraction
ICP-AES	inductively coupled plasma atomic emission spectroscopy
IPA	isopropanol
MBE	molecular-beam epitaxy
o-LuFeO <sub>3</sub>	orthorhombic LuFeO <sub>3</sub>
PDA	post deposition anneal
SEM	scanning electron microscopy
SPM	sulfuric acid mixture

## List of abbreviations

TGA	Thermogravimetric Analysis
XRD	X-Ray Diffraction
X-SEM	Cross-section Scanning Electron Microscopy

# TABLE OF CONTENTS

<b>ACKNOWLEDGMENTS .....</b>	<b>vii</b>
<b>LIST OF ABBREVIATIONS .....</b>	<b>xiii</b>
<b>TABLE OF CONTENTS .....</b>	<b>xv</b>
<b>I. INTRODUCTION .....</b>	<b>1</b>
1 Energy storage .....	3
1.1 Overview of energy storage systems .....	3
1.2 Capacitors .....	4
1.2.1 General concept: a capacitor .....	4
1.2.2 Increase of capacitance via system optimization .....	6
1.2.3 Increase of capacitance via other device designs .....	10
1.3 Batteries .....	12
1.3.1 General concept: a battery .....	12
1.3.2 Various types of secondary batteries .....	13
1.3.3 Conventional Lithium-ion batteries .....	15
1.3.4 All-solid-state lithium-ion batteries .....	17
1.3.5 3D all-solid-state lithium-ion batteries .....	22
2 Chemical solution deposition .....	29
2.1 Precursor synthesis .....	30
2.1.1 Organic polymerization routes .....	30
2.1.2 Inorganic polymerization routes .....	31
2.1.2.1 Alkoxide route .....	31
2.1.2.2 Aqueous solution-gel route .....	33
2.2 Deposition methods .....	34
2.2.1 Spin coating .....	34
2.2.2 Dip coating .....	35
2.2.3 Spray coating .....	36

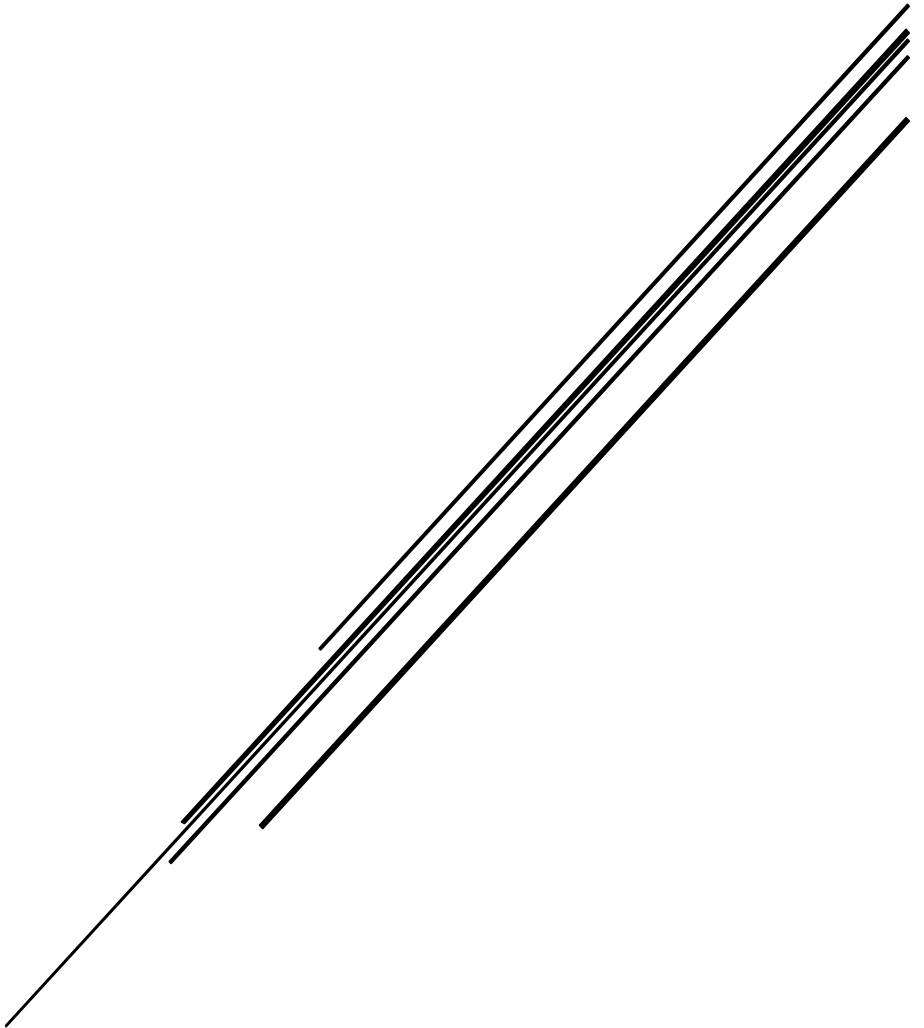
3	Characterization methods.....	43
3.1	Elastic recoil detection analysis .....	43
3.2	Electrochemical characterization .....	44
3.2.1	Electrochemical cell.....	44
3.2.2	Cyclic voltammetry .....	45
3.2.3	Galvanostatic charging/discharging measurements .....	46
3.2.4	Electrochemical impedance spectroscopy .....	46
4	Aim of the thesis .....	51
5	References .....	54
<b>II. SYNTHESIS OF MULTI-METAL OXIDES FOR USE IN ENERGY STORAGE APPLICATIONS .....</b>		<b>59</b>
1	Introduction .....	61
2	LuFeO <sub>3</sub> as possible ultra high-k dielectric in thin-film capacitors .....	62
2.1	Introduction .....	62
2.2	Experimental .....	63
2.2.1	Aqueous Lu/Fe precursor and oxide powder synthesis .....	63
2.2.2	Thin Lu/Fe oxide film deposition .....	65
2.3	Results and discussion .....	66
2.3.1	Aqueous Lu/Fe precursor and oxide powder synthesis .....	66
2.3.2	Thin Lu/Fe oxide film deposition .....	69
2.4	Conclusions .....	79
3	Li <sub>4</sub> Ti <sub>5</sub> O <sub>12</sub> as anode in thin-film Li-ion batteries .....	80
3.1	Introduction .....	80
3.2	Experimental .....	81
3.2.1	Aqueous Li/Ti precursor synthesis.....	81
3.2.2	Thin Li/Ti oxide film deposition .....	82
3.3	Results and discussion .....	84
3.3.1	Aqueous Li/Ti precursor synthesis.....	84
3.3.2	Thin Li/Ti oxide film deposition .....	85

3.3.2.1	Crystallization study .....	85
3.3.2.2	Study of electrochemical behavior .....	91
3.4	Conclusions .....	95
4	(Li <sub>x</sub> Mg <sub>1-2x</sub> Al <sub>x</sub> )Al <sub>2</sub> O <sub>4</sub> as possible solid electrolyte in all-spinel Li-ion batteries.....	96
4.1	Introduction .....	96
4.2	Experimental .....	97
4.2.1	Aqueous Li/Mg/Al precursor and oxide powder synthesis.....	97
4.2.2	Li/Mg/Al oxide film deposition.....	99
4.3	Results and discussion .....	100
4.3.1	Aqueous Li/Mg/Al precursor and oxide powder synthesis.....	100
4.3.2	Li/Mg/Al oxide film deposition.....	106
4.4	Conclusions .....	114
5	Summary .....	115
6	References .....	116
<b>III.COATING OF THREE-DIMENSIONAL SUBSTRATES VIA WET CHEMICAL SOLUTION DEPOSITION .....</b>		<b>123</b>
1	Introduction .....	125
2	Exploration of various methods.....	128
2.1	Rapid screening of the state-of-the-art .....	128
2.1.1	Liquid atomic layer deposition .....	128
2.1.2	Liquid phase deposition .....	130
2.1.3	Alkoxide based solution-gel deposition .....	132
2.1.3.1	Precursor 1 .....	133
2.1.3.2	Precursor 2 .....	133
2.1.3.3	Precursor 3 .....	133
2.1.3.4	Precursor 4 .....	133
2.1.4	Polymer complex controlled solution-gel deposition.....	134
2.2	Spray coating of TiO <sub>2</sub> .....	135

2.2.1	Experimental.....	135
2.2.2	Results and discussion.....	136
3	Aqueous chemical solution deposition as “key” to 3D coating of multi-metal oxides .....	139
3.1	Introduction .....	139
3.2	Optimization of the precursor for 3D deposition .....	140
3.2.1	Strategy .....	140
3.2.2	Experimental.....	142
3.2.3	Results and discussion.....	143
3.3	First steps towards aqueous based 3D deposition .....	144
3.3.1	Experimental.....	144
3.3.2	Results and discussion.....	144
3.4	3D deposition via spray coating .....	149
3.4.1	Strategy .....	149
3.4.2	Experimental.....	150
3.4.3	Results and discussion.....	151
3.4.3.1	Proof of coating and effect of deposition temperature .....	151
3.4.3.2	Effect of flow rate .....	158
3.4.3.3	Effect of path velocity.....	159
3.4.3.4	Effect of nozzle distance .....	161
3.4.3.5	Effect of precursor concentration .....	164
3.4.3.6	Crystallization of the TiO <sub>2</sub> coating on the pillars .....	167
3.4.3.7	Electrochemical evaluation of the TiO <sub>2</sub> coating on the pillars	172
3.5	Generalization of the novel 3D CSD method .....	174
3.5.1	Deposition of Li <sub>4</sub> Ti <sub>5</sub> O <sub>12</sub> on silicon micropillars via the CSD method .....	174
3.5.1.1	Strategy .....	174
3.5.1.2	Experimental.....	174
3.5.1.3	Results and discussion.....	175

3.5.2	Deposition of LuFeO <sub>3</sub> on silicon micropillars via the CSD method	177
3.5.2.1	Strategy	177
3.5.2.2	Experimental	177
3.5.2.3	Results and discussion	178
3.6	Determination of film thickness and conformality	179
4	Summary	181
5	References	183
<b>IV. SUMMARY, CONCLUSIONS AND OUTLOOK</b>		<b>187</b>
<b>V. SCIENTIFIC CONTRIBUTIONS</b>		<b>195</b>
1	Patents	197
2	Publications	197
2.1	Published	197
2.2	In preparation	197
3	Conference contributions	198
3.1	Oral presentations	198
3.2	Poster presentations	199

# I. INTRODUCTION





# 1 Energy storage

Humankind is facing major challenges in the coming decades, lots of them are energy related. The need for clean and highly efficient energy storage will be immense and the field of applications will be very wide. It could contribute to address global warming, thus storing energy generated by natural resources such as the wind or the sun, and release it during peak moments. Furthermore new generations of energy storage devices are necessary to follow the growth of portable electronic devices such as smartphones, tablet computers and smartwatches as well as for electrical vehicles. It will also be of great use to develop such for small medical devices which are implanted in the human body. To overcome these demands, the development of new materials and device designs is essential.[1–8]

## 1.1 Overview of energy storage systems

Different kinds of energy systems are available these days, they are schematically summarized in Figure I-1, as a Ragone plot.[3] As can be seen in the plot, the devices can be divided in mainly three groups. The first group are the fuel cells which are able to store a high amount of energy per mass, values of more than  $1000 \text{ Wh kg}^{-1}$  are reported. However their power density is low, particularly in the range of  $10\text{-}400 \text{ W kg}^{-1}$ . [3] When a higher power density is necessary, one can shift to batteries of which the Li-ion type is the most abundant these days. Power densities of more than  $10^3 \text{ W/kg}$  are achievable. They are thus characterized by a slightly higher power density, their energy density is a bit lower, particularly between  $10$  and  $500 \text{ Wh kg}^{-1}$ . [1,3–8] The last group of energy storage systems are the capacitors or, more recently, the ultracapacitors. These devices have a rather low energy density compared to fuel cells ( $10^{-2}\text{-}10 \text{ Wh kg}^{-1}$ ), but their strength lies in a very high power density (up to  $10^7 \text{ W kg}^{-1}$ ): they have the advantage of being charged and discharged faster. [2,3] Since all these devices have their advantages and limitations, one can understand that each type also has its particular application. Of course, the aim is to find the best performance (highest possible energy density and power density) to cost ratio. [3]

Since the research, reported in this thesis, will imply materials which are synthesized for Li-ion batteries and ultracapacitors, the theory behind these particular devices will be explained in more depth.

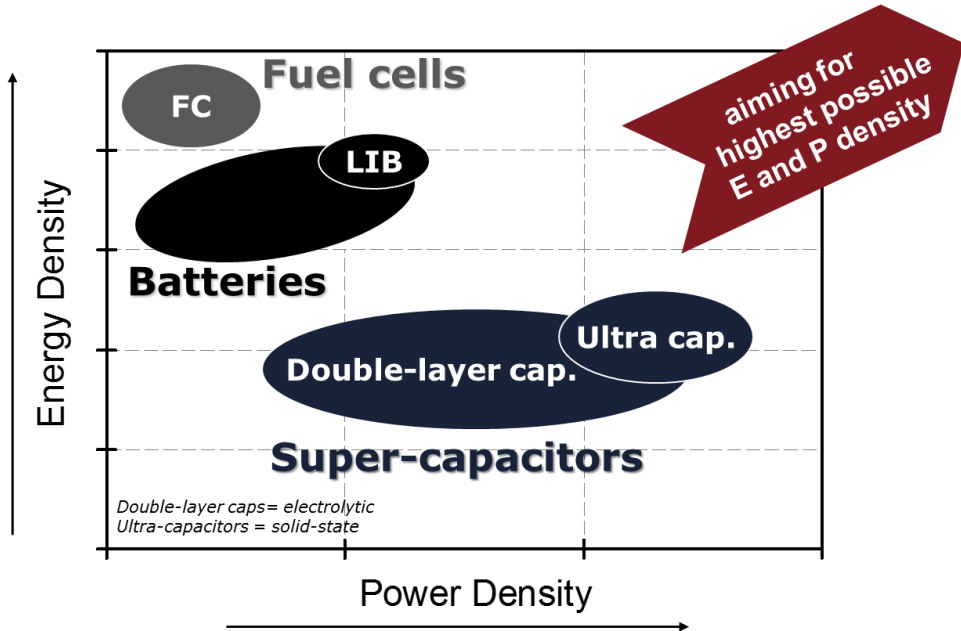


Figure I-1: Schematic representation of various kinds of energy systems, based on the Ragone plot. [Courtesy of Philippe M. Vereecken]

## 1.2 Capacitors

### 1.2.1 General concept: a capacitor

Capacitors are a group of electrical devices that store energy based on charge separation. The simplest and oldest form is the electrostatic capacitor. This device is able to store electrical energy in an electrostatic (non-Faradaic) way, i.e. the energy is stored as negative and positive electric charges on the plates of a capacitor. [2,3,9,10] The operation of such device is based on the creation of an electrostatic field between two parallel conductive plates. This field, which is presented as lines of electric force in Figure I-2, is established when applying a potential difference between two conductive plates, here A and B. The direction of the field is the direction of the force which is exerted on a positive charge: it

will be pushed away from the positive plate A towards the negative plate B. The presence of the electrostatic field indicates the presence of equal positive and negative electric charges on the two plates in Figure I-2.

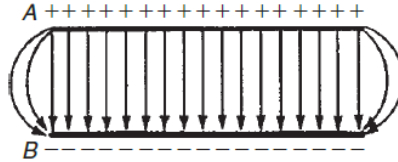


Figure I-2: Schematic representation of the electrostatic field, established between two conductive plates, A and B.[9]

A measure for the amount of charge ( $Q$ ) that can be stored on the plates when applying a voltage difference  $V$  is called the capacitance (unit: Farad) and is defined as [9,10]:

$$C = \frac{Q}{V}$$

(Equation I-1)

As mentioned, a capacitor is an energy storage system, specially constructed to possess capacitance. Therefore it consists of two conductive plates which are separated by an insulating material, i.e. the dielectric, enabling the ability to store static electricity (Figure I-3). The capacitance of such device is characterized by the dimensions and the dielectric material between the two conductive plates. It can be expressed as [9,10]:

$$C = \varepsilon \frac{A}{d}$$

(Equation I-2)

with  $\varepsilon$  and  $d$ , respectively, the absolute permittivity and the thickness of the dielectric material and  $A$  the geometric area of overlap of the plates.

The energy of the capacitor can then be calculated as [9,10]:

$$E = \frac{1}{2} CV^2$$

(Equation I-3)

with V the voltage of the capacitor.

In the early capacitors, the conductive films were separated by vacuum, as dielectric material. This is schematically presented in Figure I-3a.

### 1.2.2 Increase of capacitance via system optimization

To improve the capacitance and the amount of energy that can be stored, a dielectric material with a larger absolute permittivity can be applied between the metal plates. Such dielectric materials have a large energy gap between the valence and conduction band, making them insulators. Consequently, they do not conduct the electrical current when an electrical field is applied over the material. However they are not inert with respect to the established electrical field. The field causes limited changes in the charge distribution within a material, inducing the alignment of an electrical dipole moment, as can be seen in Figure I-3b. The dielectric potential of a material, i.e. the absolute permittivity, also called dielectric constant, is defined as [9–11]:

$$\varepsilon = \varepsilon_0 \varepsilon_r$$

(Equation I-4)

with  $\varepsilon_0$  and  $\varepsilon_r$ , respectively, the permittivity of vacuum ( $\varepsilon_0=8.85 \times 10^{-12}$  F/m) and the relative permittivity of a material.

The complex relative permittivity of a material is [12]:

$$\varepsilon_r = \varepsilon_r' - j\varepsilon_r''$$

(Equation I-5)

where  $\varepsilon_r'$  and  $\varepsilon_r''$  are, respectively, the real and imaginary part of the complex dielectric constant.

The real part in (Equation I-5),  $\epsilon_r'$ , represents the relative permittivity of the dielectric material, so it is of high influence on the capacitance and the amount of energy that can be stored in the capacitor. The imaginary part,  $\epsilon_r''$ , is defined as the dielectric energy that is lost to heat in the dielectric material. The relative magnitude of  $\epsilon_r''$  to  $\epsilon_r'$  is defined as a quantity,  $\tan \delta$ , named as the loss tangent or loss factor.[12]

By insertion of (Equation I-4) in (Equation I-2), one can understand that by the addition of a dielectric material with a large absolute permittivity, i.e. a large dielectric constant, between the metal plates in a capacitor, the capacity is increased with a factor  $\epsilon_r$ . It is thus obvious that capacitors built with a material with intrinsically high dielectric constant between the two metal plates, as schematically shown in Figure I-3b-c, should lead to a relatively higher capacitance.[9–11] Furthermore, one aims for a minimum dielectric loss over the entire range of operating frequencies.[12]

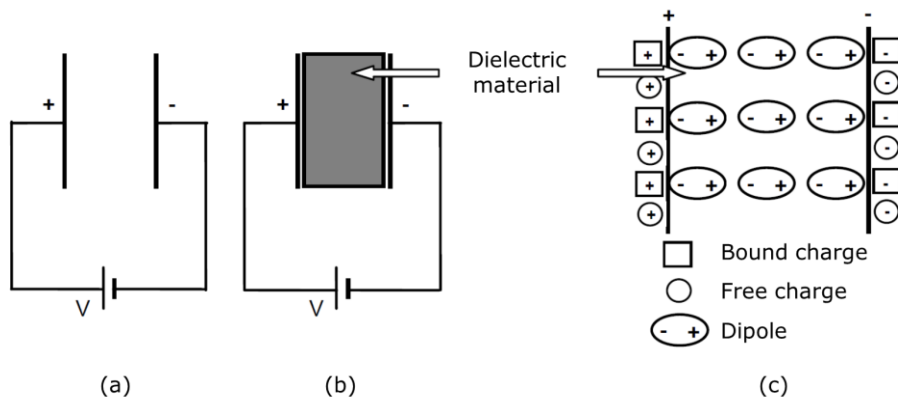


Figure I-3: Schematic representation of a capacitor (a) in vacuum and (b) with a dielectric material between the plates, and of (c) the charge distribution in the dielectric material.[11]

In Table I-1 a list of common dielectrics with their dielectric constant and loss tangent is shown. The most materials, including plastics and oils, have a relatively low relative permittivity.  $\text{BaTiO}_3$ , a widely spread ceramic material, is known for its very high dielectric constant.[13] Giant dielectric constants, till 50000 [13], can be achieved by other ceramic materials such as  $\text{BaTiO}_3$  [12],  $\text{PbZr}_x\text{Ti}_{1-x}\text{O}_3$  [12],  $\text{BaSrTiO}_3$  [12] and  $\text{CaCu}_3\text{Ti}_4\text{O}_{12}$  [14].

<i>Dielectric material</i>	<i>Dielectric constant</i>	<i>Loss tangent</i>
Air	1.0059	0
Vacuum	1.000	0
Pure cellulose or paper	5.9 – 6.0	0.0053
Polypropylene	2.25 – 2.3	<0.0002
Polyester	3.2	0.001
Polystyrene	4 – 2.7	<0.0005
Polycarbonate	2.9 – 3.0	0.0014-
Teflon	2.1	<0.0005
Polyphenylene Sulphide (PPS)	3.3	0.0002
Polyethylene naphthalate (PEN)	2.9	0.0005
HDPE	2.65	<0.0002
PVC	3.2	0.0115
LDPE	2.3	<0.0002
Nylon	3.88	0.014
Aluminium oxide	8.5	0.10
Tantalum Pentoxide Oxide ( $Ta_2O_5$ )	27	0.04
Glass (silicon)	4.8 – 8	0.0005
Mica	5.9 – 9.0	0.005
Ceramic	Up to 50,000	Variable
Castor oil	3.7	0.0007
Rapeseed oil	3.28	0.0003
Transformer oil	2.2	0.005
Diocetyl phthalate (DOP)	5.6	0.005
Polychlorinated biphenyl (PCB)	5.9	0.0025
Phenyl xylyl ethane (PXE)	2.5	0.0012
M/DBT	2.66	0.003
Paraffin	2.2	0.0002
Distilled water (for comparison)	78.5	0.005
Barium titanate	1200 +	0.01
Benzene	2.284	–

*Table I-1: Common dielectrics and their behavior.*[13]

Besides the dielectric constant and loss, there is another property which is of importance for capacitor applications, namely the breakdown voltage. It is the voltage at which the dielectric material becomes electrically conductive. Of course, dielectric materials with the lowest dielectric loss and the highest dielectric constant and breakdown voltage are desired. However, an inherent trade-off exists between the last two properties.

In Figure I-4 the breakdown field is plotted as function of the dielectric constant. The breakdown field ( $E_{BR}$ ) is directly proportional to the breakdown voltage ( $V_{BR}$ ) [12]:

$$E_{BR} = \frac{V_{BR}}{d}$$

(Equation I-6)

where  $d$  is the dielectric thickness.

The solid line in Figure I-4 is the "best one can achieve" (BOCA) line, which represents the maximum breakdown field that can be achieved using a thin-film dielectric with a well-determined dielectric constant. For high-quality films, the relationship is [12]:

$$E_{BR} = \frac{20}{\sqrt{\epsilon_r}}$$

(Equation I-7)

This empirical relationship does not hold for very thin films (a few atom layers thick).[12]

The dielectric material, which is built in a capacitor, is of great importance for the capacitance and energy density of the device. These values are correlated to the dielectric material's properties. However, not only the choice of dielectric influences the characteristics of the capacitor. The capacitance is also dependent on two geometric factors (Equation I-2). It is clear that it is indirectly proportional to the distance between the metal plates, i.e. the thickness of the dielectric



through the electrolyte. No Faradaic reactions occur between the solid material and the electrolyte. The capacitance of the device is indirectly proportional to the thickness of the formed double-layer. Since it is known to be very small (fraction of a nm in liquid electrolytes), it is clear that rather high capacitance can be achieved, more specifically in the range of 75-175 F/g for aqueous electrolytes and 40-100 F/g using organic electrolytes. The cell voltage of the device is also dependent on the electrolyte used: 1 V for aqueous electrolytes and 3-3.5 V for organic electrolytes. The total energy stored in the device ( $E = 1/2 CV^2$ ) is then ranging from 35 to 615 J/g.[2]

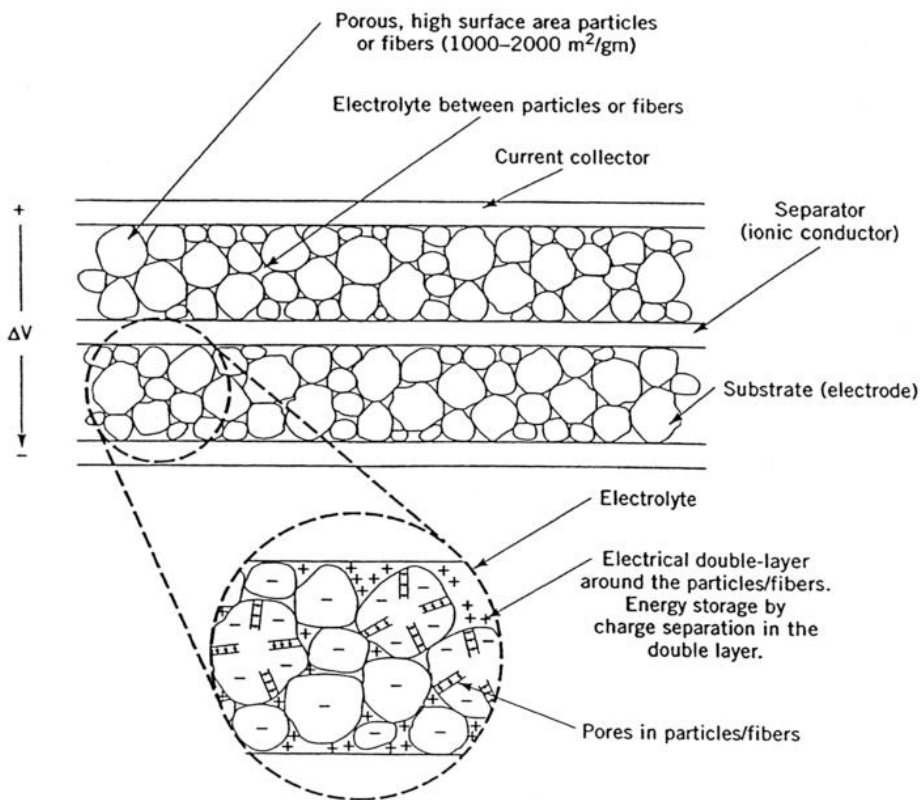


Figure I-5: Schematic representation of a double-layer ultracapacitor.[2]

Another group of electrochemical capacitors utilize pseudo-capacitance. In contrast to ideal double-layer capacitors, the capacitance is not constant and is particularly dependent on the voltage. Most of the charge is transferred at the

surface or in the bulk near the surface of the solid electrode. Hence, Faradaic reactions, mostly charge transfer reactions, are involved between the solid material and the electrolyte. These reactions, involving surface adsorption of ions from the electrolyte, redox reactions with ions from the electrolyte or the doping and undoping of active conduction polymer material in the electrolyte, are voltage-dependent. The capacitance of pseudo-capacitance materials is much higher than for the ideal double-layer materials, peaking to 650 F/g. Consequently, their resulting energy density will also be higher.

One could also combine a double-layer material electrode and a pseudo capacitance electrode in one device, named a hybrid capacitor.[2]

## 1.3 Batteries

### 1.3.1 General concept: a battery

A battery is another widely established power supply system, which has the capability to store electricity in the form of chemical energy. Inherently, a battery is simple in concept: it is an galvanic cell. As can be seen in the schematic representation in Figure I-6, such a cell is composed of two electrodes, i.e. the anode and cathode, being the electrochemically active materials of the device.

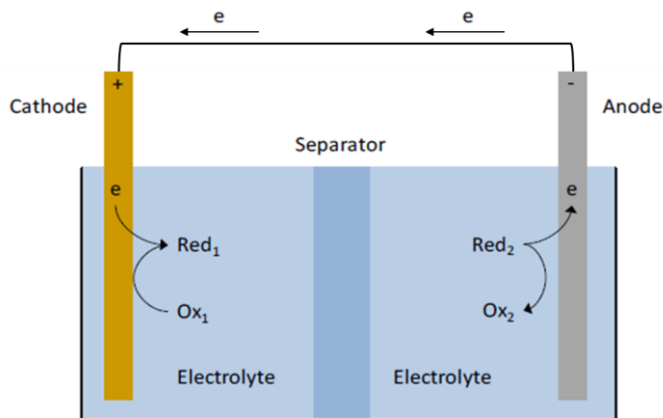


Figure I-6: A schematic representation of a galvanic cell.[15]

The electrodes are characterized by different chemical potentials, dependent on the chemistry (i.e. oxidation and reduction reactions that occur at each), the temperature, the concentrations, the environment, etc... When the anode and cathode are connected via an external circuit, electrons spontaneously flow from the more negative to the more positive potential. Electrical energy can then be tapped via an external device. However the flow of electrons via the external circuit will only occur when there is compensation for the charge at each side. Both electrodes have to be separated by an electrolyte and separator. This will allow the ionic transport through the system so that the charge balance is maintained, and at the same time, it will block the electrons from running directly through the system, thus forcing them to run through the external device.[15]

One can distinguish two main types of batteries. The first set are the primary batteries, they are non-rechargeable and thus meant for a single discharge only. The group of batteries which can be (dis)charged multiple times are the secondary batteries, consequently making use of reversible electrochemical reactions. Electrochemistry enables various combinations of oxidation and reduction reactions, both for primary and secondary batteries. However only a few of these are implemented in commercial devices. It is known that primary batteries are mostly based on zinc and manganese oxides in a basic or acid electrolyte. Many types of rechargeable batteries are on the market of which lithium ion chemistries capture the main part of the portable electronics. Moreover they are the most studied batteries nowadays, since they can obtain the highest gravimetric energy density.[15]

### **1.3.2 Various types of secondary batteries**

Various types of secondary battery devices are available. As for the energy storage devices (Figure I-1), they all are distinguished by different performance characteristics and thus appropriate for well-defined applications. In Table I-2, which is a not all-inclusive table, the major non-lithium based batteries are summarized.[16]

Lead acid batteries are one of the "oldest" and most commonly used energy storage devices today. They are known as cheap, reliable power batteries,

therefore suitable for e.g. engine starting and ignition applications. The downside is that they suffer from low cycle life only achieving 300-500 cycles.

The nickel-based batteries, based on the nickel cadmium and nickel metal hydride chemistry, offer a higher voltage, higher capacity and also more cycles. However, they suffer from the "memory effect" that will reduce the amount of available energy over time. This can be minimized by conducting full discharges, but they are also very sensitive to self-discharge as can be seen in Table I-2. The nickel-based batteries achieved very high volumes with early portable power applications. Furthermore, one can notice that Nickel Metal Hydride batteries are characterized by relatively high energy and power density at a reasonable cost, making them still the best selling battery chemistry for hybrid electric vehicles.

The last set of batteries, that is included in Table I-2, are the sodium batteries, often referred to as thermal batteries since at the moment they must operate at temperatures between 300°C and 400°C. The benefit of these batteries is that it is a very cost-effective solution for the energy and power densities that it can achieve.[16]

	Lead Acid	Nickel Cadmium	Nickel Metal Hydride	Sodium Sulfur	Sodium Nickel Chloride
Chemistry descriptor	PbA/LAB	NiCd	NiMh	NaS	NaNiCl
Specific energy (Wh/kg)	30-40	40-60	30-80	90-110	100-120
Energy density (Wh/L)	60-70	50-150	140-300	345	160-190
Specific power (W/kg)	60-180	150	250-1000	150-160	150
Power density (W/L)	100	210	400	-	-
Nominal voltage (per cell) (V)	2.0	1.2	1.2	2.0	2.6
Cycle life	300-800	1000-2000	500-1500	1000-2500	1000
Self-discharge (% per month)	3-5%	20%	30%	0%	0%
Operating temperature range (°C)	-20 to +60	-40 to +60	-20 to +60	300 to 400	300 to 400
Cost (per kWh)	\$150-\$200	\$400-\$800	\$200-\$300	\$350	\$100-\$300
Maintenance	3-6 months	30-60 days	60-90 days	None	None

Table I-2: Overview and characteristics of non-lithium ion based batteries.[16]

### 1.3.3 Conventional Lithium-ion batteries

The lithium-ion batteries, the most wide-spread secondary batteries with the highest energy density, make use of a mechanism which is based on the reversible transport of lithium ions between the cathode and anode. The most abundant commercial Li-ion battery, regardless of the form factor, consists of a lithium metal oxide (e.g.  $\text{LiCoO}_2$ ), graphitic carbon and a lithium salt dissolved in an organic solvent as, respectively, the cathode, anode and electrolyte (Figure I-7). To prevent electrical contact between the electrodes, a polymer membrane is added. This membrane acts as a separator to prevent internal shorts and self-discharge.

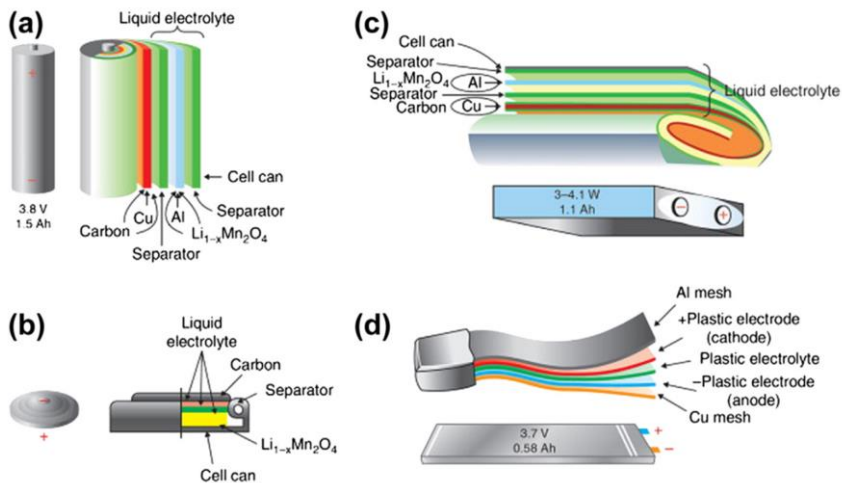
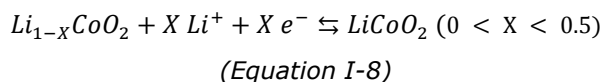
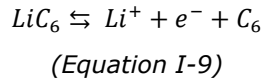


Figure I-7: Schematic representation of various forms of Li-ion batteries: (a) cylindrical, (b) coin-shaped, (c) prismatic and (d) flat configuration.[16]

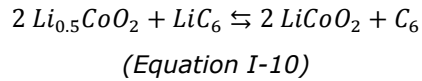
A schematic presentation of a commercially used lithium-ion electrochemical cell is presented in Figure I-8. From this figure, which represents the discharging cycle, one can deduce that the following redox system is applicable [1,7,15,17,18]:



and:



The overall reaction is thus:



representing the discharging ( $\rightarrow$ ) and charging ( $\leftarrow$ ) of the electrochemical cell.

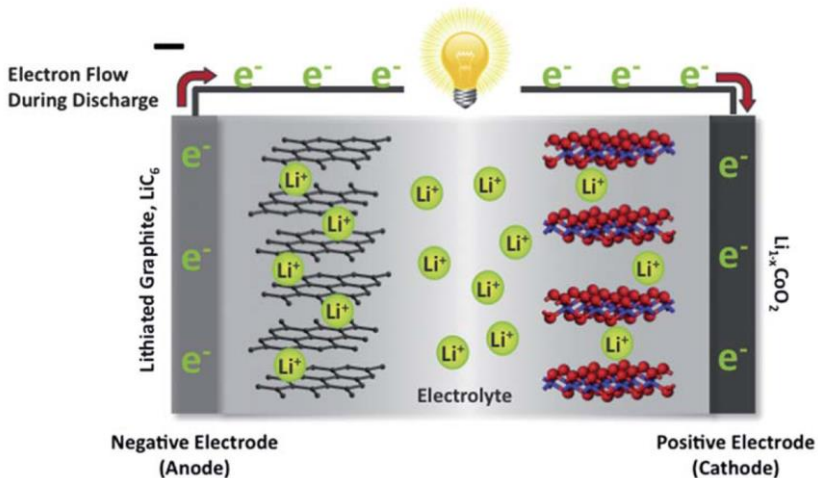


Figure I-8: A schematic representation of an Li-ion electrochemical cell (discharging).[19]

Also other anode and cathode materials can be used to accommodate lithium ion transport through redox chemistry [1,7,15,17,18]. A list of the most used chemistries can be found in Table I-3. If this table is compared to Table I-2, in which the most common non-lithium ion based batteries are summarized, it is clear that the lithium-ion batteries are characterized by a much higher energy and power density. Furthermore the lithium-ion batteries operate at a higher cell voltage, a lower rate of self-discharge and an extended cycle life.[16]

	Lithium Iron Phosphate	Lithium Manganese Oxide	Lithium Titanate	Lithium Cobalt Oxide	Lithium Nickel Cobalt Aluminum	Lithium Nickel Manganese Cobalt
Specific energy (Wh/kg)	80-130	105-120	70	120-150	80-220	140-180
Energy density (Wh/L)	220-250	250-265	130	250-450	210-600	325
Specific power (W/kg)	1400-2400	1000	750	600	1500-1900	500-3000
Power density (W/L)	4500	2000	1400	1200-3000	4000-5000	6500
Volts (per cell) (V)	3.2-3.3	3.8	2.2-2.3	3.6-3.8	3.6	3.6-3.7
Cycle life	1000-2000	>500	>4000	>700	>1000	1000-4000
Self-discharge (% per month)	<1%	5%	2-10%	1-5%	2-10%	1%
Cost (per kWh)	\$400- \$1200	\$400-\$900	\$600-\$2000	\$250-\$450	\$600-\$1000	\$500-\$900
Operating temperature range (°C)	-20 to +60	-20 to +60	-40 to +55	-20 to +60	-20 to +60	-20 to +55

Table I-3: Overview and characteristics of lithium ion based batteries. [16]

### 1.3.4 All-solid-state lithium-ion batteries

Conventional Li-ion battery technology typically uses powders as the active electrode components in combination with a liquid electrolyte. Their usable temperature window is the range between  $-20^{\circ}\text{C}$  and  $60^{\circ}\text{C}$ . Excessive evaporation of the liquid electrolyte could lead to cell rupture and consequently, due the electrolyte's high flammability, to explosions. There is also a high risk of shorts and thermal runaway. In order to overcome this risk, membrane separators and a bulky casing are necessary, resulting in a heavy battery with a large volume. This lowers the potential gravimetric and volumetric energy density of the device.

As an alternative, all-solid-state Li-ion batteries are being explored. Since this concept makes use of a solid-state electrolyte, obviously, it has advantages regarding safety. Their usable temperature window is much broader, i.e. between  $-50$  and  $150^{\circ}\text{C}$  (in the case of an inorganic electrolyte). Furthermore, the solid-state electrolyte is characterized by a higher resistivity against (electro)chemical degradation, resulting in a longer cycle life compared to wet Li-ion cells. The drawback of an all-solid-state battery and more specifically solid-state electrolytes is their relatively low ionic conductivity compared to liquid-based electrolytes,

resulting in a limited performance of the stack.[4,6,8,15,17,20] As it is known that the thickness scales inversely with the film thickness, the issue can be circumvented by the introduction of thin film based battery technology, i.e. a battery stack which is presented in Figure I-9.

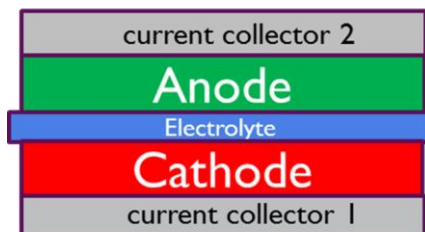


Figure I-9: Schematic representation of an all-solid-state thin-film battery.[17]

Deposition of the active battery materials is done on a planar solid current collector, which should be electronically conductive. Furthermore, it should be also chemically inert towards the deposited materials and impermeable for lithium ions so that they cannot diffuse out of the battery stack. Additionally, it should withstand the process conditions of the stacked materials. As an alternative, also a barrier layer can be deposited to ensure these characteristics.

The current collector is then covered by a cathode film (Figure I-9). The capacity of this material will obviously have a direct impact on the characteristics of the stack.[4,8,15,17,20] Already various possible cathode materials are described in literature.[4]

Lithium cobalt oxide,  $\text{LiCoO}_2$ , is a widely spread cathode material for Li-ion batteries. It exists in two crystal forms: a spinel form and a layered hexagonal structure, typically formed at higher temperatures. This layered structure makes it interesting to perform as a cathode, i.e.  $\text{Li}_x\text{CoO}_2$  can be reversibly cycled between  $0.5 < X < 1$  and is characterized by a very flat lithium intercalation/extraction plateau around 3.9 V vs.  $\text{Li}/\text{Li}^+$ . This brings the theoretical gravimetric and volumetric charge capacity at, respectively,  $137 \text{ mAh g}^{-1}$  and  $700 \text{ mAh cm}^{-3}$ .[4]

Lithium nickel oxide,  $\text{LiNiO}_2$ , is a similar layered structure: it also exists in two crystalline structures of which the hexagonal layered structure shows electrochemical behavior. Due to several phase transitions upon (de-)lithiation, the charge/discharge voltage is less stable. In particular, the (dis)charge plateaus range from 2.7 V to 4.1 V vs.  $\text{Li/Li}^+$ . Lithium in  $\text{Li}_x\text{NiO}_2$  can be cycled between  $0.35 < X < 0.85$  and is characterized by a gravimetric and volumetric capacity of, respectively,  $140 \text{ mAh g}^{-1}$  and  $650 \text{ mAh cm}^{-3}$ . [4]

Another layered structure, that is useful as cathode material, is  $\text{V}_2\text{O}_5$ . Its structure, consisting of  $\text{VO}_5$  pyramids, is characterized by three main electrochemical regions. Two sharp peaks can be observed at 3.2 V and 3.4 V vs.  $\text{Li/Li}^+$ , resulting in a lithium content (in  $\text{Li}_x\text{V}_2\text{O}_5$ ) between  $0 < X < 0.8$  during cycling. It yields a theoretical gravimetric and volumetric capacity of respectively  $118 \text{ mAh g}^{-1}$  and  $400 \text{ mAh cm}^{-3}$ . For the third region, which is found at 2.3 V vs.  $\text{Li/Li}^+$ , the lithium content can be increased up to  $X=2$ . However, a non-reversible phase transformation occurs at that voltage. Consequently this region can practically not be used. [4]

Layered structures can suffer from orientation effects because only two-dimensional paths are available. This is a drawback, especially for thin-film batteries because then precise lattice matching is necessary. Spinel structures can overcome this problem since they are cubic structures which facilitate 3D diffusion. The most known spinel material for Li-ion batteries is lithium manganese oxide ( $\text{LiMn}_2\text{O}_4$ ). It is characterized by two (de)lithiation regions, of which only one can be applied for practical battery applications. The main electrochemical response is around 4 V vs.  $\text{Li/Li}^+$  at which Li (in  $\text{Li}_x\text{Mn}_2\text{O}_4$ ) can be cycled between  $0 < X < 1$ . During cycling the crystal lattice remains cubic and only minor volumetric changes occur, resulting in a long cycle-life. It yields a gravimetric capacity of  $148 \text{ mAh g}^{-1}$  and the theoretical volumetric capacity is set at  $650 \text{ mAh cm}^{-3}$ . Another (de)lithiation region exists at 3 V vs.  $\text{Li/Li}^+$ , however due to a Jahn-Teller distortion of the crystal lattice, the cubic structure transforms into a tetragonal framework. The deformation is so large that degradation of the electrode structure and cycle-life will occur. [4]

The last widely spread group of possible cathode materials are lithium metal phosphates, of which  $\text{LiFePO}_4$ ,  $\text{LiMnPO}_4$  and  $\text{LiCoPO}_4$  are the most reported metal phosphate materials for Li-ion batteries. They possess an olivine (orthorhombic) crystal structure and entail a relatively high gravimetric capacity (Table I-4).[4]

<b>Lithium metal phosphate</b>	<b>(Dis)charge voltage</b>	<b>Gravimetric capacity</b>	<b>Volumetric capacity</b>
<b><math>\text{Li}_x\text{FePO}_4</math> (<math>0.1 &lt; X &lt; 1</math>)</b>	3.4 V	153 mAh g <sup>-1</sup>	610 mAh cm <sup>-3</sup>
<b><math>\text{Li}_x\text{MnPO}_4</math> (<math>0 &lt; X &lt; 1</math>)</b>	4.1 V	171 mAh g <sup>-1</sup>	590 mAh cm <sup>-3</sup>
<b><math>\text{Li}_x\text{CoPO}_4</math> (<math>0 &lt; X &lt; 1</math>)</b>	4.9 V	167 mAh g <sup>-1</sup>	620 mAh cm <sup>-3</sup>

Table I-4: Electrochemical characteristics of lithium metal phosphates.[4]

The next film in the Li-ion battery stack (Figure I-9) is the solid-state electrolyte, which should possess a high ionic conductivity and a minimal electronic conductivity to prevent self-discharge. In order to compensate for the lower ionic conductivity of the solid electrolyte (compared to a liquid electrolyte), the film should be scaled down in thickness. It is known that the resistance is inversely proportional to the film thickness.[4,8,15,17,20] As for the cathode, there are also various solid electrolyte materials available in literature.[4]

$\text{LiNbO}_3$  and  $\text{LiTaO}_3$  are interesting materials to act as solid-state electrolyte since their electronic conductivity is estimated to be lower than  $10^{-11}$  S cm<sup>-1</sup>. This is several magnitudes lower than their ionic conductivity which is reported to vary between  $2.2 \cdot 10^{-9}$  and  $8.4 \cdot 10^{-7}$  S cm<sup>-1</sup> for crystalline  $\text{LiNbO}_3$  films and around  $10^{-5}$  S cm<sup>-1</sup> for amorphous  $\text{LiNbO}_3$ . For  $\text{LiTaO}_3$  films an ionic conductivity of  $8 \cdot 10^{-8}$  S cm<sup>-1</sup> was reported. Also in this case higher values were obtained for amorphous bulk materials.[4]

A much higher ionic conductivity,  $10^{-3}$  S cm<sup>-1</sup>, can be achieved by crystalline lithium lanthanum titanium oxide (perovskite  $\text{Li}_3\text{La}_{(2/3)-x}\text{TiO}_3$ ). Another advantage of this material is that it has a good (electro)chemical stability above ca. 1 V.

However, very high temperatures ( $> 1000^{\circ}\text{C}$ ) are necessary to obtain this high ionic conductivity. Its electronic conductivity is slightly higher than for  $\text{LiNbO}_3$  and  $\text{LiTaO}_3$ , namely around  $10^{-8}$ - $10^{-9} \text{ S cm}^{-1}$ . Consequently a thicker electrolyte layer is required in a solid-state battery to reduce self-discharge behavior.[4]

Another class of solid electrolytes is the group of amorphous lithium phosphates. Pure  $\text{Li}_3\text{PO}_4$  has a relatively low ionic conductivity:  $3 \cdot 10^{-7} \text{ S cm}^{-1}$  for bulk material and  $7 \cdot 10^{-8} \text{ S cm}^{-1}$  for thin films. However when nitrogen is introduced (doped) in the lattice, it forms crosslinks between the phosphate chains enlarging its ionic conductivity up to  $3 \cdot 10^{-6} \text{ S cm}^{-1}$ . LIPON is a (electro)chemically stable material which is nowadays one of the most frequently used electrolytes for all-solid-state planar Li-ion batteries.[4]

Polymer electrolytes, which exist in various types, are also used as solid electrolyte in all-solid-state Li-ion batteries. A first type is a polymer membrane which is impregnated with a lithium salt solution. High ionic conductivities can be obtained, however the problem imposed by liquid electrolytes is still present. For this reason they may not be considered as solid electrolytes. Solid polymer electrolytes (e.g. lithium perchlorate salt in poly(ethylene oxide)) do not make use of liquid electrolyte solutions. When crystallization is prevented, ionic conductivities in the range of  $10^{-3}$ - $10^{-4} \text{ S cm}^{-1}$  are reported to be feasible.[4]

The stack is finished by deposition of an anode film and a second current collector. Obviously, as for the cathode, the capacity of the anode will have a direct impact on the characteristics of the stack.[4,8,15,17,20] Various possible anode materials are described in literature.[4]

The elements of the IVa group in the periodic table of elements are very interesting as anode material. Carbon (in its graphitic form) is a commonly used anode material. The other elements, including Si and Ge, are considered as the holy grail. They are known to alloy large amounts of lithium, in particular 4 or more lithium ions per alloy. This corresponds to gravimetric capacity of  $3579 \text{ mAh g}^{-1}$  and  $1385 \text{ mAh g}^{-1}$  for, resp. silicon and germanium. The theoretical volumetric capacity is set at  $2200 \text{ mAh cm}^{-3}$  and  $2300 \text{ mAh cm}^{-3}$ . However, this involves a

large volume expansion of 300%, resulting in a degradation of the electrode structure and thus a low cycle-life.[4]

A more stable material towards Li (de)intercalation is titanium oxide ( $\text{TiO}_2$ ). It commonly occurs in three crystal structures, specifically brookite, rutile and anatase. Anatase is known to have the best electrochemical response: it can intercalate up to  $X = 0.5$  in  $\text{Li}_x\text{TiO}_2$  at 1.8 V. This yields a theoretical gravimetric and volumetric capacity of, respectively, 168 mAh  $\text{g}^{-1}$  and 660 mAh  $\text{cm}^{-3}$ , thus much less compared to the IVa group elements.

Lithium titanate,  $\text{Li}_4\text{Ti}_5\text{O}_{12}$ , is another attractive candidate to serve as anode material.[21–23]  $\text{Li}_4\text{Ti}_5\text{O}_{12}$ 's stability towards electrochemical cycling is the most striking characteristic with respect to thin-film batteries. Because of its spinel structure, the lithium intercalation and de-intercalation process only entails a minor difference in lattice parameters ( $< 0.2\%$ ), resulting in an insignificant lattice strain, unit cell volume expansion and thus only a negligible capacity loss.[4,21–23] During the charging/discharging process, the lithium content is varied between  $0 < X < 3$  for  $\text{Li}_{4+X}\text{Ti}_5\text{O}_{12}$ , resulting in a maximum theoretical gravimetric and volumetric capacity of respectively 175 mAh  $\text{g}^{-1}$  and 610 mAh  $\text{cm}^{-3}$ . [4] The (de)intercalation process occurs through a two-phase equilibrium region, resulting in a very stable (dis)charge voltage between 1.5 V and 1.6 V and, consequently, in very flat charge and discharge curves.[4,22]

### **1.3.5 3D all-solid-state lithium-ion batteries**

Besides the various advantages of the proposed thin film Li-ion battery stack in Figure I-9, it is limited in performance. The active materials of the stack, i.e. the cathode, electrolyte and anode, have a large energy density. However, due to the inactive materials such as the current collector and packaging the overall energy density of a thin film Li-ion battery is limited. Therefore, 3D thin-film batteries, consisting of electrode and electrolyte thin films, coated on 3D structured surfaces, creating a larger surface area, are proposed. Since the amount of inactive material is almost the same, it will result in higher overall energy density for the system.[4,8,15,17,20]

Various 3D Li-ion battery concepts are discussed in literature, however most of them are only conceptual. Experimental results mostly focus partial solid-state devices or on half cells.[4]

A used 3D structure is a soda-lime glass microchannel plate, which has a thickness of 500  $\mu\text{m}$  with 50  $\mu\text{m}$  wide pores through it. It was used as basis for a 3D Li-ion battery cell. Since it is a non-conductive substrate, first a current collector is deposited: a few  $\mu\text{m}$ 's of nickel were deposited via electroless deposition (Figure I-10a).

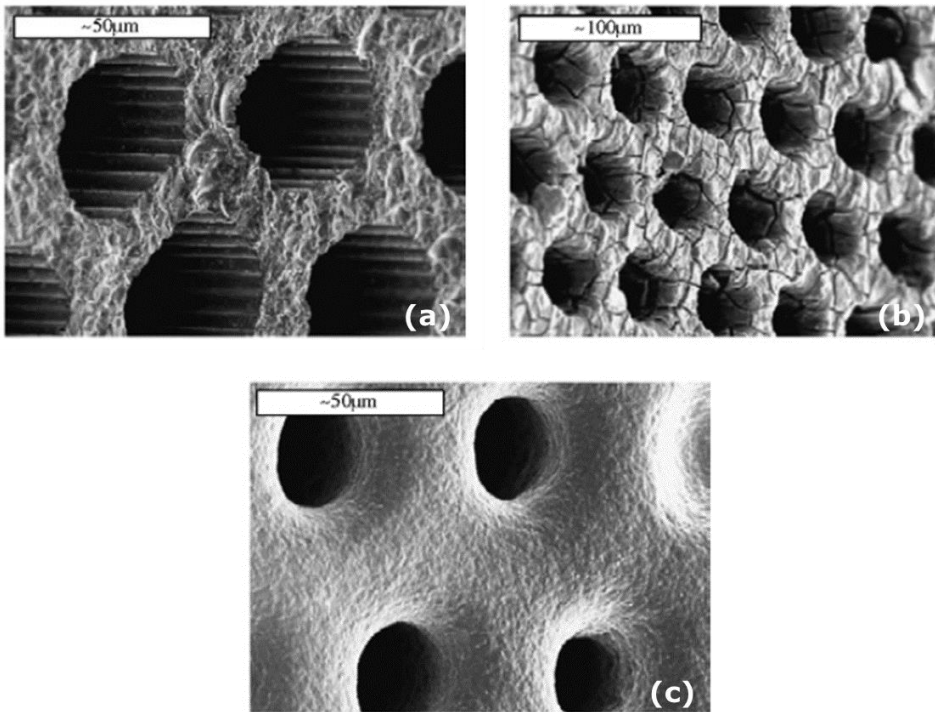


*Figure I-10: SEM images of microchannel pores coated by (a) a nickel current collector, Ni and a composite cathode, and (c) Ni, a composite cathode and a hybrid electrolyte.[24]*

This was followed by the electrodeposition of molybdenum oxysulfide which serves as cathode in the stack (Figure I-10b). Then, a hybrid polymer (Poly(vinylidene fluoride) mixed with a solvent and  $\text{SiO}_2$ ) was deposited via multiple impregnation and evacuation steps (Figure I-10c). To improve the electrochemical stability and

activity of the cathode a poly(ethyleneoxide) additive was optionally included in the electrolyte. With this electrolyte, ionic conductivities up to  $2 \cdot 10^{-3} \text{ S cm}^{-1}$  should be feasible. The anode, a slurry with graphite (mesocarbon microbeads), was spin coated on the whole until the microchannels were completely filled. After that, the stack was soaked in a liquid electrolyte ( $\text{LiBF}_4$  in ethyl carbonate/diethyl carbonate) to obtain high conductivity. Finally, a piece of lithium foil was placed on the stack in order to lithiate the graphite anode. It was found that the capacity of the 3D stacks had a capacity (per geometrical area) which was 20-30 times higher than the 2D cells, matching the 20-30 times surface area increase by switching to 3D.[24] Since a hybrid polymer electrolyte, soaked in a liquid electrolyte, is part of the whole, one can state that this is not a full 3D all-solid-state battery. However it shows that 3D stacks are feasible for battery purposes.[4]

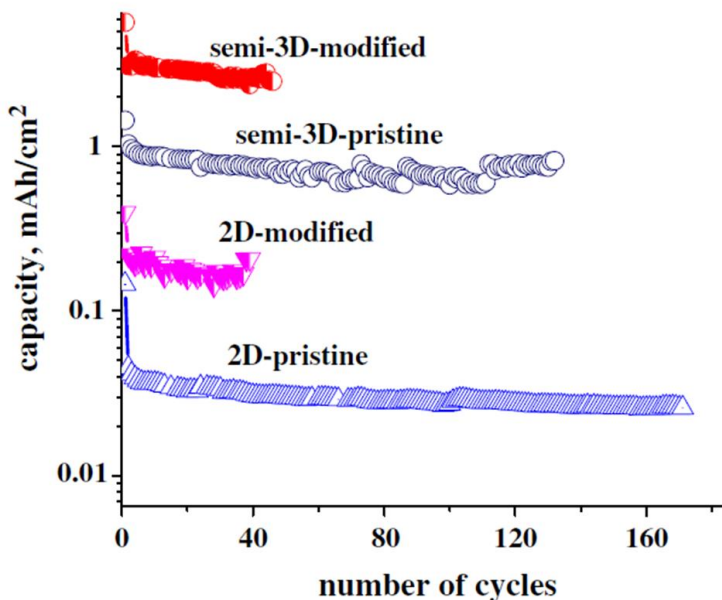
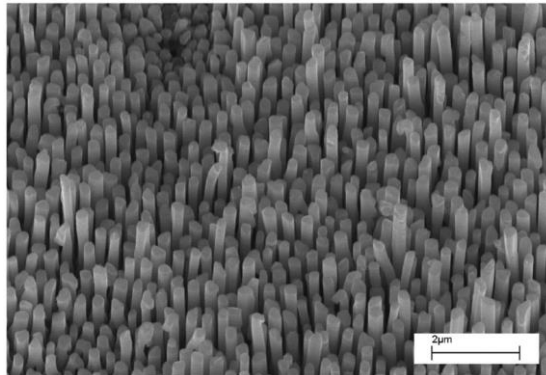


Figure I-11: Capacity (with respect to the geometrical surface area) for planar and semi-3D-MCP Li/HPE/ $\text{MoO}_y\text{S}_z$  cells.[24]

Steps towards full 3D all-solid-state batteries and in particular 3D thin-film batteries can also be found in literature. Cheah et al. reported that aluminum nanorods, which are visualized in Figure I-12, could be used as current collector. The rods were successfully covered by a 17 nm thick anatase TiO<sub>2</sub> film using atomic layer deposition. Its electrochemical characteristics were compared to a 17 nm thick anatase TiO<sub>2</sub> on a planar aluminum plate, by using a liquid electrolyte.



*Figure I-12: Aluminum nanorods as current collector for 3D Li-ion batteries.*[25]

Figure I-13 shows an increase of the capacity (for the same geometrical area) with a factor 10 for the 3D system compared to the 2D system. This is consistent with the surface area that is gained by switching from a planar system to the reported nanorods.[25] Shaijumon et al. also used aluminum nanorods as current collector. They deposited LiCoO<sub>2</sub> as cathode material on the rods via spray coating. They measured a gain in capacity with a factor 2, much less than expected. This could be attributed to the fact that the spray coating process did not result in full coverage of the Al nanorods.[26]

Since silicon is the most widely used material in semiconductor industry, it was proposed by Notten et al. that this material could act as substrate for 3D thin-film Li-ion batteries. This should enable integration of these very compact batteries. [20] The surface area enhancement of silicon can be achieved by micro-structuring the substrate, for instance, by creating trenches in the silicon substrate or by other geometries like micropillars which is schematically presented in Figure I-14.[17,20]

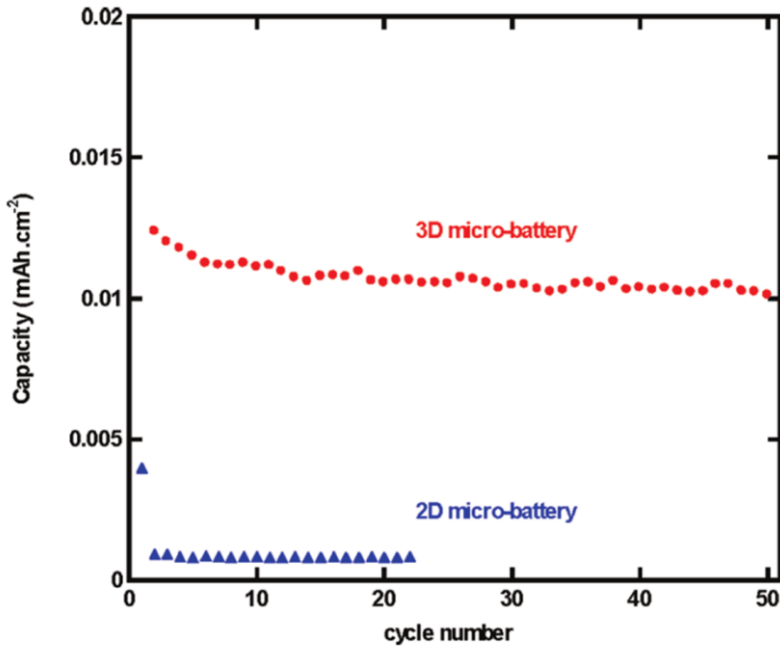


Figure I-13: Capacity (with respect to the geometrical surface area) for a 17 nm anatase  $\text{TiO}_2$  film on Al nanorods (3D) and a 2D Al plate.[25]

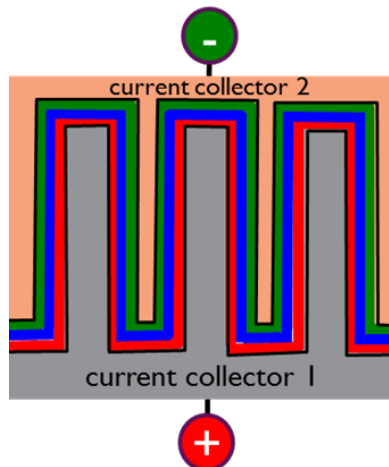
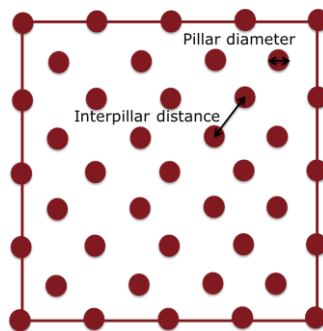


Figure I-14: Schematic representation of a 3D all-solid-state thin-film battery.[17]

As an illustration, a square array of pillars is schematically represented in Figure I-15 (top-down view). It can be characterized by three main parameters, namely the pillar length, the pillar diameter and the interpillar distance, which is the distance between two pillars. By increasing the pillar length and scaling down the diameter and interpillar distance, a very high area enhancement for a given projected area can be achieved. This is shown in the plot in Figure I-16a where the pillar area surface enhancement is plotted as function of the pillar length for various hexagonally stacked pillar areas. However the spacing between the pillars also sets the maximum thickness of the Li-ion battery stack and thus the active material (electrodes). Therefore the smallest spacing does not necessarily result in the highest volume of electrode material. This can be seen from Figure I-16b where the equivalent planar electrode thickness is plotted as a function of the pillar length for various pillar arrays.



*Figure I-15: Schematic representation (top-down view) of a square array of pillars.*

It is clear that from those arrays the pillars with a diameter and interpillar distance of both  $2\ \mu\text{m}$  result in the highest equivalent (planar) electrode thickness and thus have potential for the highest capacity. However, not only the theoretical capacity is of importance, also the film thickness of the deposited layers is crucial. First of all, the electrode thicknesses should be tuned according to their individual volumetric capacity. Furthermore, the film thicknesses are linked to the ionic and electronic conductance, and thus the power of the stack. From a certain film thickness the power is getting too small so that the potential capacity cannot be employed anymore. Obviously, an optimum condition in pattern density and film thickness exists resulting in a maximum power and capacity.[17]

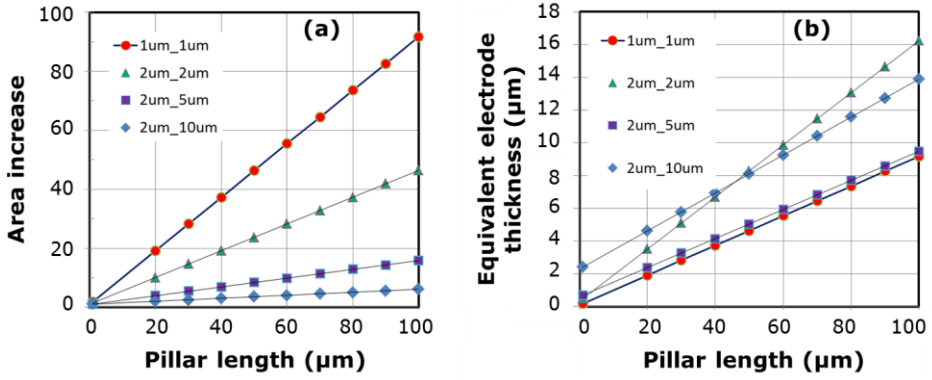


Figure I-16: (a) Area increase and (b) equivalent planar electrode thickness as a function of the pillar length for hexagonally stacked arrays of pillars with a pillar diameter of 1  $\mu\text{m}$  to 2  $\mu\text{m}$  and an interpillar distance from 1  $\mu\text{m}$  to 10  $\mu\text{m}$ . [17]

## 2 Chemical solution deposition

Chemical solution deposition (CSD) is a method to deposit (crystalline) (multi)metal oxides as thin films. This wet chemically based route, which is schematically shown in Figure I-17, is based on the deposition of a metal-containing precursor solution via e.g. spin coating, dip coating or spray coating. Via a well-defined thermal treatment firstly a gel is formed. When the organic species (present in the precursor solution) are removed out of the gel, the multi-metal oxide is formed and eventually crystallized. Multi-metal oxide powders can also be synthesized via this method. Instead of the thermal treatment of a deposited film, then, the solvent is evaporated out of the bulk precursor solution, resulting in a gel. After removal of the organic species, via an anneal, (crystalline) (multi)metal oxide powder can be obtained.[27]

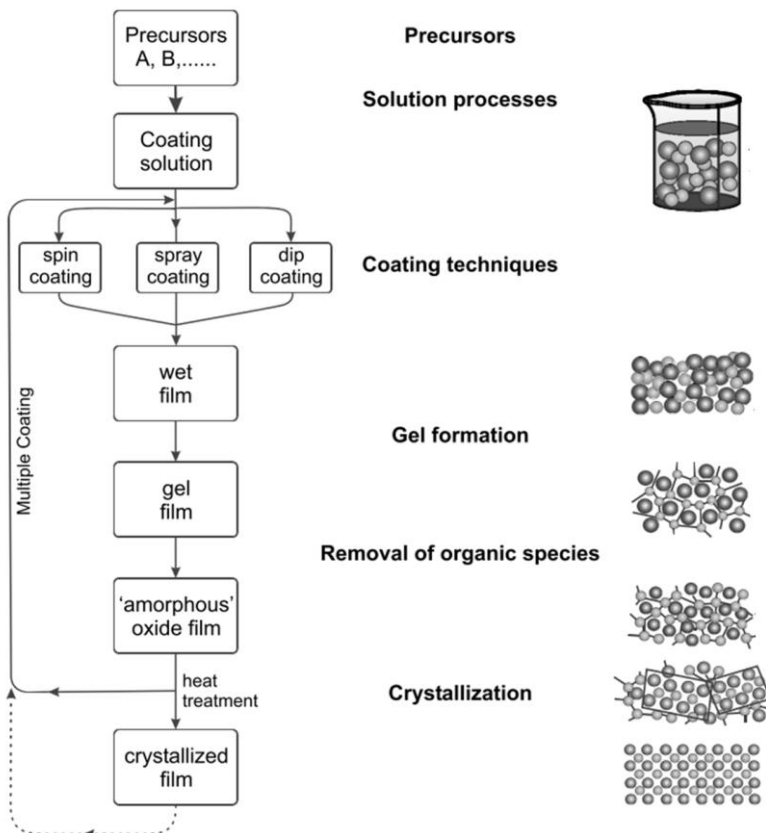


Figure I-17: Flowchart of a typical chemical solution deposition process.[27]

## 2.1 Precursor synthesis

The precursor synthesis for chemical solution deposition is directly related to sol-gel processes. Sol-gel synthesis is a process which makes use of a sol which forms a gel upon heating. The sol is a suspension of small particles (metal ion containing species) , typically 1-100 nm, which are dispersed in a liquid phase whereas the gel is a 3D network, in which metal ions are built in and which is spread uniformly through the liquid.[28] Because of this strict definition, several chemical solution processes cannot be considered as a sol-gel synthesis as they make use of precursor solutions instead of sols. However, in general, this narrow definition is mostly extended and the term "sol-gel" is used for a large variety of wet synthesis methods. Thus, not only processes which start from a sol, but also methods which start from a precursor solution in which metal ions are dissolved, are considered, as long as the highest possible degree of homogeneity is achieved. As mentioned before, by evaporation of the solvent, the precursor should transform into an amorphous gel, which is a solid or extremely viscous liquid without precipitation (Figure I-17). The homogeneity, coming from the initial start (= precursor) is captured since the ions are immobilized into the gel. Further heat treatment should lead to the formation of (crystalline) (multi)metal oxides (Figure I-17).[29]

Besides the colloidal route, there are two main streams in sol-gel chemistry, i.e. the organic and inorganic polymerization routes. They make use of, respectively, the polymerization of organic monomers and the formation of metal ion complexes.[29]

### 2.1.1 Organic polymerization routes

Organic polymerization routes make use of the formation of an organic polymer network in which cations are immobilized. There are two ways in which such network can be formed, i.e. in-situ and ex-situ. In the first case, the gel with coordinated cations is built while the monomers are polymerized. In the ex-situ case, this is done by the dissolution of a coordinated polymer to which cations can attach.[29]

The best-known organic polymerization system is Pechini's route.[29-31] Carboxylic acids, mostly citric acid, and metal carboxylate complexes, mostly citrate based, are dissolved in ethylene glycol. Through heating, an esterification will occur, as shown in Figure I-18.[29-31] Since the resulting compound has a free hydroxyl and carboxyl group, the reaction will continue so that a polymer network, with a homogenous distribution of metal cations, is formed.[29-31]

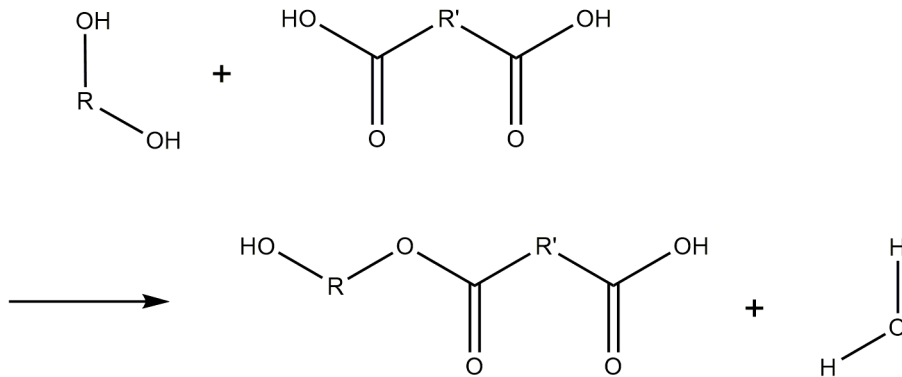
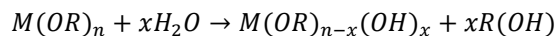


Figure I-18: Esterification reactions (Pechini's route)

## 2.1.2 Inorganic polymerization routes

### 2.1.2.1 Alkoxide route

The alkoxide route starts from metal ion alkoxides which are dissolved in an organic solvent, typically an alcohol. By the addition of water, a hydrolysis reaction is initiated [29]:



(Equation I-11)

Eventually hydrolyzed monomers are formed which will undergo a condensation reaction. This process can occur along various mechanisms as can be seen in Figure I-19. In this way, oligomers are formed, and by further condensation, clusters are formed, which tend to aggregate so that finally a 3D network is created.[29,32,33]

This system also entails some drawbacks. First of all, it is not straightforward to apply this technique for multi-metal oxides. The hydrolysis rate per metal ion alkoxide will differ so that there is a chance of segregation during the gelation. If the hydrolysis rate for metal ion A is much higher than for metal ion B, then homocondensation (A-O-A) will be favored instead of heterocondensation (A-O-B). Consequently phase segregation occurs which possibly leads to secondary phases.[27] This could be circumvented by stabilization or the use of heterometallic alkoxides.[34,35] Another disadvantage of this process is related to the start compounds. Metal alkoxides are very reactive to ambient humidity [36] and thus extra care has to be taken. Furthermore their availability is low and cost is high. Moreover, it typically makes use of teratogenic solvents (e.g. methoxy-ethanol).[36–38]

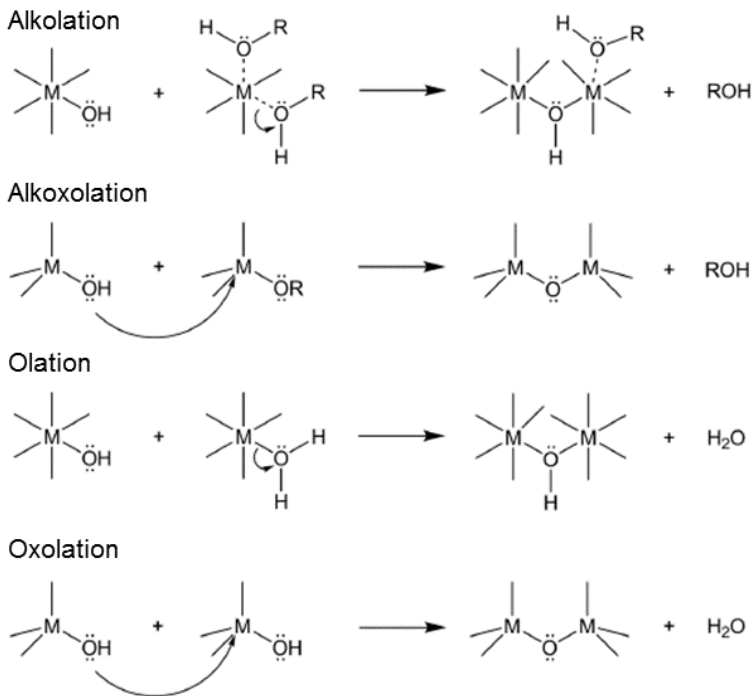
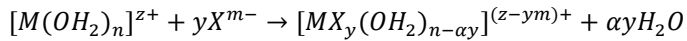


Figure I-19: Overview of condensation mechanisms.[39]

### 2.1.2.2 Aqueous solution-gel route

When metal alkoxides or metal salts are added to water, this mostly will result in the precipitation of hydrated oxides and polyanions. Therefore,  $\alpha$ -hydroxy acids, compounds that consist of a carboxylic acid group and a hydroxyl group on the adjacent carbon (e.g. citric acid), and other electron donating ligands have to be added to the system.[32,33,40,41] By metal-ligand optimization and pH adjustment, aqueous  $\alpha$ -hydroxy-carboxylato metal complexes can be formed in water [39]:



(Equation I-12)

In this reaction  $M^{z+}$  and  $n$  represent, respectively, the metal ion and the original amount of coordinated  $H_2O$  ligands.  $X^{m-}$  is the electron donating ligand which establishes  $\alpha$  coordinated bounds with the metal ion ( $M^{z+}$ ),  $y$  is the amount of ligands per metal ion.

As an example a metal complex with citric acid is shown in Figure I-20.

The aqueous solution-gel route is characterized by its high compositional flexibility. Various metal cations can be mixed in the solution and a high homogeneity of the resulting gel/oxide can be guaranteed. Since it makes use of water as a solvent, also other drawbacks such as sensitivity to water and toxicity are not applicable.[29,40]

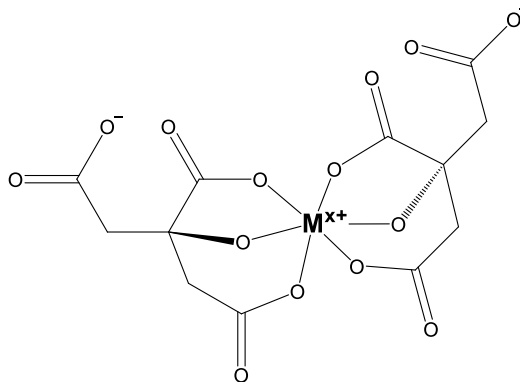


Figure I-20: Schematic representation of a metal complex with citric acid.

## 2.2 Deposition methods

The sol-gel precursor chemistry is not only used to synthesize gels and eventually powders, but also for the deposition of films. A (thin) layer of the presented precursors is deposited on a substrate, after which it is thermally treated to form a gel and eventually an inorganic crystalline film. The deposition can be done by various methods, such as spin coating, dip coating and spray coating.[27,40]

### 2.2.1 Spin coating

Spin coating is a wide spread technique to form coatings on planar substrates because it is known for its reproducibility, uniformity, simplicity and low cost. The coating process can be divided in four steps which are schematically represented in Figure I-21. The process is initiated by the loading of an excess of precursor on the substrate (a) after which the whole is accelerated till a certain rotation speed (b). Due to rapid spinning, a centrifugal force is applied on the deposited liquid, leading to a thin film on the substrate. During the process, the excess of precursor is removed from the substrate and the layer thickness is reduced. This happens via two mechanisms: first, the centrifugal forces and fluid dynamics are dominant (c), after that the film thickness is further reduced due to evaporation of the solvent (d). Consequently, there is a drastic change in viscosity, which sets a stop in thinning the layer by the centrifugal force. Since the film thickness evolves to a stationary stage, one can understand that the spin time should be long enough. This will result in reproducible film thicknesses. Further increase in time will not lead to a difference in film thickness. The important parameters, besides the wetting of the substrate are summarized in [42–44]:

$$h_f \propto \omega^{-\frac{1}{2}} \eta^{\frac{1}{3}}$$

(Equation I-13)

with  $h_f$ ,  $\omega$  and  $\eta$ , respectively, the resulting precursor film thickness, the spinning speed and the precursor viscosity.

This relationship, which was experimentally derived, shows that besides the viscosity of the precursor, the spinning speed is the most important parameter influencing the film thickness.[43,44]

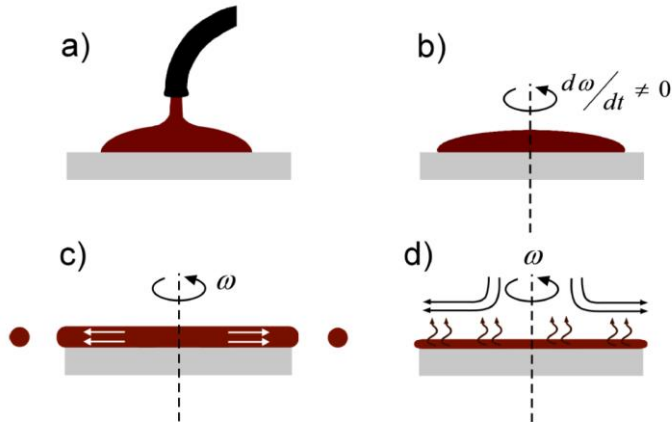


Figure I-21: Schematic representation of the steps in spin coating, i.e. (a) loading of the precursor, (b) acceleration of the substrate, (c) thinning of the layer controlled by fluid dynamics and (d) thinning of the layer dominated by evaporation.[45]

Besides the proven advantages of spin coating, this technique has also some limitations. The coated surface should be as smooth as possible. Coating of 3D structures seems therefore very hard to achieve. Furthermore, continuous (linear) processes are not possible and the process efficiency is very low. Only 2-5% of the applied material is left on the substrate after the process.[39]

### 2.2.2 Dip coating

Dip coating is another widely used technique to achieve coatings. The substrate is immersed in the precursor solution after which it is withdrawn, vertically, at a constant speed (Figure I-22).

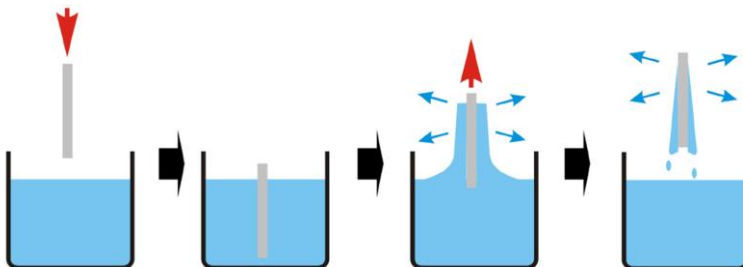


Figure I-22: Schematic representation of the dip coating process.[46]

During the withdrawal process, a thin film is formed on the substrate that dries. The resulting film thickness is dependent on the viscosity, density, surface tension, the bath temperature and the withdrawal speed of the substrate. Main advantage of this technique is that, in theory, more complex structures could be coated.[28,47]

### 2.2.3 Spray coating

The most used technique to achieve coating of rough surfaces via wet chemical solution deposition is spray coating. An advantage of spray coating is that the amount of solute deposited on the substrate is proportional to the volume of solution that is deposited on the substrate, which is not the case for spin coating.

During spray coating, the liquid precursor is introduced to a nozzle which breaks the liquid into droplets. The spray coating method is influenced by various factors. To ensure the homogeneity of the final solid film, it is thus important to control all parameters of the process.[48–50]

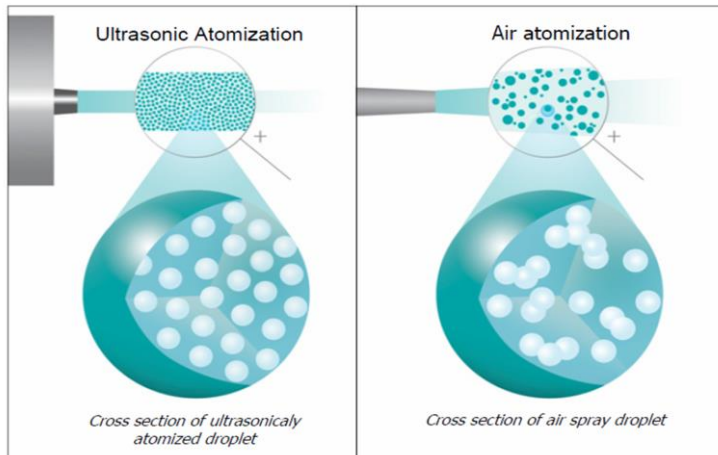


Figure I-23: Cross-section of an ultrasonically atomized and air spray droplet.[51]

The first parameter is the way of droplet formation. This can be performed through a nozzle which is based on an air atomizer: it uses pressure or force to tear the liquid apart. Disadvantage of this technique is that the drop size has a wide distribution and is very difficult to predict, as is schematically shown in the cross-

section of an air spray droplet in Figure I-23 (right). Furthermore, the result is that the atomized droplet sizes, the kinetic energy of the droplets and volume being added to the process cannot be easily separated. Changing one of these factors is basically changing them all. An alternative is ultrasonic atomizing, of which a schematic representation is shown in Figure I-24. The nozzle breaks the liquid into micrometer-sized droplets without the use of pressure. It utilizes piezoelectric transducers to create mechanical vibrations which are, via the creation of a shock wave, transferred into the material. As can be seen in Figure I-25, these shock waves are formed on the atomizing surface perpendicular to the axis of the vibration underneath. It are thus standing waves, which are typically formed when the resonating frequency matches the natural frequency of a certain compound structure. Increasing the power of electrical energy will then cause the wave peaks to get so high that droplets fall of the tips of the waves.

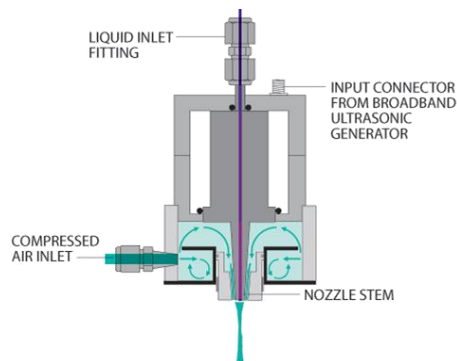


Figure I-24: Schematic representation of an ultrasonic nozzle, in particular AccuMist Precision Ultrasonic Spray Nozzle from Sono-Tek.[50]

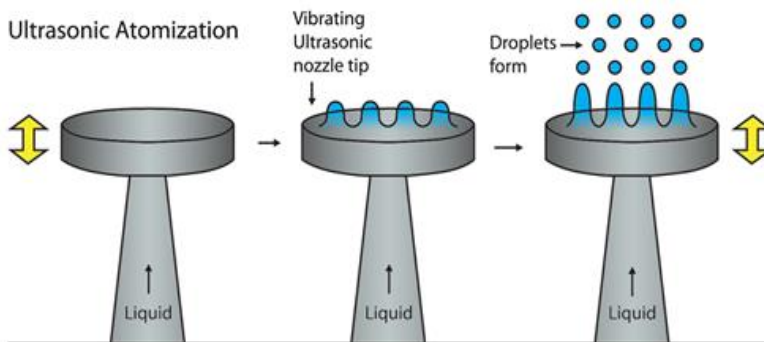


Figure I-25: Nozzle tip vibration, wave formation and ultrasonic atomization.[51]

The resulting droplets are more structured and have a narrower size distribution (Figure I-23-left).[51] These droplets have a mathematical definable size according to [51]:

$$D_{N,0.5} = 0.34 \lambda_L$$

(Equation I-14)

with  $D_{N,0.5}$  and  $\lambda_L$ , respectively, the number median diameter of droplet size and the wavelength in the liquid.

The latter can be calculated via [51]:

$$\lambda_L = \left( \frac{8\pi \theta}{\rho f^2} \right)^{1/3}$$

(Equation I-15)

with  $\theta$ ,  $\rho$  and  $f$ , respectively, the surface tension, density and nozzle frequency.

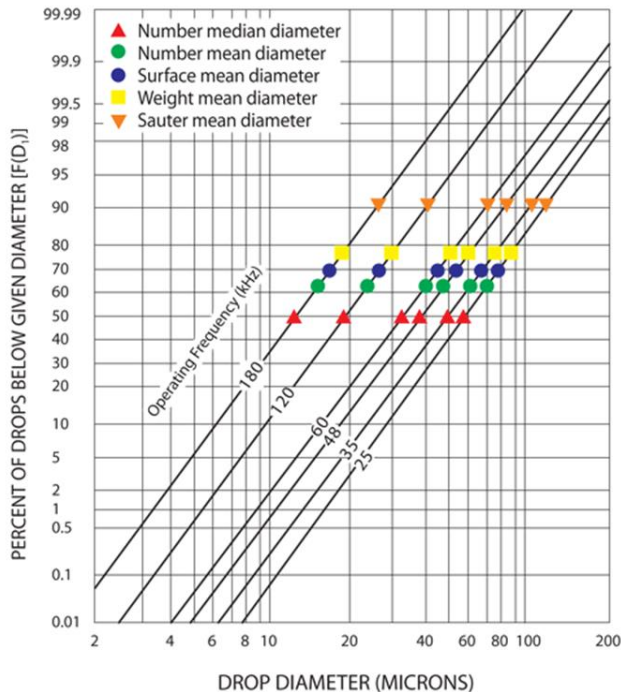


Figure I-26: Droplet size distribution of water droplets from ultrasonic nozzles as a function of the operating frequency.[51]

The frequency at which the nozzle vibrates, is the predominant factor that influences the droplet size. As an example, the droplet size distribution of water droplets as a function of the nozzle frequency, is shown in Figure I-26. The droplet size can thus be controlled in a very effective way. Furthermore, the distribution curve of droplets originating from ultrasonic nozzles is typically narrower compared to the size distribution of droplets, created via a pressure nozzle (Figure I-27).[51]

Not only the droplet size, but also the volume can be controlled: the flow can be adjusted without significantly affecting the size or the kinetic energy of the droplet (contrary to pressure based nozzles). Furthermore the droplet kinetic energy and velocity can also be controlled separately, in particular via a plume shaping device. These adjustments, which result in the minimization of overspray and thus maximize the efficiency, result in little to no changes of the droplet size and have zero effect on the flow rate.[51]

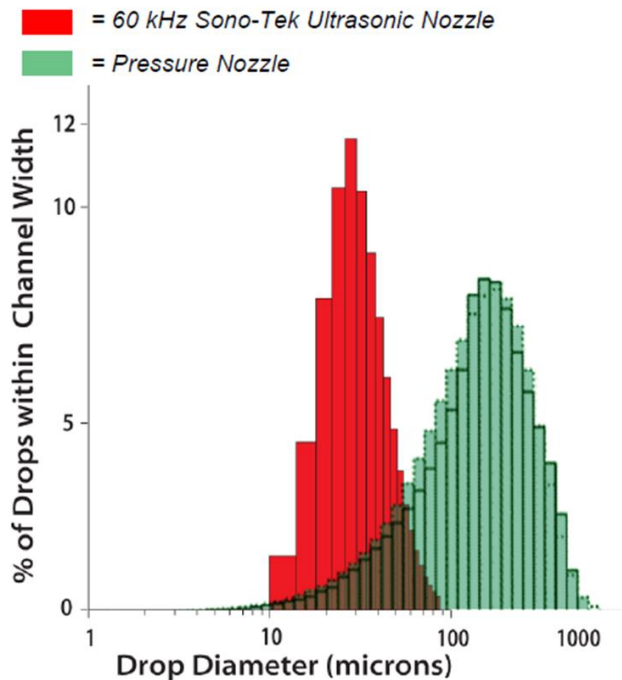


Figure I-27: Typical size distribution of droplets originating from a Sono-Tek 60 kHz ultrasonic nozzle and a pressure nozzle.[51]

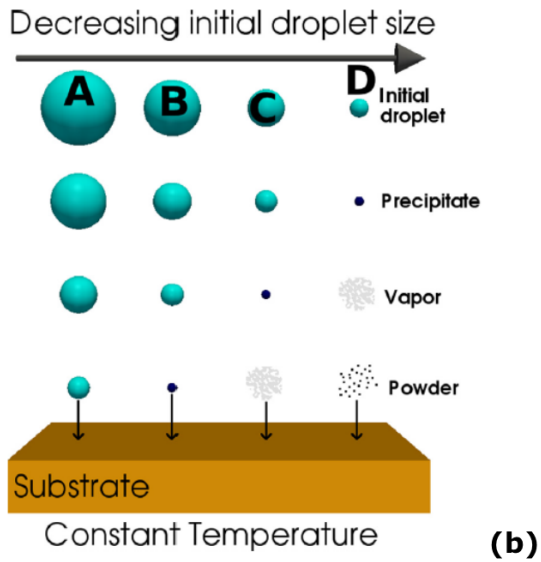
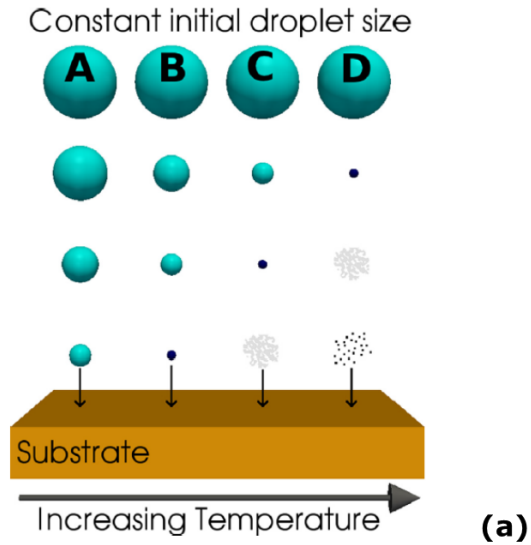


Figure I-28: Influence of (a) the temperature and (b) the initial droplet size on the spray coating process.[49]

After the formation of the droplets, these are, via the use of a carrier gas, directed to the substrate (Figure I-24). There, they merge to form a continuous layer and via evaporation of the solvent a thin film of solute is formed. A good wettability, and thus a low contact angle, is necessary to form a thin wet layer. Otherwise, it tends to create a spherical cap shape during spray coating. This leads to a less uniform evaporation over the surface and thus to a non-uniform coating. The contact angle of the precursor with the substrate ( $\theta_c$ ) is determined by the surface tension ( $\gamma$ ) [48]:

$$\cos\theta_c = \frac{\gamma_{SV} - \gamma_{SL}}{\gamma}$$

(Equation I-16)

assuming that the solid-vapor phase ( $\gamma_{SV}$ ) and the solid-liquid phase ( $\gamma_{SL}$ ) interactions are fixed.

Consequently, a low surface tension is necessary for spray coating. This can be achieved by optimizing the precursor system and/or the substrate.[48]

The formation of a continuous layer on the substrate is not only determined by the surface tension, also the path towards the deposition influences the resulting layer. When the precursor is atomized, it travels along with the carrier gas through the ambient while various forces, in particular the gravitational, Stokes and thermophoretic force, are simultaneously acting on it. One can distinguish four pathways which the droplets can follow, the spray coat parameters will determine which mechanism the droplets will follow. The influence of the deposition temperature and the initial droplet size on the different mechanisms are schematically presented in Figure I-28. As mentioned, there are four pathways, presented as A, B, C and D. The first mechanism (A) will occur in case of a large initial droplet size and/or low deposition temperature. Since the solution will not completely evaporate, the droplets will impact with the substrate and then evaporate and decompose. When the temperature is set slightly higher and/or when the initial droplet size is smaller (B), evaporation will occur mostly just as the droplet reaches the surface resulting in an amorphous precipitate which will

decompose. When even higher temperature and smaller droplets are used (C), it is more likely that the droplets evaporate prior to reaching the substrate vicinity. Consequently, the precipitate will form early and as it reaches the immediate vicinity of the substrate, it is converted into a vapor state and a heterogeneous CVD-like reaction will occur. When a very high deposition temperature and/or very small initial droplet sizes are applied, the droplets will rapidly form a precipitate (D). When this approaches the substrate, it will vaporize (when  $T_{\text{evaporation}} < T_{\text{decomposition}}$ ) and a chemical reaction will occur in the vapor phase. This homogeneous reaction will result in the condensation of molecules into crystallites in the form of a powder. Powder will thus be deposited on the surface. One can understand that for the deposition of good-quality coatings mechanisms B and C in Figure I-28 are preferred.[49] It is obvious that not only the deposition temperature and the initial droplet size play an important role in the film formation. There are several other spray coat parameters which have to be taken into account, as shown schematically shown in Figure I-29. The precursor concentration, flow rate and nozzle to substrate distance will also influence the droplet pathway and the resulting characteristics of the coating (a). Furthermore, there is the mode of spraying, two modes are available, i.e. the single pass process which covers a substrate in one pass and a multiple process (used in this thesis) in which the nozzle produces a much more narrow spray while moving over the substrate in X, Y direction. It is obvious that the latter is dependent on the path velocity and amount of passes (b). [48–50]

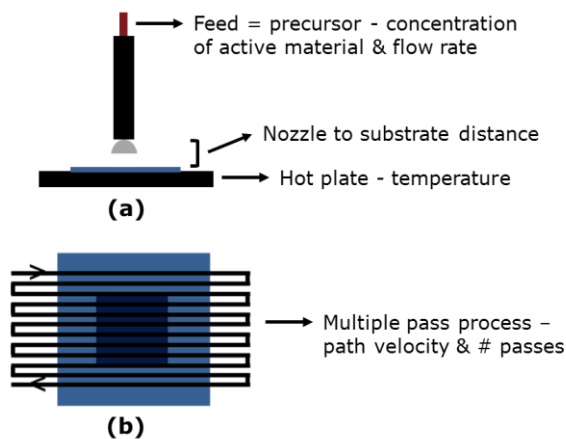


Figure I-29: Schematic representation of the parameters (discussed in this work) corresponding to (a) typical spray coating set-up and (b) multiple pass process.

### 3 Characterization methods

Various experimental methods are used to characterize the synthesized materials, i.e. precursor, powder and film.

The basic characterization of the synthesized precursor solutions includes inductively coupled plasma atomic emission spectroscopy (ICP-AES) to determine the exact metal ion concentration.

The synthesized powders are characterized via thermogravimetric analysis (TGA) and differential scanning calorimetry (DSC) to check the decomposition of the powder (and thus the precursor). Furthermore information about the crystallization of powders is obtained via X-ray diffraction (XRD) and more specifically high-temperature X-ray diffraction (HT-XRD), allowing an in-situ study of the phase (trans)formation upon heating.

Also the crystallization of thin-films is determined via XRD and in-situ XRD. Raman analysis is an extra option to determine phase formation, especially for titanium containing oxides. Possible silicate formation upon heating is determined by grazing angle attenuated total reflectance - Fourier transform infrared (GATR-FTIR) spectroscopy. The morphology of the films is checked upon using scanning electron microscopy (SEM), both in tilted view (45°) and in cross-section view (X-SEM). The latter also gives an indication about the film thickness, just as ellipsometry spectroscopy. Via energy-dispersive X-ray spectroscopy, coupled with SEM, a qualitative elemental analysis of the deposited film can be executed.

#### 3.1 Elastic recoil detection analysis

Elastic recoil detection analysis (ERDA) is a nuclear technique that allows the characterization of thin films. Via this technique, the sample composition and elemental concentration depth profiles in films can be determined. ERDA is based on an accelerated energetic ion beam which is focused on the sample. This induces an elastic nuclear (Coulomb) interaction between the ions of the beam and the atoms in the sample. The resulting atoms from the sample which are recoiled in forward direction are detected. The kinematics of the process and the energy loss

of ions in the matter regulate the quantification and the determination of the depth profiles. Elastic recoil detection analysis can be divided into two groups based on the used accelerators, namely light incident ion (LI) and heavy incident ion (HI) accelerators. Low voltage and large tandem accelerators are, respectively, used.

ERDA with light incident ions is performed using a low energy beam, namely a  $^4\text{He}$  beam (2 MeV). Typically, the recoiled hydrogen is detected by a forward detector while multiple detectors are installed at backscattering angles to detect the heavier elements by RBS. The forward detector is equipped with a "range foil", to preferentially stop atoms heavier than hydrogen.[52]

Typical ion beams for heavy incident ion ERDA are  $^{35}\text{Cl}$ ,  $^{63}\text{Cu}$ ,  $^{127}\text{I}$  and  $^{197}\text{Au}$ , accelerated at energies up to hundreds MeV. It makes typically use of element or mass sensitive detectors, such as time-of-flight telescopes, magnetic spectrographs or gas ionization detectors. The choice of detection system is often made based on the used ion beam. The advantage of HI-ERDA is that quantitative depth profiles of all present elements in the sample can be obtained in one measurement. However, ion beam induced damage and multiple scattering are possible side effects of HI-ERDA, influencing the accuracy. In order to achieve both high accuracy and high performances, heavy incident ion elastic recoil detection analysis, performed with low beam energies ( $< 20$  MeV), was developed by Giangrandi et al. A depth resolution down to 2 nm and a sensitivity better than 0.1 atomic percent for all elements should be achievable by this method.[52,53]

## **3.2 Electrochemical characterization**

### **3.2.1 Electrochemical cell**

Ideally, the electrochemical measurement should only give information about the process happening at the working electrode since this is the sample of which the properties are determined. In order to ignore the electrochemical processes occurring at the counter electrode, a three-electrode set-up is typically used. As can be seen in Figure I-30, the voltage is measured between the working and the reference electrode while applying the current through the counter electrode. The counter and reference electrode are thus separated so that the voltage can be

measured without a significant current flowing through the reference electrode.[54]

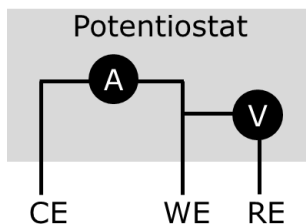


Figure I-30: Schematic representation of a three-electrode set-up. CE, WE and RE stand respectively for counter, working and reference electrode.

### 3.2.2 Cyclic voltammetry

Cyclic voltammetry (CV) is a method to study the electrochemical behavior of samples, e.g. thin films. It allows the analysis of the electrochemical reactions that occur at the electrode/electrolyte phase barrier. It is based on a scan of the potential (linearly in time, at a certain voltage the polarization direction of the scan is reversed) while measuring the current that is required to obtain the potential scan. This results in a typical plot, a cyclic voltammogram, which is shown in Figure I-31. All redox reactions have their specific potential at which they occur. Consequently, upon reaching a certain potential, a particular oxidation or reduction reaction takes place resulting in an increase of, respectively positive and negative current. Once the concentration of reducing or oxidizing species at the working electrode nears depletion, the current starts to decrease again. Obviously, in this way, particular oxidation and reduction reactions can be identified upon scanning.[54]

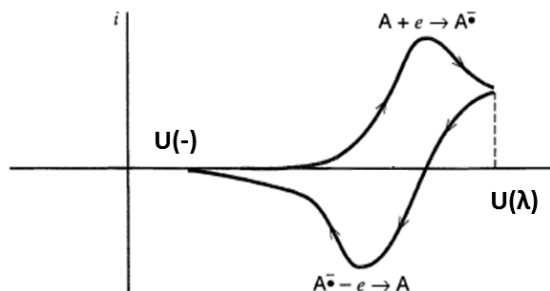


Figure I-31: A typical cyclic voltammogram.[54]

### 3.2.3 Galvanostatic charging/discharging measurements

Galvanostatic charging/discharging measurements or cycling is typically performed for electrode materials. A constant current is applied while measuring the resulting potential change. Via this method, information about the electrode's capacity and kinetics can be deduced. The capacity is mostly presented as a function of various C-rates, which represents the (dis)charging rate to its maximum capacity. At 1C an electrode is (dis)charged in 1 hour, at 2C in ½ hour and at 0.5C at 2 hours. [54]

### 3.2.4 Electrochemical impedance spectroscopy

Electrochemical impedance spectroscopy (EIS) is a technique which is used to define the properties of electrochemical systems as a function of the frequency. Therefore an alternating voltage is applied, superimposed on an offset dc-voltage and this at varying frequencies [54]:

$$U = U_{dc} + U_{ac}$$

*(Equation I-17)*

with  $U_{dc}$  and  $U_{ac}$ , respectively, the fixed and alternating voltage.

The latter can be described as [54]:

$$U_{ac} = U_m \sin(\omega t)$$

*(Equation I-18)*

with  $U_m$ ,  $\omega$  and  $t$ , respectively, the amplitude of the alternating voltage, the frequency and the time.

During the application of the alternating voltage, the current through the system is monitored and for basic systems should follow [54]:

$$I = I_{dc} + I_{ac}$$

*(Equation I-19)*

with  $I_{dc}$  and  $I_{ac}$ , respectively, the direct and alternating component of the current.

The latter can be described as [54]:

$$I_{ac} = I_m \sin(\omega t + \varphi)$$

(Equation I-20)

with  $I_m$ ,  $\omega$ ,  $t$  and  $\varphi$ , respectively, the amplitude of the alternating component of the current, the frequency, the time and the phase shift of the measured current.

When the electrochemical system behaves like an ideal resistor, there is no phase shift ( $\varphi=0$ ). Furthermore, the current through a resistor is defined via Ohm's law [54]:

$$Z = \frac{U_{ac}}{I_{ac}}$$

(Equation I-21)

with  $Z$  the impedance (ac equivalent of resistance).

By insertion of (Equation I-18) and (Equation I-20), one gets [54]:

$$Z = \frac{U_m \sin(\omega t)}{I_m \sin(\omega t)} = R$$

(Equation I-22)

with  $R$  the resistance.

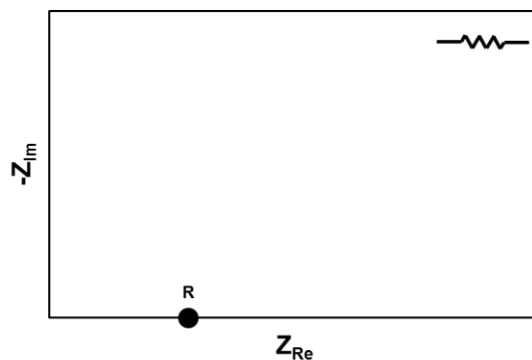


Figure I-32: Nyquist plot for an ideal resistor. As an inset the symbol of an ideal resistor is shown.

The results of electrochemical impedance spectroscopy are mostly presented using a Nyquist plot, in which the real and negative value of the imaginary part are respectively displayed on the X-and Y-axis. When plotting (Equation I-22), which represents the impedance of an ideal resistor, this results in an horizontal line on the x-axis (Figure I-32).[54]

For a capacitor, the current going through is dependent on the time derivative of the voltage [54]:

$$I = C \frac{dE}{dt}$$

(Equation I-23)

with C the capacitance.

This results in [54]:

$$I = C U_m \omega \cos(\omega t) = C U_m \omega \sin\left(\omega t + \frac{\pi}{2}\right)$$

(Equation I-24)

One can observe in this equation a phase shift of 90°. Furthermore from Euler's formula, it is known that [54]:

$$e^{ix} = \cos(x) + i \sin(x)$$

(Equation I-25)

Insertion of (Equation I-25) in (Equation I-24) results in [54]:

$$I = C U_m i \omega e^{i\omega t}$$

(Equation I-26)

The impedance of a capacitor can thus be described as [54]:

$$Z = \frac{U_{ac}}{I_{ac}} = -\frac{i}{\omega C}$$

(Equation I-27)

The Nyquist plot for an ideal capacitor, corresponding to (Equation I-27), is shown in Figure I-33.[54]



Figure I-33: Nyquist plot for an ideal capacitor. As an inset the symbol of an ideal capacitor is shown.

More complex systems can be described placing various resistors and capacitors in series or in parallel. An electrochemical reaction can, for instance, be described as a resistor (charge transfer) and an electrical double layer capacitance in parallel. The impedance of the system is then [54]:

$$\frac{1}{Z_{tot}} = \frac{1}{Z_{dl}} + \frac{1}{Z_{ct}}$$

(Equation I-28)

in which "tot", "dl" and "ct" stands, respectively, for total, double layer and charge transfer.

Insertion of (Equation I-22) and (Equation I-27) in (Equation I-28) results in [54]:

$$\frac{1}{Z_{tot}} = i \omega C_{dl} + \frac{1}{R_{ct}}$$

(Equation I-29)

The total impedance of the system can thus be described as [54]:

$$Z_{tot} = \frac{R_{ct}}{1 + \omega^2 C_{dl}^2 R_{ct}^2} - \frac{i \omega C_{dl} R_{ct}^2}{1 + \omega^2 C_{dl}^2 R_{ct}^2}$$

(Equation I-30)

When this electrochemical reaction is presented in a Nyquist plot (Figure I-34), this results in a semi-circle with a diameter  $R_{ct}$  and a maximum of [54]:

$$Z_{tot} = \frac{1}{R_{ct} C_{dl}}$$

(Equation I-31)

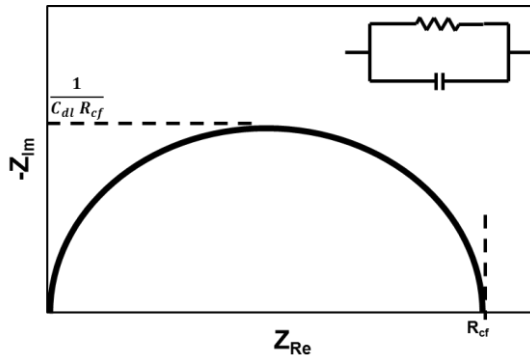


Figure I-34: Nyquist plot for a system containing a resistor (charge transfer) and an electrical double layer capacitance in parallel. As an inset equivalent circuit of the proposed system is shown.

Most electrochemical systems will be more complex, e.g. a resistance for the electrolyte solution is also encountered, resulting in an adapted Nyquist plot. Furthermore, other factors such as diffusion, roughness of the films or more process occurring at similar time-scales will influence the semi-circular behavior.[54]

## 4 Aim of the thesis

The aim of the thesis and the accompanying outline is summarized in Figure I-35. The main objective of the dissertation is to synthesize materials and develop new processes in function of energy storage applications, including thin-film capacitors and Li-ion batteries.

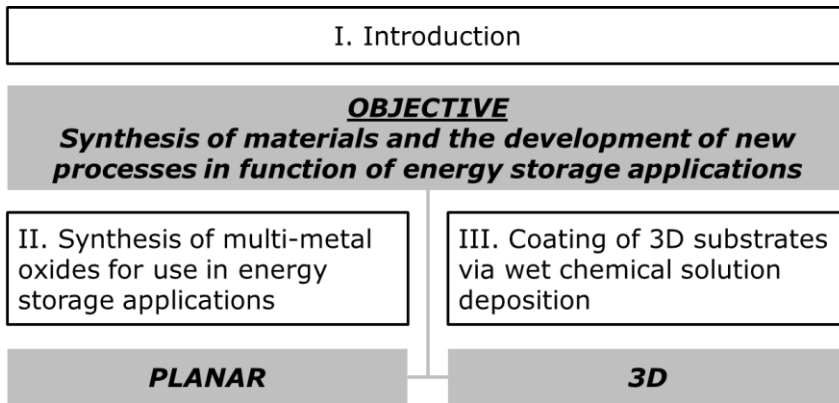


Figure I-35: Schematic representation of aim and the accompanying outline of the thesis.

The first part of the thesis will be about the synthesis of known materials, in another form (e.g. thin film instead of powder) and/or fabricated via another process. In the scientific community, a lot of interesting materials are already extensively studied. However, changing the form of the synthesized materials or the way to fabricate them can contribute to a better understanding and even an improvement of the material's and application's characteristics (approaching the theoretical potential of the material or device). A change in experimental method and parameters can for instance lead to advantages such as cost reduction. In Figure I-36 the baseline and reduced pack costs are plotted for each part of a Li-ion battery process. For all parts of the battery a cost cut-back can be obtained by changing synthesis factors such as implementing aqueous processing and reduced wetting and formation times. For some parts (cf. electrode processing), this cost cut-back is massive. Furthermore the synthesis of well-known materials in another form can enable new applications. The objective is to use chemical solution deposition, in particular aqueous CSD, as alternative synthesis method

for different materials and to study the material's and accompanying application's properties. This method would enable high-quality coatings which are fabricated easier, safer and cheaper.

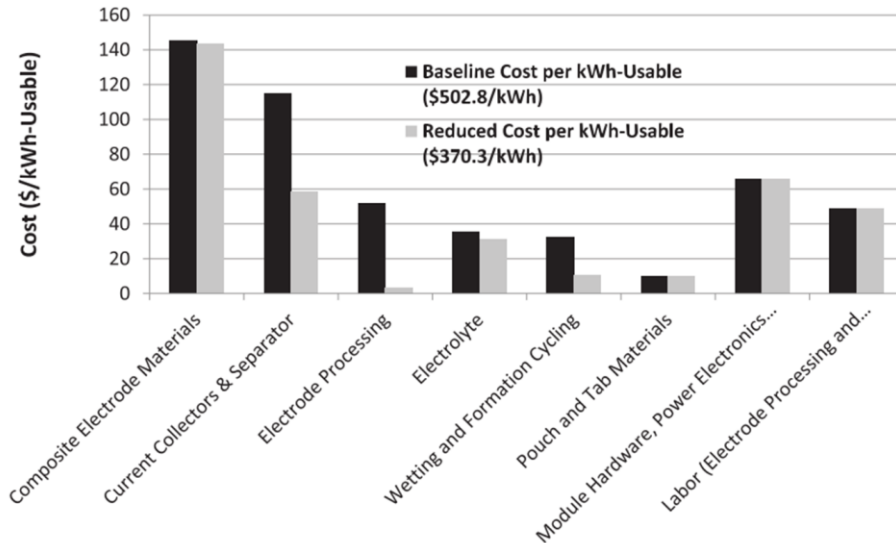


Figure I-36: Comparison of calculated baseline and reduced pack costs. The reduced costs were obtained by factors such as implementing aqueous processing, and reduced wetting and formation times. [55]

More specifically, the research on material fabrication in this dissertation can be divided in two parts according to the particular application.

The aim of the first part is the synthesis and characterization of a dielectric film which can be used in thin-film capacitors. As explained in the theoretical part, the use of an oxide with a giant dielectric constant could lead to a gain in energy density. The goal is to deposit a multi-metal oxide thin film which is characterized by an ultra-high dielectric constant, i.e.  $k \geq 10^4$ .

The research of materials in the second part should contribute to the fabrication of a thin-film Li-ion battery. Therefore an anode with a relatively high volumetric capacity ( $\geq 600 \text{ mAh/cm}^3$ ) should be deposited. Since it concerns a thin film, it is appropriate that the lattice strain upon charging and discharging is insignificant so that it only results in a negligible capacity loss.

The electrolyte film should be characterized by a relatively high ionic conductivity, i.e.  $10^{-6}$ - $10^{-8}$  S cm<sup>-1</sup> and low electronic conductivity. Furthermore it is important that there is a good matching between anode and electrolyte film. In this way, a continuous pathway for Li<sup>+</sup> ion transport is available. The deposition of a cathode film is beyond the scope of the thesis.

The aim of the second part of this dissertation is to take chemical solution deposition to a new dimension, i.e. to 3D thin-film Li-ion batteries (and 3D thin-film capacitors). As explained, for this new concept of devices, which are currently in an exploratory stage, there is a strong need for coating of various oxides (i.e. electrodes and electrolyte) on 3D surfaces. Nowadays, this deposition is typically done via atomic layer deposition (ALD) which is known to deliver high-quality conformal coatings and has proven to be of high value. However, also in this case, a change in deposition technique could lead to advantages. If these coatings could be achieved by a chemical solution deposition process, this would lead to lower running and equipment costs, a higher throughput (especially for substrates with a strongly increased surface area), and a large applicability towards complex, multi-metal oxides. Not only in view of commercial 3D devices and upscaling, there is a strong need to develop such process. Also from scientific point of view it is interesting to find out if it is possible to reach 3D coating via a CSD process.

## 5 References

- [1] P.G. Bruce, B. Scrosati, J.-M. Tarascon, Nanomaterials for rechargeable lithium batteries., *Angew. Chem. Int. Ed. Engl.* 47 (2008) 2930–2946. doi:10.1002/anie.200702505.
- [2] A. Burke, Ultracapacitors : why, how, and where is the technology, *J. Power Sources.* 91 (2000) 37–50. doi:10.1016/S0378-7753(00)00485-7.
- [3] M. Winter, R.J. Brodd, What are batteries, fuel cells, and supercapacitors?, *Chem. Rev.* 104 (2004) 4245–4269. doi:10.1021/cr020730k.
- [4] J.F.M. Oudenhoven, L. Baggetto, P.H.L. Notten, All-Solid-State Lithium-Ion Microbatteries: A Review of Various Three-Dimensional Concepts, *Adv. Energy Mater.* 1 (2011) 10–33. doi:10.1002/aenm.201000002.
- [5] V. Etacheri, R. Marom, R. Elazari, G. Salitra, D. Aurbach, Challenges in the development of advanced Li-ion batteries: a review, *Energy Environ. Sci.* 4 (2011) 3243–3262. doi:10.1039/c1ee01598b.
- [6] J.W. Long, B. Dunn, D.R. Rolison, H.S. White, Three-dimensional battery architectures., *Chem. Rev.* 104 (2004) 4463–4492. doi:10.1021/cr020740l.
- [7] J.M. Tarascon, M. Armand, Issues and challenges facing rechargeable lithium batteries., *Nature.* 414 (2001) 359–367. doi:10.1038/35104644.
- [8] L. Baggetto, R. a. H. Niessen, F. Roozeboom, P.H.L. Notten, High Energy Density All-Solid-State Batteries: A Challenging Concept Towards 3D Integration, *Adv. Funct. Mater.* 18 (2008) 1057–1066. doi:10.1002/adfm.200701245.
- [9] J. Bird, *Electrical and Electronic Principles and Technology*, Fourth edi, Newnes - Elsevier, 2010.
- [10] B.E. Conway, *Electrochemical Supercapacitors: Scientific Fundamentals and Technological Applications*, Kluwer Academic / Plenum Publishers, New York, USA, 1999.
- [11] D. Nelis, PhD thesis: Studie van de waterige oplossing-gel methode voor de bereiding van ferro-elektrische SrBi<sub>2</sub>Ta<sub>2</sub>O<sub>9</sub> en SrBi<sub>2</sub>Nb<sub>2</sub>O<sub>9</sub> poeders en dunne lagen, 2004.
- [12] P. Jain, E.J. Rymaszewski, *Thin-Film capacitors for packaged electronics*, Kluwer Academic / Plenum Publishers, 2004.

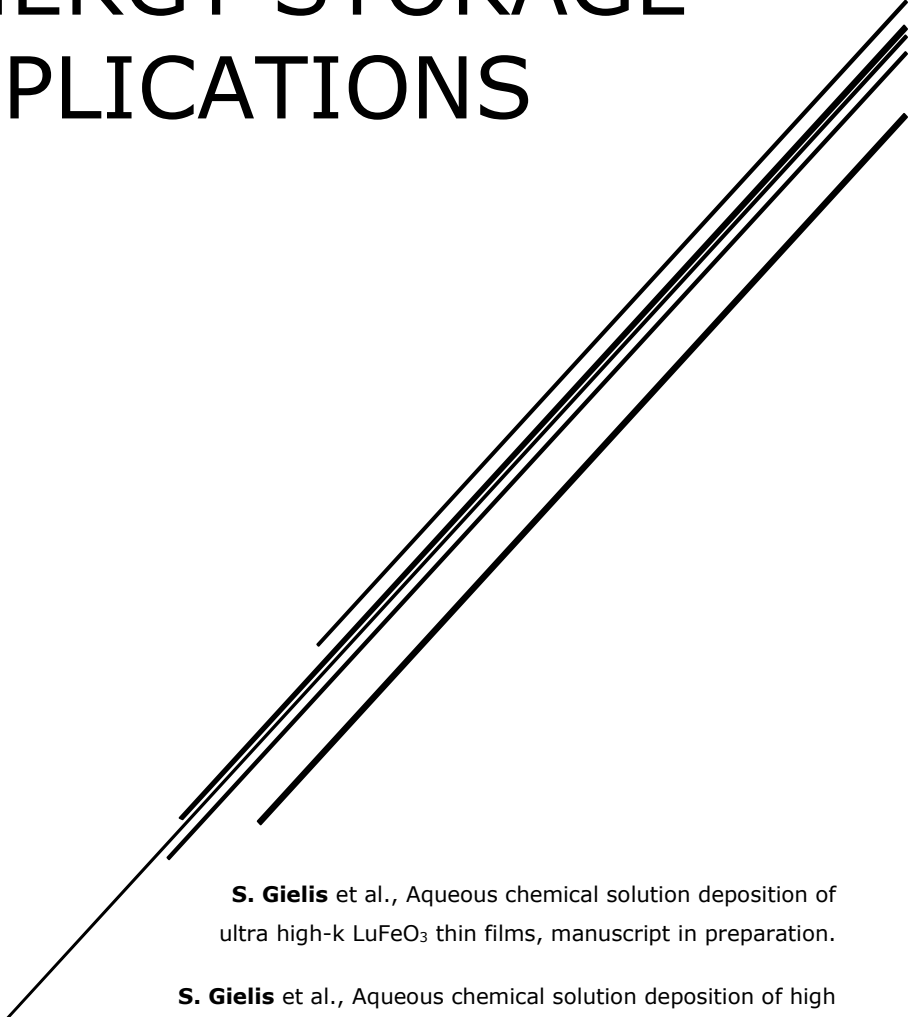
- [13] R.P. Deshpande, *Capacitors: Technology and Trends*, Tata McGraw-Hill Education, New Delhi, India, 2012.
- [14] B. a. Bender, M.-J. Pan, The effect of processing on the giant dielectric properties of  $\text{CaCu}_3\text{Ti}_4\text{O}_{12}$ , *Mater. Sci. Eng. B.* 117 (2005) 339–347. doi:10.1016/j.mseb.2004.11.019.
- [15] J. Oudenhoven, PhD thesis: *Deposition and Characterization of Thin Films for 3D Lithium-ion Micro-Batteries*, 2011. doi:10.6100/IR719293.
- [16] J. Warner, *The Handbook of Lithium-Ion Battery Pack Design: Chemistry, Components, Types and Terminology*, Elsevier, Amsterdam, The Netherlands, 2015.
- [17] P.M. Vereecken, C. Huyghebaert, Conformal Deposition For 3D Thin-Film Batteries, *ECS Trans.* 58 (2013) 111–118. doi:10.1149/05810.0111ecst.
- [18] M. Armand, J.-M. Tarascon, Building better batteries., *Nature.* 451 (2008) 652–657. doi:10.1038/451652a.
- [19] M.M. Thackeray, C. Wolverton, E.D. Isaacs, Electrical energy storage for transportation—approaching the limits of, and going beyond, lithium-ion batteries, *Energy Environ. Sci.* 5 (2012) 7854–7863. doi:10.1039/c2ee21892e.
- [20] P.H.L. Notten, F. Roozeboom, R. a. H. Niessen, L. Baggetto, 3-D Integrated All-Solid-State Rechargeable Batteries, *Adv. Mater.* 19 (2007) 4564–4567. doi:10.1002/adma.200702398.
- [21] A.N. Jansen, A.J. Kahaian, K.D. Kepler, P.A. Nelson, K. Amine, D.W. Dees, et al., Development of a high-power lithium-ion battery, *J. Power Sources.* 81-82 (1999) 902–905. doi:10.1016/S0378-7753(99)00268-2.
- [22] M. Hirayama, K. Kim, T. Toujigamori, W. Cho, R. Kanno, Epitaxial growth and electrochemical properties of  $\text{Li}_4\text{Ti}_5\text{O}_{12}$  thin-film lithium battery anodes., *Dalt. Trans.* 40 (2011) 2882–2887. doi:10.1039/c0dt01477j.
- [23] A.S. Prakash, P. Manikandan, K. Ramesha, M. Sathiya, J.-M. Tarascon, A.K. Shukla, Solution-Combustion Synthesized Nanocrystalline  $\text{Li}_4\text{Ti}_5\text{O}_{12}$  As High-Rate Performance Li-Ion Battery Anode, *Chem. Mater.* 22 (2010) 2857–2863. doi:10.1021/cm100071z.
- [24] D. Golodnitsky, M. Nathan, V. Yufit, E. Strauss, K. Freedman, L. Burstein, et al., Progress in three-dimensional (3D) Li-ion microbatteries, *Solid State Ionics.* 177 (2006) 2811–2819. doi:10.1016/j.ssi.2006.02.048.

- [25] S.K. Cheah, E. Perre, M. Rooth, M. Fondell, A. Hårsta, L. Nyholm, et al., Self-Supported Three-Dimensional Nanoelectrodes for Microbattery Applications, *Nano Lett.* 9 (2009) 3230–3233. doi:10.1021/nl9014843.
- [26] B.M.M. Shaijumon, E. Perre, B. Daffos, P. Taberna, J. Tarascon, P. Simon, Nanoarchitected 3D Cathodes for Li-Ion Microbatteries, (2010) 4978–4981. doi:10.1002/adma.201001922.
- [27] R.W. Schwartz, T. Schneller, R. Waser, Chemical solution deposition of electronic oxide films, *Comptes Rendus Chim.* 7 (2004) 433–461. doi:10.1016/j.crci.2004.01.007.
- [28] C.J. Brinker, G.W. Scherer, *Sol-Gel Science: The Physics and Chemistry of Sol-Gel Processing*, Academic Press (Elsevier), 1990.
- [29] H. Van den Rul, M.K. Van Bael, A. Hardy, K. Van Werde, J. Mullens, "Aqueous solution-based synthesis of nanostructured metal oxides" in *Handbook of Nanoceramics and Their Based Nanodevices*, American Scientific Publishers, California, 2009.
- [30] M.P. Pechini, Method of preparing lead and alkaline earth titanates and niobates and coating method using the same to form a capacitor, 1967.
- [31] M. Kakihana, Invited review: "Sol-gel" preparation of high temperature superconducting oxides, *J. Sol-Gel Sci. Technol.* 6 (1996) 7–55. doi:10.1007/BF00402588.
- [32] J. Livage, M. Henry, C. Sanchez, Sol-gel chemistry of transition metal oxides, *Prog. Solid State Chem.* 18 (1988) 259–341. doi:10.1016/0079-6786(88)90005-2.
- [33] J.-P. Jolivet, *Metal Oxide Chemistry and Synthesis: From Solution to Solid State*, John Wiley & Sons, LTD, Los Angeles, California, 2000.
- [34] K.G. Caulton, L.G. Hubert-Pfalzgraf, Synthesis, structural principles and reactivity of heterometallic alkoxides, *Chem. Rev.* 90 (1990) 969–995. doi:10.1021/cr00104a003.
- [35] J.F. Campion, D. a Payne, H.K. Chae, J.K. Maurin, S.R. Wilson, Synthesis of Bimetallic Barium Titanium Alkoxides as Precursors for Electrical Ceramics. Molecular Structure of the New Barium Titanium Oxide Alkoxide, *Inorg. Chem.* 30 (1991) 3244–3245. doi:10.1021/ic00017a003.
- [36] C.J. Brinker, G.W. Scherer, Sol - Gel - Glass: I. Gelation and Gel Structure, *J. Non. Cryst. Solids.* 70 (1985) 301–322. doi:10.1016/0022-3093(85)90103-6.

- [37] K.L. Cheever, T.F. Swearingin, R.M. Edwards, B.K. Nelson, D.W. Werren, D.L. Conover, et al., 2-Methoxyethanol metabolism, embryonic distribution, and macromolecular adduct formation in the rat: The effect of radiofrequency radiation-induced hyperthermia, *Toxicol. Lett.* 122 (2001) 53–67. doi:10.1016/S0378-4274(01)00346-0.
- [38] K.T. Eisses, Concurrent teratogenic and mutagenic action of 2-methoxyethanol in *Drosophila melanogaster* larvae resulted in similar phenotypes: Close resemblance to directed mutations, *Teratog. Carcinog. Mutagen.* 19 (1999) 183–204. doi:10.1002/(SICI)1520-6866(1999)19:33.3.CO;2-9.
- [39] C. De Dobbelaere, PhD thesis: Low temperature deposition and structure formation as new challenges for the aqueous solution-gel route: a case study of PbTiO<sub>3</sub>, 2011.
- [40] K. Van Werde, PhD thesis: Realisatie en optimalisering van de waterige oplossing-gel methode voor de bereiding van perovskiet PZN en gedopeerde PZN-verbindingen, 2003.
- [41] J. Kragten, *Atlas of Metal-Ligand Equilibrium in Aqueous Solution*, John Wiley & Sons, 1978.
- [42] D.E. Bornside, C.W. Macosko, S.L. E, On the modelling of spin coating, *J. Imaging Technol.* 13 (1987) 122–130.
- [43] T. Ohara, Y. Matsumoto, H. Ohashi, The film formation dynamics in spin coating, *Phys. Fluids A Fluid Dyn.* 1 (1989) 1949–1959. doi:10.1109/ITHERM.1992.187776.
- [44] W.J. Daughton, An Investigation of the Thickness Variation of Spun-on Thin Films Commonly Associated with the Semiconductor Industry, *J. Electrochem. Soc.* 129 (1982) 173. doi:10.1149/1.2123749.
- [45] S.L. Hellstrom, Basic Models of Spin Coating, <http://large.stanford.edu/courses/2007/ph210/hellstrom1/>. (2007).
- [46] Wikipedia, Céramique technique, [https://fr.wikipedia.org/wiki/C%C3%A9ramique\\_technique#/media/File:SolGel\\_DipCoating1.jpg](https://fr.wikipedia.org/wiki/C%C3%A9ramique_technique#/media/File:SolGel_DipCoating1.jpg). (2015).
- [47] C.J. Brinker, A. Hurd, Fundamentals of sol-gel dip-coating, *J. Phys. III Fr.* 4 (1994) 1231–1242.
- [48] C. Girotto, D. Moia, B.P. Rand, P. Heremans, High-Performance Organic Solar Cells with Spray-Coated Hole-Transport and Active Layers, *Adv. Funct. Mater.* 21 (2011) 64–72. doi:10.1002/adfm.201001562.

- [49] L. Filipovic, S. Selberherr, G.C. Mutinati, E. Brunet, S. Steinhauer, A. Köck, et al., Methods of simulating thin film deposition using spray pyrolysis techniques, *Microelectron. Eng.* 117 (2014) 57–66. doi:10.1016/j.mee.2013.12.025.
- [50] Sono-Tek, Spray coating, [Http://www.sono-Tek.com/](http://www.sono-Tek.com/). (2015).
- [51] R. Engle, Advantages of Ultrasonic Spray Coatings of Biomaterials onto Devices and Implantables (Sono-Tek), in: *Int. Coat. Sci. Technol. Symp.*, 2010: pp. 1–22.
- [52] S. Giangrandi, PhD thesis: Low-Energy Elastic Recoil Detection and Ion Beam Analysis for Quantitative Elemental Profiling of Thin Films, 2010.
- [53] S. Giangrandi, T. Sajavaara, B. Brijs, K. Arstila, a. Vantomme, W. Vandervorst, Low-energy heavy-ion TOF-ERDA setup for quantitative depth profiling of thin films, *Nucl. Instruments Methods Phys. Res. Sect. B Beam Interact. with Mater. Atoms.* 266 (2008) 5144–5150. doi:10.1016/j.nimb.2008.08.018.
- [54] A.J. Bard, L.R. Faulkner, *Electrochemical methods: Fundamentals and Applications*, 2nd editio, John Wiley & Sons, New York, USA, 2001. doi:10.1016/B978-0-12-381373-2.00056-9.
- [55] D.L. Wood, J. Li, C. Daniel, Prospects for reducing the processing cost of lithium ion batteries, *J. Power Sources.* 275 (2015) 234–242. doi:10.1016/j.jpowsour.2014.11.019.

# II. SYNTHESIS OF MULTI-METAL OXIDES FOR USE IN ENERGY STORAGE APPLICATIONS



**S. Gielis** et al., Aqueous chemical solution deposition of ultra high-k  $\text{LuFeO}_3$  thin films, manuscript in preparation.

**S. Gielis** et al., Aqueous chemical solution deposition of high performance phase-pure  $\text{Li}_4\text{Ti}_5\text{O}_{12}$  films for thin film Li-ion batteries, manuscript in preparation.



# 1 Introduction

The aim of the thesis is to synthesize materials and develop new chemical solution deposition processes in function of energy storage applications (Figure II-1).

This first part of this chapter is about the deposition of orthorhombic  $\text{LuFeO}_3$  thin films. As a potential ultra high-k dielectric material, it can possibly be used in thin-film capacitors.

The second part describes the synthesis of spinel  $\text{Li}_4\text{Ti}_5\text{O}_{12}$  films for the use as anode material in a thin-film Li-ion battery. Since this anode film should be structurally compatible with spinel  $(\text{Li}_x\text{Mg}_{1-2x}\text{Al}_x)\text{Al}_2\text{O}_4$ , which has been suggested as a good candidate as Li-ion electrolyte in thin-film Li-ion batteries, the third part will report on the synthesis of  $(\text{Li}_x\text{Mg}_{1-2x}\text{Al}_x)\text{Al}_2\text{O}_4$  thin films.

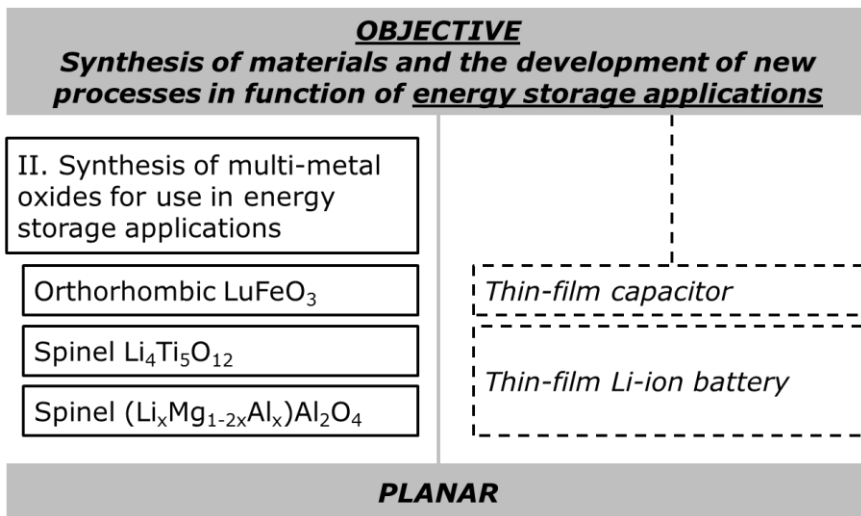


Figure II-1: Schematic representation of aim and the accompanying outline of the thesis, focusing on chapter II.

## 2 LuFeO<sub>3</sub> as possible ultra high-k dielectric in thin-film capacitors

### 2.1 Introduction

Ultra high- $k$  materials are very attractive for applications in the field of energy storage, which has recently attracted great attention. [1–3] As described in chapter I, thin film capacitors are built of a thin film of dielectric material which is sandwiched between two conductive layers. According to theory, the amount of energy stored in the stack is proportional to the capacitance of the capacitor (see chapter I). Consequently it is clear that the use of an oxide with a giant dielectric constant will lead to a gain in energy density.[1] For orthorhombic (o) LuFeO<sub>3</sub> ceramics, a dielectric constant ( $\epsilon_r$  or  $k$ ) of ca.  $10^4$  (frequency  $\leq$  1kHz) has been reported at room temperature. [4,5] This is much higher compared to the other abundant crystalline form, i.e. hexagonal LuFeO<sub>3</sub>, which has a  $k$ -value of only  $3 \cdot 10^2$  (frequencies  $\leq$  1kHz) at room temperature.[6] However, it is mainly due to the latter crystalline phase that LuFeO<sub>3</sub>, a member of the rare-earth orthoferrites family, has attracted considerable attention in recent years. Hexagonal (h) LuFeO<sub>3</sub> has promising multiferroic, magnetic and optical properties which can be used for next generation applications in information technology, sensing and actuation. [4,7–11] It was suggested by experiments that hexagonal LuFeO<sub>3</sub> is both ferroelectric and antiferromagnetic at room temperature. Since it is one of the few known room-temperature multiferroics, its potential towards practical applications is very large.[4,6,8,12] Therefore, the synthesis of bulk h-LuFeO<sub>3</sub> via solid-state reactions is well described in literature.[4,5,13] Also the deposition of thin films has been reported, in particular using pulsed laser deposition [6–8], metal-organic chemical vapor deposition [6], molecular-beam epitaxy (MBE) [12] and sol-gel chemistry [6], as well as the characteristics of hexagonal LuFeO<sub>3</sub>.

Orthorhombic LuFeO<sub>3</sub> was much less investigated in the past, only reports concerning the study of bulk o-LuFeO<sub>3</sub> could be found.[4,5] The reason for this is that the perovskite oxide is not ferroelectric and thus not interesting for multiferroic applications. However, as mentioned, o-LuFeO<sub>3</sub> and, particularly, as thin film has great potential when it comes to energy storage applications.

Literature on the deposition of ultra high- $k$   $\alpha$ -LuFeO<sub>3</sub> thin films is even more scarcely available. The deposition of an orthorhombic LuFeO<sub>3</sub> film on LaNiO<sub>3</sub>/Si via pulsed laser deposition has been shown, however the dielectric constant of the layer was not reported.[14]

Here, the development of a new aqueous chemical solution (CSD) process for the deposition of orthorhombic LuFeO<sub>3</sub> thin films is reported. It was shown before that citrate-complexes of several lanthanides (i.e. Nd, Pr, Eu, Sm, Gd) in water could be successfully synthesized and that these precursors were useful for the deposition of oxide films.[15,16]

## 2.2 Experimental

### 2.2.1 Aqueous Lu/Fe precursor and oxide powder synthesis

As can be seen in Figure II-2, first, the mono-metal Fe (III) and Lu (III) ion solutions were prepared separately.

The Fe (III) precursor synthesis was reported earlier by Hardy et al.[17] The required Fe (III) citrate hydrate (FeC<sub>6</sub>H<sub>5</sub>O<sub>7</sub>·H<sub>2</sub>O, 98%, 18-20% Fe, Acros) was refluxed in water at 80°C overnight and had a concentration of 0.1 mol/l. The pH of the solution was brought to 7 by the addition of concentrated ammonia (NH<sub>3</sub>, extra pure, 32%, Merck).

For the Lu (III) precursor, Lutetium (III) oxide (Lu<sub>2</sub>O<sub>3</sub>, 99.9%, Alfa Aesar) and citric acid (C<sub>6</sub>H<sub>8</sub>O<sub>7</sub>, 99%, Sigma-Aldrich) were added in water (citric acid to Lu<sup>3+</sup> = 1:1) and refluxed for 24h at 120°C. The pH was adjusted to 11 with concentrated ammonia (NH<sub>3</sub>, extra pure, 32%, Merck) after which the mixture was refluxed again for 24h at 110°C, finally yielding a clear, colorless 0.1 M solution, with a pH of about 7.5.

The mono-metal ion precursor solutions were filtered using a membrane filter (Nalgene, 0.2 μm) to remove particles, impurities and undissolved fractions. Subsequently their exact concentration was determined by ICP-AES (Optima 3000, PerkinElmer).

The multi-metal ion precursor for  $\text{LuFeO}_3$  was prepared by mixing the Fe (III) and Lu (III) solutions in the desired amounts so that the total metal ion concentration was 0.1 M.

For the powder synthesis, first, the precursor solutions were evaporated in air at  $80^\circ\text{C}$  to allow gelation of the system. The obtained gels were then crushed and ground manually in an agath mortar before further thermal treatment in view of crystallization.

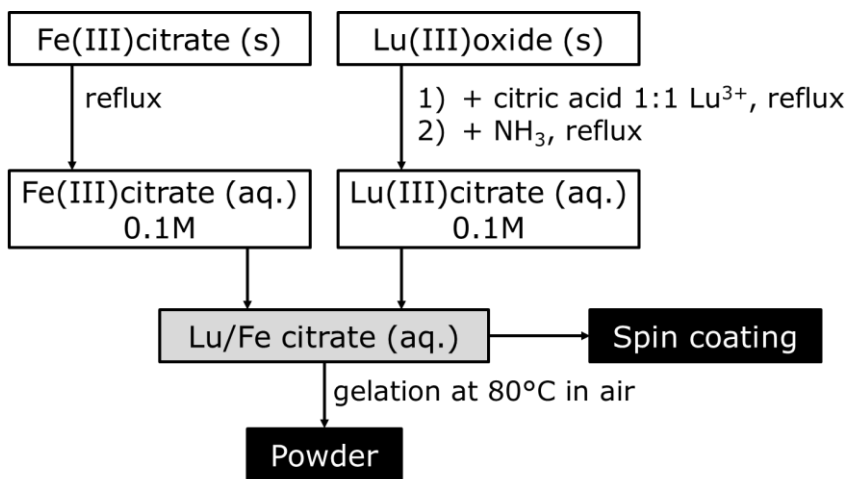


Figure II-2: Synthesis flowchart of the Lu/Fe precursor, powder and thin films.

The decomposition of the gel was studied by means of a simultaneous thermogravimetric (TG) / differential scanning calorimetry (DSC) analysis in a TA Instruments SDT Q600. The gel was heated from room temperature to  $1000^\circ\text{C}$  at a heating rate of  $10^\circ\text{C min}^{-1}$  in dry air ( $100 \text{ ml min}^{-1}$ ). The crystallization behavior of Lu/Fe powder, which was precalcined at  $200^\circ\text{C}$  for 30 minutes, as function of the temperature was studied in-situ by high-temperature X-ray diffraction (HT-XRD, Bruker, D8, step size  $0.02^\circ 2\theta$ ). The measurements were carried out between  $10$  and  $60^\circ 2\theta$  at a heating rate of  $10^\circ\text{C/min}$ , with intervals of  $50^\circ\text{C}$  from  $500$  to  $1100^\circ\text{C}$ .

### 2.2.2 Thin Lu/Fe oxide film deposition

Thin films were deposited via spin coating (3000 rpm, 30 s) of the Lu/Fe multi-metal ion precursor onto SiO<sub>2</sub>/Si (1.2 nm thermally grown SiO<sub>2</sub>) and Si<sub>3</sub>N<sub>4</sub>/SiO<sub>2</sub>/Si (70 nm Si<sub>3</sub>N<sub>4</sub>/1.2 nm SiO<sub>2</sub>).

To allow deposition of uniform films, the SiO<sub>2</sub>/Si and Si<sub>3</sub>N<sub>4</sub>/SiO<sub>2</sub>/Si substrate surfaces were first cleaned. For the SiO<sub>2</sub>/Si stack, this was done by cleaning in SPM (sulfuric acid mixture, consisting of 4:1 H<sub>2</sub>SO<sub>4</sub> (p.a., 95-97%, Merck) : H<sub>2</sub>O<sub>2</sub> (stabilized p.a., 35%, Acros Organic)) followed by an APM treatment (ammonia peroxide mixture, 5:1:1 H<sub>2</sub>O : H<sub>2</sub>O<sub>2</sub> (stabilized p.a., 35%, Acros Organic): NH<sub>3</sub> (extra pure, 32%, Merck)).[18] The Si<sub>3</sub>N<sub>4</sub>/SiO<sub>2</sub>/Si surface was pretreated in a UV/O<sub>3</sub> environment at 60°C for 30 minutes.[19]

Multiple layers were deposited on the substrates, after each layer the sample was placed on hot plates to decompose the precursor. The complete stack was further annealed for 30 minutes (heating rate of 10°C/min) in dry air (100 ml min<sup>-1</sup>) using a furnace (post deposition anneal - PDA) to trigger the crystallization.

Film thicknesses were determined by means of ellipsometry (Plasmos, single wavelength) using a refractive index of 2.00 for a single layer model, and checked by cross-section scanning electron microscopy (X-SEM, FEI, NOVA 200) in secondary electron imaging mode. The film morphology was visualized in a tilted view (45°). The Lu/Fe thin film oxide phase formation was determined by X-Ray Diffraction (XRD) on a PANalytical X'pert Pro tool with Cu K $\alpha$  radiation in a Bragg-Brentano configuration (coupled  $\theta$ -2 $\theta$  scan) with a PIXcel detector in scanning mode (step size 0.0098°). Possible silicate formation was detected by grazing angle attenuated total reflectance Fourier transform infrared (GATR-FTIR) spectroscopy. It was carried out using a 65° single reflection Ge-ATR (Harrick), placed inside the sample compartment of an FTIR spectrometer (Bruker, Vertex 70, 36 scans). To ensure intimate contact between the sample and the Ge-crystal, 0.4 Nm of torque was applied.

The dielectric constant was determined by Ivanov et al. at Vilnius University (Faculty of Physics, Vilnius, Lithuania). This was done via impedance spectroscopy using a HP LCR meter 4284A (20 Hz – 1 MHz) at room temperature. Therefore, Au electrodes were deposited on the films as interdigitated finger structures by means of a standard lithographic method. The interdigitated finger structure, which is shown in Figure II-3, is characterized by 24 lanes (or fingers). The dimensions are  $X = 17 \mu\text{m}$ ,  $Y = 23 \mu\text{m}$ ,  $Z = 1910 \mu\text{m}$ . The dielectric permittivity was determined using the model proposed by Kidner et al.[20] A substrate with deposited contacts of the same geometry was measured to account for the electrical properties of the substrate.

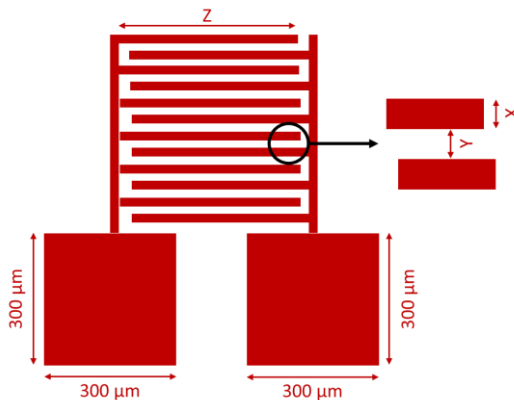


Figure II-3: Interdigitated finger structure ( $X = 17 \mu\text{m}$ ,  $Y = 23 \mu\text{m}$ ,  $Z = 1910 \mu\text{m}$ , 24 lanes) deposited via a standard lithographic method.

## 2.3 Results and discussion

### 2.3.1 Aqueous Lu/Fe precursor and oxide powder synthesis

Information about the thermal decomposition of the precursor was gathered by a thermogravimetric study (TGA/DSC) of a gel powder. This gel was obtained via evaporating water from the precursor. Consulting earlier studies on the decomposition of metal-citrate based gels lead to a good understanding of the decomposition profile. [21–23] Till  $150^\circ\text{C}$  the precursor's decomposition profile, which is shown in Figure II-4, is characterized by a small weight loss. This decrease in weight can be ascribed to the evaporation of water, still present in the gel after precalcination or adsorbed afterwards. This step, known as the drying

step, is followed by an abrupt weight loss, initiated at 180°C. This can be explained by the partial decomposition of the ammonium citrate gel matrix. Then, around 350°C, the decomposition of the direct coordination sphere of the metal ions is initiated, further shown by strongly exothermic processes at 400°C and 800°C, due to the removal of organic residual fractions and probably Lutetium dioxymonocarbonate,  $\text{Lu}_2\text{O}_2\text{CO}_3$  which was confirmed by GATR-FTIR of deposited films (cf. thin Lu/Fe oxide film deposition).[21–23]

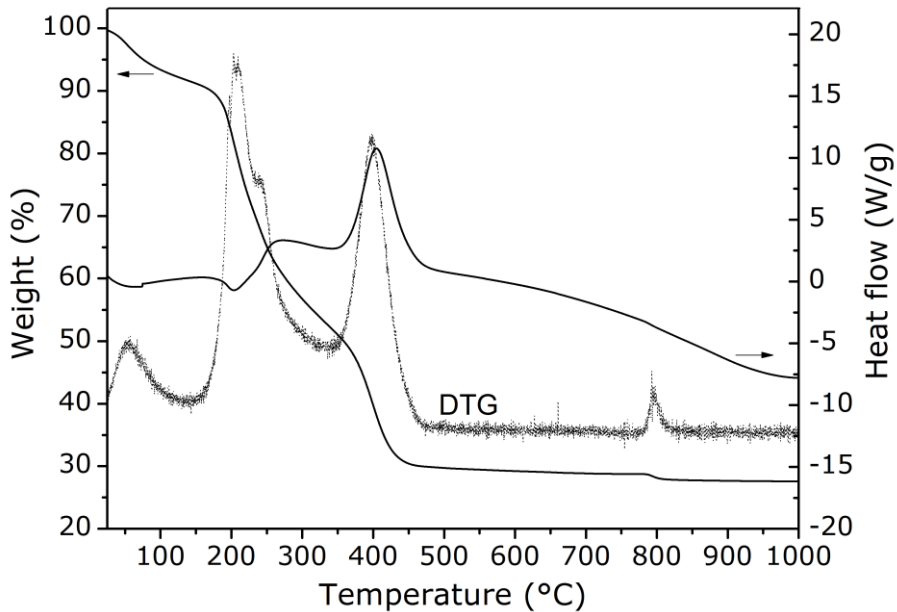


Figure II-4: TGA and DTG ( $10^\circ\text{C}/\text{min}$ ,  $100\text{ ml}/\text{min}$  in dry air) of the Lu/Fe (1:1) citrate gel.

The crystallization behavior of  $\text{LuFeO}_3$  was studied on gel powders and followed using high-temperature XRD, allowing in-situ study of the phase (trans)formation during heating ( $10^\circ\text{C}/\text{min}$ , air). In Figure II-5 the in-situ XRD results are shown, for convenience only the patterns from  $600^\circ\text{C}$  and up are presented. The XRD patterns show that no crystallization seems to occur till  $650^\circ\text{C}$ . From this temperature on, the formation of h- $\text{LuFeO}_3$  phase can be observed in the XRD pattern, no secondary phases are present. Then, from  $700^\circ\text{C}$  the onset of the formation of the o- $\text{LuFeO}_3$  phase is noticeable.

Between 700°C and 850°C both o-LuFeO<sub>3</sub> and h-LuFeO<sub>3</sub> are present in the powder: the signal intensities of o-LuFeO<sub>3</sub> diffractions, increase as the peak intensities of the hexagonal phase decrease and eventually fade away at 900°C. One can conclude that in this temperature range, the hexagonal phase transforms into the more thermodynamically stable orthorhombic phase. Consequently, an anneal at 900°C results in phase-pure o-LuFeO<sub>3</sub> powder. No secondary phases are developed by further increasing the temperature. The obtained o-LuFeO<sub>3</sub> phase is maintained after cooling the sample down to room temperature.

It can be concluded that the presented aqueous citrate precursor allows the crystallization of both the phase-pure hexagonal and orthorhombic LuFeO<sub>3</sub> crystalline powders. It should be noted that for the latter, interesting for the described energy storage applications, temperatures as high as 900°C seem necessary to form the pure phase.

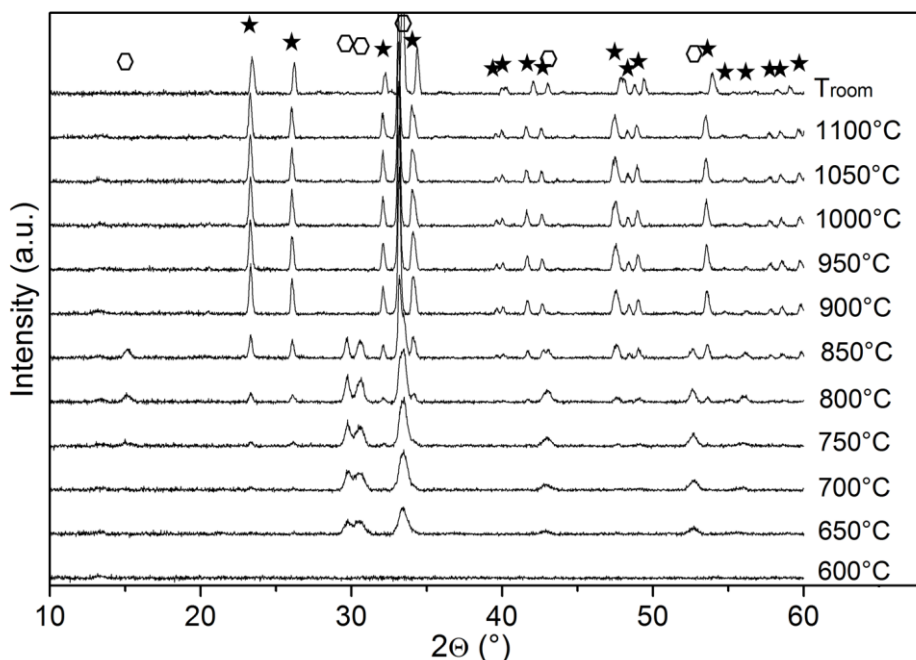


Figure II-5: HT-XRD patterns of the Lu/Fe citrate gel at the temperatures indicated in air. As a reference the XRD signals originating from hexagonal (◊) and orthorhombic (★) LuFeO<sub>3</sub> are shown.[26]

### 2.3.2 Thin Lu/Fe oxide film deposition

The study of the Lu/Fe precursor decomposition (Figure II-4) was used to determine the thermal treatment conditions for fabrication of thin films after each spin coating cycle. A hot plate (HP) treatment was favored over a furnace treatment to avoid the formation of a brittle skin before the interior of the film is decomposed completely, and consequently the formation of cracks when gases escape from the interior and break through the skin.[15] Three HP steps were defined to allow gel decomposition and carbon removal out of the layer: (1) a hot plate step was set at 110°C for 1 minute to evaporate the water in the film, (2) another at 320°C for 2 minutes and (3) a last one at 510°C for 2 minutes, thus after every major decomposition step (Figure II-4).

In this way, amorphous Lu/Fe oxide films were obtained on SiO<sub>2</sub>/Si, a common substrate in semiconductor industry. In the ideal case, the film thickness can be controlled by the amount of deposited layers. However, as recent reports on CSD using similar precursors suggested a non-linear thickness increase due to partial etching of the underlying layer, this was checked.[24] In Figure II-6 the film thicknesses, determined by ellipsometry (a) and verified by X-SEM after 16 deposition cycles (b), are plotted as a function of the number of deposition cycles. It is clear that the films are very smooth after deposition (see SEM image) and that the resulting film thickness varies linearly with the number of cycles:

$$Th = 3.9 X + 1.3$$

(Equation II-1)

with Th and X respectively the film thickness and the number of cycles.

The intersection at the y-axis can be attributed to the 1.2 nm SiO<sub>2</sub> which is present on the silicon substrate. The single layer ellipsometrical model implies that the reported values are those of the entire stack, being 1.2 nm SiO<sub>2</sub> and the deposited Lu/Fe oxide film. One can conclude that the Lu/Fe oxide film thickness can be well controlled by varying the number of deposition cycles.

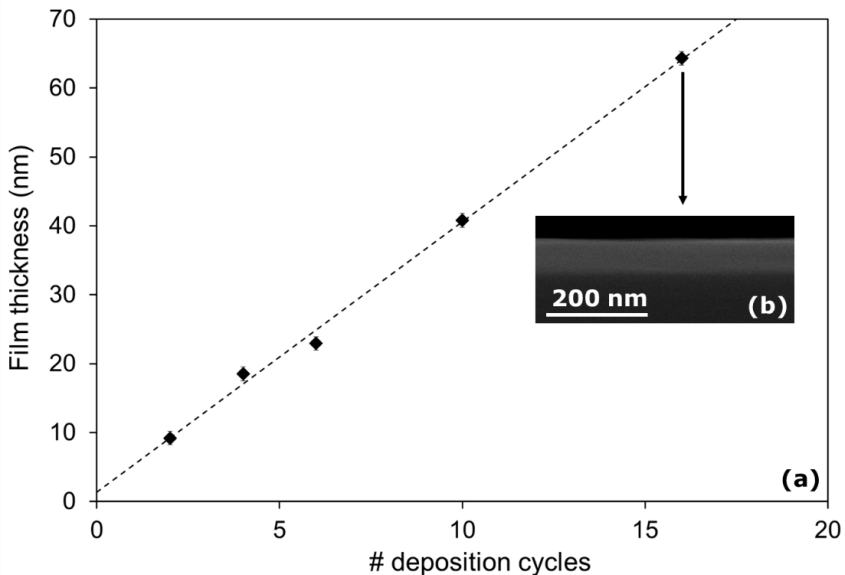


Figure II-6: (a) Plot of the film thickness of Lu/Fe oxide films, determined via spectroscopic ellipsometry, as a function of the amount of deposition cycles (i.e. spin coating and subsequent thermal treatment on hot plates) and (b) X-SEM image of the Lu/Fe oxide film after 16 deposition cycles.

To investigate the phase formation on  $\text{SiO}_2/\text{Si}$ , 30 layers were spin coated resulting in a film thickness of ca. 130 nm (X-SEM), confirming the linear fit in Figure II-6. These films were further treated for 30 min in a furnace (post deposition anneal – PDA – in air,  $10^\circ\text{C}/\text{min}$ ) in order to crystallize. The XRD results in Figure II-7 show that  $700^\circ\text{C}$  is too low for the films to trigger the crystallization: an amorphous Lu/Fe oxide film is present after the heat treatment. A post deposition anneal at  $800^\circ\text{C}$  is necessary to initiate the crystallization of the film: a h-LuFeO<sub>3</sub> film is obtained at this temperature. It can be inferred that the crystallization temperature for LuFeO<sub>3</sub> films is much higher compared to powders, which crystallize to the hexagonal phase at already  $650^\circ\text{C}$ . This can be explained by an increase in activation energy for the crystallization of thin films compared to bulk material, considering volume induced crystallization, i.e. crystallization occurs throughout the bulk of the film.[25]

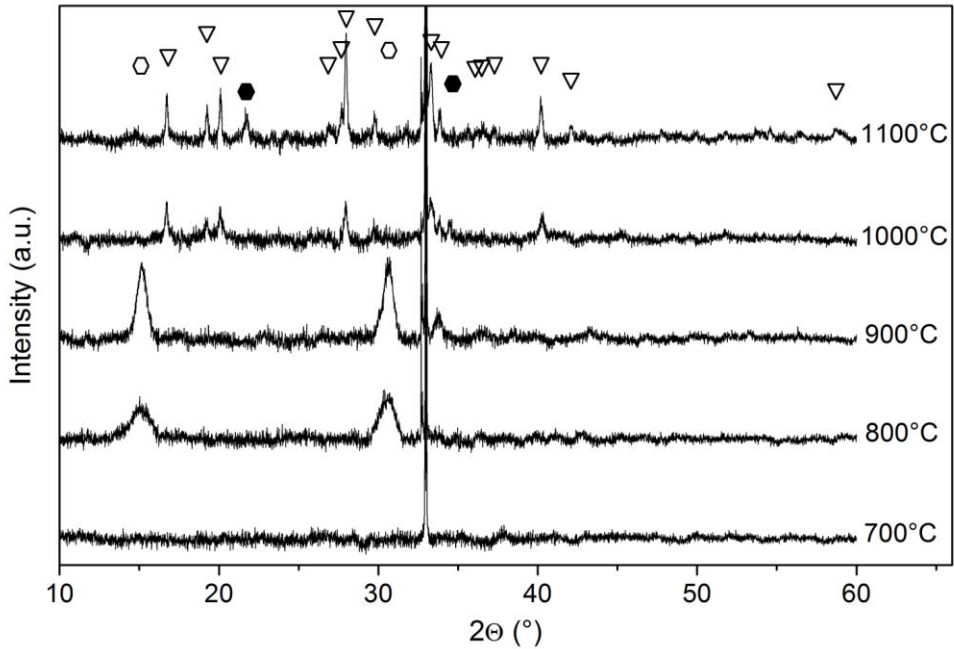
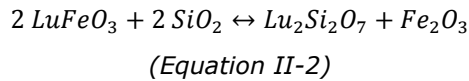


Figure II-7: XRD patterns of ca. 130 nm Lu/Fe films on SiO<sub>2</sub>/Si, deposited via spin coating and crystallized via a post deposition anneal in dry air at the temperatures indicated. As a reference the XRD signals originating from hexagonal LuFeO<sub>3</sub> (○), Lu<sub>2</sub>Si<sub>2</sub>O<sub>7</sub> (▽) and hexagonal Fe<sub>2</sub>O<sub>3</sub> (●) are shown.[26]

Increasing the PDA temperature of the films to 900°C results in stronger signal intensities of the hexagonal phase, however also traces of Lu<sub>2</sub>Si<sub>2</sub>O<sub>7</sub> can be found in the XRD pattern. The presence of this silicate is very plausible since it is known that rare earth oxides tend to form silicates in contact with SiO<sub>2</sub> at high temperatures [16,26]:



At 1000°C Lu<sub>2</sub>Si<sub>2</sub>O<sub>7</sub> takes the upper hand and LuFeO<sub>3</sub> is not present anymore in the film, instead, hexagonal Fe<sub>2</sub>O<sub>3</sub> seems to be formed. At 1100°C the effect is even more pronounced.

Further proof of silicate formation in these films at high temperatures can be found in the GATR spectra in Figure II-8. The longitudinal (LO) and transverse (TO) optic vibration of  $\text{SiO}_2$ , originating from the silicon substrate, are positioned at respectively  $1240 \text{ cm}^{-1}$  and  $1065 \text{ cm}^{-1}$ . [27] In the  $1000\text{-}600 \text{ cm}^{-1}$  region, the bands originate from the metal-oxygen stretching of Lu-O/Fe-O. Starting at  $800^\circ\text{C}$  and very clear at  $1000^\circ\text{C}$  and  $1100^\circ\text{C}$  there is a change in the bands in this region. A set of intense peaks appears in the GATR spectrum between  $1020$  and  $780 \text{ cm}^{-1}$ . This set, including the intense peak at approximately  $1100 \text{ cm}^{-1}$ , is indicative of rare earth silicate structures, thus confirming the formation of  $\text{Lu}_2\text{Si}_2\text{O}_7$  in the film. [28,29] Since GATR is able to detect amorphous silicates [30] and thus complementary to XRD, one can understand that already at  $800^\circ\text{C}$  silicate formation, being amorphous, could be observed. These silicates turn crystalline by elevating the PDA temperature (see XRD).

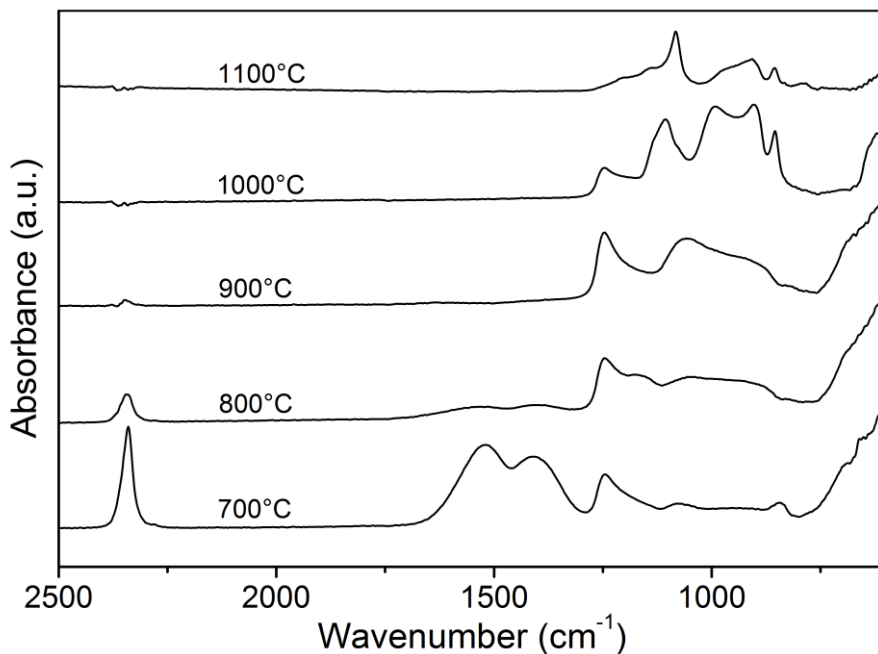


Figure II-8: GATR spectra of ca. 130 nm Lu/Fe films on  $\text{SiO}_2/\text{Si}$ , deposited via spin coating and crystallized by a post deposition anneal in dry air at the temperatures indicated.

From the GATR study in Figure II-8 it is also clear that after a PDA at 700°C Lutetium dioxymonocarbonate species are still present in the film, indicated by the double peak at 1550  $\text{cm}^{-1}$  and 1400  $\text{cm}^{-1}$ . [31,32] Higher anneal temperatures are thus necessary to remove all carbon containing species, which was already indicated by the TG analysis of the gel (Figure II-4). Furthermore,  $\text{CO}_2/\text{CO}$  can be seen at 2350  $\text{cm}^{-1}$  at 700-800°C, which is probably adsorbed from the air as well during as after the thermal treatment. [32]

The silicate crystallization at high temperatures can also be linked to the film morphology, as can be seen from the SEM images (tilted view, 45°) in Figure II-9. The Lu/Fe oxide films after a post deposition anneal at 800°C (A) and 900°C (B) have a rather smooth morphology. This drastically changes when further increasing the temperature to 1000°C (C) and 1100°C (D): these films are quite rough, indicating phase formation and accompanying interaction with the substrate, i.e. the crystallization of  $\text{Lu}_2\text{Si}_2\text{O}_7$ .

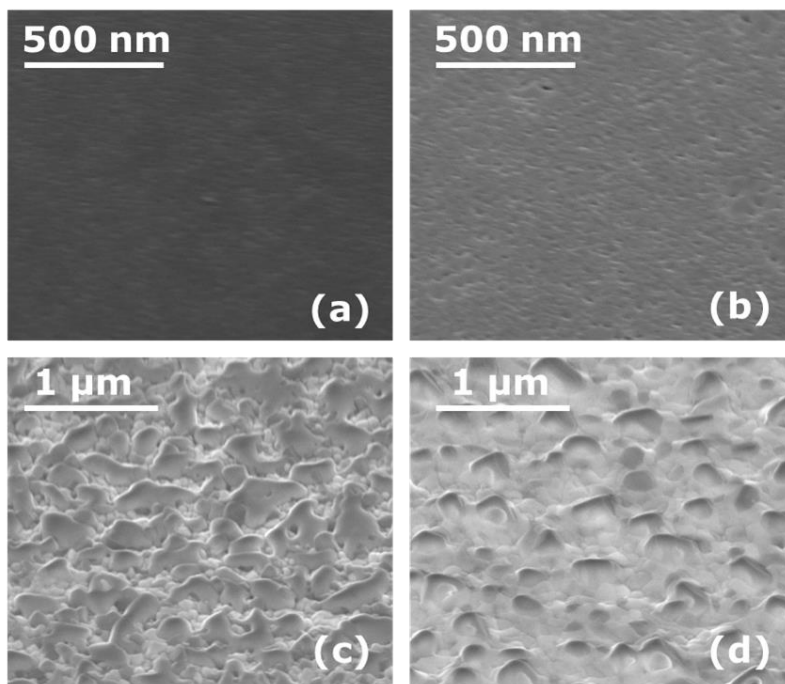


Figure II-9: SEM images (tilted view, 45°) of ca. 130 nm Lu/Fe films on  $\text{SiO}_2/\text{Si}$ , deposited via spin coating and crystallized via a post deposition anneal in dry air at (a) 800°C, (b) 900°C, (c) 1000°C and (d) 1100°C.

It was shown before for powders that the o-LuFeO<sub>3</sub> could be achieved at high temperature (Figure II-5), so one could assume that it should be possible for films, however at more elevated temperature due to the higher activation energy in the case of films.[25] At these temperatures, however, Lu-silicate formation occurs, preventing the formation of the intended phase.

In order to study the LuFeO<sub>3</sub> crystallization independently from interfacial reactions with the substrate, Si<sub>3</sub>N<sub>4</sub>/SiO<sub>2</sub>/Si was used as a substrate. The Si<sub>3</sub>N<sub>4</sub> layer is known for its chemical inertness and high thermal stability [33,34], and should act here as a protection layer against silicate formation. Via spin coating and accompanied hot plate treatment 65 nm Lu/Fe oxide films were deposited on Si<sub>3</sub>N<sub>4</sub>/SiO<sub>2</sub>/Si. These samples were further treated for 30 min in a furnace (post deposition anneal in air, 10°C/min). The XRD patterns in Figure II-10 demonstrate again that a thermal treatment at 700°C is not sufficient to form a crystalline Lu/Fe oxide film.

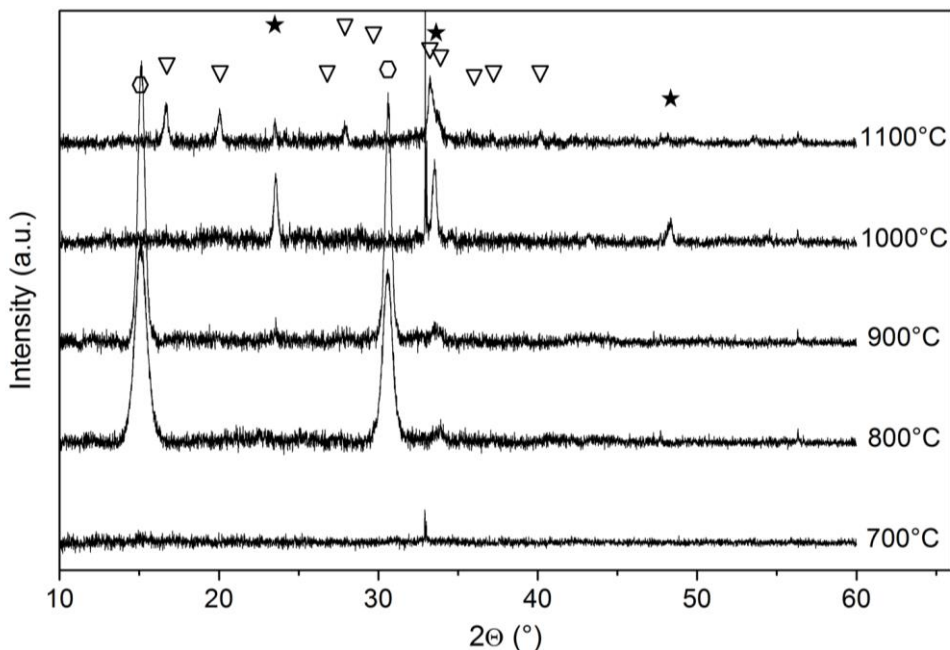


Figure II-10: XRD patterns of ca. 65 nm Lu/Fe films on Si<sub>3</sub>N<sub>4</sub>/SiO<sub>2</sub>/Si, deposited via spin coating and crystallized via a post deposition anneal in dry air at the temperatures indicated. As a reference the XRD signals originating from hexagonal LuFeO<sub>3</sub> (○), Lu<sub>2</sub>Si<sub>2</sub>O<sub>7</sub> (▽) and orthorhombic (★) LuFeO<sub>3</sub> are shown.[35]

A temperature of 800°C was necessary to trigger the crystallization, it results in h-LuFeO<sub>3</sub> as primary phase and o-LuFeO<sub>3</sub> as secondary phase. Phase-pure orthorhombic LuFeO<sub>3</sub> can be obtained by annealing the film at 1000°C in air. No secondary phases are observed in the XRD pattern. However when increasing the temperature to 1100°C, the Lu<sub>2</sub>Si<sub>2</sub>O<sub>7</sub> signals appear in the XRD pattern and the o-LuFeO<sub>3</sub> loses peak intensity. GATR analysis was performed, also on these films, to check for possible silicate formation even before crystallization (Figure II-11). As a reference the GATR spectrum of a Si<sub>3</sub>N<sub>4</sub>/SiO<sub>2</sub>/Si substrate is also presented. The signals at 815 cm<sup>-1</sup> and 875 cm<sup>-1</sup> are related to absorbance by stretching vibrations of the Si–N bonds [34,36–38], whereas the peak at 1080 cm<sup>-1</sup> can be attributed to the stretching vibration of SiO<sub>2</sub>. [37]

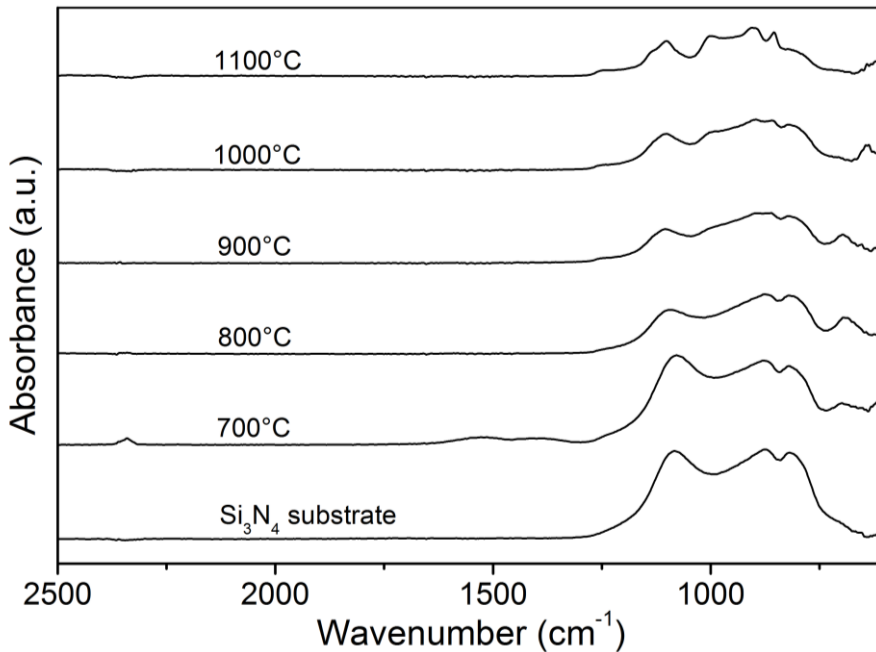


Figure II-11: GATR spectra of ca. 65 nm Lu/Fe films on Si<sub>3</sub>N<sub>4</sub>/SiO<sub>2</sub>/Si, deposited via spin coating and crystallized via a post deposition anneal in dry air at the temperatures indicated.

The intensity of the spectra diminishes in function of the anneal temperature. Since it concerns the overall intensity, i.e. the peaks related to substrate and deposited material, it is obvious that this is measurement related. In the 1000-

600  $\text{cm}^{-1}$  region, the other bands basically originate from the metal-oxygen vibrations of Lu-O/Fe-O. It seems that there is no change in bands in this region up to 1000°C. No other intense peaks seem to form, thus confirming that there is no silicate formation on the  $\text{Si}_3\text{N}_4$  substrate and that a phase-pure  $\text{o-LuFeO}_3$  film can be formed by a PDA at 1000°C. However when increasing the anneal temperature to 1100°C, other signals in this region seem to appear, at the same position as the films  $\text{SiO}_2/\text{Si}$ , indicating silicate formation.[28,29]

Additionally, the GATR study of these films in Figure II-11 gives information about the presence of Lutetium dioxymonocarbonate species and adsorbed  $\text{CO}_2/\text{CO}$  in the film, indicated by, respectively, the double peak at 1550  $\text{cm}^{-1}$  and 1400  $\text{cm}^{-1}$  [31,32] resp. the peak at 2350  $\text{cm}^{-1}$ . As for the films on  $\text{SiO}_2/\text{Si}$  (Figure II-8), high anneal temperatures ( $> 700^\circ\text{C}$ ) are necessary to remove these carbon species.[32]

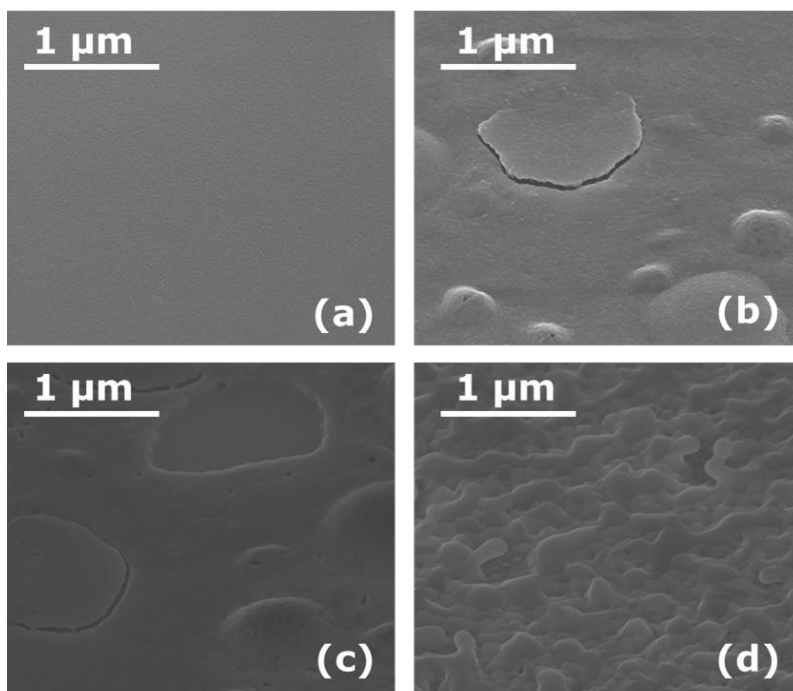


Figure II-12: SEM images (tilted view, 45°) of ca. 65 nm Lu/Fe films on  $\text{Si}_3\text{N}_4/\text{SiO}_2/\text{Si}$ , deposited via 10 cycles of spin coating and crystallized via a post deposition anneal in dry air at (a) 800°C, (b) 900°C, (c) 1000°C and (d) 1100°C.

The SEM images (tilted view, 45°) of the Lu/Fe oxide films on Si<sub>3</sub>N<sub>4</sub> are shown in Figure II-12. Also in this case the formation of Lu<sub>2</sub>Si<sub>2</sub>O<sub>7</sub> in the film can be linked to a drastic morphology change: a PDA at 1100°C (Figure II-12d) results in a quite rough film, thus indicating crystalline silicate formation.

It has been shown that a phase-pure o-LuFeO<sub>3</sub> film can be obtained via spin coating and subsequent annealing at 1000°C. The dielectric constant of a 20 nm o-LuFeO<sub>3</sub> film was determined by means of impedance spectroscopy. These experiments were performed by Ivanov et al. at Vilnius University (Faculty of Physics, Vilnius, Lithuania). Since the deposition was done on Si<sub>3</sub>N<sub>4</sub>/SiO<sub>2</sub>/Si which is a non-conducting substrate, Au electrodes were deposited on the film. In order to obtain reliable results, the electrodes were deposited as interdigitated structures, thus very close to each other. Via calculations using the obtained impedance spectroscopy data, proposed by Kidner et al. [20], the dielectric constant ( $\epsilon'$ ), dielectric loss ( $\epsilon''$ ) and conductivity ( $\sigma$ ) of the o-LuFeO<sub>3</sub> film were calculated and plotted as a function of the frequency in Figure II-13.

It is clear that, for low frequencies, the dielectric constant is equal or higher than 10<sup>4</sup> (Figure II-13a). These measurements confirm, to the authors' knowledge for the first time, that the dielectric properties of bulk o-LuFeO<sub>3</sub> [5] could be successfully transferred to the thin film variant.

As can also be seen on the plot, the dielectric loss is quite high at low frequencies while it decreases with the frequency, behavior typical for a slightly conductive material. This was also observed for the bulk material and it can possibly be linked to the origin of high permittivity. It is believed that it is due to charge separation, most likely in the inter-grain medium. When the blocking is not perfect, then the current can still flow and this results in high losses at low frequencies.[5]

At high frequencies there is a dispersion in conductivity (Figure II-13b), which can be attributed to charge relaxation at inter-grain boundaries of the film.

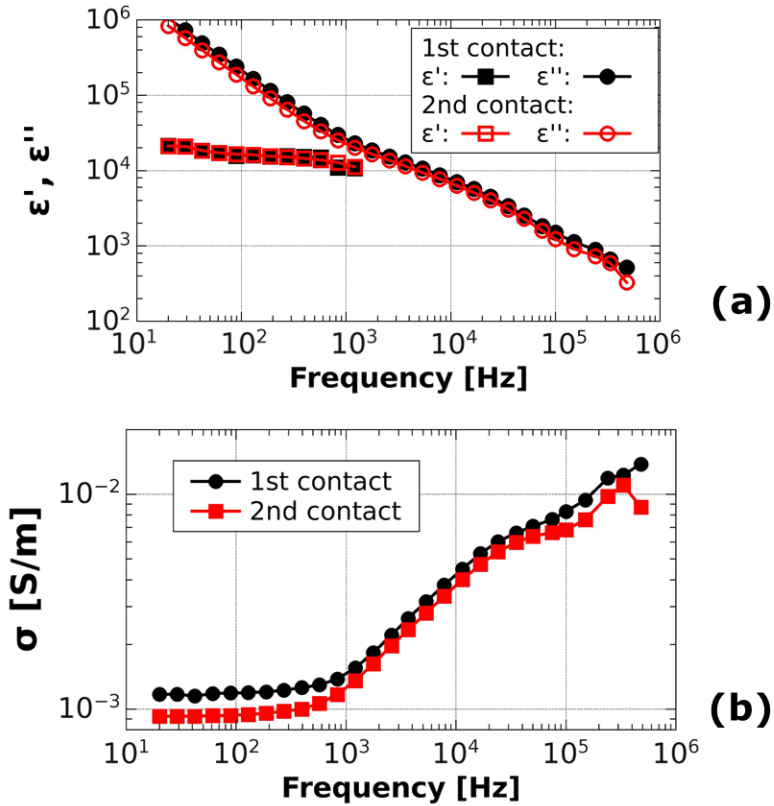


Figure II-13: Plot of the (a) dielectric constant ( $\epsilon'$ ), dielectric loss ( $\epsilon''$ ) and (b) conductivity ( $\sigma$ ) of a 20 nm  $o\text{-LuFeO}_3$  film, determined via impedance spectroscopy. For the measurement Au electrodes were deposited on the film as an interdigitated finger structures. [Courtesy of Ivanov et al. - Faculty of Physics, Vilnius University, Vilnius, Lithuania].

## 2.4 Conclusions

The development of a stable aqueous Lu/Fe precursor, which could be used for the synthesis of LuFeO<sub>3</sub> powders and for the chemical solution deposition of LuFeO<sub>3</sub> thin films, was shown. Both the hexagonal and the orthorhombic phase could be obtained, depending on the post deposition anneal temperature, i.e. respectively 700°C and 1000°C. Typically high temperatures were necessary, entering the zone of possible Lu silicate formation. This characteristic reaction of rare earth oxides with the substrate could be successfully delayed by the use of Si<sub>3</sub>N<sub>4</sub> as protection layer. For the phase-pure o-LuFeO<sub>3</sub> film on Si<sub>3</sub>N<sub>4</sub>/SiO<sub>2</sub>/Si, to the authors' knowledge for the first time, a giant dielectric constant equal or higher than 10<sup>4</sup> was shown for low frequencies (< 10<sup>3</sup> Hz), which makes it promising for the use in thin film capacitors. The downside of the material is that the dielectric loss is quite high at low frequencies.

### 3 $\text{Li}_4\text{Ti}_5\text{O}_{12}$ as anode in thin-film Li-ion batteries

#### 3.1 Introduction

For the thin-film Li-ion battery technology, lithium titanate,  $\text{Li}_4\text{Ti}_5\text{O}_{12}$ , is an attractive candidate to serve as anode material.[39–41]  $\text{Li}_4\text{Ti}_5\text{O}_{12}$ 's stability towards electrochemical cycling is the most striking characteristic with respect to thin-film batteries. Because of its spinel structure, the lithium intercalation and de-intercalation process only entails a minor difference in lattice parameters ( $< 0.2\%$ ), resulting in an insignificant lattice strain, unit cell volume expansion and thus only a negligible capacity loss.[39–42] During the charging/discharging process, the lithium content is varied between  $0 < X < 3$  for  $\text{Li}_{4+X}\text{Ti}_5\text{O}_{12}$ , resulting in a maximum theoretical gravimetric and volumetric capacity of respectively  $175 \text{ mAh g}^{-1}$  and  $610 \text{ mAh cm}^{-3}$ . [42] The (de)intercalation process occurs through a two-phase equilibrium region, resulting in a very stable (dis)charge voltage between 1.5 V and 1.6 V and, consequently, in very flat charge and discharge curves. [40,42]

Lithium titanate has been synthesized as bulk material or as thin films by various chemical and physical synthesis routes, such as the solid-state method [43,44], hydrothermal synthesis [45,46], molten-salt synthesis [47,48], pulsed laser deposition [40,49], magnetron sputtering [50] and sol-gel techniques [51–53]. The purpose of this work is to develop a new aqueous solution-gel process for the deposition of  $\text{Li}_4\text{Ti}_5\text{O}_{12}$  thin films.

## 3.2 Experimental

### 3.2.1 Aqueous Li/Ti precursor synthesis

First, the mono-metal Li (I) and Ti (IV) ion solutions were prepared separately, as schematically illustrated in Figure II-14.

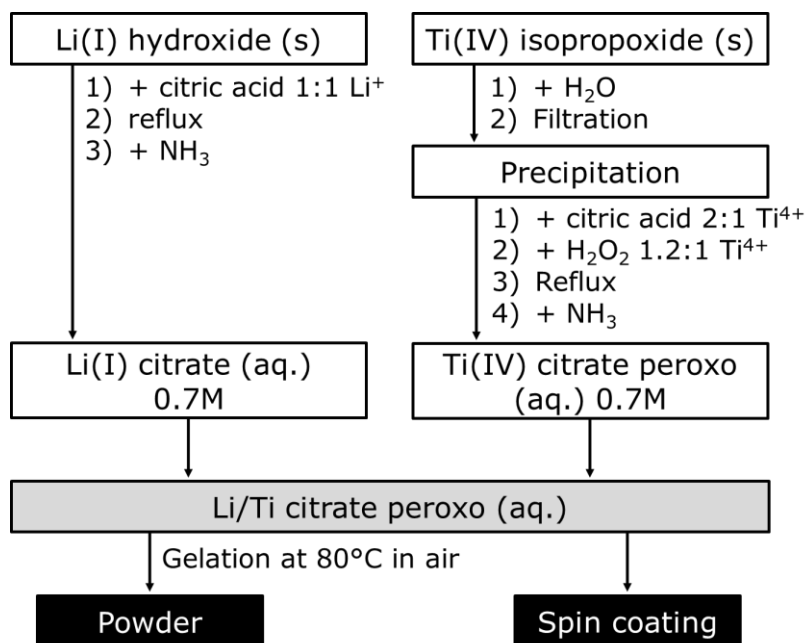


Figure II-14: Synthesis flowchart of the Li/Ti precursor, powder and thin films.

The synthesis procedure for the Ti(IV) precursor with a metal concentration of 0.73 M has been reported earlier.[22,54–58] Ti(IV)isopropoxide (Ti(OiPr)<sub>4</sub>, 98+%, Acros Organics) was hydrolyzed and condensated by the addition of a tenfold volume of water resulting in a white precipitate, which was filtered and washed with water. After that, a mixture of citric acid (CA, C<sub>6</sub>H<sub>8</sub>O<sub>7</sub>, 99%, Sigma-Aldrich) and hydrogen peroxide (H<sub>2</sub>O<sub>2</sub>, stabilized p.a., 35%, Acros Organic) was added to the fresh precipitate so that the molar ratio Ti<sup>4+</sup>:CA:H<sub>2</sub>O<sub>2</sub> was 1:2:1.2 and the whole was refluxed at 80°C. After a short time, a clear solution with a pH of 1 was obtained. The solution was cooled to room temperature and the pH was adjusted to 7 by the addition of concentrated ammonia (NH<sub>3</sub>, extra pure, 32%, Merck).

For the Li (I) precursor, lithium hydroxide (LiOH,  $\geq 98\%$ , Sigma-Aldrich) and citric acid (CA,  $C_6H_8O_7$ , 99%, Sigma-Aldrich) were added in water so that the final Li (I) ion concentration and  $Li^+:CA$  ratio were, respectively, 0.7 M and 1:1. Then, the mixture was refluxed at  $80^\circ C$ , which after a short time yielded a clear solution, with a pH of about 3.5. The solution was cooled to room temperature and in the third step, ammonia ( $NH_3$ , extra pure, 32%, Merck) was added dropwise to the solution in order to increase the pH to 7.

The mono-metal ion precursor solutions were filtered using a membrane filter (Nalgene,  $0.2 \mu m$ ) to remove particles, impurities and undissolved fractions. Subsequently their exact concentration was determined by ICP-AES (Optima 3000, PerkinElmer).

The multi-metal ion Li/Ti precursors were then prepared by mixing the Li(I) and Ti (IV) solutions in the desired amounts. Different molar ratios were prepared, going from the theoretical ratio of 4:5 ( $Li^+:Ti^{4+}$ ) to a ratio with an excess of 300% Li, i.e.  $Li^+:Ti^{4+} = 16:5$ . The total metal ion concentration was kept at 0.5 M for all prepared precursors.

To study the decomposition of the precursor ( $Li^+:Ti^{4+} = 4:5$ ), first, the solution was evaporated in air at  $80^\circ C$  to allow gelation of the system. The obtained gel was crushed and ground manually in an agath mortar and its decomposition behavior was investigated by means of a thermal gravimetric (TG) analysis in a TA Instruments TGA 951–2000. The gel was heated from room temperature to  $700^\circ C$  at a heating rate of  $10^\circ C \text{ min}^{-1}$  in dry air ( $100 \text{ ml min}^{-1}$ ).

### 3.2.2 Thin Li/Ti oxide film deposition

Thin films were deposited via spin coating (3000 rpm, 30 s) of the Li/Ti multi-ion precursor onto  $Si_3N_4/SiO_2/Si$  (70 nm  $Si_3N_4 / SiO_2$ ) and  $Pt/TiN/SiO_2/Si$  (70 nm Pt / 40 nm TiN /  $SiO_2$ ). To allow deposition of uniform films, the  $Si_3N_4$  and Pt substrate surfaces were first pretreated in an  $UV/O_3$  environment at  $60^\circ C$  for 30 minutes.[19] Multiple layers were deposited on the substrates, after each layer the sample was brought on hot plates to decompose the precursor.

The Li/Ti thin film oxide phase formation was studied using ex-situ XRD on a PANalytical X'pert Pro tool with Cu K $\alpha$  radiation in a Bragg-Brentano configuration (coupled  $\theta$ - $2\theta$  scan) with a PIXcel detector in scanning mode (step size 0.0098°). Therefore, after deposition, the films were further annealed in a furnace (post deposition anneal - PDA) to trigger the crystallization.

For a more thorough study of the crystallization, in-situ XRD was performed by Mattelaer et al. (CoCoon group – Ghent University). The annealing processes were performed in an experimental heating chamber, also mounted in a Bruker D8 Discover, dedicated for in-situ X-ray diffraction (XRD). [59,60] Cu K $\alpha$  radiation was used as an X-ray source, while a linear detector monitored the crystallinity of the thin films. More specifically, the diffraction pattern over a range of 20° in  $2\theta$  was captured every 5 s during the annealing process, while the temperature was increased at a rate of 4°C/min or 40°C/min.

The composition of the deposited films was determined by elastic recoil detection (ERDA), using a *imec* home-built system [61], whereas the film morphology and thickness were visualized by scanning electron microscopy (SEM, FEI, NOVA 200), respectively, in a tilted view (45°) and cross-section view (90°).

The electrochemical performance of the deposited films was evaluated by means of cyclic voltammetry (scan rate: 10 mV/s) and (dis)charge measurements using a three-electrode cell (working electrode = sample, reference electrode = Li, counter electrode = Li) with 1M LiClO<sub>4</sub> in propylene carbonate as electrolyte. The whole was connected to a Autolab PGTAT 100 potentiostat, placed in a glove-box (under Ar) at 21°C. The electrochemical characterization was performed by Moitzheim et al. (*imec*).

### 3.3 Results and discussion

#### 3.3.1 Aqueous Li/Ti precursor synthesis

The prepared multi-metal ion Li/Ti precursors, going from solutions with the theoretical  $\text{Li}^+:\text{Ti}^{4+}$  ratio of 4:5 to solutions with a Li excess of 300% Li ( $\text{Li}^+:\text{Ti}^{4+} = 16:5$ ), were clear and stable. Via spin coating of 5 layers of this precursor, amorphous Li/Ti oxide films were deposited on  $\text{Si}_3\text{N}_4/\text{SiO}_2/\text{Si}$  substrates. The  $\text{Si}_3\text{N}_4$ , here acting as a blocking layer in order to prevent Li diffusion into the substrate, is known for its chemical inertness and thermal stability.[33,34] For the decomposition of the precursor and the accompanying oxide formation, there was opted for a hot plate treatment between each spin coat cycle. This was done to avoid the formation of a brittle skin before the interior of the film is decomposed completely, and consequently the formation of cracks when gases escape from the interior and break through the skin.[15] The hot plate conditions (1' at 110°C, 2' at 260°C, 2' at 470°C) were defined based on the precursor's thermal decomposition profile, which was obtained by a thermal gravimetric study (TGA) of the precursor gel, formed by evaporation of the water out of the precursor at 80°C. Earlier studies on the decomposition of citrate-based metal gels lead to a good understanding of the obtained profile.[21–23] In the decomposition signature of the Li/Ti precursor, shown in Figure II-15, the small weight loss till 150°C can be ascribed to the evaporation of water, present in the gel. This drying step is followed by an abrupt weight loss at 180°C and finished at 260°C, due to the partial decomposition of the ammonium citrate gel matrix. At 240°C the decomposition of the direct coordination sphere of the metal ions starts, followed by an exothermic process at 420°C: there is an increase in the temperature vs. time plot at that temperature, cause by the decomposition of the gel. The accompanying removal of organic residual fractions is completely ended at 470°C.

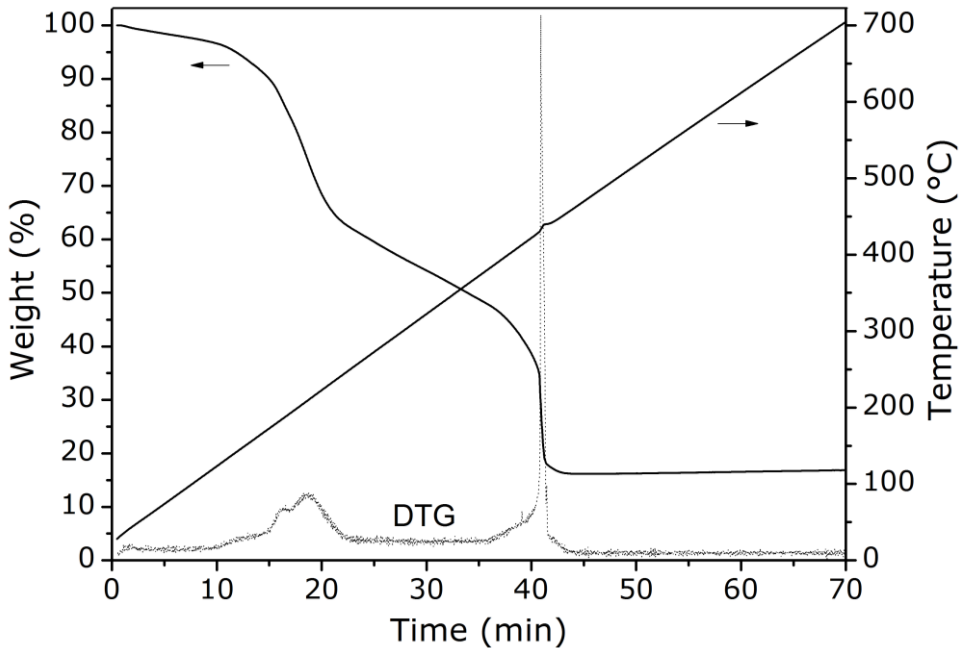


Figure II-15: TGA and DTG ( $10^{\circ}\text{C}/\text{min}$ ,  $100\text{ ml}/\text{min}$  in dry air) of the Li/Ti (4:5) citrate gel.

### 3.3.2 Thin Li/Ti oxide film deposition

#### 3.3.2.1 Crystallization study

Crystallization of the spin coated Li/Ti oxide films was done by heating in dry air from room temperature onwards with a heating rate of  $4^{\circ}\text{C}/\text{min}$  and an isothermal period of 20 min at the end temperature of  $750^{\circ}\text{C}$  (= PDA; post deposition anneal). Figure II-16 shows XRD patterns of different Li/Ti oxide films starting from Li/Ti precursors with an excess of Li content between 0% and 300%. It is found that the initial metal ratio in the precursor has a large influence on the crystallization behavior of the deposited films. When a precursor with a  $\text{Li}^+:\text{Ti}^{4+}$  ratio of 4:5, thus 0% of Li excess, was spin coated on the  $\text{Si}_3\text{N}_4/\text{SiO}_2/\text{Si}$  substrate,  $\text{Li}_4\text{Ti}_5\text{O}_{12}$  is hardly formed, and the rutile  $\text{TiO}_2$  phase is much more abundant: only a very small peak that is linked to the  $\text{Li}_4\text{Ti}_5\text{O}_{12}$  phase is visible in the XRD pattern in Figure II-16a. When 50% excess of lithium is added to the precursor, this results in a more obvious presence of  $\text{Li}_4\text{Ti}_5\text{O}_{12}$  (Figure II-16b) However the rutile titanium oxide phase still takes the upper hand.

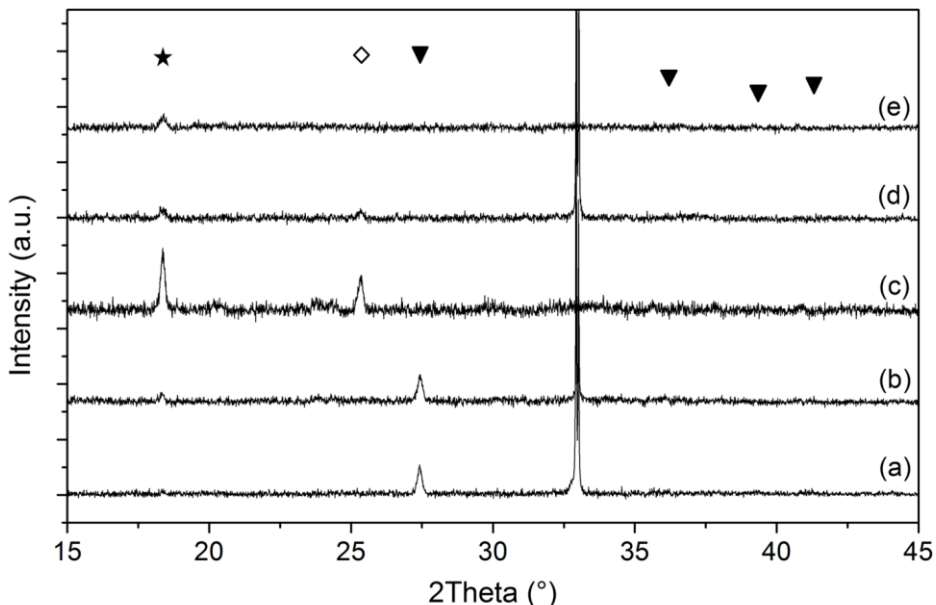


Figure II-16: XRD patterns of Li/Ti oxide films on  $\text{Si}_3\text{N}_4/\text{SiO}_2/\text{Si}$ , deposited via spin coating and crystallized via a post deposition anneal in dry air at  $750^\circ\text{C}$  for 20 minutes, starting from a Ti/Li precursor with (a) 0%, (b) 50%, (c) 100%, (d) 200% and (e) 300% Li excess. As a reference the XRD signals originating from  $\text{Li}_4\text{Ti}_5\text{O}_{12}$  (★), rutile  $\text{TiO}_2$  (▼) and anatase  $\text{TiO}_2$  (◇) are shown.[35]

Adding 100% excess of Li leads to the formation of anatase  $\text{TiO}_2$  instead of rutile in the final film (Figure II-16c). Also the spinel  $\text{Li}_4\text{Ti}_5\text{O}_{12}$  phase is more pronounced. Starting from a solution of 200% of Li excess gives a similar result: a mixture of anatase  $\text{TiO}_2$  and  $\text{Li}_4\text{Ti}_5\text{O}_{12}$  is obtained after spin coating and the subsequent heat treatments (Figure II-16d). Phase-pure spinel  $\text{Li}_4\text{Ti}_5\text{O}_{12}$  films could be obtained by the deposition of the Li/Ti precursor with a Li excess of 300% of lithium as can be seen in Figure II-16e. The XRD pattern only has one peak which can be attributed to the (111) crystalline direction of spinel  $\text{Li}_4\text{Ti}_5\text{O}_{12}$ .

Besides the Li:Ti ratio in the precursor, also the hot plate treatment and in particular the temperature of the last hot plate step after each spin coat cycle tends to influence the crystallization behavior and thus the phase formation. This is demonstrated in Figure II-17, where the XRD patterns of the Li/Ti oxide films on  $\text{Si}_3\text{N}_4/\text{SiO}_2/\text{Si}$ , deposited via spin coating of the precursor with a Li:Ti molar ratio of 4:5 (without Li excess) and a post deposition anneal in dry air at  $750^\circ\text{C}$

(4°C/min, 20 min), are shown. The temperature of the hot plates after each spin coat cycle was kept constant for the first two hot plates, namely 110°C and 260°C, but was gradually increased for the final hot plate treatment from 470°C to 750°C.

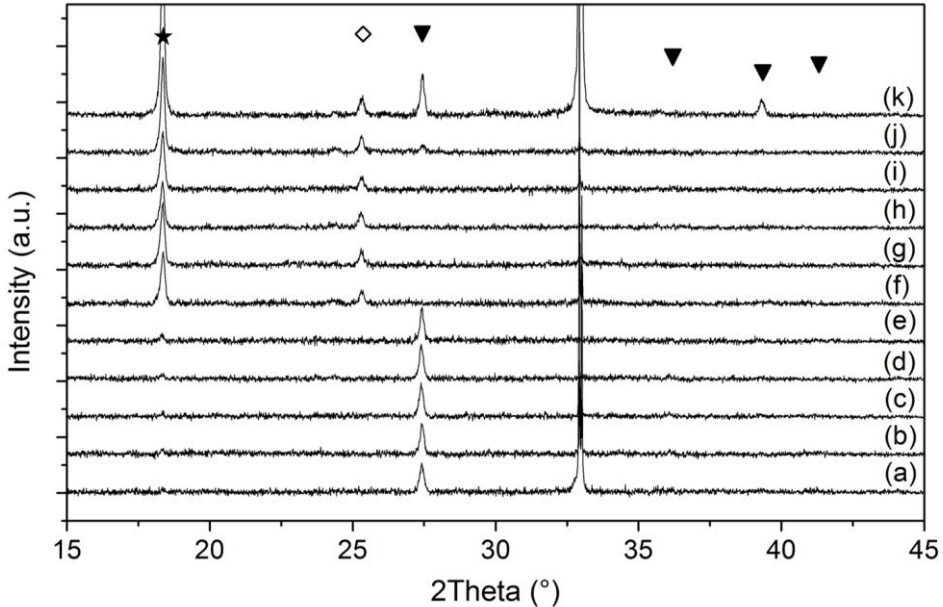


Figure II-17: XRD patterns of Li/Ti oxide films on  $\text{Si}_3\text{N}_4/\text{SiO}_2/\text{Si}$ , deposited via spin coating and a subsequent heat treatment at 110°C for 1 min, 260°C for 2 min and (a) 470°C, (b) 490°C, (c) 510°C, (d) 540°C, (e) 570°C, (f) 600°C, (g) 630°C, (h) 660°C, (i) 690°C, (j) 720°C and (k) 750°C for 2 min. The layers were crystallized via a post deposition anneal in dry air at 750°C for 20 minutes, starting from a Ti/Li precursor with molar ratio of 5:4. As a reference the XRD signals originating from  $\text{Li}_4\text{Ti}_5\text{O}_{12}$  (★), rutile  $\text{TiO}_2$  (▼) and anatase  $\text{TiO}_2$  (◇) are shown.[35]

Increasing the final hot plate step from 470°C (a) to 490°C (b), 510°C (c), 540°C (d) and 570°C (e) seems not to affect the phase formation: mainly rutile  $\text{TiO}_2$  is formed during the post deposition anneal, only a small peak, indicating spinel  $\text{Li}_4\text{Ti}_5\text{O}_{12}$ , can be found in the XRD patterns. A change in crystallization behavior is observed when the hot plate temperature was increased to 600°C. The clear formation of crystalline  $\text{Li}_4\text{Ti}_5\text{O}_{12}$  and the presence of anatase titanium oxide as secondary phase can be observed in the XRD plot (Figure II-17f). The intermediate heat treatment temperature was further increased to 630°C (g), 660°C (h), 690°C (i) and 720°C (j) in a furnace since the temperature limit for the hot plates was

exceeded, the conclusions are identical to the films which were treated at 600°C after each spin coating cycle (f). When an intermediate temperature step at 750°C is applied, the crystallization behavior of the film changes again: rutile TiO<sub>2</sub> is present in the crystalline mixed film, besides anatase and Li<sub>4</sub>Ti<sub>5</sub>O<sub>12</sub>.

From the above study, it follows that by controlling all levels of the process (Li content and anneal), different crystalline Li/Ti oxide films can be obtained. Phase-pure Li<sub>4</sub>Ti<sub>5</sub>O<sub>12</sub> films could be achieved when a large excess of lithium is added to the precursor.

To check the lithium content in the samples, elastic recoil detection analysis was performed. The results in Table II-1a show that for the precursor with 0% excess of lithium and an intermediate anneal at 600°C between every spin coating cycle, resulted in lithium deficient films. The atomic percentage of Li in the film is 12.3% whereas it should be 19.0%. This is of course also reflected by a higher titanium %, i.e. 27.5%. From the ERDA results in Table II-1b, it follows that by the addition of a large excess of lithium, i.e. 300%, in the precursor and a conventional intermediate anneal on hot plates till 470°C, the theoretical atomic percentages could be achieved. Both observations suggest that a large amount of lithium is lost during the deposition process and that this predominantly influences the film crystallization behavior.

	<b>Theory</b>	<b>(a)</b>	<b>(b)</b>
<b>Lithium</b>	19.0%	12.3%	20.0%
<b>Titanium</b>	23.8%	27.5%	21.4%
<b>Oxygen</b>	57.1%	59.2%	57.4%
<b>Carbon</b>	/	0.3%	0.7%
<b>Hydrogen</b>	/	0.7%	0.6%

*Table II-1: Atomic fractions (%) of Li/Ti oxide films on Si<sub>3</sub>N<sub>4</sub>/SiO<sub>2</sub>/Si determined by ERDA. The films were deposited via spin coating and crystallized via a post deposition anneal in dry air at 750°C for 20 minutes: (a) a film consisting of spinel Li<sub>4</sub>Ti<sub>5</sub>O<sub>12</sub> and anatase TiO<sub>2</sub> obtained starting from a Ti/Li precursor with 0% Li excess and an intermediate anneal till 600°C and (b) a phase-pure spinel Li<sub>4</sub>Ti<sub>5</sub>O<sub>12</sub> film, obtained starting from a Ti/Li precursor with 300% Li excess and an intermediate anneal till 470°C. As a reference the theoretical values are shown.*

It seems that the intermediate anneal process, particularly the maximum anneal temperature after each spin coating cycle, has also an effect on the amount of lithium that is retained in the film. When a precursor with the theoretical  $\text{Li}^+:\text{Ti}^{4+}$  ratio of 4:5 was spin coated on the  $\text{Si}_3\text{N}_4/\text{SiO}_2/\text{Si}$  substrate followed by the hot plate treatment till  $470^\circ\text{C}$ ,  $\text{Li}_4\text{Ti}_5\text{O}_{12}$  is hardly formed, instead the rutile  $\text{TiO}_2$  phase is much more abundant (Figure II-16a). One could ascribe this due to the lack of lithium in the deposited film. When an extra intermediate anneal step of  $600^\circ\text{C}$  or higher was added, this lead to the same effect as was seen for the addition of 100% excess of lithium ions to the precursor, i.e. an intense XRD signal indicating the presence of spinel  $\text{Li}_4\text{Ti}_5\text{O}_{12}$  accompanied by smaller peak that could be ascribed to anatase titanium oxide. It seems that the extra anneal step at  $600^\circ\text{C}$  or more lead to a larger conservation of lithium in the thin film. However these films are still characterized by a lack of lithium.

It is known that lithium is very mobile. However since it cannot migrate through the  $\text{Si}_3\text{N}_4$  film acting as barrier layer for lithium, it is believed that lithium is lost due to walk-off via the edges of the substrate during the deposition process. This effect can be diminished, however not excluded, by the higher intermediate anneal temperature, i.e.  $600^\circ\text{C}$ . It is believed that by the higher intermediate anneal temperature, more lithium is retained due to a larger immediate fixation of the ion in the oxide lattice.

In view of Li-ion thin-film battery processing, the temperature will be a limiting factor. Therefore, it is more favorable to deposit the phase-pure spinel  $\text{Li}_4\text{Ti}_5\text{O}_{12}$  films via the precursor with the excess of lithium compared to the process using the higher intermediate anneal treatment. For that reason, i.e. limiting the overall thermal budget, also the post deposition anneal was more investigated. At the same time, the effect of atmosphere was studied: the PDA was performed in an inert atmosphere. Also this could be beneficial towards the deposition of the  $\text{Li}_4\text{Ti}_5\text{O}_{12}$  film on the rest of the Li-ion battery stack, thus a smaller chance of affecting the other films. Both effects were studied by means of in-situ XRD by Mattelaer et al. (CoCoon group – Ghent University): the Li/Ti oxide crystallization of the films, deposited via spin coating the Li/Ti precursor with 300% excess of lithium and subsequent intermediate treatment at the hot plates till  $470^\circ\text{C}$ , was

followed during the post deposition anneal in Helium. In Figure II-18 the in-situ XRD results are shown, the heating rate was, respectively, (a) 4°C/min and (b) 40°C/min. The  $2\theta$  window was defined so that it incorporated the major peak attributed to spinel  $\text{Li}_4\text{Ti}_5\text{O}_{12}$  and the possible secondary phases rutile and anatase. While heating at 4°C/min (Figure II-18a), it is clear that phase-pure spinel  $\text{Li}_4\text{Ti}_5\text{O}_{12}$  is initiated at 600°C. This phase is retained by further heating, however, from 780°C an unidentified crystalline structure is formed as a secondary phase.

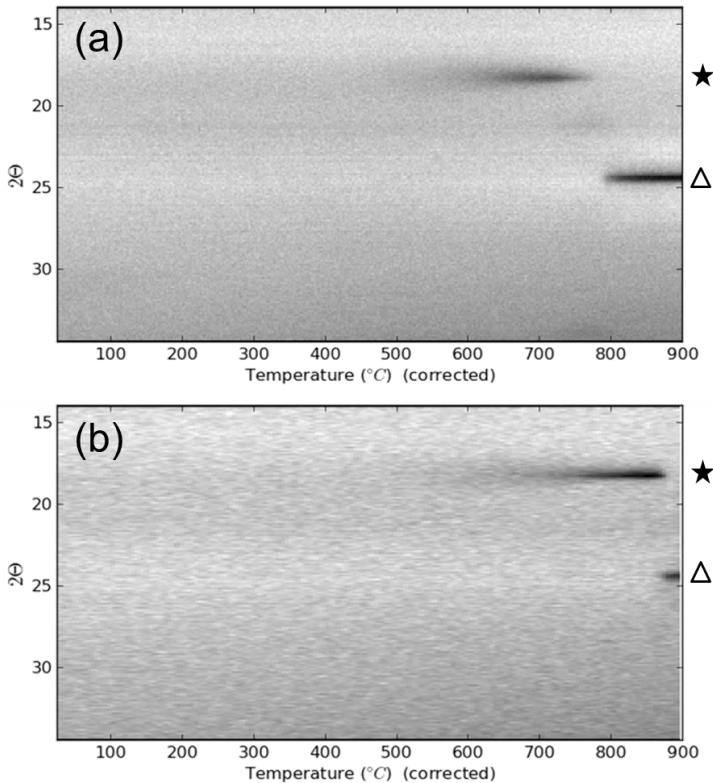


Figure II-18: In-situ XRD of Li/Ti oxide films on  $\text{Si}_3\text{N}_4/\text{SiO}_2/\text{Si}$  - deposited via spin coating and a subsequent heat treatment at 110°C for 1 min, 260°C for 2 min and 470°C for 2 min - during a ramp anneal with ramp rate (a) 4°C/min and (b) 40°C/min in He. The grey color indicates the lowest intensities (i.e. background), black shows the highest intensities (i.e. diffraction peaks). As a reference the XRD signals originating from  $\text{Li}_4\text{Ti}_5\text{O}_{12}$  (★) and an unidentified phase (Δ) are shown.

The same effect was observed while heating at 40°C/min (see Figure II-18b), the same sequence of peak appearances could be observed in the XRD pattern. Nonetheless, the appearance of the peaks was retarded and shifted to a slightly higher temperature due to the faster heating rate. Hence, phase-pure spinel  $\text{Li}_4\text{Ti}_5\text{O}_{12}$  films could be achieved by performing the post deposition anneal in an inert atmosphere at a lower temperature than the proposed 750°C, in particular in the range between 650°C and 700°C.

### 3.3.2.2 Study of electrochemical behavior

Since the phase-pure spinel  $\text{Li}_4\text{Ti}_5\text{O}_{12}$  films were demonstrated on  $\text{Si}_3\text{N}_4/\text{SiO}_2/\text{Si}$  substrates, the process was transferred to a Pt/TiN/TiO<sub>2</sub>/Si substrate for the electrochemical behavior of the films as negative electrode material. For comparison, both a  $\text{Li}_4\text{Ti}_5\text{O}_{12}$  film with a fraction of anatase (from the ERDA results in Table II-1a, ca. 30% of anatase TiO<sub>2</sub> is expected in the film) and a phase-pure  $\text{Li}_4\text{Ti}_5\text{O}_{12}$  film were deposited on Pt, using the appropriate process conditions (based on the crystallization study of  $\text{Li}_4\text{Ti}_5\text{O}_{12}$  on  $\text{Si}_3\text{N}_4/\text{SiO}_2/\text{Si}$ ).

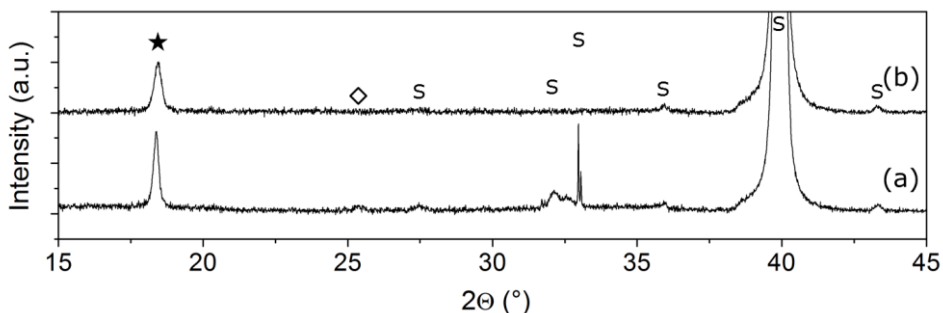


Figure II-19: XRD patterns of (a) a  $\text{Li}_4\text{Ti}_5\text{O}_{12}$ /anatase film and (b) a phase-pure  $\text{Li}_4\text{Ti}_5\text{O}_{12}$  film on Pt/TiN/TiO<sub>2</sub>/Si, deposited via spin coating, using the appropriate process conditions (cf. study of  $\text{Li}_4\text{Ti}_5\text{O}_{12}$  on  $\text{Si}_3\text{N}_4/\text{SiO}_2/\text{Si}$ ). The films were crystallized via a post deposition anneal in  $\text{N}_2$  at 700°C (4°C/min) for 20 minutes.

The XRD patterns in Figure II-19 show that the process had been transferred successfully (Figure II-19a for the former and Figure II-19b for the latter). The SEM images of both Li/Ti oxide films on Pt are shown in Figure II-20. The films are dense, completely covering the substrate and that they have a thickness of ca. 100 nm for the  $\text{Li}_4\text{Ti}_5\text{O}_{12}$  + anatase (Figure II-20a) and 65 nm for the  $\text{Li}_4\text{Ti}_5\text{O}_{12}$  film (Figure II-20b).

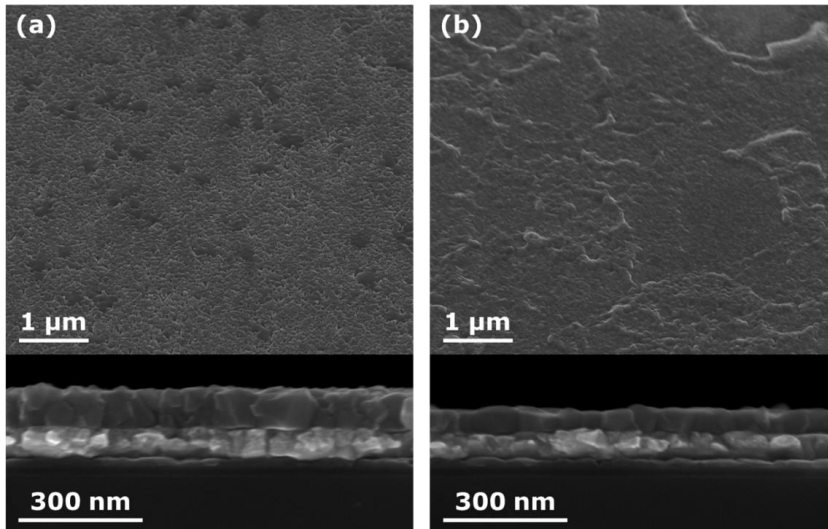


Figure II-20: SEM images (tilted view, 45° and X-view) of (a) a  $\text{Li}_4\text{Ti}_5\text{O}_{12}$ /anatase film and (b) a phase-pure  $\text{Li}_4\text{Ti}_5\text{O}_{12}$  film on  $\text{Pt}/\text{TiN}/\text{TiO}_2/\text{Si}$ , deposited via spin coating, using the appropriate process conditions (cf. study of  $\text{Li}_4\text{Ti}_5\text{O}_{12}$  on  $\text{Si}_3\text{N}_4/\text{SiO}_2/\text{Si}$ ). The films were crystallized via a post deposition anneal in  $\text{N}_2$  at 700°C (4°C/min) for 20 minutes.

The electrochemical characterization of the deposited films was performed by Moitzheim et al. (imec). Figure II-21 shows cyclic voltammograms of the studied Li/Ti oxide films, i.e. the  $\text{Li}_4\text{Ti}_5\text{O}_{12}$ /anatase (a) and phase-pure  $\text{Li}_4\text{Ti}_5\text{O}_{12}$  film (b). In both cases reduction and oxidation peaks are present at respectively ca. 1.45 V and 1.75 V, representing the reversible lithium insertion and extraction reactions in  $\text{Li}_4\text{Ti}_5\text{O}_{12}$ .

The charge-discharge curves of the Li/Ti oxide films for various C-rates are represented in Figure II-22. For these plots the film thickness, estimated from SEM characterization, is taken into account: 100 nm and 65 nm for respectively the  $\text{Li}_4\text{Ti}_5\text{O}_{12}$ /anatase film and the phase-pure  $\text{Li}_4\text{Ti}_5\text{O}_{12}$  film. The curves, which are characterized by flat charge/discharge plateau region, show a clear difference depending on the Li/Ti oxide film. The  $\text{Li}_4\text{Ti}_5\text{O}_{12}$ /anatase film results in an additional plateau around 2.1 V (see Figure II-22a). This indicates the crystalline impurity (anatase  $\text{TiO}_2$ , which is also known to be electrochemically active) and results in a capacity for low c-rates (0.5C/1C) around 500  $\text{mAh}/\text{cm}^3$ , thus smaller than the theoretical capacity of spinel  $\text{Li}_4\text{Ti}_5\text{O}_{12}$ , i.e. 610  $\text{mAh}/\text{cm}^3$ . [42] At 50C 70% of the capacity could be maintained. The capacity of the fabricated phase-

pure spinel  $\text{Li}_4\text{Ti}_5\text{O}_{12}$  film (Figure II-22b) is 60% higher compared to the impure film, i.e. ca.  $800 \text{ mAh/cm}^3$  for the low C-rates. At 50C, 80% of this capacity is maintained. The increase in capacity is related to the increase in lithium compared to the mixed film which was ca. 67%. It seems that the capacity is higher than the theoretical value. This is of course impossible, thus it means that the amount of active  $\text{Li}_4\text{Ti}_5\text{O}_{12}$  material was underestimated.

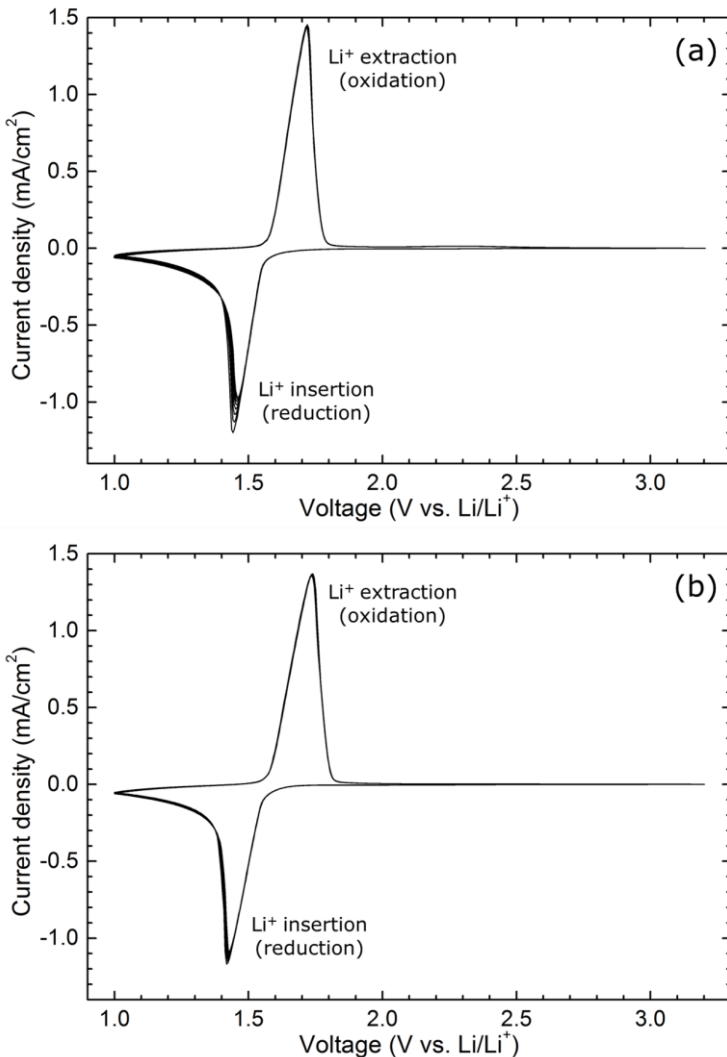


Figure II-21: Cyclic voltammetry (scan rate: 10 mV/s) of (a) a  $\text{Li}_4\text{Ti}_5\text{O}_{12}$ /anatase film and (b) a phase-pure  $\text{Li}_4\text{Ti}_5\text{O}_{12}$  film on Pt/TiN/TiO<sub>2</sub>/Si, deposited via spin coating, using the appropriate process conditions (cf. study of  $\text{Li}_4\text{Ti}_5\text{O}_{12}$  on  $\text{Si}_3\text{N}_4/\text{SiO}_2/\text{Si}$ ). The films were crystallized via a post deposition anneal in  $\text{N}_2$  at 700°C (4°C/min) for 20 minutes.

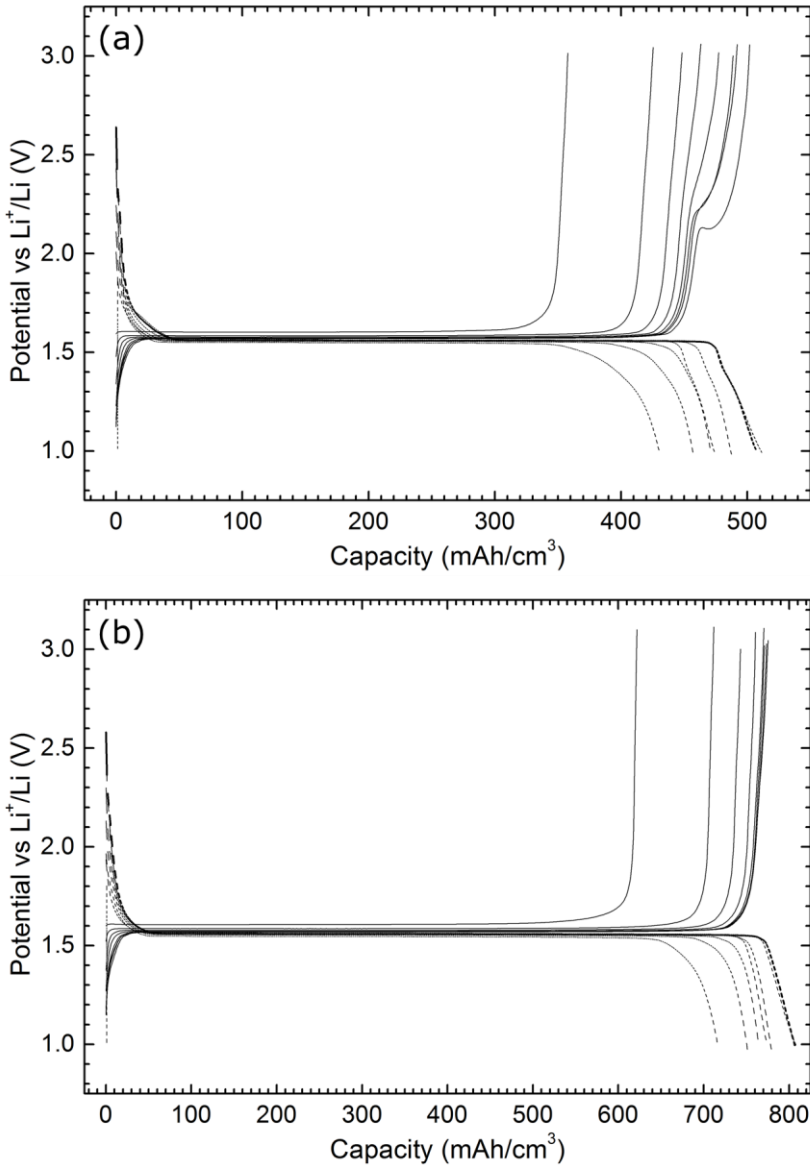


Figure II-22: Charge-discharge curves (from high capacity to low capacity: 0.5C; 1C, 1C, 2C, 5C, 10C, 20C, 50C) of (a) a  $\text{Li}_4\text{Ti}_5\text{O}_{12}$ /anatase film and (b) a phase-pure  $\text{Li}_4\text{Ti}_5\text{O}_{12}$  film on Pt/TiN/TiO<sub>2</sub>/Si, deposited via spin coating, using the appropriate process conditions. The films were crystallized via a post deposition anneal in N<sub>2</sub> at 700°C (4°C/min) for 20 minutes. The films were crystallized via a post deposition anneal in N<sub>2</sub> at 700°C (4°C/min) for 20 minutes.

### 3.4 Conclusions

A stable aqueous Li/Ti precursor, which could be used for the chemical solution deposition of  $\text{Li}_4\text{Ti}_5\text{O}_{12}$  thin films, was developed. While compensating for the lithium loss during the deposition process, phase-pure films could be achieved via spin coating after a post deposition anneal at  $700^\circ\text{C}$ . The phase-pure film was characterized by a very high capacity, particularly ca.  $800 \text{ mAh/cm}^3$  for the low C-rates (0.5C-1C), while the mixed  $\text{Li}_4\text{Ti}_5\text{O}_{12}$ /anatase film's capacity was  $500 \text{ mAh/cm}^3$  at 0.5C and 1C. Since  $800 \text{ mAh/cm}^3$  is higher than what is theoretical possible, probably the amount of active material was underestimated. However, it seems that this aqueous solution-gel process can deliver spinel  $\text{Li}_4\text{Ti}_5\text{O}_{12}$  films which can be incorporated in thin-film Li-ion batteries. A more precise determination of the amount of active material and a more thorough electrochemical study should be performed to check all electrochemical characteristics including the exact capacity and cycle life. LTO is expected to have a long cycle life.[40,42]

## 4 (Li<sub>x</sub>Mg<sub>1-2x</sub>Al<sub>x</sub>)Al<sub>2</sub>O<sub>4</sub> as possible solid electrolyte in all-spinel Li-ion batteries

### 4.1 Introduction

As was described in the previous section, spinel Li<sub>4</sub>Ti<sub>5</sub>O<sub>12</sub> thin films were successfully fabricated using aqueous chemical solution deposition. These films show promising electrochemical properties. As mentioned in chapter I, LiMn<sub>2</sub>O<sub>4</sub> is a widely studied cathode material. This material, which also possesses the spinel structure, seems to fit with Li<sub>4</sub>Ti<sub>5</sub>O<sub>12</sub> since they are characterized by a similar capacity. The capacity of LiMn<sub>2</sub>O<sub>4</sub> is only a bit lower, in particular ca. 25 mAh g<sup>-1</sup>. The use of these spinel materials as anode and cathode in a thin-film battery, together with a spinel-type electrolyte would allow matching of the electrode and electrolyte crystals. In this way, a continuous pathway for Li<sup>+</sup> ion transport should be enabled (see Figure II-23a), which could result in a lower interfacial resistance and a faster ionic transport through the device compared to a battery with complex electrode-electrolyte interfaces (see Figure II-23b). In the case of spinel matching, there is no need to match exact crystal directions at the interfaces between electrodes and electrolyte because of the fact that spinel structures are characterized by 3D conductivity.[62]

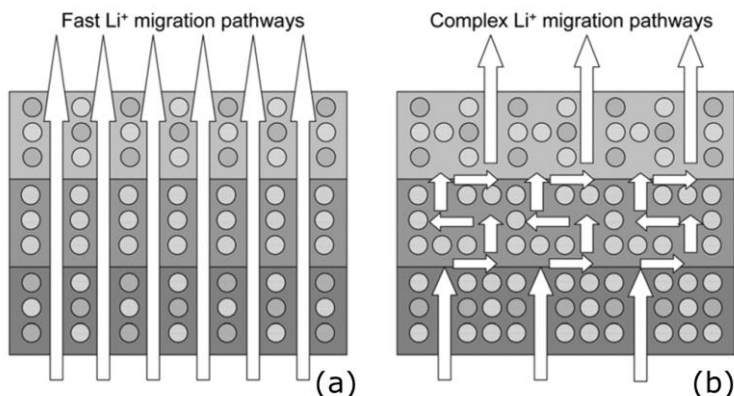


Figure II-23: Schematic representation of (a) lattice matching and (b) non lattice matching in an all-solid-state Li-ion battery.[62]

Recently,  $(\text{Li}_x\text{Mg}_{1-2x}\text{Al}_x)\text{Al}_2\text{O}_4$  ( $0 < X < 0.5$ ) has been suggested as a novel spinel Li-ion electrolyte. Successful powder synthesis via co-precipitation chemistry (in water) was reported.[62]

It is the aim to develop a new aqueous solution-gel process for the deposition of  $(\text{Li}_x\text{Mg}_{1-2x}\text{Al}_x)\text{Al}_2\text{O}_4$  thin films. Since the mixing of metal ions is typically done at the precursor level, various compositions for  $(\text{Li}_x\text{Mg}_{1-2x}\text{Al}_x)\text{Al}_2\text{O}_4$  can be easily and relatively fast synthesized and investigated.[63–65]

## 4.2 Experimental

### 4.2.1 Aqueous Li/Mg/Al precursor and oxide powder synthesis

First, the mono-metal Li (I), Mg (II) and Al (III) ion solutions were prepared separately, as illustrated in Figure II-24.

For the Li (I) precursor, lithium hydroxide ( $\text{LiOH}$ ,  $\geq 98\%$ , Sigma-Aldrich) and citric acid (CA,  $\text{C}_6\text{H}_8\text{O}_7$ , 99%, Sigma-Aldrich) were added in water so that the final Li (I) ion concentration and  $\text{Li}^+:\text{CA}$  ratio were, respectively, 0.7 M and 1:1. Then, the mixture was refluxed at  $80^\circ\text{C}$ , which after a short time yielded a clear solution, with a pH of about 3.5. The solution was cooled to room temperature and in the third step, ammonia ( $\text{NH}_3$ , extra pure, 32%, Merck) was added dropwise to the solution in order to increase the pH to exactly 7.

The synthesis procedure for the Mg (II) precursor starts with magnesium hydroxide ( $\text{Mg}(\text{OH})_2$ , 95-100.5%, Alfa Aesar) and citric acid (CA,  $\text{C}_6\text{H}_8\text{O}_7$ , 99%, Sigma-Aldrich) which were added in water so that the final Mg (II) ion concentration and  $\text{Mg}^{2+}:\text{CA}$  ratio were, respectively, 0.7 M and 1:1. The mixture was refluxed at  $80^\circ\text{C}$ , which after a short time yielded a clear, acidic solution. The solution was cooled to room temperature and in the third step, ammonia ( $\text{NH}_3$ , extra pure, 32%, Merck) was added dropwise to the solution in order to increase the pH to exactly 7.

For the Al (III) precursor, a previously reported method [66] was adjusted to make it highly compatible with the other metal ion solutions. It was synthesized by the addition of the metal hydroxide, i.e. aluminum hydroxide ( $\text{Al}(\text{OH})_3$ , reagent

grade, Sigma-Aldrich) and citric acid (CA,  $C_6H_8O_7$ , 99%, Sigma-Aldrich) in water so that the final Al (III) ion concentration and  $Al^{3+}:CA$  ratio were, respectively, 0.7 M and 1:1. Then, the whole was refluxed at  $80^\circ C$ , which after a short time yielded a clear, acidic solution. The solution was cooled to room temperature and in the third step, ammonia ( $NH_3$ , extra pure, 32%, Merck) was added dropwise to the solution in order to increase the pH to exactly 7.

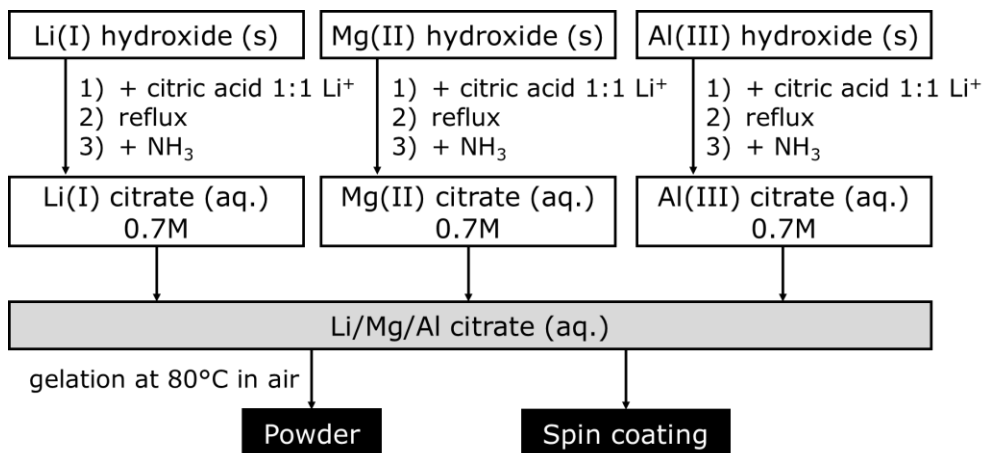


Figure II-24: Synthesis flowchart of the Li/Mg/Al precursor, powder and thin films.

The mono-metal ion precursor solutions were filtered using a membrane filter (Nalgene,  $0.2 \mu m$ ) to remove particles, impurities and undissolved fractions. Subsequently their exact concentration was determined by ICP-AES (Optima 3000, PerkinElmer).

The multi-metal ion Li/Mg/Al precursors were then prepared by mixing the Li (I), Mg (II) and Al (III) ion solutions in the desired amounts. Different molar ratios were prepared in view of  $(Li_xMg_{1-2x}Al_x)Al_2O_4$  with  $0 \leq X < 0.5$ . The total metal ion concentration was kept at 0.5 M for all prepared precursors.

For the powder synthesis, first, the precursor solutions were evaporated in air at  $80^\circ C$  to allow gelation of the system. The obtained gels were then crushed and ground manually in an agath mortar before further thermal treatment in view of crystallization. The decomposition of the gel was studied by means of a

simultaneous thermal gravimetric (TG) analysis in a TA Instruments TGA 951–2000. The gel was heated from room temperature to 800°C at a heating rate of 10°C min<sup>-1</sup> in dry air (100 ml min<sup>-1</sup>). The crystallization behavior of the Li/Mg/Al powders, which were precalcined at 200°C for 30 minutes, as a function of the temperature was studied in-situ by high-temperature X-ray diffraction (HT-XRD, Bruker, D8, step size 0.02°2 $\theta$ ). The measurements were carried out between 10 and 60° 2 $\theta$  at a heating rate of 10°C/min, with intervals of 50°C from 500 to 800°C.

#### 4.2.2 Li/Mg/Al oxide film deposition

Thin films were deposited via spin coating (3000 rpm, 30 s) of the Li/Mg/Al multi-ion precursors onto Si<sub>3</sub>N<sub>4</sub>/SiO<sub>2</sub>/Si (70 nm Si<sub>3</sub>N<sub>4</sub>/1.2 nm thermally grown SiO<sub>2</sub>), Pt/ZnO/SiO<sub>2</sub>/Si and Pt/TiN/SiO<sub>2</sub>/Si (70 nm Pt/40 nm TiN/SiO<sub>2</sub>). To allow deposition of uniform films, the Si<sub>3</sub>N<sub>4</sub> and Pt substrate surfaces were first pretreated in an UV/O<sub>3</sub> environment at 60°C for 30 minutes.[19] Multiple layers were deposited on the substrates, after each layer the sample was brought on hot plates to decompose the precursor. After deposition, the films were annealed in a furnace (post deposition anneal – PDA: 10°C/min, 30 min isothermal) to trigger the crystallization. The Li/Mg/Al film oxide phase formation was studied using ex-situ XRD on a PANalytical X'pert Pro tool with Cu K $\alpha$  radiation in a Grazing Incidence configuration (coupled  $\theta$ -2 $\theta$  scan) with a PIXcel detector in scanning mode (step size 0.0098°). The film morphology and thickness were visualized by scanning electron microscopy (SEM, FEI, NOVA 200) in a tilted view (45°) and cross-section view (90°). The composition of the deposited films was determined by elastic recoil detection (ERDA), using a *imec* home-built system.[61]

The ionic conductivity of the deposited films at room temperature was evaluated by means of electrochemical impedance spectroscopy. This was measured at open circuit potential in 1M LiClO<sub>4</sub> in propylene carbonate solutions using a three-electrode cell (working electrode = sample, reference electrode = Li, counter electrode = Li). The whole was connected to a Autolab PGSTAT 100 potentiostat and placed in a glove-box (under Ar) at 21°C. The electrochemical evaluation was performed by Put et al. (*imec*).

## 4.3 Results and discussion

### 4.3.1 Aqueous Li/Mg/Al precursor and oxide powder synthesis

The multi-metal ion Li/Mg/Al precursors, prepared in view of  $(\text{Li}_x\text{Mg}_{1-2x}\text{Al}_x)\text{Al}_2\text{O}_4$  with  $0 \leq X < 0.5$ , were clear and stable. The precursor decomposition was studied by a thermal gravimetric analysis (TGA) of the precursor gels, formed by evaporation of the water out of the precursor at  $80^\circ\text{C}$ . Earlier studies on the decomposition of citrate-based metal gels lead to a good understanding of the obtained profile.[21–23] From the precursors' decomposition profiles, shown in Figure II-25, it follows that the gel composition ( $0 \leq X < 0.5$ ) does not significantly affect the decomposition behavior. The small weight loss until  $150^\circ\text{C}$  can be ascribed to the evaporation of water, absorbed by the gel. This drying step is followed by a more intense weight loss, initiated at  $200^\circ\text{C}$  and finished at  $300^\circ\text{C}$ , due to the partial decomposition of the ammonium citrate gel matrix. For  $T > 300^\circ\text{C}$ , the decomposition of the direct coordination sphere of the metal ions starts. The accompanying removal of organic residual fractions is completed at  $600^\circ\text{C}$ .

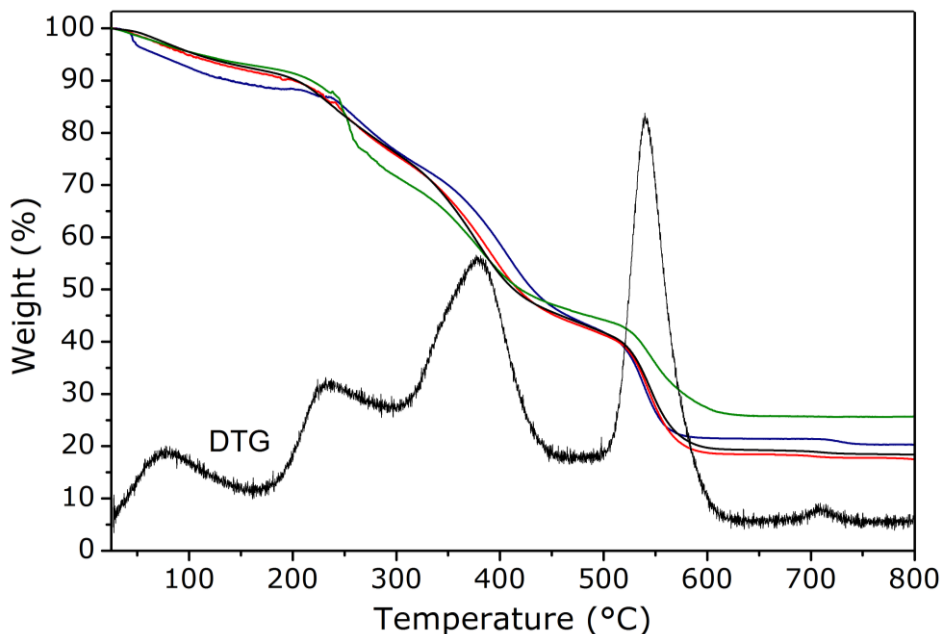


Figure II-25: TGA and DTG ( $10^\circ\text{C}/\text{min}$ ,  $100 \text{ ml}/\text{min}$  in dry air) of the Li/Mg/Al citrate gels with composition  $X=0.0$  (blue plot),  $X=0.3$  (red plot),  $X=0.4$  (black plot) and  $X=0.5$  (green plot) in  $(\text{Li}_x\text{Mg}_{1-2x}\text{Al}_x)\text{Al}_2\text{O}_4$ .

The crystallization behavior of Li/Mg/Al oxide was studied on the bulk material, i.e. powders obtained by evaporating water out of the precursor and crushing it. The oxide crystallization, in view of  $(\text{Li}_x\text{Mg}_{1-2x}\text{Al}_x)\text{Al}_2\text{O}_4$  with  $0 \leq X < 0.5$ , was followed using high-temperature XRD, allowing in-situ study of the phase (trans)formation during heating ( $10^\circ\text{C}/\text{min}$ , air, intervals of  $50^\circ\text{C}$  from  $500$  to  $800^\circ\text{C}$ ). In Figure II-26 the in-situ XRD results for the powder without lithium ( $X=0$ ), i.e. for the formation of  $\text{MgAl}_2\text{O}_4$ , are shown. Crystallization starts at  $600^\circ\text{C}$  with the formation of  $\text{MgAl}_2\text{O}_4$  spinel peaks in the XRD pattern, no secondary phases are present. These signals are intensified by increasing the temperature and, moreover, other signals which can all be attributed to the spinel phase are developed. One can thus conclude that via this sol-gel method phase-pure spinel  $\text{MgAl}_2\text{O}_4$  powders can be synthesized.

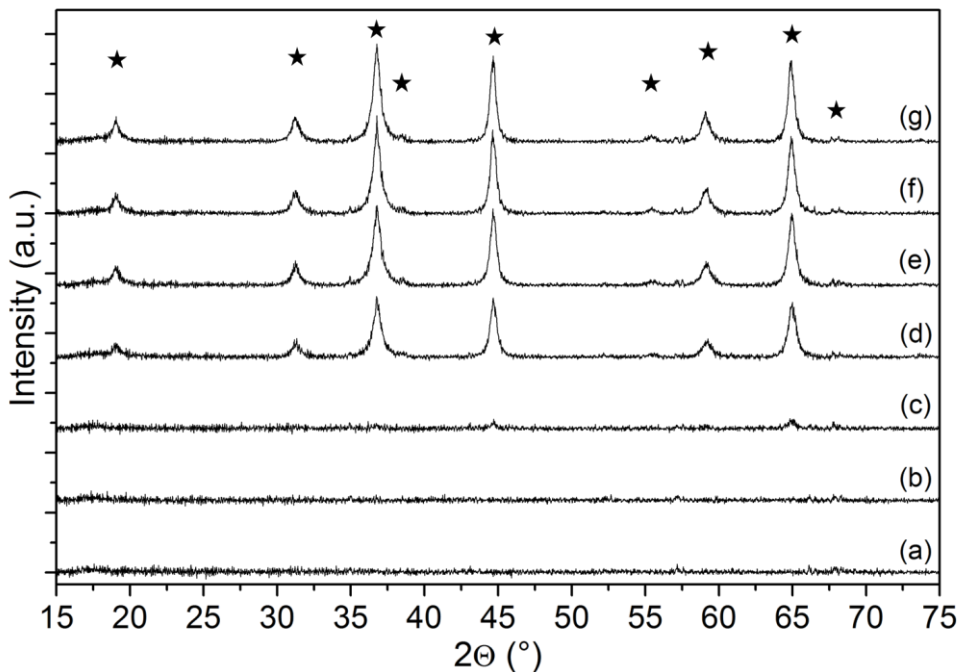


Figure II-26: HT-XRD patterns of the Li/Mg/Al citrate gel ( $X=0.0$  in  $(\text{Li}_x\text{Mg}_{1-2x}\text{Al}_x)\text{Al}_2\text{O}_4$  at (a)  $500^\circ\text{C}$ , (b)  $550^\circ\text{C}$ , (c)  $600^\circ\text{C}$ , (d)  $650^\circ\text{C}$ , (e)  $700^\circ\text{C}$ , (f)  $750^\circ\text{C}$  and (g)  $800^\circ\text{C}$  in air. As a reference the XRD signals originating from spinel ( $\star$ )  $\text{MgAl}_2\text{O}_4$  are shown. [35,62]

When a small amount of lithium is included in the system, the crystallization behavior is similar, as can be seen in Figure II-27 for  $X=0.1$ . However, the crystallization seems to be initiated earlier, i.e. at 500°C. Further increasing the temperature, results in the formation of other peaks which can also be linked to the spinel  $(\text{Li}_x\text{Mg}_{1-2x}\text{Al}_x)\text{Al}_2\text{O}_4$  phase. It must be noted that also peaks from the  $\text{Al}_2\text{O}_3$  substrate holder are visible in the XRD pattern since they tend to occur before crystallization starts. This is probably due to incomplete coverage of the substrate holder by the investigated powder. However, presence of crystalline  $\text{Al}_2\text{O}_3$  as secondary phase during the crystallization process can thus not be either shown or excluded in this case.

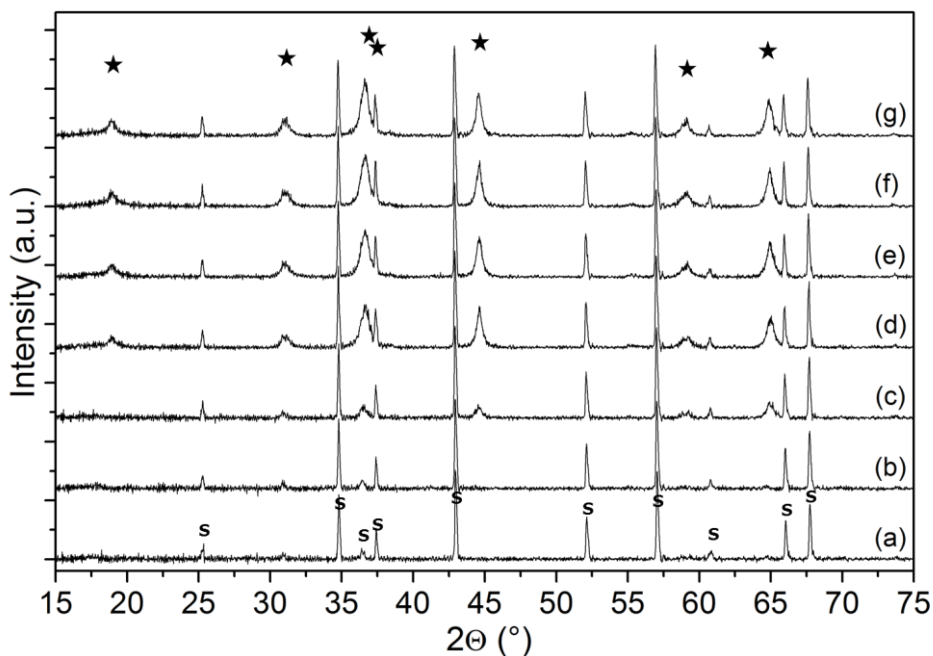


Figure II-27: HT-XRD patterns of the Li/Mg/Al citrate gel ( $X=0.1$  in  $(\text{Li}_x\text{Mg}_{1-2x}\text{Al}_x)\text{Al}_2\text{O}_4$  at (a) 500°C, (b) 550°C, (c) 600°C, (d) 650°C, (e) 700°C, (f) 750°C and (g) 800°C in air. As a reference the XRD signals originating from the (s)  $\text{Al}_2\text{O}_3$  substrate holder and spinel (★)  $(\text{Li}_x\text{Mg}_{1-2x}\text{Al}_x)\text{Al}_2\text{O}_4$  are shown. [35,62]

The in-situ XRD results for the “ $X=0.2$ ” powder are shown in Figure II-28. Also here, some peaks, originating from the substrate holder, can be noticed before crystallization. The crystallization of the bulk material starts at 600°C. By

increasing the temperature, these signals are intensifying, and moreover an extra peak, linked to the spinel ( $\text{Li}_x\text{Mg}_{1-2x}\text{Al}_x$ ) $\text{Al}_2\text{O}_4$  phase, appears. However, at the same time, also tetragonal  $\text{LiAlO}_2$  appears as secondary phase. Thus spinel ( $\text{Li}_x\text{Mg}_{1-2x}\text{Al}_x$ ) $\text{Al}_2\text{O}_4$  without the presence of  $\text{LiAlO}_2$  can be obtained in the temperature range  $600^\circ\text{C} \leq T < 650^\circ\text{C}$ .

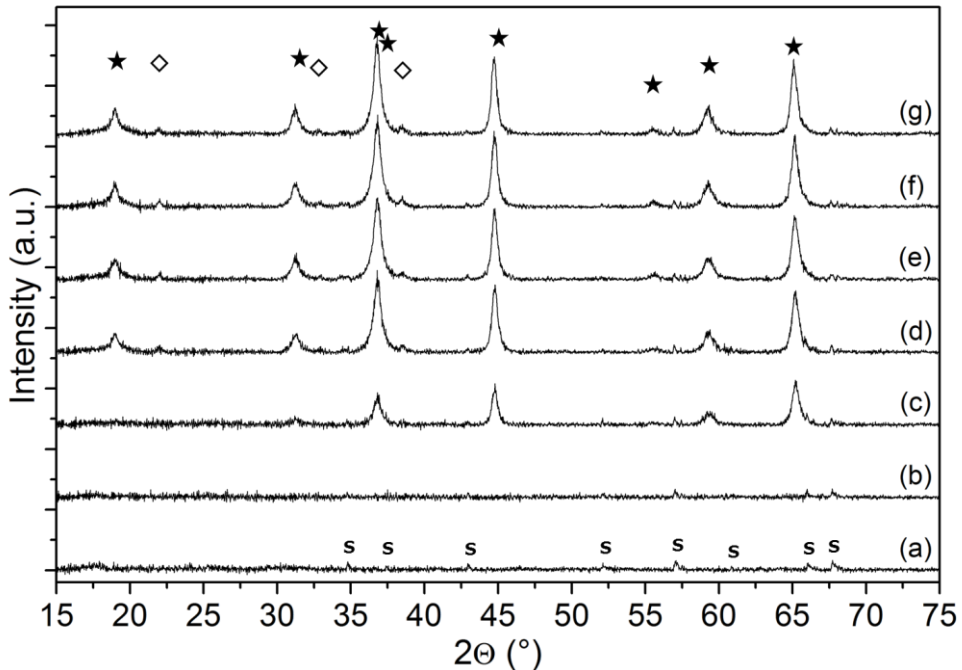


Figure II-28: HT-XRD patterns of the Li/Mg/Al citrate gel ( $X=0.2$  in  $\text{Li}_x\text{Mg}_{1-2x}\text{Al}_x$ ) $\text{Al}_2\text{O}_4$  at (a)  $500^\circ\text{C}$ , (b)  $550^\circ\text{C}$ , (c)  $600^\circ\text{C}$ , (d)  $650^\circ\text{C}$ , (e)  $700^\circ\text{C}$ , (f)  $750^\circ\text{C}$  and (g)  $800^\circ\text{C}$  in air. As a reference the XRD signals originating from originating from the (s)  $\text{Al}_2\text{O}_3$  substrate holder, tetragonal ( $\diamond$ )  $\text{LiAlO}_2$  and spinel ( $\star$ ) ( $\text{Li}_x\text{Mg}_{1-2x}\text{Al}_x$ ) $\text{Al}_2\text{O}_4$  are shown. [35,62]

Similarly, spinel ( $\text{Li}_x\text{Mg}_{1-2x}\text{Al}_x$ ) $\text{Al}_2\text{O}_4$  without the presence of  $\text{LiAlO}_2$  was obtained, starting from the precursor/gel with  $X=0.3$ , in the temperature range  $600^\circ\text{C} \leq T < 650^\circ\text{C}$  (see Figure II-29). The formation of spinel ( $\text{Li}_x\text{Mg}_{1-2x}\text{Al}_x$ ) $\text{Al}_2\text{O}_4$  starts at  $600^\circ\text{C}$  whereas the  $\text{LiAlO}_2$  is initiated at  $650^\circ\text{C}$ . Also here, there cannot be distinguished between the possibility of  $\text{Al}_2\text{O}_3$  impurities and the substrate holder.

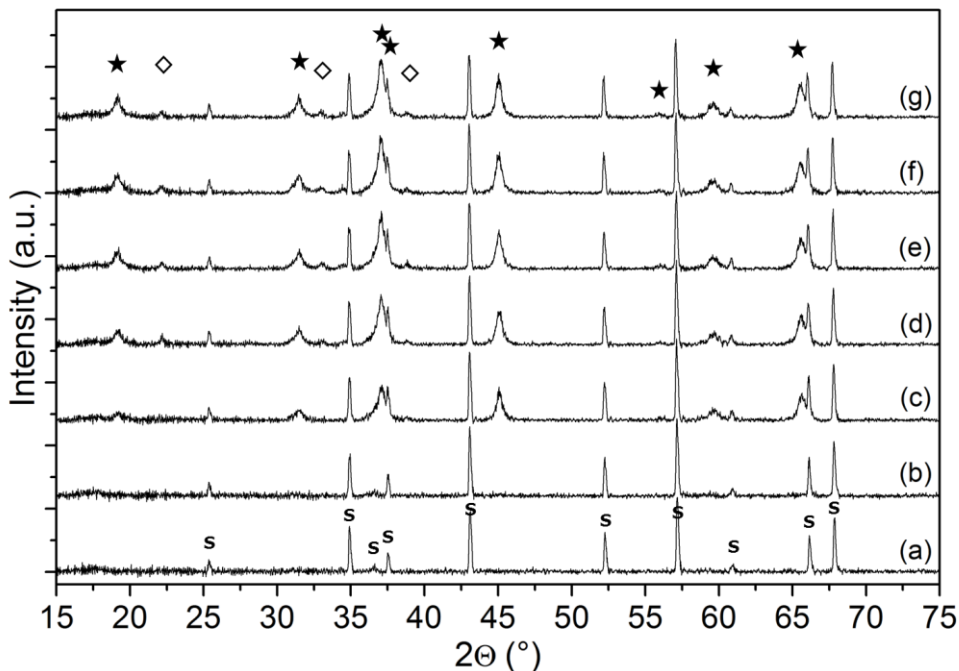


Figure II-29: HT-XRD patterns of the Li/Mg/Al citrate gel ( $X=0.3$  in  $(\text{Li}_x\text{Mg}_{1-2x}\text{Al}_x)\text{Al}_2\text{O}_4$ ) at (a)  $500^\circ\text{C}$ , (b)  $550^\circ\text{C}$ , (c)  $600^\circ\text{C}$ , (d)  $650^\circ\text{C}$ , (e)  $700^\circ\text{C}$ , (f)  $750^\circ\text{C}$  and (g)  $800^\circ\text{C}$  in air. As a reference the XRD signals originating from originating from the (s)  $\text{Al}_2\text{O}_3$  substrate holder, tetragonal ( $\diamond$ )  $\text{LiAlO}_2$  and spinel ( $\star$ )  $(\text{Li}_x\text{Mg}_{1-2x}\text{Al}_x)\text{Al}_2\text{O}_4$  are shown. [35,62]

For  $X=0.4$  (precursor/gel composition), it seems that the spinel phase without  $\text{LiAlO}_2$  is very difficult to achieve (Figure II-30). The formation of crystalline spinel  $(\text{Li}_x\text{Mg}_{1-2x}\text{Al}_x)\text{Al}_2\text{O}_4$ , which is initiated at  $600^\circ\text{C}$ , comes directly with tetragonal  $\text{LiAlO}_2$  as secondary phase. This indicates that  $(\text{Li}_{0.4}\text{Mg}_{0.2}\text{Al}_{0.4})\text{Al}_2\text{O}_4$  is not formed. Instead,  $(\text{Li}_x\text{Mg}_{1-2x}\text{Al}_x)\text{Al}_2\text{O}_4$  with  $X \leq 0.3$  is formed and the excess is immediately expelled in  $\text{LiAlO}_2$ . Elevating the temperature, intensifies the signals of  $(\text{Li}_x\text{Mg}_{1-2x}\text{Al}_x)\text{Al}_2\text{O}_4$  phase together with the unwanted lithium aluminate.

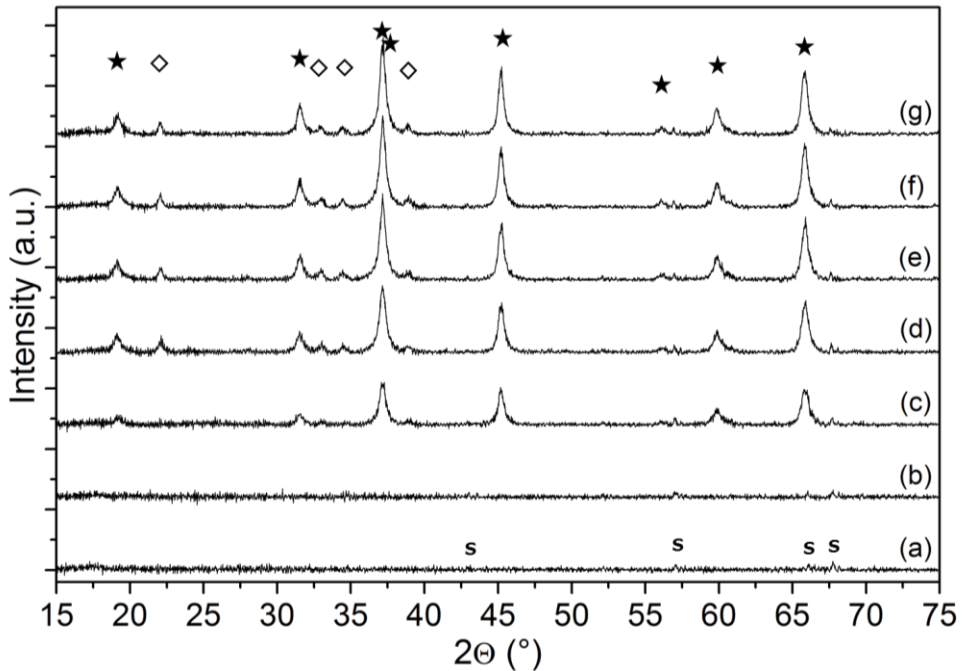


Figure II-30: HT-XRD patterns of the Li/Mg/Al citrate gel ( $X=0.4$  in  $(\text{Li}_x\text{Mg}_{1-2x}\text{Al}_x)\text{Al}_2\text{O}_4$ ) at (a)  $500^\circ\text{C}$ , (b)  $550^\circ\text{C}$ , (c)  $600^\circ\text{C}$ , (d)  $650^\circ\text{C}$ , (e)  $700^\circ\text{C}$ , (f)  $750^\circ\text{C}$  and (g)  $800^\circ\text{C}$  in air. As a reference the XRD signals originating from originating from the (s)  $\text{Al}_2\text{O}_3$  substrate holder, tetragonal ( $\diamond$ )  $\text{LiAlO}_2$  and spinel ( $\star$ )  $(\text{Li}_x\text{Mg}_{1-2x}\text{Al}_x)\text{Al}_2\text{O}_4$  are shown. [35,62]

For the powder without Mg ( $X=0.5$ ), the in-situ XRD results are shown in Figure II-31. Also, in this case, the formation of crystalline phases starts at  $600^\circ\text{C}$ . At that temperature spinel  $(\text{Li}_x\text{Mg}_{1-2x}\text{Al}_x)\text{Al}_2\text{O}_4$  powder can be obtained, no  $\text{LiAlO}_2$  secondary phase is present. There cannot be distinguished between the possibility of  $\text{Al}_2\text{O}_3$  impurities and the substrate holder. When further increasing the temperature the phase-pure spinel phase is maintained, the peaks which are associated with it are gaining in intensity.

It has been shown that phase-pure  $(\text{Li}_x\text{Mg}_{1-2x}\text{Al}_x)\text{Al}_2\text{O}_4$  bulk material can be obtained for  $X \leq 0.3$ , by using the reported aqueous sol-gel method. For  $X > 0.3$ , the actual formed  $(\text{Li}_x\text{Mg}_{1-2x}\text{Al}_x)\text{Al}_2\text{O}_4$  phase will be deficient ( $X \leq 0.3$ ) and therefore a secondary phase consuming the excess is unavoidable. This is in agreement with the theoretical calculations: it was found that segregation is more likely to occur

at higher lithium concentration due to the more pronounced endothermicity of the reaction.[67]

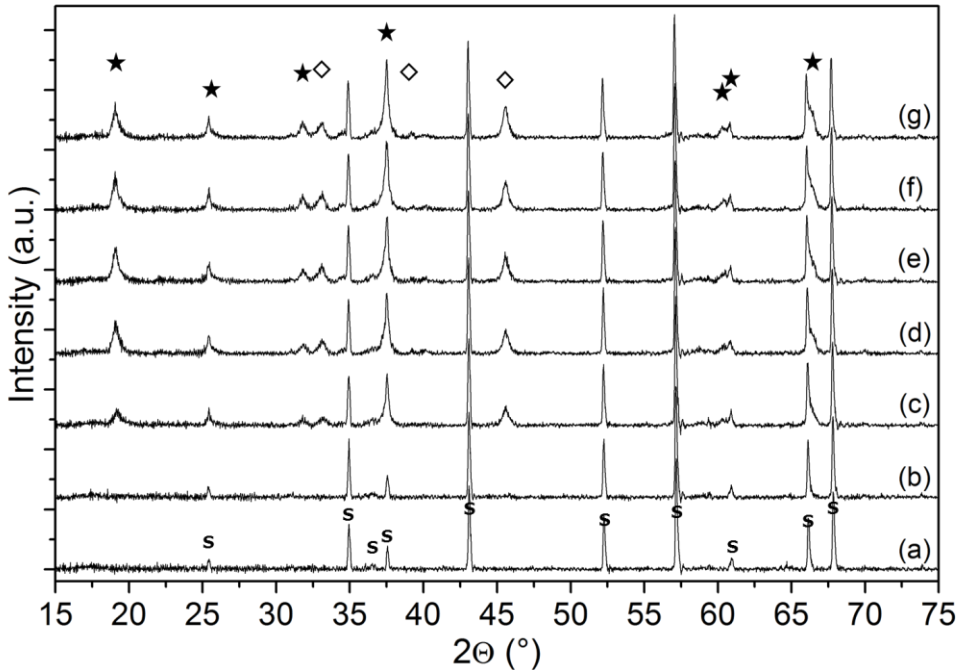


Figure II-31: HT-XRD patterns of the Li/Al citrate gel ( $X=0.5$  in  $(Li_xMg_{1-2x}Al_x)Al_2O_4$ ) at (a) 500°C, (b) 550°C, (c) 600°C, (d) 650°C, (e) 700°C, (f) 750°C and (g) 800°C in air. As a reference the XRD signals originating from originating from the (s)  $Al_2O_3$  substrate holder, tetragonal ( $\diamond$ )  $LiAlO_2$  and spinel ( $\star$ )  $(Li_xMg_{1-2x}Al_x)Al_2O_4$ ) are shown. [35,62]

#### 4.3.2 Li/Mg/Al oxide film deposition

Via spin coating of several layers of the Li/Mg/Al precursor, amorphous lithium magnesium aluminate films were deposited on  $SiO_2/Si$  substrates. For the decomposition of the precursor and the accompanying oxide formation, also for this system, there was opted for a hot plate treatment between each spin coat cycle. This was done to avoid the formation of a solidified skin before the interior of the film is decomposed completely, and consequently the formation of cracks when gases escape from the interior and break through the skin.[15] The hot plate conditions (1' at 110°C, 2' at 300°C, 2' at 480°C, 2' at 600°C) were defined based on the precursors' thermal decomposition profiles (Figure II-25), which

were obtained by a thermal gravimetric study (TGA/DTA) of the precursor gels, formed by evaporation of the water out of the precursor at 80°C.

In order to study the film deposition, the precursor with a composition of  $X=0.05$  in  $(\text{Li}_x\text{Mg}_{1-2x}\text{Al}_x)\text{Al}_2\text{O}_4$  was selected as model material. It has been shown for  $(\text{Li}_x\text{Mg}_{1-2x}\text{Al}_x)\text{Al}_2\text{O}_4$  powders that for a low lithium amount ( $X \leq 0.3$ ), the spinel phase could be obtained without the presence of  $\text{LiAlO}_2$ .

In the absence of etching/dissolution of underlying layers, the film thickness can be controlled by the number of deposited layers, as was shown for the  $\text{LuFeO}_3$  system. Each deposition cycle comprises spin coating and a thermal treatment on hot plates. In Figure II-32 the thicknesses of  $(\text{Li}_x\text{Mg}_{1-2x}\text{Al}_x)\text{Al}_2\text{O}_4$  films (precursor with  $X=0.05$ ) on 1.2 nm  $\text{SiO}_2/\text{Si}$ , determined by X-SEM, are plotted as a function of the number of deposition cycles. The inset shows the X-SEM image of the film after four deposition cycles.

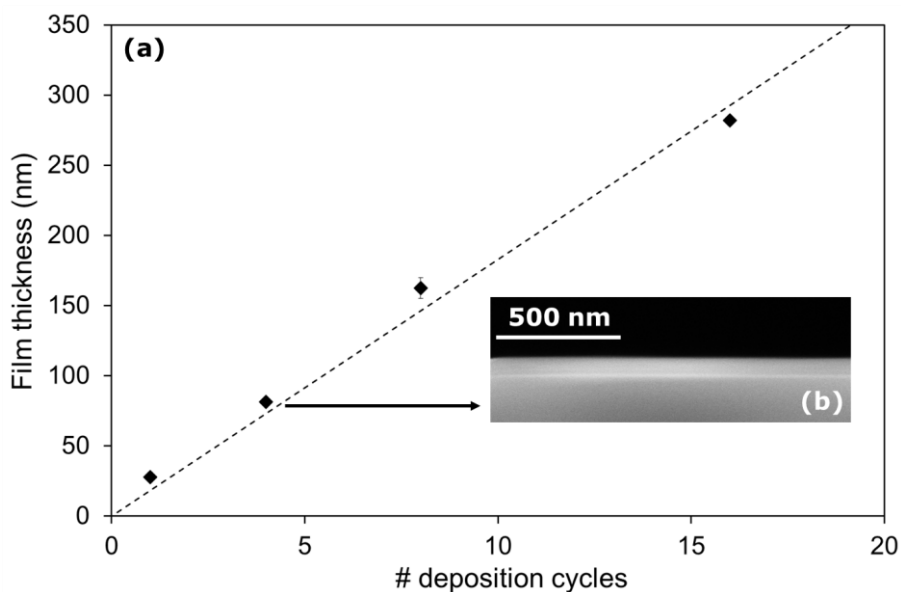


Figure II-32: (a) Plot of the film thickness of  $(\text{Li}_x\text{Mg}_{1-2x}\text{Al}_x)\text{Al}_2\text{O}_4$  oxide films (precursor with  $X=0.05$ ) on 1.2 nm  $\text{SiO}_2/\text{Si}$ , determined via X-SEM, as a function of the amount of deposition cycles (i.e. spin coating and subsequent thermal treatment on hot plates) and (b) X-SEM image of the Li/Mg/Al oxide film after 4 deposition cycles.

It can be observed that the films are very smooth after deposition (see SEM image) and that the resulting film thicknesses vary linearly with the number of cycles. Hence, the Li/Mg/Al oxide film thickness can be controlled by the number of deposition cycles.

Via spin coating 4 layers of the precursor, Li/Mg/Al amorphous oxide films with a thickness of ca. 80 nm were deposited on Pt/ZnO/Si substrates. This type of substrate was selected because of its electrical conductivity enabling the possibility for electrochemical measurements. Furthermore it is known that this substrate prevents Li diffusion into the substrate and also the formation of silicates ( $\text{LuFeO}_3$ ) is excluded by using this stack. Moreover it was experimentally found that these layers could stand temperatures till 1000°C.

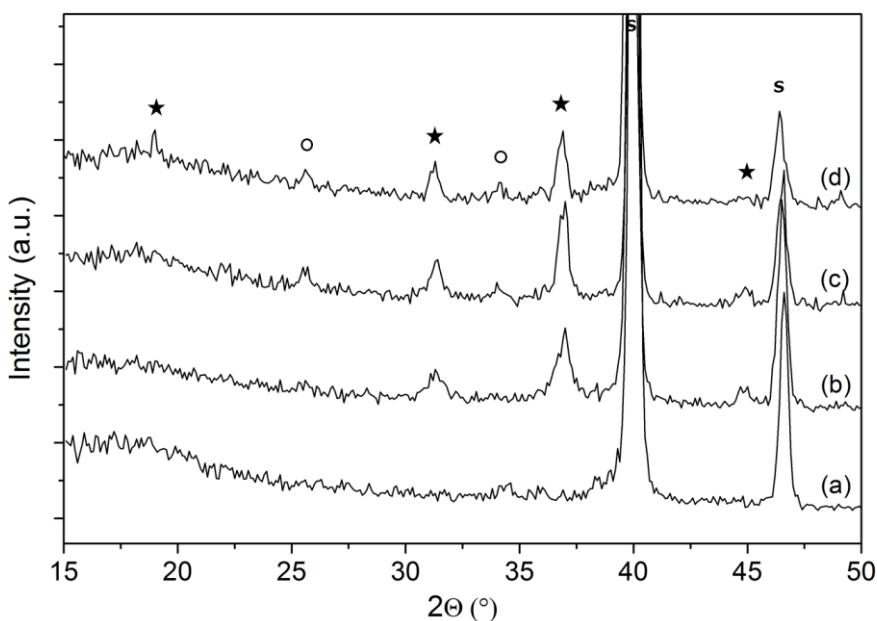


Figure II-33: GI-XRD patterns of ca. 80 nm  $(\text{Li}_x\text{Mg}_{1-2x}\text{Al}_x)\text{Al}_2\text{O}_4$  (precursor with  $X = 0.05$ ) oxide films on Pt/ZnO/Si, deposited via spin coating after hot plate treatment and crystallized via a post deposition anneal in dry air at (a) 700°C, (b) 800°C, (c) 900°C, (d) 1000°C. As a reference the XRD signals originating from the substrate (s), rhombohedral (○)  $\text{Al}_2\text{O}_3$  and spinel (★)  $(\text{Li}_x\text{Mg}_{1-2x}\text{Al}_x)\text{Al}_2\text{O}_4$  are shown. [35,62]

The deposited films were further annealed for 30 min in a furnace in order to crystallize. The GI-XRD patterns in Figure II-33 show that after the hot plates and an anneal in a furnace at 700°C, the Li/Mg/Al oxide film is not yet crystalline (Figure II-33a). A temperature of 800°C was necessary to trigger the film crystallization as spinel ( $\text{Li}_x\text{Mg}_{1-2x}\text{Al}_x$ ) $\text{Al}_2\text{O}_4$  phase formation is observed in the XRD pattern of Figure II-33b. A crystallization temperature of 800°C for spinel formation is much higher than that needed for ( $\text{Li}_x\text{Mg}_{1-2x}\text{Al}_x$ ) $\text{Al}_2\text{O}_4$  powders (600°C–650°C). This can be explained by an increase in activation energy for the crystallization of thin films compared to bulk material, considering volume induced crystallization.[25] Elevating the post deposition anneal temperature to 900°C or 1000°C (Figure II-33b-d) results in the appearance of peaks attributed to rhombohedral  $\text{Al}_2\text{O}_3$ , formed as secondary phase in the ( $\text{Li}_x\text{Mg}_{1-2x}\text{Al}_x$ ) $\text{Al}_2\text{O}_4$  films at these high temperatures.

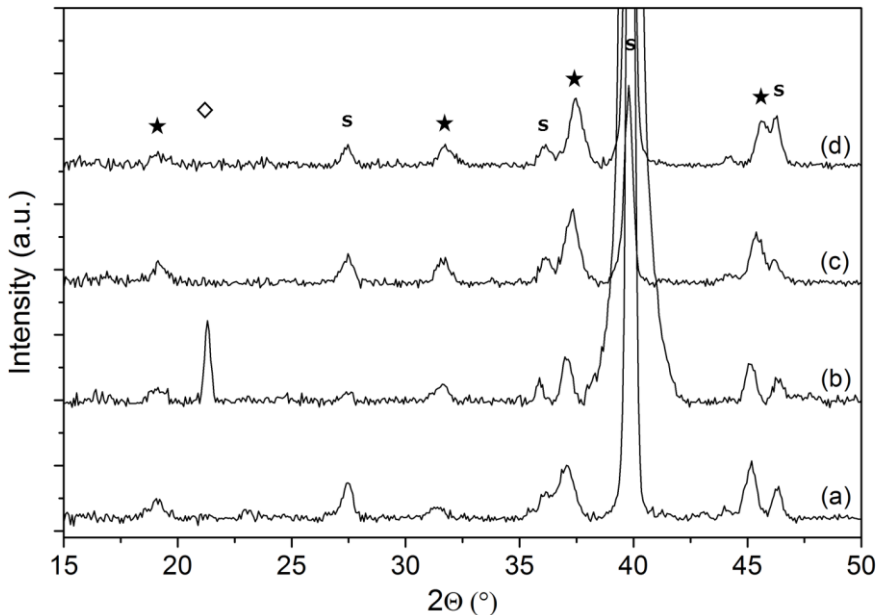


Figure II-34: GI-XRD patterns of ca. 80 nm Li/Mg/Al oxide films (precursor with (a)  $X=0.1$ , (b)  $X=0.2$ , (c)  $X=0.3$  and (d)  $X=0.4$ ) on Pt/TiN/Si, deposited via spin coating after hot plate treatment and crystallized via a post deposition anneal in dry air at 800°C. As a reference the XRD signals originating from the substrate (s), tetragonal ( $\diamond$ )  $\text{LiAlO}_2$  and spinel ( $\star$ ) ( $\text{Li}_x\text{Mg}_{1-2x}\text{Al}_x$ ) $\text{Al}_2\text{O}_4$  are shown. [35,62]

It can be concluded that 800°C is the optimal temperature to obtain spinel ( $\text{Li}_x\text{Mg}_{1-2x}\text{Al}_x$ ) $\text{Al}_2\text{O}_4$  without crystalline secondary phases for  $X=0.05$ . The crystallization at 800°C was also studied for films deposited via precursors with all other compositions ( $X=0.1$ ,  $X=0.2$ ,  $X=0.3$  and  $X=0.4$ ). Via spin coating 4 layers of the appropriate precursor, Li/Mg/Al amorphous oxide films with a thickness of ca. 80 nm were deposited on Pt/TiN/Si substrates. In all cases the spinel ( $\text{Li}_x\text{Mg}_{1-2x}\text{Al}_x$ ) $\text{Al}_2\text{O}_4$  is obtained (Figure II-34). Moreover it seems that no secondary crystalline phases are present for  $X=0.1$ ,  $X=0.3$  and  $X=0.4$ . For  $X=0.2$ , the XRD pattern is characterized by a signal, related to tetragonal  $\text{LiAlO}_2$ .

The morphology of the films was studied by SEM. In Figure II-35a, a SEM image of a ( $\text{Li}_x\text{Mg}_{1-2x}\text{Al}_x$ ) $\text{Al}_2\text{O}_4$ / $\text{LiAlO}_2$  film ( $X=0.2$ ) is shown. One can observe species which are separated from the film, suggesting that there is indeed phase segregation. For the ( $\text{Li}_x\text{Mg}_{1-2x}\text{Al}_x$ ) $\text{Al}_2\text{O}_4$  film ( $X=0.4$ ), for which XRD did not show secondary phases, a continuous but rough film can be seen in Figure II-35b.

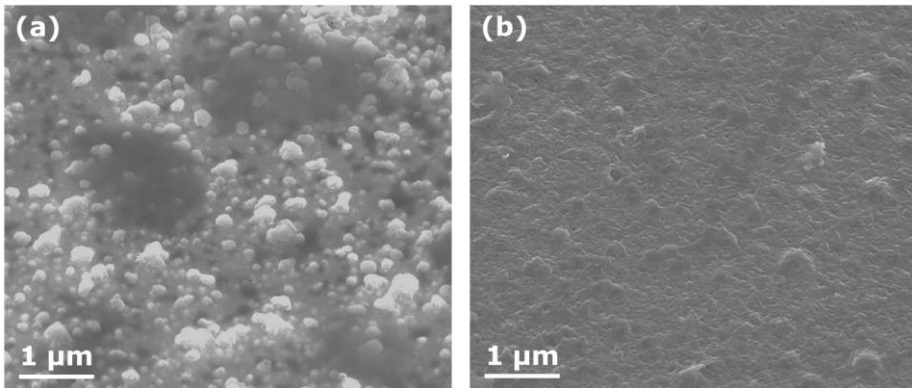


Figure II-35: SEM images (tilted view, 45°) of (a) a ( $\text{Li}_x\text{Mg}_{1-2x}\text{Al}_x$ ) $\text{Al}_2\text{O}_4$ / $\text{LiAlO}_2$  film and (b) a ( $\text{Li}_x\text{Mg}_{1-2x}\text{Al}_x$ ) $\text{Al}_2\text{O}_4$  film on Pt/TiN/ $\text{TiO}_2$ /Si, deposited via spin coating of a Li/Mg/Al precursor with a composition of respectively  $X=0.2$  and  $X=0.4$ , followed by a subsequent heat treatment. The films were crystallized via a post deposition anneal in dry air at 800°C.

The composition of the deposited films was measured by ERDA. Since this technique cannot be applied for films deposited on Pt, the Li/Mg/Al oxide films were deposited on  $\text{Si}_3\text{N}_4$ / $\text{SiO}_2$ /Si, followed by a heat treatment and a PDA in at 800°C in dry air. In Figure II-36, a plot of the (a) lithium, (b) magnesium and (c)

aluminum content in the deposited film expressed as  $(\text{Li}_x\text{Mg}_{1-2x}\text{Al}_x)\text{Al}_2\text{O}_4$  and determined by ERDA, as a function of the metal content in the precursor, is shown. The solid (linear) lines represent the ideal case, i.e. the composition that was aimed for in the films. For lithium, the concentration is systematically lower than the targeted amount. The lower amount of lithium in the films could explain why the secondary phase is less likely formed. Furthermore, the aluminum amount is typically higher than the targeted concentration, except for  $X=0.4$ . The magnesium concentration is decreasing with  $X$ . This observation, combined with the fact that the offset for lithium seems to be constant for  $X \leq 0.2$ , probably explains why, in the case of  $X=0.2$ , the secondary  $\text{LiAlO}_2$  phase is formed, and thus in the other films not. The magnesium content is further decreasing from  $X=0.2$  onwards, however, the Li content is probably too low to result in  $\text{LiAlO}_2$  secondary phases.

The electrochemical properties of the deposited  $(\text{Li}_x\text{Mg}_{1-2x}\text{Al}_x)\text{Al}_2\text{O}_4$  films were evaluated by means of electrochemical impedance spectroscopy. These experiments were performed at imec by Put et al. The results are presented, as a Nyquist plot, in Figure II-37. One should be able to distinguish a semi-circle, especially for the first part of the plot which is magnified and shown as an inset. Simplified, the electrolyte system can be presented as a resistor and a capacitor in parallel. However, such semi-circular behavior could not be observed. Hence, almost no ionic conductivity is present in the  $(\text{Li}_x\text{Mg}_{1-2x}\text{Al}_x)\text{Al}_2\text{O}_4$  films. Furthermore, it seems that there is no dependency of the ionic conductivity on the stoichiometry of the deposited material. A possible hypothesis is that at the grain boundaries an amorphous  $\text{Al}_2\text{O}_3$  interface was formed, which thus deteriorates the high potential of this newly defined electrolyte material. This is plausible since typically there was an excess of Al available in the films (Figure II-36c) and rhombohedral  $\text{Al}_2\text{O}_3$  was found after a PDA at  $900^\circ\text{C}$  and more (Figure II-33).

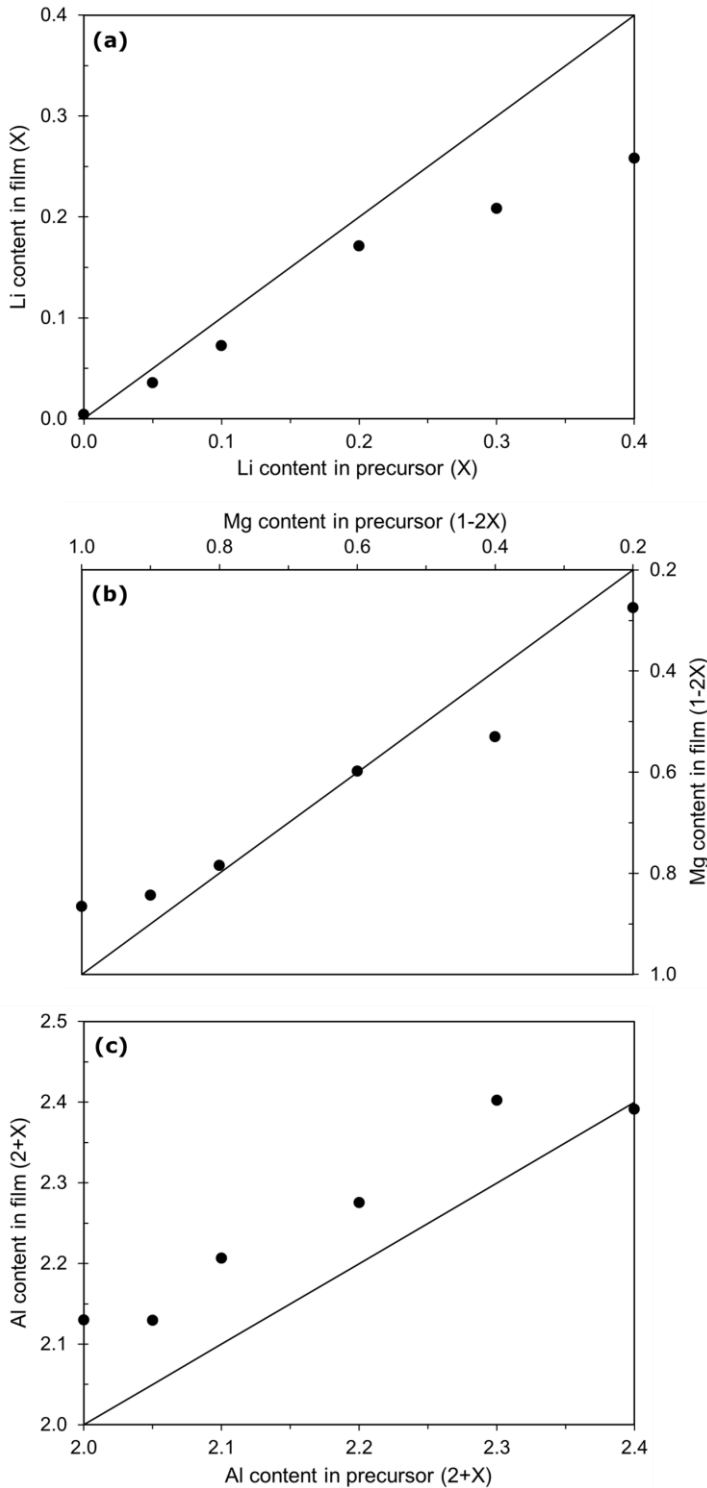


Figure II-36: Plot of the (a) lithium, (b) Mg and (c) Al content in the deposited film – expressed as  $(Li_xMg_{1-2x}Al_x)Al_2O_4$  and determined by ERDA, as a function of the metal content in the precursor. The solid (linear) lines represent the ideal case. The films on  $Si_3N_4/SiO_2/Si$  were deposited via spin coating of a Li/Mg/Al precursor, followed by a heat treatment. The films were crystallized via a PDA in at  $800^\circ\text{C}$  in dry air.

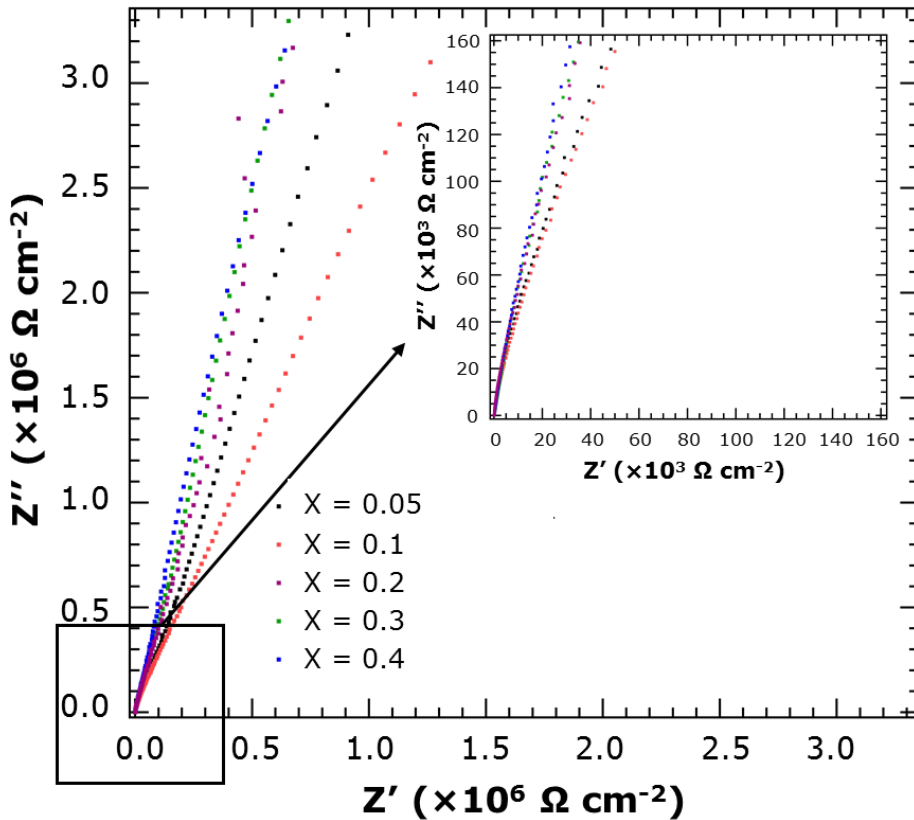


Figure II-37: Electrochemical impedance spectroscopy (Nyquist plot) of  $(Li_xMg_{1-2x}Al_x)Al_2O_4$  films (precursor with  $X=0.1$ ,  $X=0.2$ ,  $X=0.3$  and  $X=0.4$ ) on Pt/TiN/TiO<sub>2</sub>/Si, deposited via spin coating of a Li/Mg/Al precursor, followed by a subsequent heat treatment. The films were crystallized via a post deposition anneal in dry air at 800°C. For convenience, as an inset the first part of the plot is magnified. [Courtesy of Put et al., imec]

## 4.4 Conclusions

The synthesis of a stable aqueous Li/Mg/Al precursor, which could be used for the chemical solution deposition of  $(\text{Li}_x\text{Mg}_{1-2x}\text{Al}_x)\text{Al}_2\text{O}_4$  thin films (spin coating), was shown. Spinel films could be achieved after a post deposition anneal at 800°C. A too high Li:Mg ratio for  $X=0.2$  lead to the formation of  $\text{LiAlO}_2$  as secondary phase, deteriorating the intrinsic film quality and morphology. Electrochemical impedance spectroscopy showed that none of the deposited films possess a decent ionic conductivity. This is due to the formation of an amorphous  $\text{Al}_2\text{O}_3$  interface at the grain boundaries, caused by an excess of Al available in the films (observed by ERDA). This observation tackles the potential use of these solid electrolyte films in thin-film Li-ion batteries, at least tentatively. If the formation of  $\text{Al}_2\text{O}_3$  could be avoided, e.g. by a more elaborate tuning of the Li:Mg:Al ratio, this could result in a higher ionic conductivity.

## 5 Summary

Several new aqueous based chemical solution deposition processes were developed in order to deposit thin films of  $\text{LuFeO}_3$ ,  $\text{Li}_4\text{Ti}_5\text{O}_{12}$  and  $(\text{Li}_x\text{Mg}_{1-2x}\text{Al}_x)\text{Al}_2\text{O}_4$ , and their interesting characteristics were investigated.

For the obtained phase-pure  $\alpha\text{-LuFeO}_3$  film on  $\text{Si}_3\text{N}_4/\text{SiO}_2/\text{Si}$ , to the authors' knowledge for the first time, a giant dielectric constant equal or higher than  $10^4$  was shown for low frequencies ( $< 10^3$  Hz), which makes it promising for the use in thin film capacitors. The downside of the material is that the dielectric loss is quite high at low frequencies.

Furthermore, it also seems that the aqueous solution-gel process can deliver spinel  $\text{Li}_4\text{Ti}_5\text{O}_{12}$  films which are very promising for incorporation in thin-film Li-ion batteries. A more precise determination of the amount of active material and a more thorough electrochemical study should be performed to check all electrochemical characteristics including the exact capacity and cycle life.

Chemical solution deposition of spinel  $(\text{Li}_x\text{Mg}_{1-2x}\text{Al}_x)\text{Al}_2\text{O}_4$  thin films was also shown. Electrochemical impedance spectroscopy showed that the deposited films did not possess a decent ionic conductivity, probably due to the formation of an amorphous  $\text{Al}_2\text{O}_3$  interface at the grain boundaries. This is caused by an excess of Al available in the films. If the formation of  $\text{Al}_2\text{O}_3$  could be avoided, e.g. by tuning the Li:Mg:Al ratio, this could result in a higher ionic conductivity and make the material interesting as solid electrolyte film in thin-film Li-ion batteries.

These processes are all marked by their low cost, relative easiness and environmental friendly character. It is obvious that a transfer of the process to a 3D substrate would take them even a step higher.

## 6 References

- [1] A. Burke, Ultracapacitors : why, how, and where is the technology, *J. Power Sources*. 91 (2000) 37–50. doi:10.1016/S0378-7753(00)00485-7.
- [2] B. Hudec, K. Husekova, E. Dobrocka, T. Lalinsky, J. Aarik, A. Aidla, et al., High-permittivity metal-insulator-metal capacitors with TiO<sub>2</sub> rutile dielectric and RuO<sub>2</sub> bottom electrode, *IOP Conf. Ser. Mater. Sci. Eng.* 8 (2010) 012024. doi:10.1088/1757-899X/8/1/012024.
- [3] C. Zhu, B.-J. Cho, M.-F. Li, Atomic Layer Deposited High- $\kappa$  Films and Their Role in Metal-Insulator-Metal Capacitors for Si RF/Analog Integrated Circuit Applications, *Chem. Vap. Depos.* 12 (2006) 165–171. doi:10.1002/cvde.200506393.
- [4] L.P. Zhu, H.M. Deng, L. Sun, J. Yang, P.X. Yang, J.H. Chu, Optical properties of multiferroic LuFeO<sub>3</sub> ceramics, *Ceram. Int.* 40 (2014) 1171–1175. doi:10.1016/j.ceramint.2013.07.001.
- [5] L. Zhang, X.M. Chen, Dielectric relaxation in LuFeO<sub>3</sub> ceramics, *Solid State Commun.* 149 (2009) 1317–1321. doi:10.1016/j.ssc.2009.05.036.
- [6] L. Zhu, H. Deng, J. Liu, L. Sun, P. Yang, Preparation and characterization of Bi-doped LuFeO<sub>3</sub> thin films grown on LaNiO<sub>3</sub> substrate, *J. Cryst. Growth.* 387 (2014) 6–9. doi:10.1016/j.jcrysgro.2013.10.039.
- [7] W. Wang, J. Zhao, W. Wang, Z. Gai, N. Balke, M. Chi, et al., Room-temperature multiferroic hexagonal LuFeO<sub>3</sub> films, *Phys. Rev. Lett.* 110 (2013) 237601. doi:10.1103/PhysRevLett.110.237601.
- [8] W. Wang, H. Wang, X. Xu, L. Zhu, L. He, E. Wills, et al., Crystal field splitting and optical bandgap of hexagonal LuFeO<sub>3</sub> films, *Appl. Phys. Lett.* 101 (2012) 241907. doi:10.1063/1.4771601.
- [9] D. Khomskii, Classifying multiferroics: Mechanisms and effects, *Physics (College. Park. Md)*. 2 (2009) 20. doi:10.1103/Physics.2.20.
- [10] N.A. Spaldin, S.-W. Cheong, R. Ramesh, Multiferroics: Past, present, and future, *Phys. Today*. 63 (2010) 38. doi:10.1063/1.3502547.
- [11] W. Eerenstein, N.D. Mathur, J.F. Scott, Multiferroic and magnetoelectric materials., *Nature*. 442 (2006) 759–65. doi:10.1038/nature05023.
- [12] J.A. Moyer, R. Misra, J.A. Mundy, C.M. Brooks, J.T. Heron, D.A. Muller, et al., Intrinsic magnetic properties of hexagonal LuFeO<sub>3</sub> and the effects of nonstoichiometry, *APL Mater.* 2 (2014) 012106. doi:10.1063/1.4861795.

- [13] K. Kuribayashi, K. Nagashio, K. Niwata, M.S.V. Kumar, T. Hibiya, Novel criterion for formation of metastable phase from undercooled melt, *Mater. Sci. Eng. A.* 449-451 (2007) 675–679. doi:10.1016/j.msea.2006.02.430.
- [14] L.P. Zhu, H.M. Deng, X.X. Li, P.X. Yang, J.H. Chu, Optical properties of LuFeO<sub>3</sub> thin films prepared by pulsed laser deposition, *J. Phys. Conf. Ser.* 276 (2011) 012200. doi:10.1088/1742-6596/276/1/012200.
- [15] A. Hardy, S. Van Elshocht, J. D’Haen, O. Douhéret, S. De Gendt, M. Caymax, et al., Aqueous chemical solution deposition of ultrathin lanthanide oxide dielectric films, *J. Mater. Res.* 22 (2007) 3484–3493. doi:10.1557/JMR.2007.0433.
- [16] D. Dewulf, N. Peys, S. Van Elshocht, G. Rampelberg, C. Detavernier, S. De Gendt, et al., Interfacial reactions of Gd- and Nb-oxide based high-k layers deposited by aqueous chemical solution deposition, *Microelectron. Eng.* 88 (2011) 1338–1341. doi:10.1016/j.mee.2011.03.045.
- [17] A. Hardy, S. Gielis, H. Van den Rul, J. D’Haen, M.K. Van Bael, J. Mullens, Effects of precursor chemistry and thermal treatment conditions on obtaining phase pure bismuth ferrite from aqueous gel precursors, *J. Eur. Ceram. Soc.* 29 (2009) 3007–3013. doi:10.1016/j.jeurceramsoc.2009.05.018.
- [18] M.K. Van Bael, D. Nelis, A. Hardy, D. Mondelaers, K. Van Werde, J. D’Haen, et al., Integrated Ferroelectrics : An Aqueous Chemical Solution Deposition of Ferroelectric Thin Films, *Integr. Ferroelectr.* 45 (2002) 113–122. doi:10.1080/10584580215353.
- [19] J.R. Vig, *Treatise on Clean Surface Technology - Volume 1*, 1st ed., Plenum Press, New York, 1987.
- [20] N.J. Kidner, Z.J. Homrighaus, T.O. Mason, E.J. Garboczi, Modeling interdigital electrode structures for the dielectric characterization of electroceramic thin films, *Thin Solid Films.* 496 (2006) 539–545. doi:10.1016/j.tsf.2005.08.350.
- [21] K. Van Werde, D. Mondelaers, G. Vanhoyland, D. Nelis, M.K. Van Bael, J. Mullens, et al., Thermal decomposition of the ammonium zinc acetate citrate precursor for aqueous chemical solution deposition of ZnO, *J. Mater. Sci.* 37 (2002) 81–88. doi:10.1023/A:1013141723764.
- [22] A. Hardy, K. Van Werde, G. Vanhoyland, M.K. Van Bael, J. Mullens, L.C. Van Poucke, Study of the decomposition of an aqueous metal – chelate gel precursor for (Bi,La)4Ti3O12 by means of TGA – FTIR , TGA – MS and HT-DRIFT, *Thermochim. Acta.* 397 (2003) 143–153. doi:10.1016/S0040-6031(02)00272-1.

- [23] D. Nelis, D. Mondelaers, G. Vanhoyland, A. Hardy, K. Van Werde, H. Van Den Rul, et al., Synthesis of strontium bismuth niobate (SrBi<sub>2</sub>Nb<sub>2</sub>O<sub>9</sub>) using an aqueous acetate–citrate precursor gel: thermal decomposition and phase formation, *Thermochim. Acta.* 426 (2005) 39–48. doi:10.1016/j.tca.2004.07.005.
- [24] N. Peys, Y. Ling, D. Dewulf, S. Gielis, C. De Dobbelaere, D. Cuypers, et al., V<sub>6</sub>O<sub>13</sub> films by control of the oxidation state from aqueous precursor to crystalline phase, *Dalt. Trans.* 42 (2013) 959–968. doi:10.1039/c2dt31857a.
- [25] V.I. Trofimov, I. V. Trofimov, J.-I. Kim, The effect of finite film thickness on the crystallization kinetics of amorphous film and microstructure of crystallized film, *Thin Solid Films.* 495 (2006) 398–403. doi:10.1016/j.tsf.2005.08.221.
- [26] S. Van Elshocht, C. Adelman, T. Conard, A. Delabie, A. Franquet, L. Nyns, et al., Silicate formation and thermal stability of ternary rare earth oxides as high-k dielectrics, *J. Vac. Sci. Technol. A Vacuum, Surfaces, Film.* 26 (2008) 724. doi:10.1116/1.2891257.
- [27] K. Ishikawa, Y. Uchiyama, H. Ogawa, S. Fujimura, Dependence of TO and LO mode frequency of thermally grown silicon dioxide films on annealing temperature, *Appl. Surf. Sci.* 117/118 (1997) 212–215. doi:10.1016/S0169-4332(97)80081-5.
- [28] H. Ono, T. Katsumata, Interfacial reactions between thin rare-earth-metal oxide films and Si substrates, *Appl. Phys. Lett.* 78 (2001) 1832. doi:10.1063/1.1357445.
- [29] H. Ohashi, M.D. Alba, A.I. Becerro, P. Chain, A. Escudero, Structural study of the Lu<sub>2</sub>Si<sub>2</sub>O<sub>7</sub>–Sc<sub>2</sub>Si<sub>2</sub>O<sub>7</sub> system, *J. Phys. Chem. Solids.* 68 (2007) 464–469. doi:10.1016/j.jpcs.2006.12.025.
- [30] N. Rochat, A. Chabli, F. Bertin, C. Vergnaud, P. Mur, S. Petitdidier, et al., Infrared analysis of thin layers by attenuated total reflection spectroscopy, *Mater. Sci. Eng. B.* 102 (2003) 16–21. doi:10.1016/S0921-5107(02)00749-3.
- [31] T. Gougousi, M.J. Kelly, D.B. Terry, G.N. Parsons, Properties of La-silicate high-K dielectric films formed by oxidation of La on silicon, *J. Appl. Phys.* 93 (2003) 1691. doi:10.1063/1.1531818.
- [32] D. Dewulf, A. Hardy, S. Van Elshocht, C. De Dobbelaere, W.C. Wang, M. Badylevich, et al., Gadolinium -niobates and -tantalates: Amorphous High-k Materials by Aqueous CSD, *J. Electrochem. Soc.* 159 (2012) G75. doi:10.1149/2.072206jes.

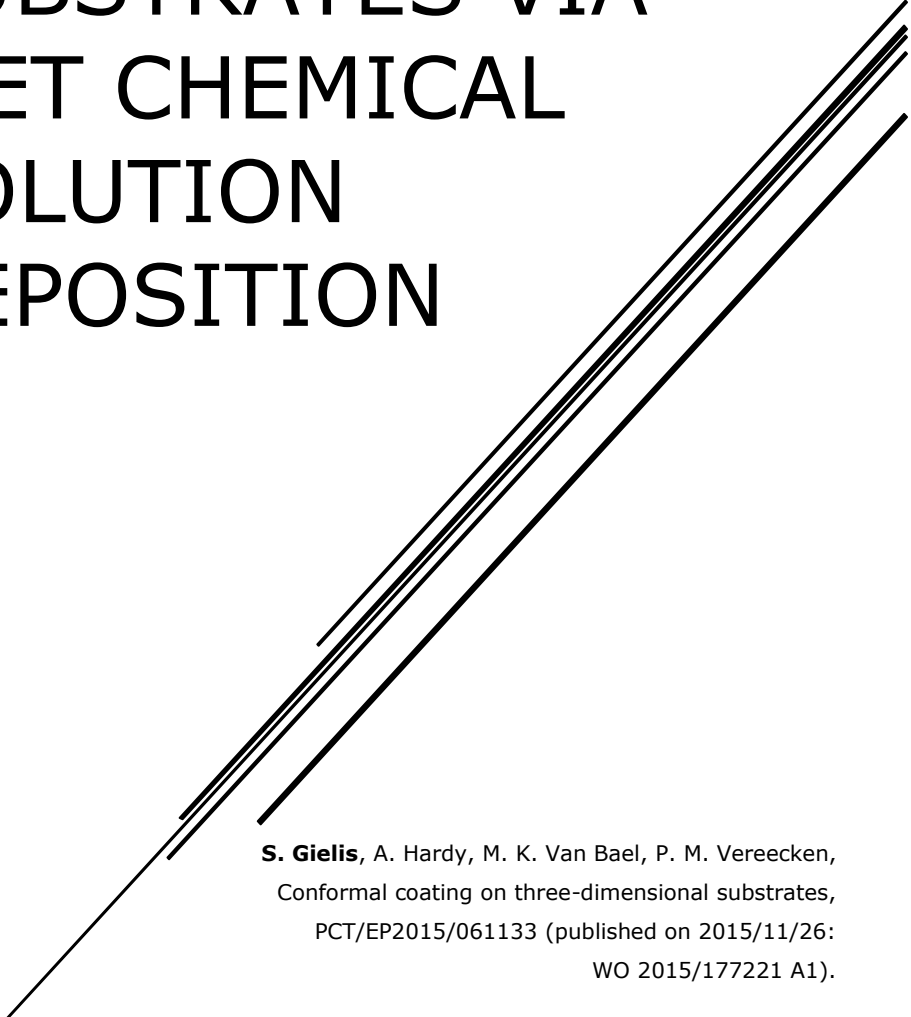
- [33] J.H. Kim, K.W. Chung, Microstructure and properties of silicon nitride thin films deposited by reactive bias magnetron sputtering, *J. Appl. Phys.* 83 (1998) 5831. doi:10.1063/1.367440.
- [34] E.A. Taft, Characterization of Silicon Nitride Films, *J. Electrochem. Soc.* 118 (1971) 1341. doi:10.1149/1.2408318.
- [35] JCPDS, Powder Diffraction File of Inorganic Phases, Joint Committee on Powder Diffraction Standards, Swarthmore, (1997).
- [36] N. Wada, S.A. Solin, J. Wong, S. Prochazka, Raman and IR absorption spectroscopic studies on alpha, beta and amorphous Si<sub>3</sub>N<sub>4</sub>, *J. Non. Cryst. Solids.* 43 (1981) 7–15. doi:10.1016/0022-3093(81)90169-1.
- [37] V. Tsu, G. Lucovsky, M.J. Mantini, Local atomic structure in thin films of silicon nitride and silicon diimide produced by remote plasma-enhanced chemical-vapor deposition, *Phys. Rev. B.* 33 (1986) 7069–7076. doi:10.1103/PhysRevB.33.7069.
- [38] K.O. Bugaev, A.A. Zelenina, V.A. Volodin, Vibrational Spectroscopy of Chemical Species in Silicon and Silicon-Rich Nitride Thin Films, *Int. J. Spectrosc.* 2012 (2012) 1–5. doi:10.1155/2012/281851.
- [39] A.N. Jansen, A.J. Kahaian, K.D. Kepler, P.A. Nelson, K. Amine, D.W. Dees, et al., Development of a high-power lithium-ion battery, *J. Power Sources.* 81-82 (1999) 902–905. doi:10.1016/S0378-7753(99)00268-2.
- [40] M. Hirayama, K. Kim, T. Toujigamori, W. Cho, R. Kanno, Epitaxial growth and electrochemical properties of Li<sub>4</sub>Ti<sub>5</sub>O<sub>12</sub> thin-film lithium battery anodes., *Dalt. Trans.* 40 (2011) 2882–2887. doi:10.1039/c0dt01477j.
- [41] A.S. Prakash, P. Manikandan, K. Ramesha, M. Sathiya, J.-M. Tarascon, A.K. Shukla, Solution-Combustion Synthesized Nanocrystalline Li<sub>4</sub>Ti<sub>5</sub>O<sub>12</sub> As High-Rate Performance Li-Ion Battery Anode, *Chem. Mater.* 22 (2010) 2857–2863. doi:10.1021/cm100071z.
- [42] J.F.M. Oudenhoven, L. Baggetto, P.H.L. Notten, All-Solid-State Lithium-Ion Microbatteries: A Review of Various Three-Dimensional Concepts, *Adv. Energy Mater.* 1 (2011) 10–33. doi:10.1002/aenm.201000002.
- [43] S.W. Han, J.H. Ryu, J. Jeong, D.H. Yoon, Solid-state synthesis of Li<sub>4</sub>Ti<sub>5</sub>O<sub>12</sub> for high power lithium ion battery applications, *J. Alloys Compd.* 570 (2013) 144–149. doi:10.1016/j.jallcom.2013.03.203.
- [44] C.H. Hong, A. Noviyanto, J.H. Ryu, J. Kim, D.H. Yoon, Effects of the starting materials and mechanochemical activation on the properties of solid-state reacted Li<sub>4</sub>Ti<sub>5</sub>O<sub>12</sub> for lithium ion batteries, *Ceram. Int.* 38 (2012) 301–310. doi:10.1016/j.ceramint.2011.07.007.

- [45] W. Zhang, J. Li, Y. Guan, Y. Jin, W. Zhu, X. Guo, et al., Nano-Li<sub>4</sub>Ti<sub>5</sub>O<sub>12</sub> with high rate performance synthesized by a glycerol assisted hydrothermal method, *J. Power Sources*. 243 (2013) 661–667. doi:10.1016/j.jpowsour.2013.06.010.
- [46] Z. Zhang, L. Cao, J. Huang, D. Wang, J. Wu, Y. Cai, Hydrothermal synthesis of Li<sub>4</sub>Ti<sub>5</sub>O<sub>12</sub> microsphere with high capacity as anode material for lithium ion batteries, *Ceram. Int.* 39 (2013) 2695–2698. doi:10.1016/j.ceramint.2012.09.036.
- [47] Y. Bai, F. Wang, F. Wu, C. Wu, L.Y. Bao, Influence of composite LiCl-KCl molten salt on microstructure and electrochemical performance of spinel Li<sub>4</sub>Ti<sub>5</sub>O<sub>12</sub>, *Electrochim. Acta.* 54 (2008) 322–327. doi:10.1016/j.electacta.2008.07.076.
- [48] V.D. Nithya, R. Kalai Selvan, K. VEDIAPPAN, S. Sharmila, C.W. Lee, Molten salt synthesis and characterization of Li<sub>4</sub>Ti<sub>5</sub>-xMnxO<sub>12</sub> (x=0.0, 0.05 and 0.1) as anodes for Li-ion batteries, *Appl. Surf. Sci.* 261 (2012) 515–519. doi:10.1016/j.apsusc.2012.08.047.
- [49] J. Deng, Z. Lu, I. Belharouak, K. Amine, C.Y. Chung, Preparation and electrochemical properties of Li<sub>4</sub>Ti<sub>5</sub>O<sub>12</sub> thin film electrodes by pulsed laser deposition, *J. Power Sources*. 193 (2009) 816–821. doi:10.1016/j.jpowsour.2009.03.074.
- [50] C.-L. Wang, Y.C. Liao, F.C. Hsu, N.H. Tai, M.K. Wu, Preparation and Characterization of Thin Film Li<sub>4</sub>Ti<sub>5</sub>O<sub>12</sub> Electrodes by Magnetron Sputtering, *J. Electrochem. Soc.* 152 (2005) A653. doi:10.1149/1.1861193.
- [51] Y.H. Rho, K. Kanamura, M. Fujisaki, J. Hamagami, S. Suda, T. Umegaki, Preparation of Li<sub>4</sub>Ti<sub>5</sub>O<sub>12</sub> and LiCoO<sub>2</sub> thin film electrodes from precursors obtained by sol – gel method, *Solid State Ionics*. 151 (2002) 151–157. doi:10.1016/S0167-2738(02)00594-5.
- [52] J. Mosa, J.F. Vélez, J.J. Reinoso, M. Aparicio, a. Yamaguchi, K. Tadanaga, et al., Li<sub>4</sub>Ti<sub>5</sub>O<sub>12</sub> thin-film electrodes by sol-gel for lithium-ion microbatteries, *J. Power Sources*. 244 (2013) 482–487. doi:10.1016/j.jpowsour.2012.11.037.
- [53] C. Zhang, Y. Zhang, J. Wang, D. Wang, D. He, Y. Xia, Li<sub>4</sub>Ti<sub>5</sub>O<sub>12</sub> prepared by a modified citric acid sol-gel method for lithium-ion battery, *J. Power Sources*. 236 (2013) 118–125. doi:10.1016/j.jpowsour.2013.01.135.
- [54] K. Van Werde, G. Vanhoyland, D. Nelis, D. Mondelaers, M.K. Van Bael, J. Mullens, et al., Phase formation of ferroelectric perovskite<sub>0.75</sub> Pb(Zn<sub>1/3</sub>,Nb<sub>2/3</sub>)O<sub>3</sub>-0.25BaTiO<sub>3</sub> prepared by aqueous solution-gel chemistry, *J. Mater. Chem.* 11 (2001) 1192–1197. doi:10.1039/B100209K.

- [55] A. Hardy, D. Mondelaers, M.K. Van Bael, J. Mullens, L.C. Van Poucke, G. Vanhoyland, et al., Synthesis of  $(\text{Bi},\text{La})_4\text{Ti}_3\text{O}_{12}$  by a new aqueous solution-gel route, *J. Eur. Ceram. Soc.* 24 (2004) 905–909. doi:10.1016/S0955-2219(03)00420-5.
- [56] A. Hardy, D. Mondelaers, G. Vanhoyland, M.K. Van Bael, J. Mullens, The Formation of Ferroelectric Bismuth Titanate ( $\text{Bi}_4\text{Ti}_3\text{O}_{12}$ ) from an Aqueous Metal-Chelate Gel, *J. Sol-Gel Sci. Technol.* 26 (2003) 1103–1107. doi:10.1023/A:1020762824990.
- [57] I. Truijen, M.K. Van Bael, H. Van Den Rul, J. D’Haen, J. Mullens, Synthesis of thin dense titania films via an aqueous solution-gel method, *J. Sol-Gel Sci. Technol.* 41 (2007) 43–48. doi:10.1007/s10971-006-0123-8.
- [58] A. Hardy, J. D’Haen, M.K. Bael, J. Mullens, An aqueous solution-gel citratoperoxo-Ti(IV) precursor: synthesis, gelation, thermo-oxidative decomposition and oxide crystallization, *J. Sol-Gel Sci. Technol.* 44 (2007) 65–74. doi:10.1007/s10971-007-1601-3.
- [59] W. Knaepen, C. Detavernier, R.L. Van Meirhaeghe, J. Jordan Sweet, C. Lavoie, In-situ X-ray Diffraction study of Metal Induced Crystallization of amorphous silicon, *Thin Solid Films.* 516 (2008) 4946–4952. doi:10.1016/j.tsf.2007.09.037.
- [60] W. Knaepen, S. Gaudet, C. Detavernier, R.L. Van Meirhaeghe, J.J. Sweet, C. Lavoie, In situ x-ray diffraction study of metal induced crystallization of amorphous germanium, *J. Appl. Phys.* 105 (2009) 083532. doi:10.1063/1.3110722.
- [61] S. Giangrandi, T. Sajavaara, B. Brijs, K. Arstila, a. Vantomme, W. Vandervorst, Low-energy heavy-ion TOF-ERDA setup for quantitative depth profiling of thin films, *Nucl. Instruments Methods Phys. Res. Sect. B Beam Interact. with Mater. Atoms.* 266 (2008) 5144–5150. doi:10.1016/j.nimb.2008.08.018.
- [62] F. Rosciano, P.P. Pescarmona, K. Houthoofd, A. Persoons, P. Bottke, M. Wilkening, Towards a lattice-matching solid-state battery: synthesis of a new class of lithium-ion conductors with the spinel structure., *Phys. Chem. Chem. Phys.* 15 (2013) 6107–12. doi:10.1039/c3cp50803j.
- [63] A. Hardy, S. Van Elshocht, C. Adelman, T. Conard, A. Franquet, O. Douhéret, et al., Aqueous solution-gel preparation of ultrathin  $\text{ZrO}_2$  films for gate dielectric application, *Thin Solid Films.* 516 (2008) 8343–8351. doi:10.1016/j.tsf.2008.04.017.
- [64] S. Van Elshocht, A. Hardy, C. Adelman, M. Caymax, T. Conard, A. Franquet, et al., Impact of Process Optimizations on the Electrical Performance of High-k Layers Deposited by Aqueous Chemical Solution Deposition, *J. Electrochem. Soc.* 155 (2008) G91. doi:10.1149/1.2840628.

- [65] A. Hardy, S. Van Elshocht, W. Knaepen, J. D'Haen, T. Conard, B. Brijs, et al., Crystallization resistance of barium titanate zirconate ultrathin films from aqueous CSD: a study of cause and effect, *J. Mater. Chem.* 19 (2009) 1115. doi:10.1039/b816856c.
- [66] H. Damm, P. Adriaensens, C. De Dobbelaere, B. Capon, K. Elen, J. Drijkoningen, et al., Factors Influencing the Conductivity of Aqueous Sol(ution)-Gel- Processed Al-Doped ZnO Films, *Chem. Mater.* 26 (2014) 5839–5851. doi:10.1021/cm501820a.
- [67] M.J. Mees, G. Pourtois, F. Rosciano, B. Put, P.M. Vereecken, A. Stesmans, First-principles material modeling of solid-state electrolytes with the spinel structure., *Phys. Chem. Chem. Phys.* 16 (2014) 5399–5406. doi:10.1039/c3cp54610a.

# III. COATING OF THREE- DIMENSIONAL SUBSTRATES VIA WET CHEMICAL SOLUTION DEPOSITION



**S. Gielis**, A. Hardy, M. K. Van Bael, P. M. Vereecken,  
Conformal coating on three-dimensional substrates,  
PCT/EP2015/061133 (published on 2015/11/26:  
WO 2015/177221 A1).

**S. Gielis** et al., A novel solution-based process for the deposition of  
(multi-)metal oxide coatings on high aspect ratio features,  
manuscript in preparation.



# 1 Introduction

As discussed in the first chapter, the second aim of this thesis is to evolve to a cheap, simple method that allows conformal coating of metal oxides on 3D substrates (Figure III-1). This could be used to develop the concept of 3D thin-film Li-ion batteries (and 3D thin-film capacitors), which are currently in an exploratory stage. Atomic layer deposition is generally seen as the ideal method for conformal coating of microstructured surfaces since it can deliver conformal high-quality coatings. However, a new chemical solution deposition process, which is characterized by low operation and equipment costs, a high throughput and large applicability, would give a strong impulse towards commercial 3D devices.

The development of such process was firstly done for  $\text{TiO}_2$  as model material. Besides the fact that this is mono-metal oxide, it has also interesting properties towards Li-ion batteries, as anode material.

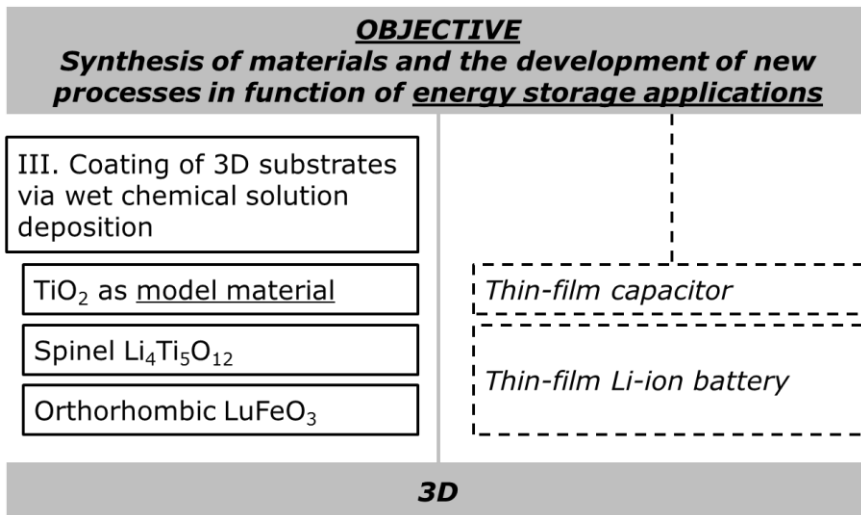


Figure III-1: Schematic representation of aim and the accompanying outline of the thesis, focusing on chapter III.

As three-dimensional substrate, etched silicon micropillars were used. These Si pillars, which were still in a development stage during the beginning of this research, were fabricated by imec. Consequently, in the beginning, various kinds of Si micropillars were used for this research: the shape as well as the dimensions of the pillars were varied. Thus one will consequently notice different kind of Si micropillars in the research results. However at the time that the process at imec was fully developed, a good candidate for three-dimensional coating via wet chemical deposition was found and further development could be done on a well-defined substrate, i.e. square arrays of Si micropillars. In view of the application, as substrate in a thin-film battery, the silicon micropillars were coated with a thin conductive layer of TiN (ca. 20 nm). This layer can be used as a current collector and acts as blocking layer for lithium.

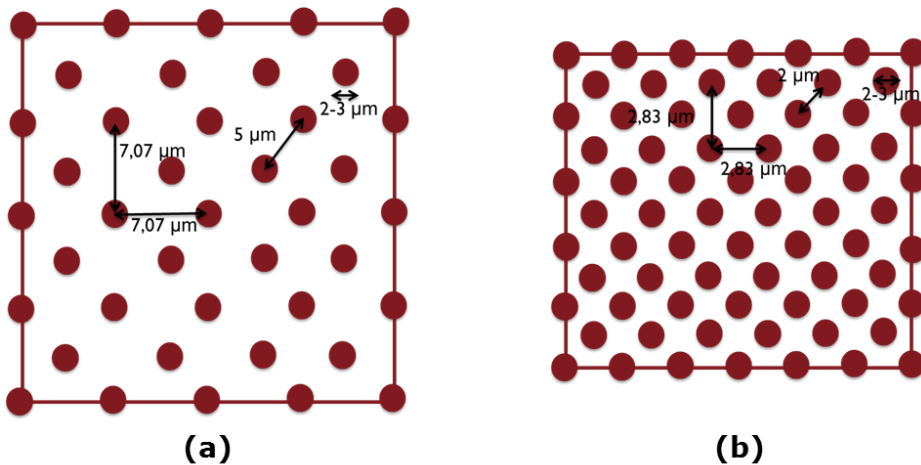


Figure III-2: Schematic representation of 2 X 5 and 2 X 2 Si micropillars.

During research two types of pillar arrays were used, in particular, 2 X 5 and 2 X 2 silicon micropillars. As can be seen in Figure III-2, these only differ in interpillar distance. Both arrays have pillars which are approximately 50 μm long and have a nominal diameter of 2 μm (ca. 1.85-2.85 μm dependent on the vertical position on the pillar). The only difference is thus that the pillars are separated, respectively, by 5 μm and 2 μm of interpillar distance. The aspect ratio of the silicon pillars, of which SEM images are shown in Figure III-3, is estimated to be around 22. As discussed before, deposition of active layers on 2 X 2 pillars should

lead to the highest possible capacity. However, the development of a new deposition process will be executed on 2 X 5 pillars. After that it might be transferred to 2 X 2 pillar arrays.

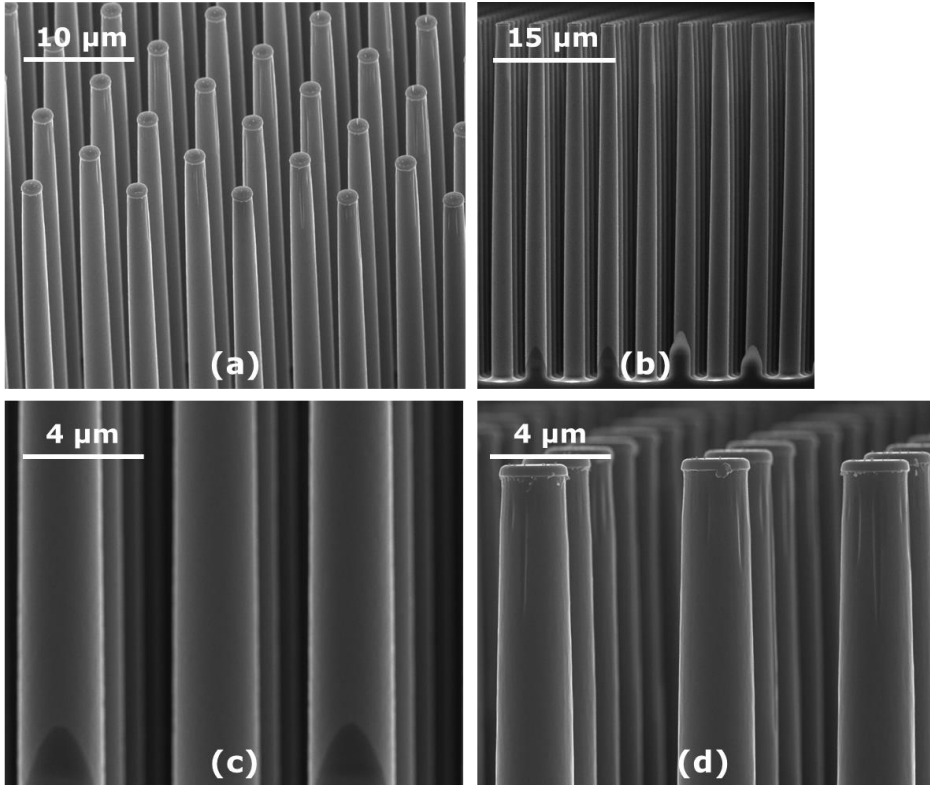


Figure III-3: SEM images of 2 X 5 Si micropillars with 20 nm TiN coating: (a) 45° tilted view, X-section view of, resp., (b) pillar overview, (c) the bottom and (d) top of the pillars.

## 2 Exploration of various methods

In literature, several chemical solution deposition methods can be found. As starting point, a couple of those techniques were selected and rapidly investigated.

### 2.1 Rapid screening of the state-of-the-art

#### 2.1.1 Liquid atomic layer deposition

Liquid atomic layer deposition (LALD) was used by Foong et al. to fabricate arrays of  $\text{TiO}_2$  nanotubes. A  $\text{TiO}_2$  layer was deposited on an anodized aluminum oxide template (substrate with holes acting as three-dimensional carrier) after which the template was removed so that nanotubes were released. This is schematically shown in Figure III-4. Interesting for this review, is the deposition of  $\text{TiO}_2$  on the nanostructured surface of AAO.

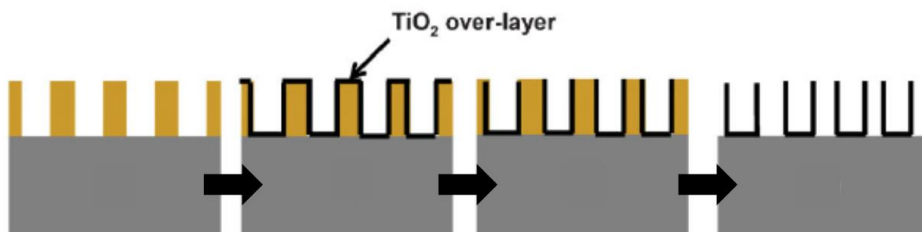


*Figure III-4: Schematic overview of the formation of  $\text{TiO}_2$  nanotubes via  $\text{TiO}_2$  deposition on anodized aluminum oxide (AAO) by liquid atomic layer deposition (LALD) and subsequent removal of the AAO template.[1]*

The used method, i.e. LALD, is similar to conventional gas-phase ALD. As can be seen in Figure III-5, it is a 4-step process that makes use of subsequent chemisorption and hydrolysis reactions. In practice, the substrate is first immersed in a bath of titanium(IV)isopropoxide (TIP) dissolved in toluene for a short time (step 1). A chemisorption reaction occurs between the substrate and the titanium alkoxide. Afterwards the sample is sonicated in isopropanol (IPA) to remove the unreacted species (step 2) where after it is put in a mixture of ethanol and water (ethanol:water = 0.9:0.1 by volume). Consequently, during this third step, the chemisorbed TIP is hydrolyzed to form titanium hydroxide on the

nanostructured surface. The addition of ethanol is necessary to decrease the surface tension so that the water can penetrate all the pore channels of the template. In the last step, the mixture of ethanol and water in the pores is removed by drying with a  $N_2$  flow and a heat treatment at  $90^\circ C$ . When the aforementioned steps are repeated, the titanium hydroxide layer will grow in thickness. When the intended thickness is obtained, (crystalline) titanium oxide can be formed by a post deposition anneal (PDA).[1]

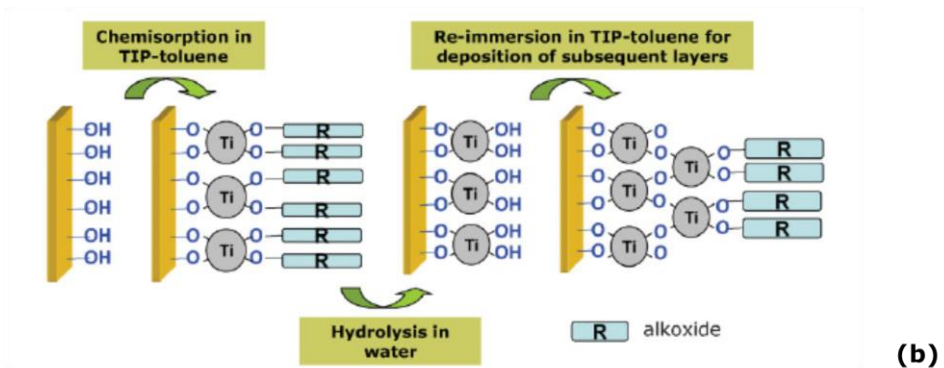
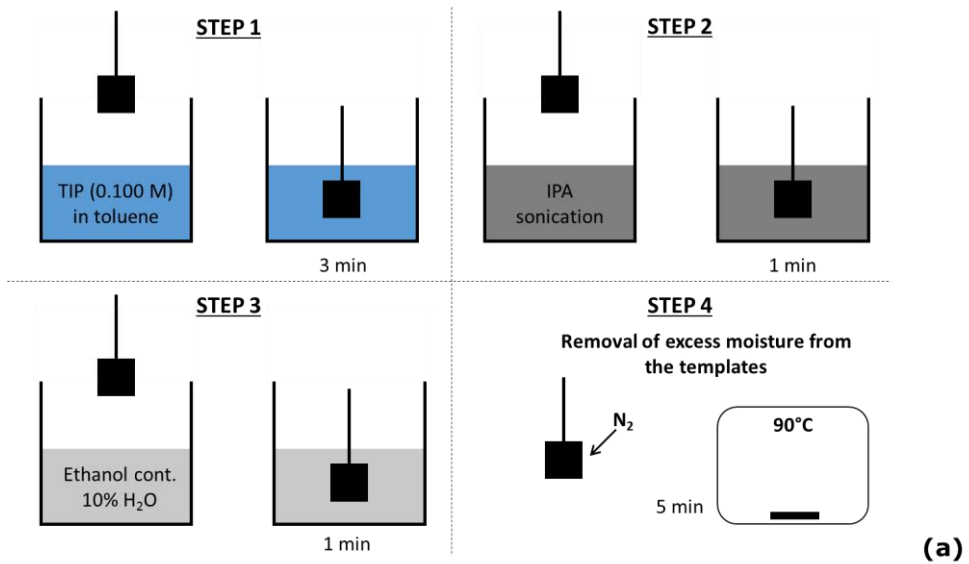


Figure III-5: Schematic representation of (a) the 4-step LALD cycle and (b) the chemisorption/hydrolysis mechanism behind LALD.[1]

This wet chemically method shows potential towards three-dimensional coating, however the toluene solution is very sensitive to (atmospheric) humidity. To avoid a spontaneous hydrolysis reaction and thus Ti hydroxide precipitation in the toluene solution, the process should be performed in a glovebox. This does not contribute to its potential operational simplicity. Furthermore the processing time of the technique is very long. It was reported by Foong et al. that LALD entails similar growth rates as conventional atomic layer deposition. Per cycle only 0.16-0.24 nm of titanium hydroxide is grown, so one can understand that for a 100 nm layer, 500 deposition cycles are necessary. Taking into account the time needed per cycle (ca. 15 minutes), it will take approximately 125 hours to achieve a thickness of 100 nm.

Guo et al. reported a similar process: they showed the deposition of  $\text{TiO}_2$  on a AAO template by layer-by-layer deposition, based on adsorption of charged ions.[2] However, because of the long deposition times, liquid atomic layer deposition cannot be considered as a candidate for 3D deposition.

### 2.1.2 Liquid phase deposition

Liquid phase deposition (LPD) is another reported method which is promising to coat 3D substrates. It allows the preparation of metal oxide or hydroxide films by simply immersing the substrate in a treatment solution. Since this method relies on the chemical equilibrium between a metal-fluoro complex, homogeneous thin films on various kinds of substrates with large areas and complex morphologies should be accessible. It is based on a good controllability of the hydrolysis reaction and of the supersaturation of the solution. A schematic overview of the method is presented by Lee et al. and shown in Figure III-6.[3]

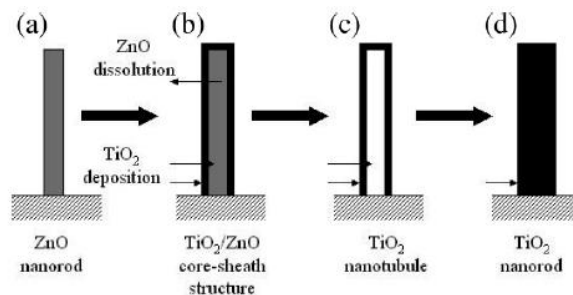
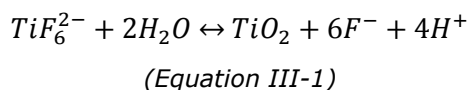


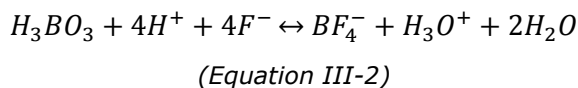
Figure III-6: Schematic overview of liquid phase deposition for the synthesis of  $\text{TiO}_2$  nanorods.[3]

TiO<sub>2</sub> is deposited along the ZnO nanorods by a mechanism which proceeds through two equilibrium reactions occurring at the same time.

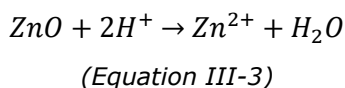
The ZnO nanorods are immersed in a solution of hexafluorotitanate (AHFT) and boric acid (1:1, 0.15 M) which initiates the reaction mechanism. The first reaction is the deposition of TiO<sub>2</sub> from the metal-fluoro complex ion, [TiF<sub>6</sub><sup>2-</sup>], which is presumed to proceed as:



The presence of boric acid in the treatment solution shifts this reaction to the right as it acts as an F<sup>-</sup> scavenger. H<sub>3</sub>BO<sub>3</sub> easily reacts with the fluorine anions to form the much more stable BF<sub>4</sub><sup>-</sup> complex:



The presence of boric acid leads to the consumption of non-coordinated F<sup>-</sup> ions and consequently the acceleration of the hydrolysis reaction. In this way the ZnO are covered with a thin layer of TiO<sub>2</sub> and the ZnO core-sheath structures of Figure III-6b are obtained. However the process also involves a second reaction which yields the formation of TiO<sub>2</sub> nanotubes (Figure III-6c). The formed HF also attacks the ZnO nanorods through:



Since these reactions are all initiated when the sample is added in the treatment solution, the dissolution of ZnO nanorods accompanies the deposition of TiO<sub>2</sub>. As can be derived from (Equation III-3), the dissolution behavior depends on the solution characteristics and in particular on the acidity of the mixed aqueous

solution. It is possible to tune the amount of ZnO that is etched away during the process. Lee et al. chose conditions so that the ZnO dissolution kinetics were faster than that of the TiO<sub>2</sub> deposition in the initial stage. In this way the ZnO nanorods were etched out completely and TiO<sub>2</sub> nanotubes could be formed (Figure III-6c). Then the void space, coming from the ZnO dissolution, was filled with TiO<sub>2</sub> by the diffusion of Ti-containing species in the LPD process at the same time. By maintaining the process, the space within the nanotube was gradually filled with TiO<sub>2</sub> and a nanorod was finally obtained (Figure III-6d). Lee et al. also claimed that this technique is applicable on other templates than ZnO, e.g. on NiO, MgO and CuO. Therefore liquid phase deposition can be considered as a potential candidate for the coating of three-dimensional substrates. Because of the direct reaction with the substrate, it would allow a conformal coating. The limiting factor is that only restricted substrates can be used. A quick screening shows that deposition can only be achieved on metal oxides. This is logic since the deposition mechanism is based on the dissolution of a metal oxide.

### 2.1.3 Alkoxide based solution-gel deposition

In literature, several reports about alkoxide sol-gel processes which could possibly be used to cover 3D structures via dip coating, such as ZnO nanorods, can be found.[4–7] As described earlier (Chapter I), the synthesis of alkoxide based sol-gel processes is based on the hydrolysis of metal oxides to form hydrolyzed monomers after which these are connected in a 3D network by condensation reactions.

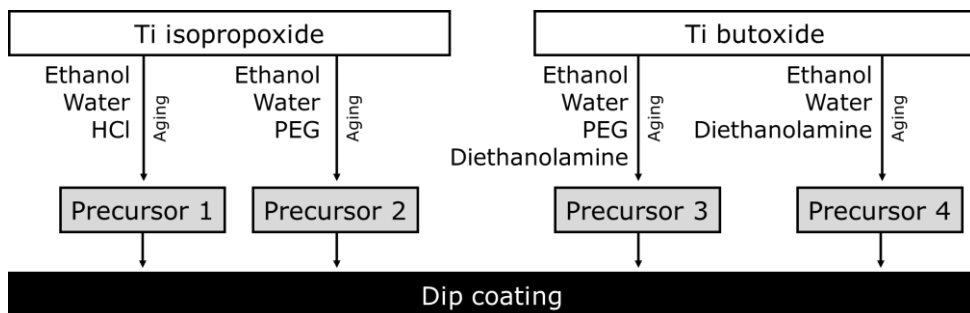


Figure III-7: Schematic representation of the synthesis and deposition of various alkoxide based sol-gel precursors.

Four different precursors and their accompanying precursor synthesis and deposition are schematically shown in Figure III-7 and fully described below.

### **2.1.3.1 Precursor 1**

For the procedure, described by Prabakar et al. [4], first titanium isopropoxide was slowly added to ethanol under stirring conditions so that the molar ratio was 1:52. This was immediately followed by the addition of water (TIP:ethanol:H<sub>2</sub>O = 1:52:5.6) which turned the solution into a milky white color. For accelerating the hydrolysis process, also hydrogen chloride was added in a 1:52:5.6:3.3 molar ratio. As a result the solution turned back into transparent. After 24h of aging, the solution was yellowish transparent and ready to be deposited on the silicon micropillars.

### **2.1.3.2 Precursor 2**

The second procedure is described by Qiu et al.[5] Titanium isopropoxide, water, ethanol and polyethylene glycol (PEG 2000) were mixed at a mole ratio of 1:3:20:0.03 at room temperature. After stirring for 2 hours, the TiO<sub>2</sub> sol was stored in a brown glass bottle and aged for 48 hours.

### **2.1.3.3 Precursor 3**

For another synthesis method, presented by Zhang et al. [6], titanium butoxide (Ti(OC<sub>4</sub>H<sub>9</sub>)<sub>4</sub>) was added together with diethanolamine (NH(OC<sub>2</sub>H<sub>5</sub>)<sub>2</sub>) to a mixture of water and ethanol so that a molar ratio of 1:1:1:1:26.5 was achieved. After stirring for 15 minutes, the light yellow solution was stored in a brown glass bottle to age for 5 days.

### **2.1.3.4 Precursor 4**

Qiu et al. described a fourth alkoxide based synthesis method.[7] Titanium butoxide (Ti(OC<sub>4</sub>H<sub>9</sub>)<sub>4</sub>) was dissolved in a solution of ethanol and diethanolamine (NH(OC<sub>2</sub>H<sub>5</sub>)<sub>2</sub>) so that the molar ratio was 1:23.6:1.2. After stirring for 2 hours, the solution was hydrolyzed by the addition of a solution of ethanol and water (total molar ratio Ti butoxide:ethanol:diethanolamine:water = 1:26.7:1.2:1). After 2 hours of stirring the Ti precursor was stored in a brown glass bottle to age for 24 hours.

Silicon micropillars were dip coated in the various sol-gel precursors, followed by a drying and anneal step to decompose the precursor, form the oxide, and crystallize the deposited material. None of the ascribed methods resulted in a significant deposition of  $\text{TiO}_2$  on the silicon micropillars. Hence, they don't meet the criteria for 3D deposition.

#### 2.1.4 Polymer complex controlled solution-gel deposition

Shaikumon et al. reported a method, which is based on a polymer complex controlled sol-gel process, which enables spray coating of  $\text{LiCoO}_2$  on Al nanorods using spray coating as a deposition method.[8]

For the preparation of the Li/Co sol-gel precursor (Figure III-8), the stoichiometric amount of lithium nitrate ( $\text{LiNO}_3$ ) and cobalt nitrate ( $\text{Li}(\text{NO}_3)_2$ ) were dissolved in water (Li:Co = 1:1) after which it was thoroughly mixed with ethylene glycol and citric acid in a 1:4 ratio. The precursor was then heated under stirring conditions for 6 hours at  $80^\circ\text{C}$  to form a transparent sol.[8]

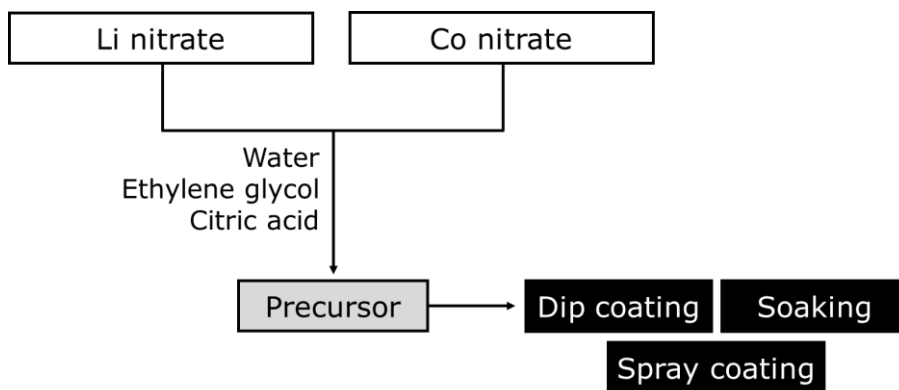


Figure III-8: Schematic representation of a polymer complex controlled sol-gel Li/Co precursor synthesis, proposed by Shaikumon et al., and the applied deposition methods.

A rapid screening of various deposition methods was performed. Dip coating of the precursor did not result in a uniform coating, only a minor part of the pillars was covered by material. Soaking of the pillars in the precursor resulted in deposition on only the lower part of the pillars. Finally, air brushing ( $\sim$  spray

coating with pressure nozzle) of the precursor on the silicon micropillars lead to some deposition, however as was also mentioned by Shaijumon et al.: the 3D structures are not completely covered by this method. The synthesized polymer complex controlled Li/Co precursor has thus large potential towards the deposition on 3D structures, preferentially via spray coating. Further steps are necessary to make the deposition more smooth and conformal.

## 2.2 Spray coating of TiO<sub>2</sub>

Since the aforementioned Li/Co precursor showed potential towards the coating of the Si micropillars, the nature of the precursor was used for the model material in this chapter, namely TiO<sub>2</sub>. The precursor is a polymer complex controlled solution, also known as a typical Pechini's precursor. A synthesis path of such precursor [9] from literature was used to coat the silicon micropillars with titanium oxide.

### 2.2.1 Experimental

The synthesis of the polymer controlled sol-gel titanium precursor was extensively reported by Ronconi et al. and schematically represented in Figure III-9.

The solution was prepared by heating ethylene glycol (C<sub>2</sub>H<sub>6</sub>O<sub>2</sub>, 99.8%, Sigma-Aldrich) to 60°C, followed by the addition of titanium isopropoxide (Ti(OiPr)<sub>4</sub>, 98+%, Acros Organics) under stirring so that the ethylene glycol:Ti molar ratio was 8:1. After that, citric acid (CA, C<sub>6</sub>H<sub>8</sub>O<sub>7</sub>, 99%, Sigma-Aldrich) was added (TIP:CA = 1:2) and the temperature was further increased to 90°C. The solution was kept overnight under reflux conditions.

As for the Li:Co precursor, multiple deposition methods were used to study the coating potential of the synthesized titanium precursor on silicon micropillars, both untreated as pre-cleaned with SPM/APM.[10] Dip coating (speed: 2 cm/min) and soaking (1h in 20 ml of precursor) were selected as deposition methods (Figure III-9). For spray coating the precursor was too viscous. After deposition, the pillars were heated for 10 min at 250°C (thermal shock) and 15 min at 525°C (thermal shock) in dry air. The deposited material was visualized by scanning electron microscopy (SEM, FEI, NOVA 200), in a tilted view (45°) mode.

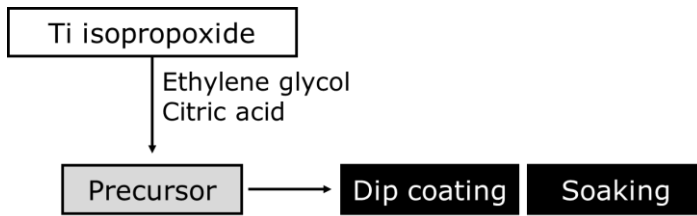


Figure III-9: Schematic representation of a polymer complex controlled sol-gel Ti precursor synthesis, proposed by Ronconi et al., and the applied deposition methods.

### 2.2.2 Results and discussion

Through the synthesis, a stable, clear, colorless Ti precursor was obtained. Dip coating of the pillars in the synthesized precursor and the subsequent anneal did lead to coating of the pillars, both for the untreated (Figure III-10a-b) and the pre-cleaned Si micropillars (Figure III-10c-d).

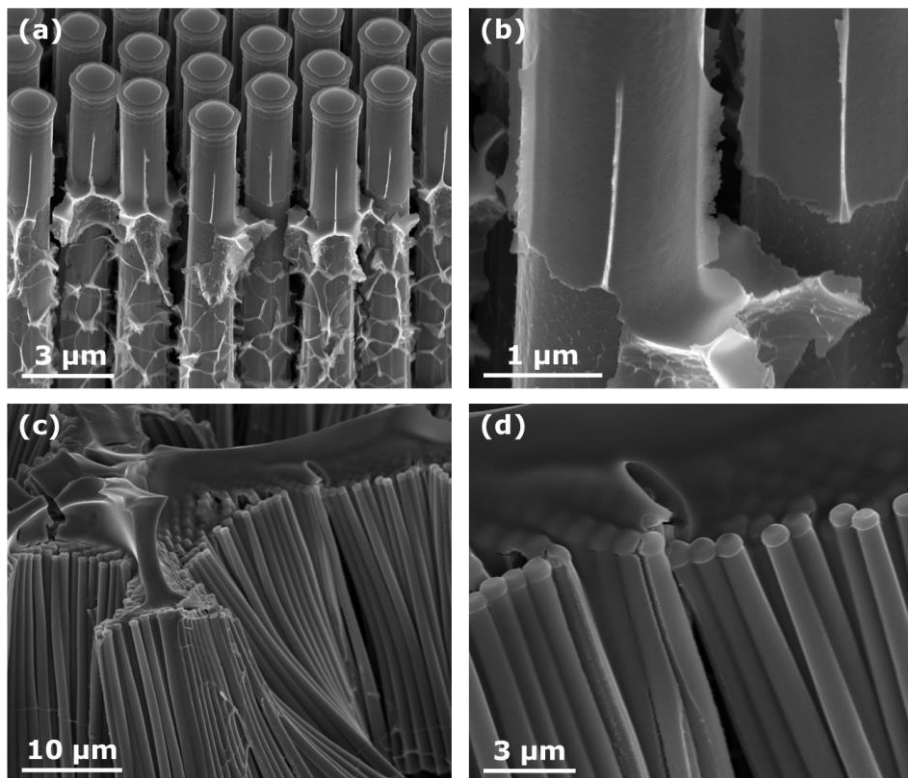


Figure III-10: SEM images of Si micropillars, (a-b) untreated and (c-d) pre-cleaned with SPM/APM after dip coating (2 cm/min) in the Ti sol-gel precursor and a subsequent anneal at 250°C and 525°C for, respectively, 10 and 15 min.

However, the deposition is neither conformal nor complete. Moreover the deposition process lead to the collapse of the silicon pillars. When soaking was tried, collapse of most of the pillars was also observed (Figure III-11). This was the not the case for the Li/Co precursor, so it has to be related to the precursors' differences. Besides the other nature of metal ions in the precursor, another important difference exists between the two systems. The Li/Co precursor consists of both ethylene glycol and water as solvent whereas the Ti precursor only consists of ethylene glycol. According to reported chemical data, this results in a ca. 32% decrease of the surface tension [11] which is expected to be beneficial for the deposition process. However, the absence of water in the Ti precursor results in a viscosity which is approximately 14 times higher (therefore spray coating was not possible). This increases the capillary force according to [12]:

$$\text{Capillary force} \sim \gamma \cos^2\theta$$

(Equation III-4)

with  $\gamma$  and  $\theta$ , respectively, the surface tension and the contact angle.

The capillary force thus directly depends on the surface tension. It seems that the decrease of surface tension for the Ti precursor thus results in a slight decrease of the capillary force. However, the other factor,  $\cos\theta$ , is also dependent on the surface tension. This term can be evaluated by Lucas-Washburn's equation for a capillary, since the pores between the micropillars can be defined as capillaries [13]:

$$\cos\theta = \frac{2 \eta x^2}{r \gamma t}$$

(Equation III-5)

with  $\theta$ ,  $\eta$ ,  $x$ ,  $r$ ,  $\gamma$  and  $t$ , respectively, the contact angle, viscosity, penetration depth, capillary radius (thus half of the interpillar distance), surface tension and the penetration time.

Since the penetration depth, capillary radius and penetration time are the same for the Li/Co and the Ti system, it is concluded that  $\cos \theta$  must be determined by the differences in viscosity and surface tension between the two systems.

The surface tension and viscosity of the Ti system are, respectively, approximately 32% lower and 14 times higher than that of the Li/Co system, thus resulting in a much higher  $\cos\theta$  for the Ti system. Since the capillary force is directly proportional to  $\cos^2\theta$ , it follows that the capillary force will be much higher for the Ti system. Due to this increased capillary force, it is much more likely that the silicon micropillars starts bending and eventually collapse.

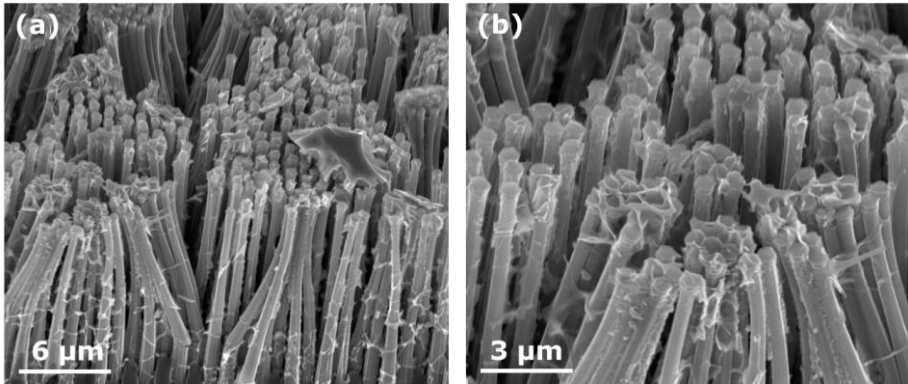


*Figure III-11: SEM images of Si micropillars, untreated, after soaking in 20 ml of the Ti sol-gel precursor for 1h and a subsequent anneal at 250°C and 525°C for, respectively, 10 and 15 min.*

### 3 Aqueous chemical solution deposition as “key” to 3D coating of multi-metal oxides

#### 3.1 Introduction

The discussion of various methods (and experimental results) in view of 3D deposition, presented in the previous section, is summarized in Table III-1. It shows that it is not easy to reach a complete coating of 3D structures via a wet chemically based method. However, very interesting and important information was gathered during these experiments: one should proceed to a process with lowered surface tension without further increasing the viscosity of the solution-gel precursor system. In this way, it would be more likely for the precursor to penetrate between the pillars. This knowledge was used to develop an aqueous chemical solution deposition process for 3D coating.

Process	+	-
Liquid atomic layer deposition [1,2]	Potential towards 3D deposition	Sensitive to humidity Long deposition times
Liquid phase deposition [3]	Potential towards 3D deposition	Restricted to metal oxide substrates
Alkoxide based solution-gel deposition [4-7]	/	No significant deposition on 3D
Polymer complex controlled solution-gel deposition (LiCoO <sub>2</sub> ) [8]	Potential of spray coating for 3D deposition	No complete coverage on 3D
Polymer complex controlled solution-gel deposition (TiO <sub>2</sub> ) [9]	Potential towards 3D deposition (due to lower surface tension)	Collapse of pillars due to high viscosity

Table III-1: Overview of various methods in view of 3D deposition

## 3.2 Optimization of the precursor for 3D deposition

### 3.2.1 Strategy

For the model material  $\text{TiO}_2$ , already an aqueous solution-gel system is available that delivers smooth, uniform coatings on planar substrates (via spin coating) as can be seen in Figure III-12.[14,15]

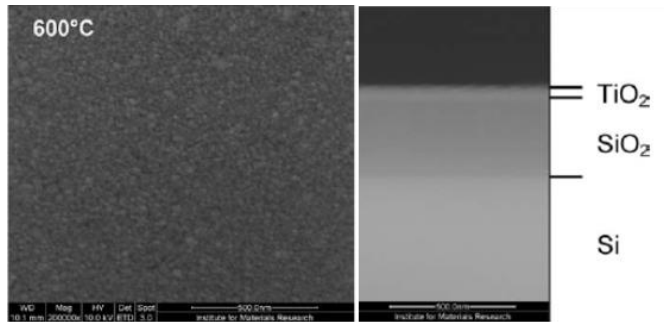


Figure III-12:  $\text{TiO}_2$  films (anatase and rutile) deposited by the aqueous titanium solution-gel precursor.[14]

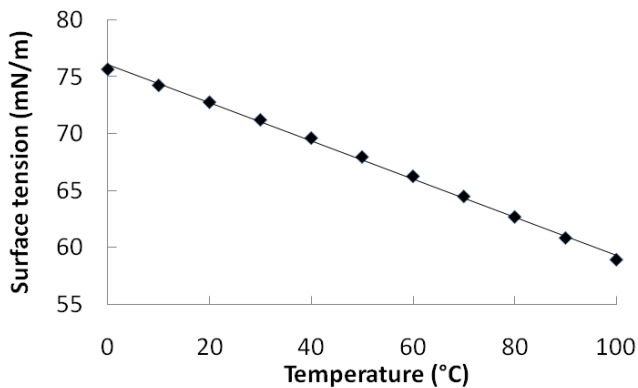


Figure III-13: Plot of the surface tension of water as a function of the temperature.[16]

However for the coating of three-dimensional substrates, the precursor synthesis and deposition technique needs some optimization. As basis, the aqueous titanium precursor was selected. Since it was shown before that lowering the surface tension while maintaining the viscosity of the precursor was one of the key factors, parameters that create such effect needed to be found.

Two main factors tend to influence the surface tension in a significant way. The first parameter is the temperature: from Figure III-13, it is shown that for water there is a linear relationship between the surface tension and the temperature. The higher the temperature, the lower the surface tension. Since the used precursor, consists of water as a solvent, one can understand that the deposition at higher temperature will result in a lower surface tension. The first option is thus to heat the precursor or substrate during the deposition process.

An even more drastic effect can be achieved by adding an alcohol, and in particular ethanol, to the precursor solution. In Figure III-14 the surface tension is represented as a function of the molar amount of ethanol in a water/ethanol mixture. A larger amount of ethanol results in lower surface tension of the system. Already a relative small amount of ethanol, added to water, reduces the surface tension largely. The second option is, consequently, adding ethanol to the precursor.

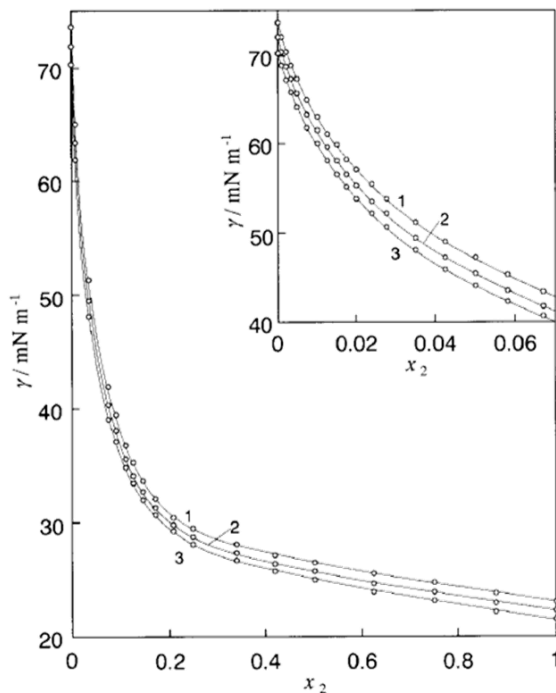


Figure III-14: Plot of the surface tension as a function of the mole fraction of ethanol added to water at constant temperature: (1) 15°C, (2) 25°C and (3) 35°C.[17]

The two described factors, i.e. the temperature and the addition of ethanol, could also be combined in order to strengthen the effect of surface tension decrease.

### 3.2.2 Experimental

As starting point, the aqueous titanium precursor, which was described earlier by Hardy et al. [15] and Truijen et al.[14], was selected. The precursor synthesis, which is schematically shown in Figure III-15 (first part), starts with liquid Ti(IV)isopropoxide ( $\text{Ti}(\text{OiPr})_4$ , Acros organics, 98+%). The appropriate amount of Ti(IV)isopropoxide to obtain a 0.730 mol/l solution was added to a tenfold volume of water, leading to immediate hydrolysis and condensation and finally to the formation of a white precipitate. This precipitate was filtered and washed with water. The hydrolysis product was processed quickly in order to avoid it becoming insoluble. In a next step, a mixture of citric acid (CA,  $\text{C}_6\text{H}_8\text{O}_7$ , Sigma-Aldrich, 99%, 1 mol/l) and hydrogen peroxide ( $\text{H}_2\text{O}_2$ , stabilized, Acros, 35% p.a aqueous solution) were added to the fresh, wet precipitate, both in a molar ratio of 2:1 so that the molar ratio  $\text{Ti}^{4+}:\text{CA}:\text{H}_2\text{O}_2$  was 1:2:1.2.

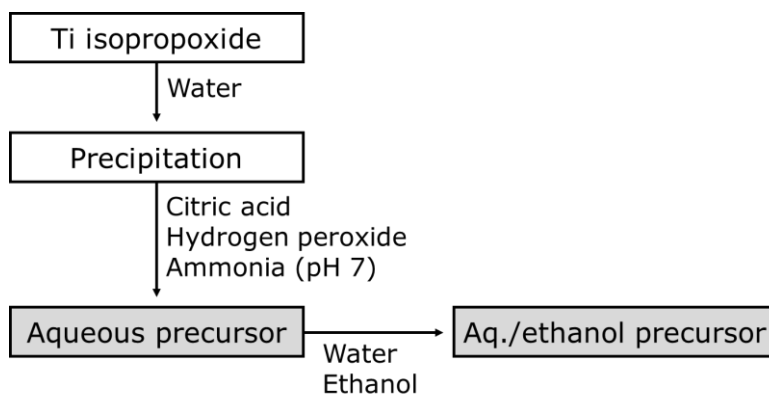


Figure III-15: Schematic representation of the synthesis of the aqueous/ethanol Ti precursor.

The mixture was then stirred at 80°C, which after a short time yielded a clear, burgundy colored solution, with a pH of about 1. The solution was cooled to room temperature. During the third step, ammonia ( $\text{NH}_3$ , Merck, 32% aqueous solution, extra pure) was added dropwise to the hot solution in order to increase the pH (pH electrode, WTW inoLab 740 with Sentix 81 electrode Schott Geräte). This was accompanied by intense gas evolution and an increase of the solution's

temperature. The solution was then again cooled to room temperature and its pH was adjusted to 7. During the third step, the solution's color changed from burgundy (pH = 1) to yellow-orange (pH = 7).

The synthesized aqueous titanium precursor was then further diluted with water and to obtain a lower surface tension, optionally, ethanol was added so that the  $Ti^{4+}$  concentration and the volumetric ethanol:water ratio were, respectively, 0.05 M and 0:1, 0.5:1, 0.9:1, 1.5:1, 2:1 or 4:1 (Figure III-15 part 2).

### 3.2.3 Results and discussion

Because it is known that the addition of an alcohol can result in precipitation of metal ions, the stability of the aqueous Ti precursor was checked upon the addition of ethanol. Various ethanol:water volumetric ratios were investigated as can be seen in Table III-2. It is found that an ethanol:water ratio below or equal to 1.5 did not result in precipitation and, consequently, could be used. A volumetric ratio of 2:1 or higher did result in precipitation, thus those systems cannot be used.

<b>Ethanol:water volumetric ratio</b>	<b>Precipitation?</b>
0:1	No
0.5:1	No
0.9:1	No
1.5:1	No
2:1	Yes
4:1	Yes

*Table III-2: Stability of the aqueous Ti precursor upon addition of ethanol.*

Based on these results, an ethanol:water ratio of 0.9:1 was selected as standard ratio. This corresponds to a molar ethanol:water ratio of 0.28:1 which already entails a drastic decrease in surface tension for the system (Figure III-14). The addition of a larger amount of ethanol would lead to an even more decrease. However, this is not significant compared to the amount of ethanol that has to be added to achieve this.

### 3.3 First steps towards aqueous based 3D deposition

#### 3.3.1 Experimental

Prior to deposition, the silicon micropillars were cleaned. In order to remove the SiO<sub>2</sub> cap which was present on this set of pillars and is likely to hinder the deposition process, the micropillars were dipped in an HF (4 vol%) solution. After that an optional SPM/APM cleaning was performed to improve the wetting for aqueous based solutions.[10] The synthesized aqueous and aqueous/ethanol titanium precursor were deposited on the silicon micropillars via drop casting so that the substrate was completely covered. This coating process was performed at room temperature and at 80°C. After deposition, the substrate was rinsed with water and a 2 min anneal on hot plates at 180°C, 300°C and 600°C was applied.

The deposited material was visualized by scanning electron microscopy (SEM, FEI, NOVA 200), in a tilted view (45°) mode and the composition was checked by energy-dispersive X-ray spectroscopy (SEM-EDX, FEI, Quanta 200).

#### 3.3.2 Results and discussion

During the deposition process of the aqueous or aqueous/ethanol titanium precursor via drop casting, typically a gel as shown in Figure III-16, is formed on the substrate of silicon micropillars. Therefore, to remove the excess of precursor, the substrates were rinsed with water prior to the annealing process. After annealing, the samples were evaluated by means of SEM.

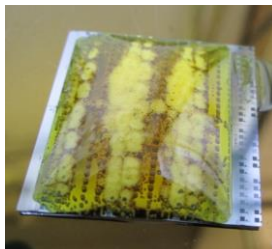


*Figure III-16: Typical gel formation of the aqueous/ethanol Ti precursor on a 2X2 cm substrate of Si micropillars during drop casting. The small squares are the areas containing silicon micropillars.*

When the aqueous Ti precursor (without ethanol) was drop casted on the silicon micropillars, followed by the rinse process and annealing till 600°C, one could notice from Figure III-17 that none or only few deposition is found on the silicon pillars. No considerable difference could be found between drop casting on HF cleaned (Figure III-17a, c) or SPM/APM cleaned (Figure III-17b, d) Si pillars. Also the deposition temperature, in particular room temperature (Figure III-17a, b) and 80°C (Figure III-17c, d) seemed not to influence the results.

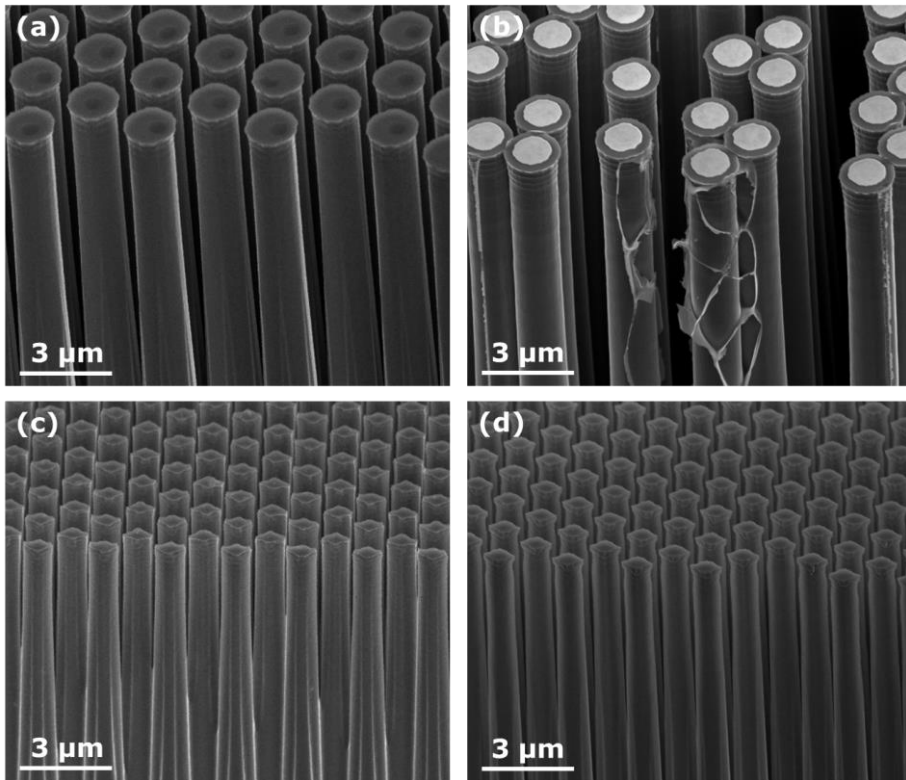


Figure III-17: SEM images of Si micropillars which were pre-treated with (a, c) HF and (b, d) HF, followed by SPM/APM, after drop casting with the aqueous Ti precursor at (a, b) room temperature and (c, d) 80°C, followed by rinsing and a 2 min anneal on hot plates at 180°C, 300°C and 600°C.

However an interesting observation was found when drop casting the aqueous/ethanol titanium precursor on the silicon micropillars. Figure III-18a shows a coating after drop casting at room temperature and annealing till 600°C for HF cleaned pillars, however complete coating of the pillars was not achieved.

In the case of SPM/APM cleaned pillars, there is less coating present (Figure III-18b). When the drop casting process was performed at elevated temperature, particularly 80°C, it is striking that the morphology of the silicon pillars, which were cleaned with HF, is highly different compared to the morphology before deposition (Figure III-18c). This could indicate TiO<sub>2</sub> deposition along the pillars, the phenomenon was not observed for the pillars which got an extra clean in SPM/APM to improve the wetting (Figure III-18d).

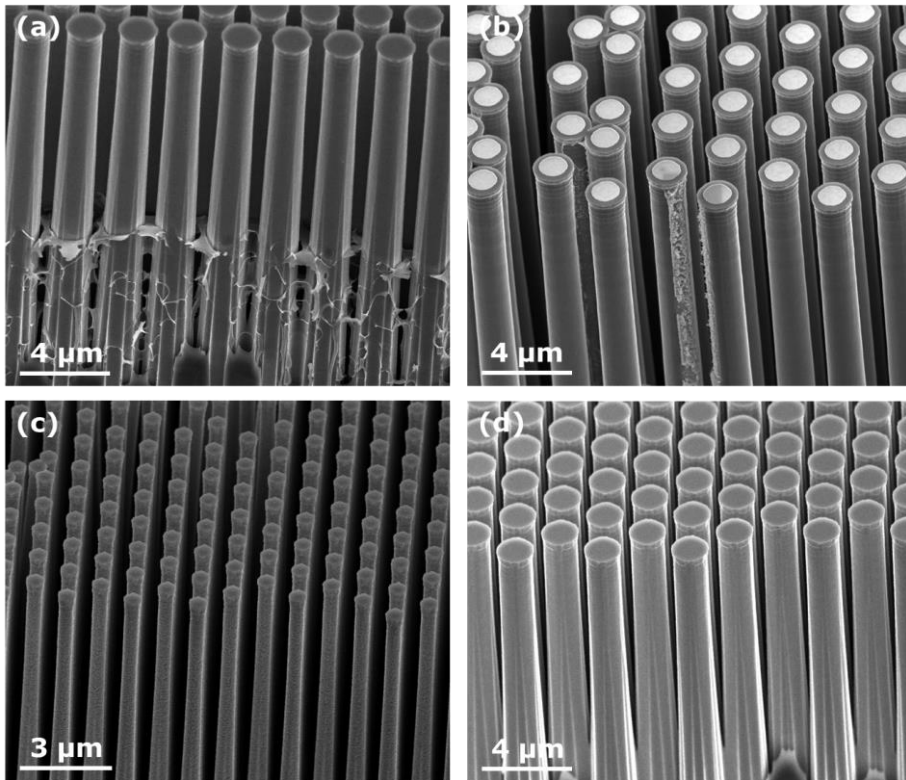


Figure III-18: SEM images of Si micropillars which were pre-treated with (a, c) HF and (b, d) SPM/APM, followed by drop casting with the aqueous/ethanol Ti precursor at (a, b) room temperature and (c, d) 80°C, followed by rinsing and a 2 min anneal on hot plates at 180°C, 300°C and 600°C.

The morphology change in the case of HF cleaned pillars after drop casting and subsequent annealing is much clearer in the magnified SEM images in Figure III-19. In Figure III-19b, the HF clean was not as effective as in Figure III-19a so that a part of the (white) SiO<sub>2</sub> cap was not removed. This cap seemed unaffected

after the drop casting and annealing process, suggesting that the morphology change along the pillars is not related to deposition. Probably, a reaction of the precursor with the surface occurs during the drop casting process.

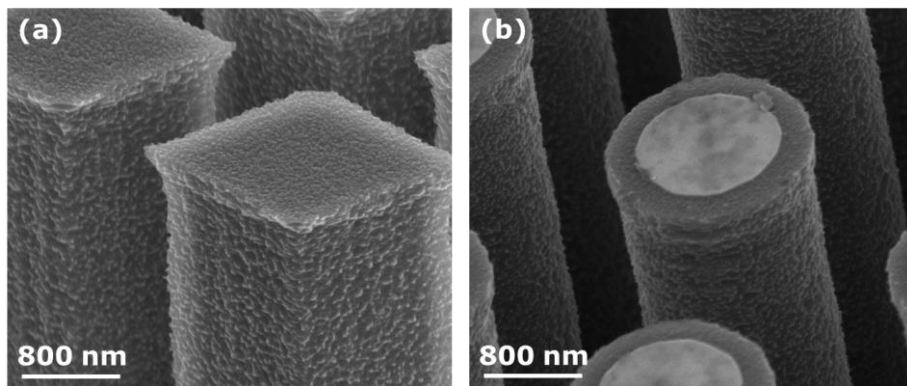


Figure III-19: SEM images of (a, b) Si micropillars, which were pre-treated with HF, after drop casting with the aqueous/ethanol Ti precursor at 80°C, followed by rinsing and a 2 min anneal on hot plates at 180°C, 300°C and 600°C.

The origin of the morphology change was further investigated by an EDX/SEM analysis. In Figure III-20a the EDX/SEM analysis of bare silicon pillars after drop casting and annealing is shown. Obviously, the silicon peak (related to the substrate) is present in the spectrum. Also an oxygen signal, probably originating from native SiO<sub>2</sub> (grown in ambient) and a carbon signal are present. The positions of titanium are, for convenience, shown in the spectrum, but none of them could be detected, meaning that the change in morphology cannot be attributed to titania deposition. For the SiO<sub>2</sub> cap, after drop casting and annealing, the results are identical, as can be deduced from the SEM/EDX analysis in Figure III-20b.

It is striking that, besides the reaction of the precursor with the silicon surface, almost no deposited material is present on the micropillars after drop casting (Figure III-18). This is probably caused by the rinsing step after the deposition process, removing the deposited species. When the washing step is left out of the process, there is material present between the pillars, as can be seen in Figure III-21. However, one could notice that the pillars are far from being completely covered by the process.



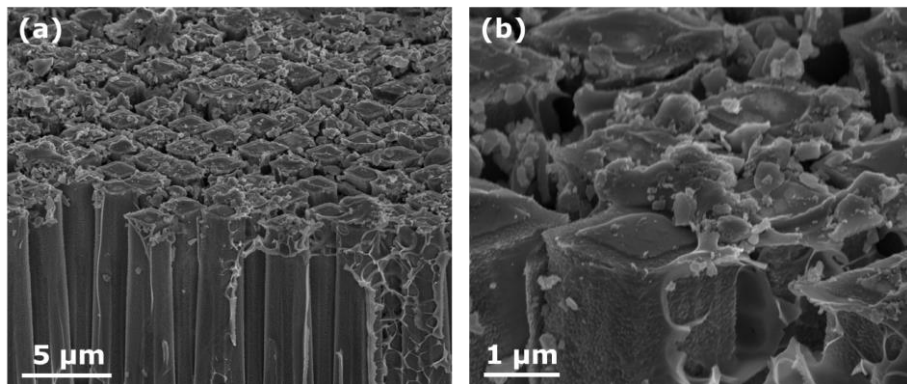


Figure III-21: SEM images of (a, b) Si micropillars, which were pre-treated with HF, after drop casting with the aqueous/ethanol Ti precursor at 80°C, followed by a 2 min anneal on hot plates at 180°C, 300°C and 600°C.

### 3.4 3D deposition via spray coating

#### 3.4.1 Strategy

The previous section showed that some deposition can be achieved via the use of the aqueous/ethanol titanium precursor. However complete coverage could not be achieved yet. The lack of complete coating can probably be attributed to the deposition technique, i.e. drop casting, which seems to be another important factor apart from the optimized precursor synthesis. Because of the high potential of the precursor, spray coating was applied. It was shown for LiCoO<sub>2</sub> that more decent coatings could be achieved via this technique. As was discussed in Chapter I, many parameters influence this technique. It starts with the type of nozzle that is used: an ultrasonic nozzle is favored to a pressure nozzle, e.g. air brushing. The ultrasonic nozzle is more reliable and has more possibilities towards tuning of the process. It means that it will also result in a larger coating efficiency. Many parameters tend to influence the quality of the coating. Therefore, a thorough study needed to be performed in order to evolve to a complete coverage of the silicon micropillars.

Since the new batch of Si pillars [18] did not have a SiO<sub>2</sub> cap, the removing step (HF clean) was not necessary anymore. It was also decided to move to a dry cleaning method to improve the wetting, i.e. the UV/O<sub>3</sub> cleaning. This pre-treatment method also entails a good wetting of the substrate.[19] It must also

be noted that the new batch contained pillars which were covered by a conductive layer, i.e. 20 nm of TiN, necessary to evaluate the electrochemical behavior.

### 3.4.2 Experimental

The optimized aqueous/ethanol Ti precursor was used.

Prior to the deposition process, to allow a good wetting, the silicon micropillars, covered with 20 nm of TiN, were pretreated in an UV/O<sub>3</sub> environment at 60°C for 30 minutes.[19]

Deposition was performed in an ExactaCoat Ultrasonic Coating system of Sono-Tek Corporation in combination with an 120 kHz AccuMist Precision Ultrasonic Spray Nozzle, set at 1.5 psi.[20] As an illustration, a photograph of the tool can be seen in Figure III-22.

A multiple pass process, in which the nozzle produces a very narrow spray while moving over the substrate in X, Y direction for multiple times, was applied. During spray coating, the sample was heated via a hot plate, which is built in the device. Various spray coating parameters were varied and thus investigated during the process, i.e. the deposition temperature, flow rate, path velocity, nozzle distance, the amount of passes and precursor concentration.



*Figure III-22: Photograph of an ExactaCoat Ultrasonic Coating system of Sono-Tek Corporation in combination with an AccuMist Precision Ultrasonic Spray Nozzle.[20]*

After the deposition process, an optional anneal was applied. This was performed on hot plates (2' at 300°C, 1h at 450°C, 500°C, 550°C or 600°C) or in a furnace (thermal shock in dry air - 100 ml min<sup>-1</sup>, 1h at 650°C).

The deposited films were evaluated by means of scanning electron microscopy (SEM, FEI, NOVA 200), respectively, in a tilted view (45°) and cross-section view (90°). To check the crystallization, Raman spectra were acquired at room temperature using a Jobin-Yvon T64000 system.

The electrochemical performance of the deposition was evaluated by means of cyclic voltammetry (scan rate: 10 mV/s) using a three-electrode cell with 1M LiClO<sub>4</sub> in propylene carbonate as electrolyte, making a back contact with GaIn. The whole was connected to a Autolab PGSTAT 100 potentiostat, placed in a glove-box (O<sub>2</sub><1ppm) at room temperature. These measurements were performed by Moitzheim et al. (imec).

### 3.4.3 Results and discussion

#### 3.4.3.1 Proof of coating and effect of deposition temperature

Firstly, the deposition temperature during spray coating was investigated. The substrate temperature was varied between 110°C and 250°C while spray coating the aqueous/ethanol titanium precursor. In Table III-3 all spray coat parameters of the experiment are listed.

Parameter	Set point
Temperature (°C)	110-250
Flow rate (ml/min)	0.20
Path velocity (mm/s)	100
Nozzle distance (mm)	36
# passes	5-10
Ti <sup>4+</sup> concentration (mM)	50

Table III-3: Overview of the spray coat parameters to investigate the effect of the temperature on the coating behavior.

From macroscopic evaluation, it follows that a temperature higher than 150°C was necessary. Spray coating at 110°C and 150°C did result in a film which had obvious signs of non-conformality: clear spots of material accumulation could be

observed. This is probably linked to the coffee stain effect. For temperatures of 180°C and up, the resulting depositions seemed uniform, by macroscopic point of view. Consequently, these coatings were further microscopically evaluated by means of (X-)SEM. After spraying five passes on TiN coated Si micropillars at 250°C, which were pre-treated by UV/O<sub>3</sub>, one could observe that the pillars were covered by the precursor which was already transformed to a gel (Figure III-23). The main part of each pillar deposition was coated (Figure III-23). However it is also striking that the precursor could not reach the bottom of the pillars, and in particular the bottommost 5-6 µm.

When increasing the amount of passes to 10, one could expect a thicker layer of deposition and possibly some deeper coverage along the silicon micropillars. Figure III-24 seems to confirm this hypothesis: qualitatively a thicker layer and deposition till the last 4-5 µm along the pillars could be observed. Nevertheless the pillars were not completely covered by spray coating the titanium precursor on the pillars at 250°C.

By lowering the deposition temperature to 180°C, one can notice in the SEM images in Figure III-25 that almost the complete pillars were covered with the Ti precursor after 5 passes of spray coating. Only a small bottom part of the pillars did seem to be blank.

When increasing the amount of passes to 10, a thicker layer of deposition could be obtained. Moreover complete coverage of the silicon pillars by the Ti precursor (gel) was reported. These observations can be deduced from Figure III-26.

From the experimental results, it is clear that 180°C seems to be the optimal temperature for the deposition of TiO<sub>2</sub> on silicon pillars via spray coating. Slightly lowering the temperature to 170°C also gives completely coated pillars, however when studying the SEM images in Figure III-27, one can state that the achieved layer on the pillars is less conformal, and moreover contains more artefacts compared to spraying at 180°C. Consequently, this temperature is set as the optimal temperature for the spray coating process.

The question is now of course: “how does this work”? To allow an answer, one could spend a PhD on it, but at least here some ideas are presented. The droplet size of the system is known. Since a 120 kHz nozzle was used during spray coating, from the plot of droplet size distribution for water in Figure I-26 typically 20-40  $\mu\text{m}$  droplets are formed. As was stated in Chapter I, the equations regarding the droplet size distribution, are [21]:

$$D_{N,0.5} = 0.34 \lambda_L$$

(Equation III-6)

with  $D_{N,0.5}$  and  $\lambda_L$ , respectively, the number median diameter of droplet size and the wavelength in the liquid.

The latter can be calculated via [21]:

$$\lambda_L = \left( \frac{8\pi \theta}{\rho f^2} \right)^{1/3}$$

(Equation III-7)

with  $\theta$ ,  $\rho$  and  $f$ , respectively, the surface tension, density and nozzle frequency.

The Ti precursor which was spray coated on the silicon micropillars contains an amount of ethanol which results in a drastic decrease of the surface tension (Figure III-14). Furthermore its density will definitely be higher. Therefore from the equations above, it is believed that the droplet size will a bit lower, however it will be still in the  $\mu\text{m}$ -range. This means that in order to allow droplets to penetrate between the micropillars, there should be another droplet size reducing effect. The hypothesis is that because of the elevated substrate temperature, i.e. 180°C-250°C, the drying process of the precursor is already induced before the spray touches the surface. Therefore, the size of the droplets in the spray will be become smaller. This is in agreement with Figure I-28a, which indicates that an increasing deposition temperature will lead to droplet downsizing before touching the substrate.[22] Consequently, during the process, the solution is instantly transformed into a gel, consisting of coordinated complexes in which the Ti ions are immobilized. Moreover, because of the elevated temperature, this gel is already partly decomposed during the spray coat process.

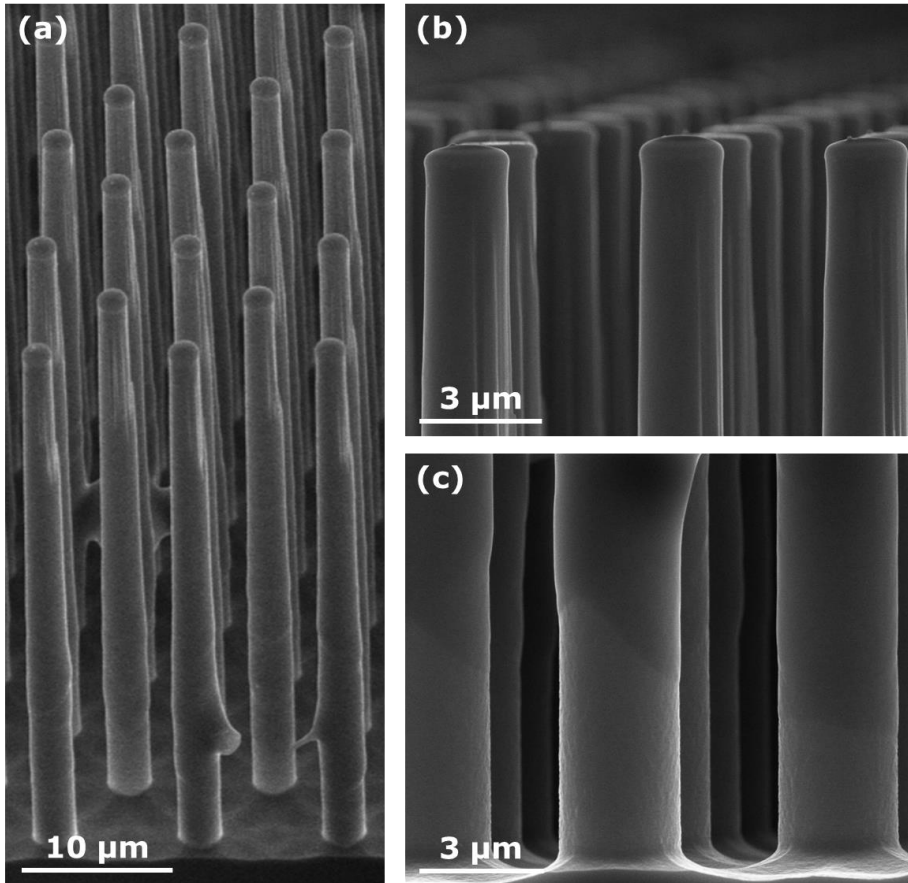


Figure III-23: SEM images of TiN coated Si micropillars, which were pre-treated by UV/O<sub>3</sub>, after spray coating (5 passes) with the aqueous/ethanol Ti precursor at 250°C. The flow rate, path velocity, nozzle distance and Ti<sup>4+</sup> concentration were, respectively, 0.20 ml/min, 100 mm/s, 36 mm and 50 mM.

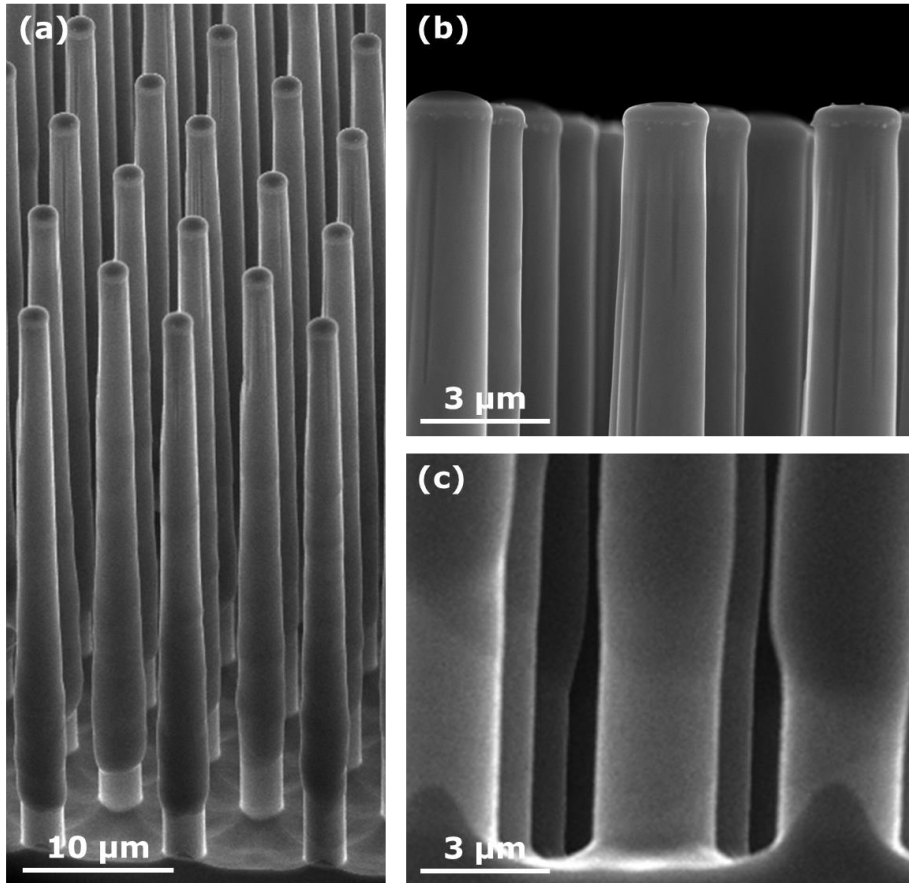


Figure III-24: SEM images of TiN coated Si micropillars, which were pre-treated by UV/O<sub>3</sub>, after spray coating (10 passes) with the aqueous/ethanol Ti precursor at 250°C. The flow rate, path velocity, nozzle distance and Ti<sup>4+</sup> concentration were, respectively, 0.20 ml/min, 100 mm/s, 36 mm and 50 mM.

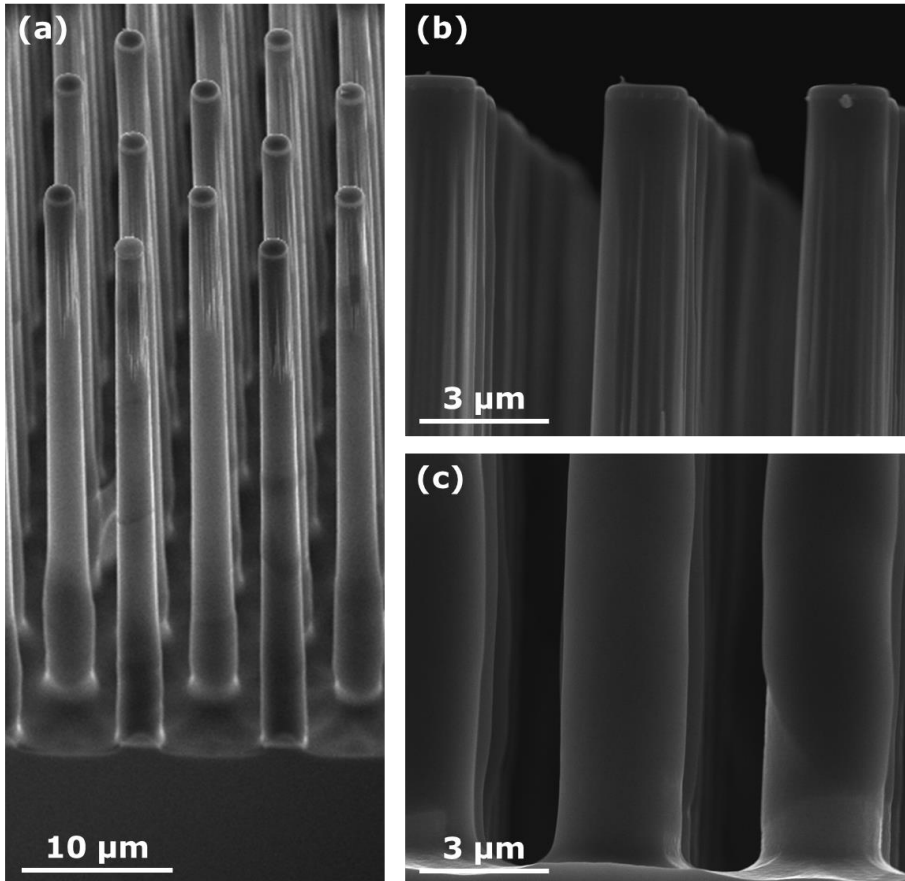


Figure III-25: SEM images of TiN coated Si micropillars, which were pre-treated by UV/O<sub>3</sub>, after spray coating (5 passes) with the aqueous/ethanol Ti precursor at 180°C. The flow rate, path velocity, nozzle distance and Ti<sup>4+</sup> concentration were, respectively, 0.20 ml/min, 100 mm/s, 36 mm and 50 mM.

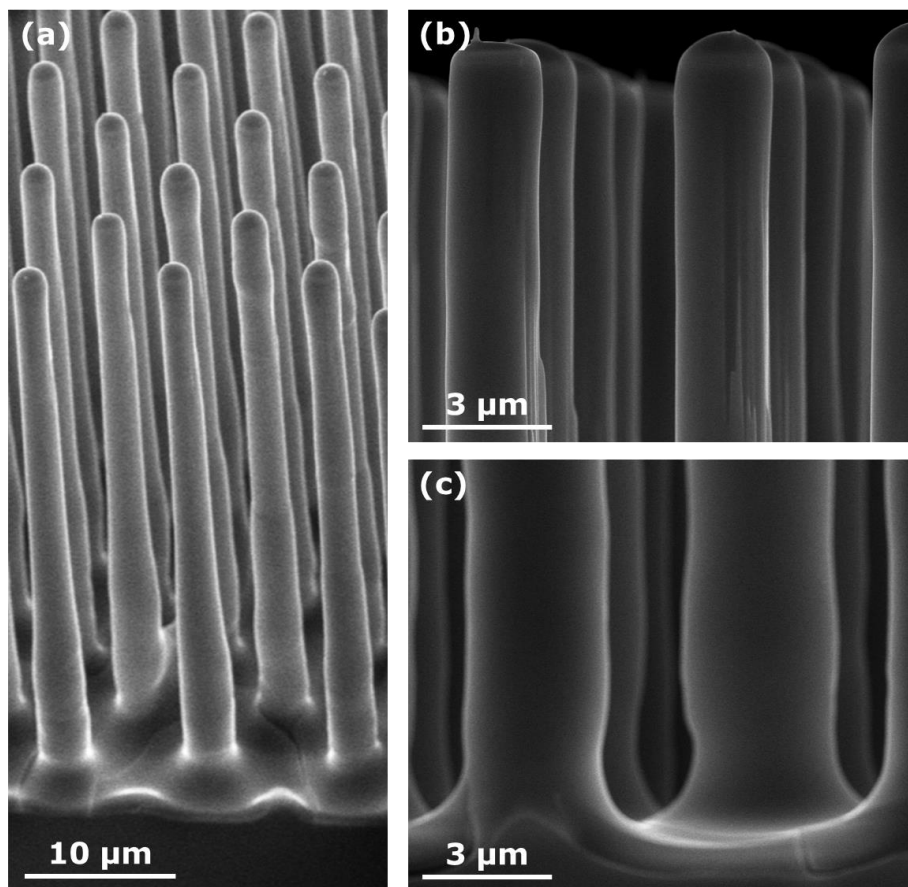


Figure III-26: SEM images of TiN coated Si micropillars, which were pre-treated by UV/O<sub>3</sub>, after spray coating (10 passes) with the aqueous/ethanol Ti precursor at 180°C. The flow rate, path velocity, nozzle distance and Ti<sup>4+</sup> concentration were, respectively, 0.20 ml/min, 100 mm/s, 36 mm and 50 mM.

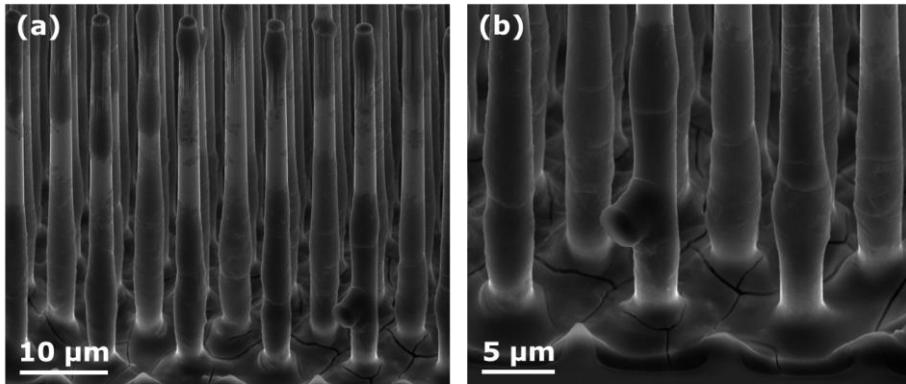


Figure III-27: SEM images of TiN coated Si micropillars, which were pre-treated by UV/O<sub>3</sub>, after spray coating (10 passes) with the aqueous/ethanol Ti precursor at 170°C. The flow rate, path velocity, nozzle distance and Ti<sup>4+</sup> concentration were, respectively, 0.20 ml/min, 100 mm/s, 36 mm and 50 mM.

### 3.4.3.2 Effect of flow rate

Besides the temperature at which the deposition is performed, a set of other factors are also known to influence the spray coating method. Intuitively, one can expect that the flow rate, at which the precursor is being sprayed on the substrate, is an important parameter. To investigate the effect of the precursor flow, the rate was varied between 0.20 and 0.30 ml/min, the other parameters were kept constant and are listed in Table III-4.

Parameter	Set point
Temperature (°C)	180
Flow rate (ml/min)	0.20-0.30
Path velocity (mm/s)	100
Nozzle distance (mm)	36
# passes	10
Ti <sup>4+</sup> concentration (mM)	50

Table III-4: Overview of the spray coat parameters to investigate the effect of the flow rate on the coating behavior.

It seems that a minimal deviation in flow rate already has a large effect on the spray coating process. If the result for spraying 10 layers at 0.20 ml/min, which can be seen Figure III-26 is compared to the SEM images after spraying 10 layers at 0.25 ml/min (Figure III-28a) and 0.30 ml/min (Figure III-28b), one could clearly observe a trend. When increasing the flow rate, more artifacts seem to develop, resulting in a lack of conformality. The reason for this phenomenon probably is that the amount of precursor that is deposited per time is too high so that the drying process cannot follow. This is indicated by the observed cracks at the bottom between the pillars which is probably because of accumulated stress initiated during the drying step. This explains the formation of non-conformal layers on the silicon micropillars.

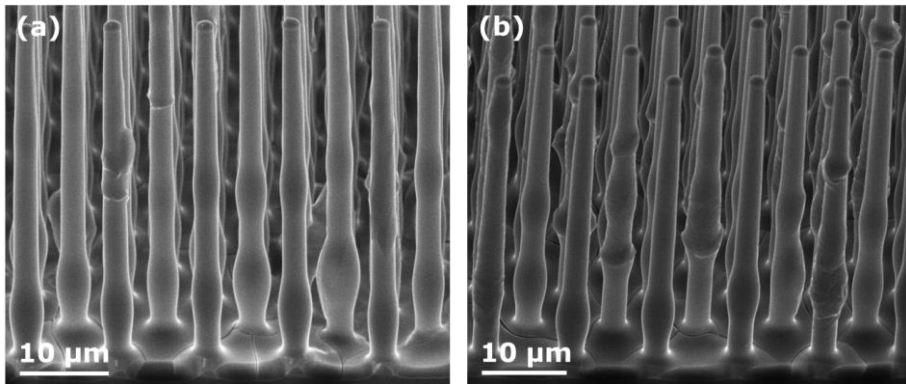


Figure III-28: SEM images of TiN coated Si micropillars, which were pre-treated by UV/O<sub>3</sub>, after spray coating (10 passes) with the aqueous/ethanol Ti precursor with a flow rate of (a) 0.25 and (b) 0.30 ml/min. The deposition temperature, path velocity, nozzle distance and Ti<sup>4+</sup> concentration were, respectively, 180°C, 100 mm/s, 36 mm and 50 mM.

### 3.4.3.3 Effect of path velocity

The path velocity of the nozzle is another factor that was investigated as part of the parameter study. The velocity was varied between 80 and 100 mm/s while the other parameters were kept constant (Table III-5 for the list of applied parameters). The results after spray coating 10 passes with the aqueous/ethanol Ti precursor with a path velocity of 80, 90 and 100 mm/s are shown in, respectively, Figure III-29a, Figure III-29b and Figure III-26. A similar trend compared to the influence of the flow rate was found: lower path velocities did

result in more artifacts in the deposited layers. A lower velocity implies that a higher amount of precursor is delivered to the substrate. That is why also here the same hypothesis as for the influence of the flow rate seems to be valuable, the cracks at the bottom between the pillars strengthen this hypothesis.

Parameter	Set point
Temperature (°C)	180
Flow rate (ml/min)	0.20
Path velocity (mm/s)	80-100
Nozzle distance (mm)	36
# passes	10
Ti <sup>4+</sup> concentration (mM)	50

Table III-5: Overview of the spray coat parameters to investigate the effect of the path velocity on the coating behavior.

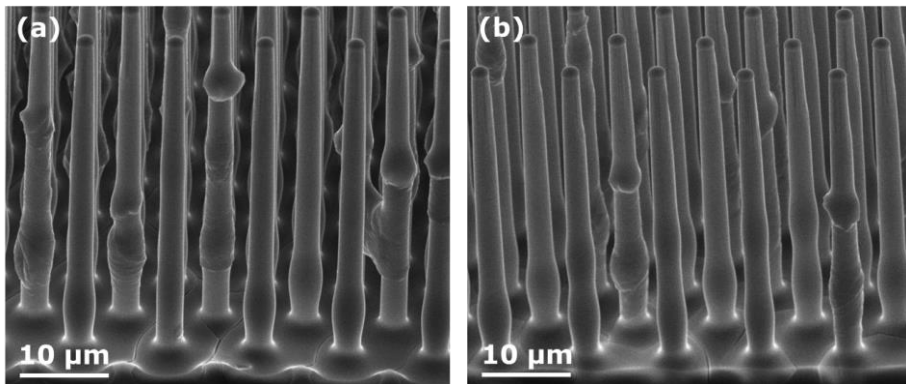


Figure III-29: SEM images of TiN coated Si micropillars, which were pre-treated by UV/O<sub>3</sub>, after spray coating (10 passes) with the aqueous/ethanol Ti precursor with a path velocity of (a) 80 and (b) 90 mm/s. The deposition temperature, flow rate, nozzle distance and Ti<sup>4+</sup> concentration were, respectively, 180°C, 0.20 ml/min, 36 mm and 50 mM.

### 3.4.3.4 Effect of nozzle distance

Another factor, that has to be taken into account, is the nozzle distance with respect to the substrate during spray coating: the nozzle distance was varied between 26 and 36 mm, keeping the other parameters constant as shown in Table III-6. Spray coating of the aqueous/ethanol Ti precursor for 10 passes with a nozzle to substrate distance of 36, 31 and 26 mm did result in coatings which are presented in resp. Figure III-26, Figure III-30 and Figure III-31. When studying the SEM images qualitatively, one could state that the overall uniformity along the pillar axis seems to be higher when the nozzle is brought closer to the substrate during spray coating. Therefore a nozzle distance of 26 mm was selected as the optimal parameter for the benchmark process.

Parameter	Set point
Temperature (°C)	180
Flow rate (ml/min)	0.20
Path velocity (mm/s)	100
Nozzle distance (mm)	26-36
# passes	10
Ti <sup>4+</sup> concentration (mM)	50

Table III-6: Overview of the spray coat parameters to investigate the effect of the nozzle distance on the coating behavior.

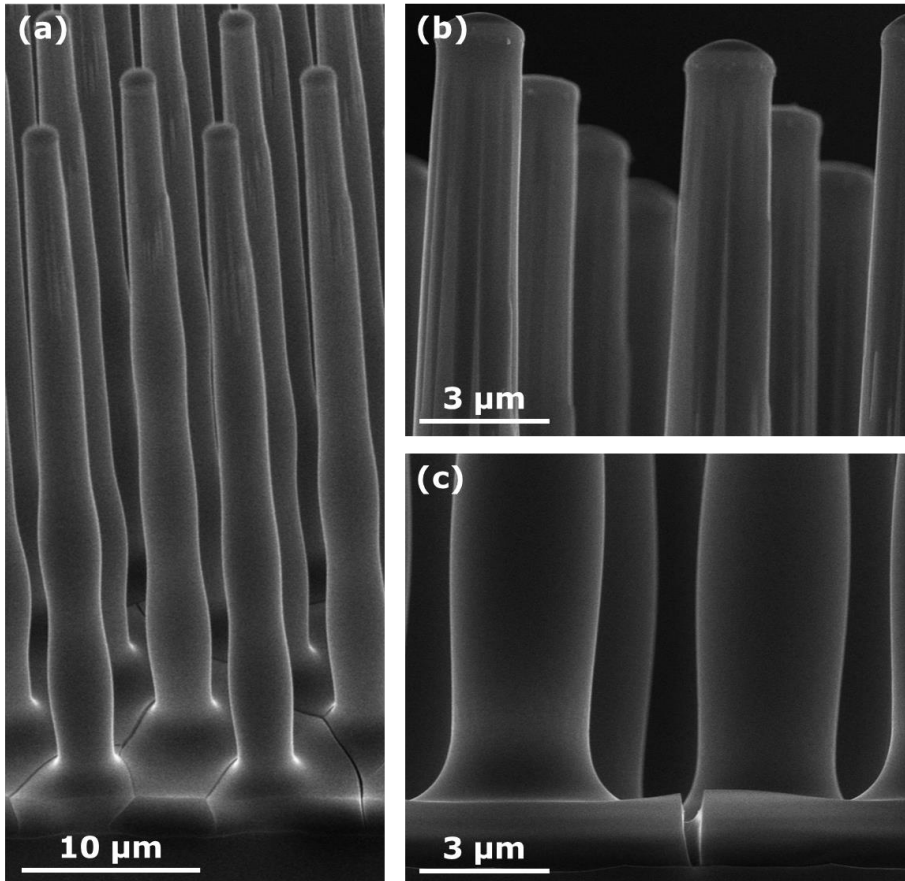


Figure III-30: SEM images of TiN coated Si micropillars, which were pre-treated by UV/O<sub>3</sub>, after spray coating (10 passes) with the aqueous/ethanol Ti precursor, applying a nozzle distance of 31 mm. The deposition temperature, flow rate, path velocity and Ti<sup>4+</sup> concentration were, respectively, 180°C, 0.20 ml/min, 100 mm/s and 50 mM.

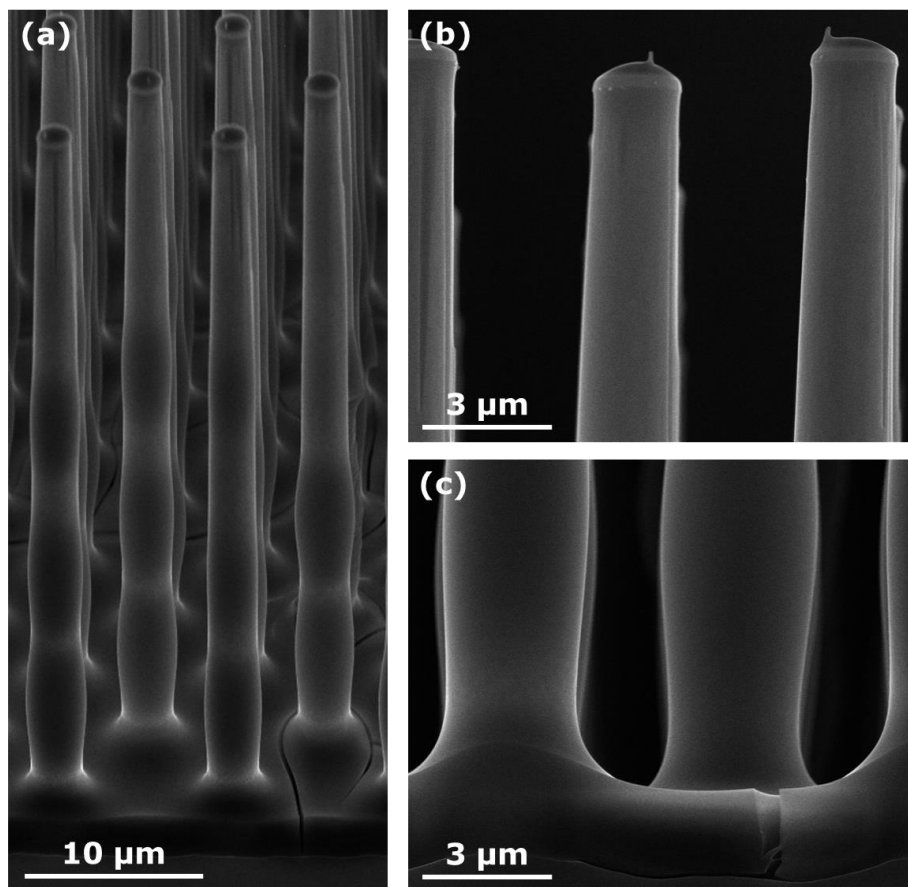


Figure III-31: SEM images of TiN coated Si micropillars, which were pre-treated by UV/O<sub>3</sub>, after spray coating (10 passes) with the aqueous/ethanol Ti precursor, applying a nozzle distance of 26 mm. The deposition temperature, flow rate, path velocity and Ti<sup>4+</sup> concentration were, respectively, 180°C, 0.20 ml/min, 100 mm/s and 50 mM.

### 3.4.3.5 Effect of precursor concentration

One could observe that for the optimal parameters still cracks were present at the bottom between the pillars (Figure III-31). This is probably caused by the accumulated stress originating from the fact that the drying process is not able to follow the delivery of material to the surface. Therefore the amount of active material, that is spray coated, was lowered by adjusting the  $Ti^{4+}$  concentration from 50 mM Ti to 25 mM and 10 mM as is summarized in Table III-7. The coatings deposited by these experiments can be evaluated based on the SEM images in, respectively, Figure III-31, Figure III-32 and Figure III-33. It is obvious that the films get thinner with decreasing  $Ti^{4+}$  concentration. Furthermore for these conditions no cracks could be observed at the bottom between the pillars. This confirms that the reduced amount of material that is delivered to the substrate is allowing the coating enough time to dry, avoiding the accumulation of stress during the spray coating process.

Parameter	Set point
Temperature (°C)	180
Flow rate (ml/min)	0.20
Path velocity (mm/s)	100
Nozzle distance (mm)	26
# passes	10
$Ti^{4+}$ concentration (mM)	10-50

Table III-7: Overview of the spray coat parameters to investigate the effect of the metal ion concentration in the precursor on the coating behavior.

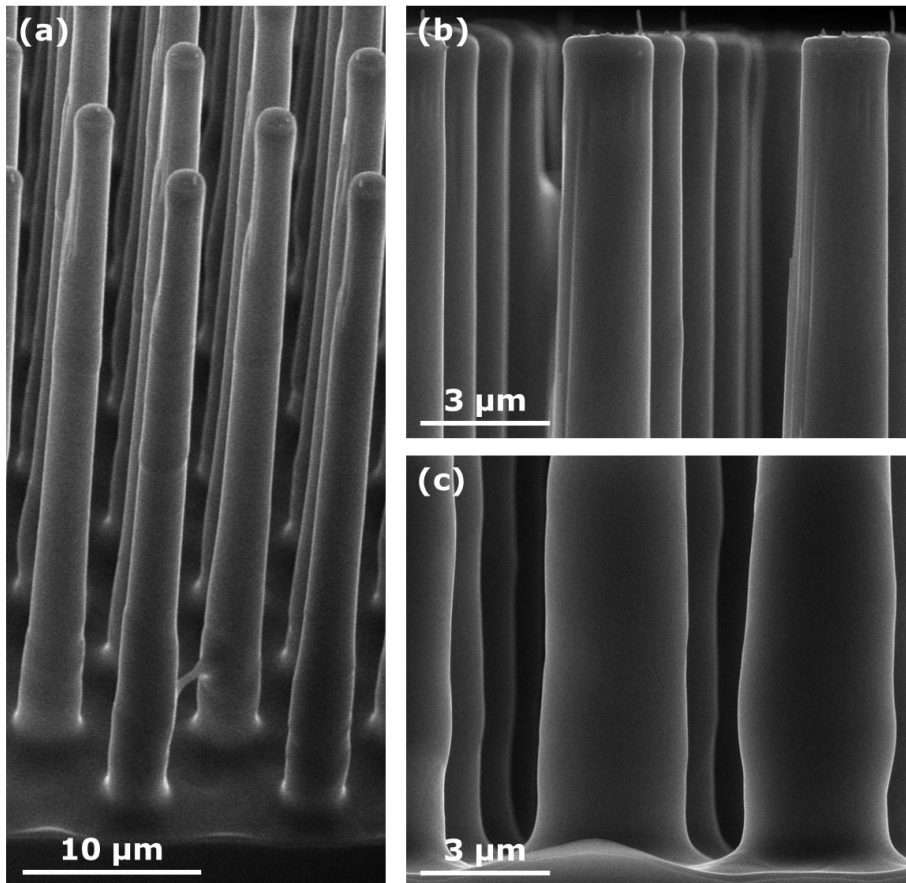


Figure III-32: SEM images of TiN coated Si micropillars, which were pre-treated by UV/O<sub>3</sub>, after spray coating (10 passes) with the aqueous/ethanol Ti precursor, which has a total metal ion concentration of 25 mM. The deposition temperature, flow rate, path velocity and nozzle distance were, respectively, 180°C, 0.20 ml/min, 100 mm/s and 26 mm.

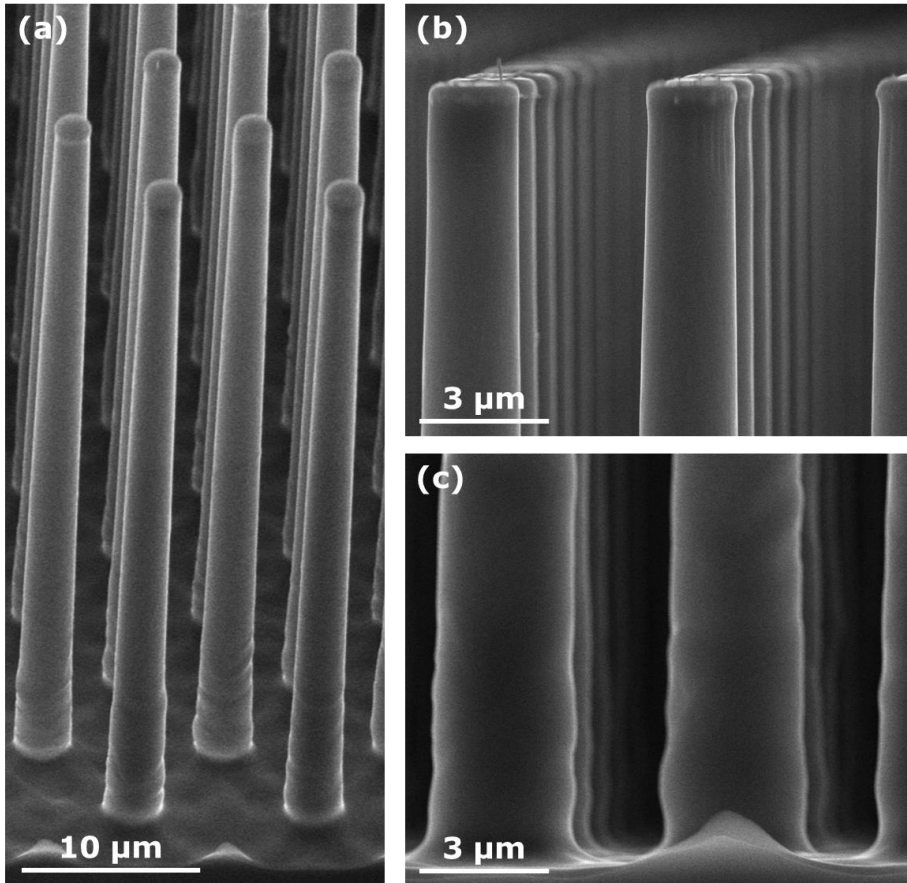


Figure III-33: SEM images of TiN coated Si micropillars, which were pre-treated by UV/O<sub>3</sub>, after spray coating (10 passes) with the aqueous/ethanol Ti precursor, which has a total metal ion concentration of 10 mM. The deposition temperature, flow rate, path velocity and nozzle distance were, respectively, 180°C, 0.20 ml/min, 100 mm/s and 26 mm.

### 3.4.3.6 Crystallization of the TiO<sub>2</sub> coating on the pillars

In view of the application of the deposited films, i.e. Li-ion batteries, the coatings must be annealed in order to completely decompose the precursor and to form crystalline TiO<sub>2</sub> films. For the use in batteries the crystalline phase anatase is selected as the # 1 pick, as it is known to have the best electrochemical response, especially compared to rutile titanium oxide.[23]

The crystallization study was performed simultaneously with the optimization of the spray coating parameters. Consequently, coatings originating from a non-optimized spray coating procedure (i.e. 10 passes, deposition temperature of 180°C, flow rate of 0.20 ml/min, path velocity of 100 mm/s, nozzle to substrate distance of 36 mm and Ti<sup>4+</sup> concentration of 50 mM) were used. However, as can be seen in Figure III-26, the silicon pillars were completely covered by the process. The coating, being amorphous, was then annealed on a hot plate set-up: 2 min at 300°C and 60 min at 600°C. These temperatures were chosen based on existing decomposition studies of the aqueous citrate-peroxo titanium precursor. [14,15] The morphology of the coating after annealing is presented in the SEM images of Figure III-34. It is obvious that the morphology was drastically changed compared to the coated pillars before the post deposition anneal (Figure III-26), indicating the crystallization of the film. One could state that the TiN layer which was deposited on the silicon pillars prior to the spray coating process is also (partially) oxidized to TiO<sub>2</sub>. However because of the presence of an artefact (Figure III-34b) one can conclude that it is the deposited film which is observed in the SEM images and that there is thus a clear indication of crystallization of the TiO<sub>2</sub> film on the silicon micropillars. The observed layer is too thick to be TiN oxidation: 20 nm of TiN would result in maximum 40 nm TiO<sub>2</sub>. Since it is known that, by the use of Raman spectroscopy, information about the composition, and in particular information about the phase formation of TiO<sub>2</sub> (Raman is very sensitive to the detection of crystalline titanium oxide phases), at a local spot on the substrate could be gathered [24], this technique was applied on top of a pillar. The Raman spectra of both the uncoated pillars (treated at 250°C for 20 minutes) as a reference and coated pillars are presented in Figure III-35. One could clearly notice that the deposited film is crystalline (Figure III-35b). Particularly, the presence of anatase titanium oxide on top of the pillars can be observed. Also a small contribution of the spectrum can be assigned to rutile TiO<sub>2</sub>.

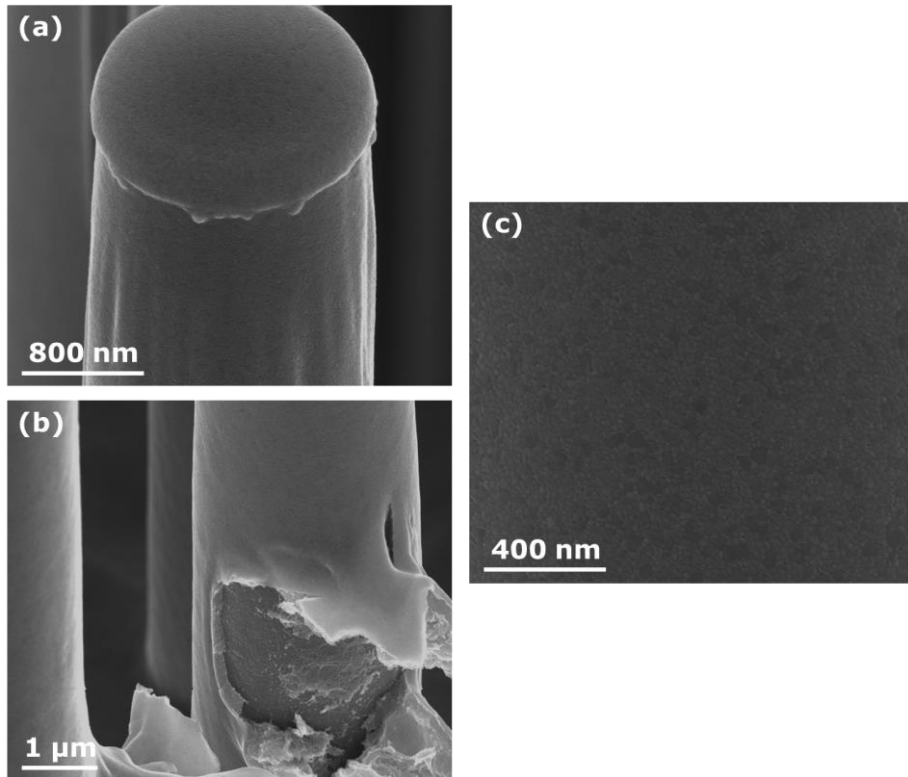


Figure III-34: SEM images of TiN coated Si micropillars (a: top, b: bottom, c: zoom in on coating), which were pre-treated by UV/O<sub>3</sub>, after spray coating (10 passes) with the aqueous/ethanol Ti precursor at 180°C and a thermal treatment at hot plates (2 min at 300°C, 1h at 600°C). The flow rate, path velocity, nozzle distance and Ti<sup>4+</sup> concentration were, respectively, 0.20 ml/min, 100 mm/s, 36 mm and 50 mM.

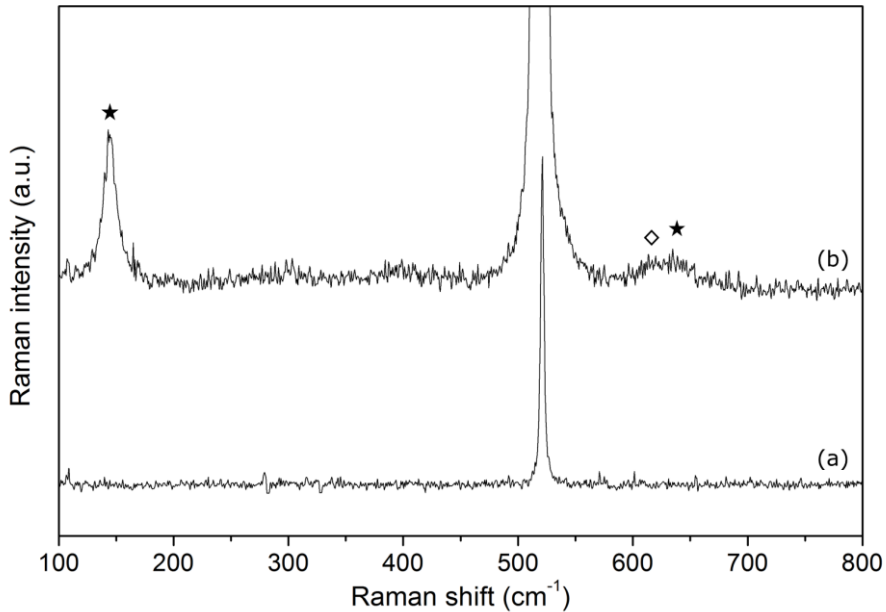
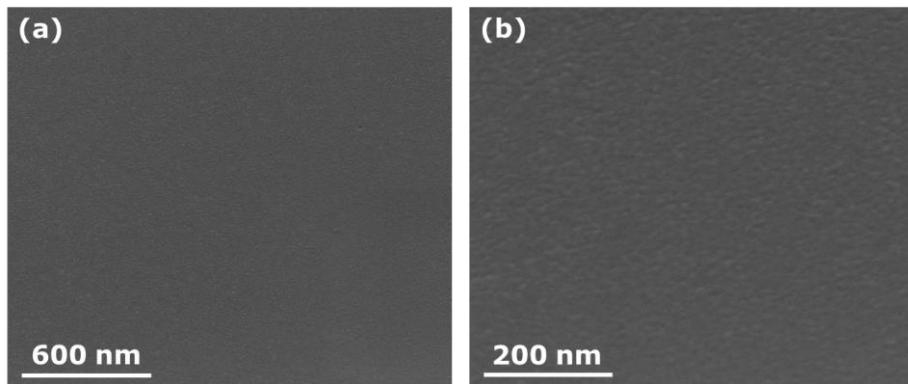


Figure III-35: Raman spectra of the top of TiN coated Si micropillars, which were pre-treated by UV/O<sub>3</sub>, after (a) a thermal treatment on hot plates at 250°C for 20 minutes and (b) spray coating (10 passes) with the aqueous/ethanol Ti precursor at 180°C and a thermal treatment at hot plates (2 min at 300°C, 1h at 600°C). The flow rate, path velocity, nozzle distance and Ti<sup>4+</sup> concentration were, respectively, 0.20 ml/min, 100 mm/s, 36 mm and 50 mM. As a reference the Raman signals originating from anatase (★) and rutile (◇) TiO<sub>2</sub> are shown.

Since in function of possible application in thin-film batteries, it was aimed to deposit a phase-pure anatase TiO<sub>2</sub> film, a crystallization study was performed on a 2D substrate. The films were deposited on 1.2 nm SiO<sub>2</sub>/Si substrates, which were pre-treated by a UV/O<sub>3</sub> treatment. Deposition was done via spray coating (1 pass only since the specific area is much less compared to pillars) with the aqueous/ethanol Ti precursor while applying the same spray parameters as for the studied 3D deposited TiO<sub>2</sub> films, i.e. the deposition temperature, flow rate, path velocity, nozzle distance and Ti<sup>4+</sup> concentration were, respectively, 180°C, 0.20 ml/min, 100 mm/s, 36 mm and 50 mM. Annealing was done on hot plates: 2 minutes at 300°C and 1h at, respectively, 450°C, 500°C, 550°C, 600°C and 650°C. For the latter, a lab furnace was used since the hot plate was limited to 600°C only. The morphology of the films was comparable to the films on the silicon

micropillars as can be deduced from the SEM images of the film which was annealed at 500°C (Figure III-36).

The deposited films were then investigated by Raman spectroscopy, as can be seen in Figure III-37. It is clear that annealing the spray coated layer at 450°C (Figure III-37b) already results in a crystalline TiO<sub>2</sub> film. It is obvious that all peaks, which are not coming from the substrate (Figure III-37a), can be attributed to the anatase TiO<sub>2</sub>, thus the interesting phase in view of electrode applications in batteries. Increasing the anneal temperature to 500°C, 550°C and 600°C did not affect the crystallization behavior (Figure III-37c-e). The fact that only anatase titanium oxide is found at 600°C seems to be in contrast with the Raman results on pillars at that temperature (Figure III-35) which showed that a mixture of anatase and rutile TiO<sub>2</sub> was present on the pillars after annealing at 600°C. However, it seems that 600°C is the temperature limit for the formation of phase-pure TiO<sub>2</sub> and that a decrease of the final anneal temperature is necessary. Also for the application, a lower temperature should be beneficial. Taking into account the TGA results of the precursor, 500°C was picked as the ideal annealing temperature to form phase-pure anatase titanium oxide after deposition. This is well below the temperature limit for the formation of phase-pure TiO<sub>2</sub>, but also high enough to completely decompose the precursor.[14,15]



*Figure III-36: SEM images of 1.2 nm SiO<sub>2</sub>/Si substrates, after deposition via spray coating (1 pass) with the aqueous/ethanol Ti precursor at 180°C and a thermal treatment at hot plates: 2 minutes at 300°C and 1 hour at 500°C. The pre-treatment was done via UV/O<sub>3</sub> and the flow rate, path velocity, nozzle distance and Ti<sup>4+</sup> concentration were, respectively, 0.20 ml/min, 100 mm/s, 36 mm and 50 mM.*

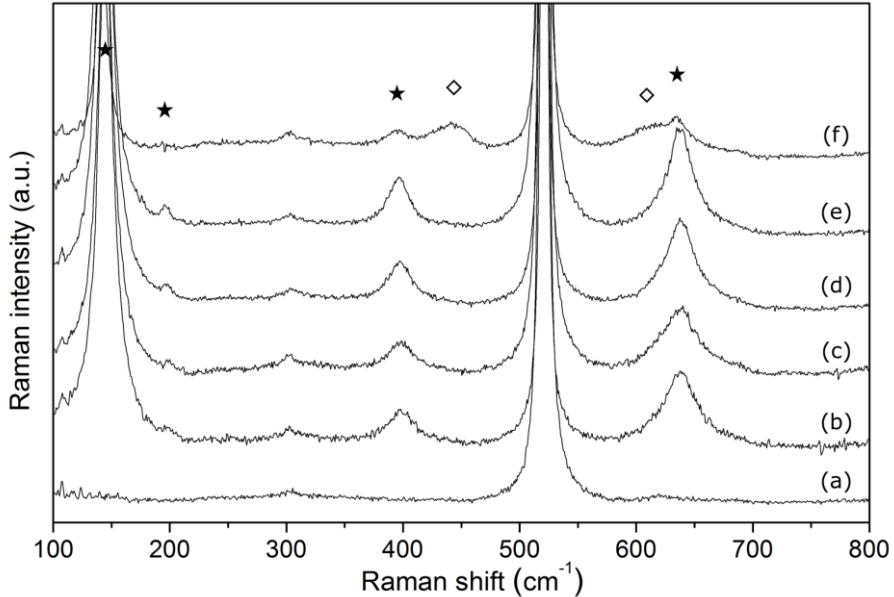
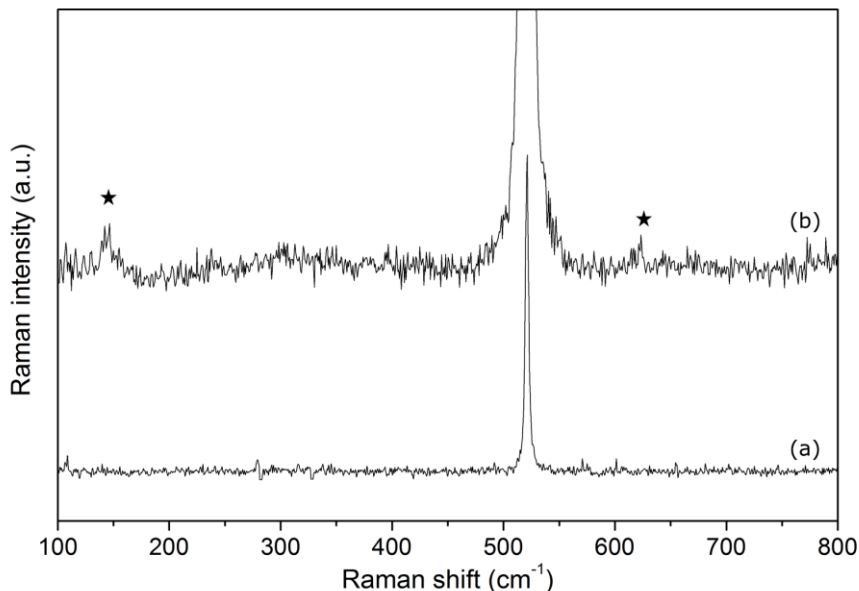


Figure III-37: Raman spectra of 1.2 nm  $\text{SiO}_2/\text{Si}$  substrates, as-received (a) and after deposition via spray coating (1 pass) with the aqueous/ethanol Ti precursor at  $180^\circ\text{C}$  and a thermal treatment at hot plates: 2 minutes at  $300^\circ\text{C}$  and 1 hour at (b)  $450^\circ\text{C}$ , (c)  $500^\circ\text{C}$ , (d)  $550^\circ\text{C}$ , (e)  $600^\circ\text{C}$  and (f)  $650^\circ\text{C}$ . The pre-treatment was done via UV/ $\text{O}_3$  and the flow rate, path velocity, nozzle distance and  $\text{Ti}^{4+}$  concentration were, respectively, 0.20 ml/min, 100 mm/s, 36 mm and 50 mM. As a reference the Raman signals originating from anatase (★) and rutile (◇)  $\text{TiO}_2$  are shown.

The crystallization at the optimal temperature, i.e.  $500^\circ\text{C}$ , was also checked for the films which were deposited at the pillars. The Raman spectra of the uncoated pillars (treated at  $250^\circ\text{C}$  for 20 minutes) as a reference and the coated pillars which were annealed for 2 minutes at a hot plate of  $300^\circ\text{C}$  and 1 hour at  $500^\circ\text{C}$  are presented in Figure III-38. Deposition was done using the optimized spray coat parameters (50 passes), i.e. the deposition temperature, flow rate, path velocity, nozzle distance and  $\text{Ti}^{4+}$  concentration were, respectively,  $180^\circ\text{C}$ , 0.20 ml/min, 100 mm/s, 26 mm and 10 mM. The film thickness of this coating was estimated at 100 nm. The spectra show clearly that anatase titanium oxide is present on top of the pillars after the deposition process. It seems that no secondary phases were formed.



*Figure III-38: Raman spectra of the top of TiN coated Si micropillars, which were pre-treated by UV/O<sub>3</sub>, after (a) a thermal treatment on hot plates at 250°C for 20 minutes and (b) spray coating (50 passes) with the aqueous/ethanol Ti precursor at 180°C and a thermal treatment at hot plates (2 min at 300°C, 1h at 500°C). The flow rate, path velocity, nozzle distance and Ti<sup>4+</sup> concentration were, respectively, 0.20 ml/min, 100 mm/s, 26 mm and 10 mM. As a reference the Raman signals originating from anatase (★) are shown.*

### 3.4.3.7 Electrochemical evaluation of the TiO<sub>2</sub> coating on the pillars

Another proof of coating could be found in the cyclic voltammogram of the deposited 3D anatase film (ca. 100 nm) on silicon micropillars, which was measured by Moitzheim et al. (imec) and is presented in Figure III-39b. As a reference, also the CV measurement of a planar anatase layer on Pt/TiN/TiO<sub>2</sub>/Si is shown (Figure III-39a). This film was deposited via spin coating of the aqueous Ti precursor, has a thickness of ca. 100 nm and is known to be of high quality with respect to morphology and crystallization.[14,15] One could observe that in both cases, there are clear reduction and oxidation peaks present at respectively ca. 1.50 V and 2.25 V. It is obvious that these signals represent the reversible lithium insertion and extraction reactions in anatase TiO<sub>2</sub>. Furthermore one can notice that the intensity of the signals (current density per projected area) is ca. 10 times higher for the 3D film compared to the planar anatase film. Since the thicknesses of these films are in the same range (ca. 100 nm), this is a clear confirmation for

the 3D concept. Remarkable higher capacities per projected area can be achieved by depositing the active layers on three-dimensional substrates, such as silicon micropillars.

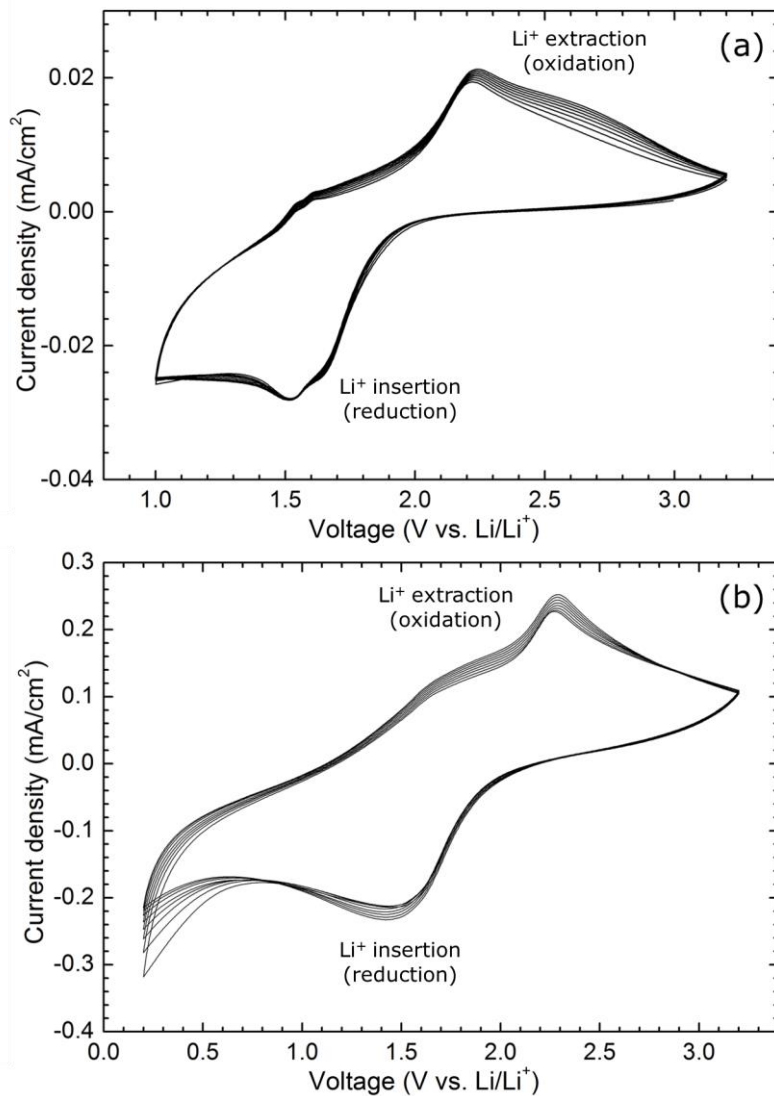


Figure III-39: Cyclic voltammetry (scan rate: 10 mV/s – current density is per projected area) of (a) a planar anatase film on Pt/TiN/TiO<sub>2</sub>/Si and (b) a 3D anatase film on TiN coated silicon micropillars, deposited via, respectively, spin coating and spray coating of the appropriate Ti precursor. Phase-pure anatase films were obtained after the thermal treatment on hot plates (2 min at 180°C, 2 min at 300°C, 1h at 500°C). [Courtesy of Moitzheim et al. – imec]

### **3.5 Generalization of the novel 3D CSD method**

Titanium oxide was chosen as model material for the development of a novel wet chemically based deposition technique. However it should be of high value if this method could be extended to other oxides, and in particular multi-metal oxides. The ability of depositing various multi-metal oxides on three-dimensional substrates should lead to a generalization of the technique, and consequently to a higher impact in the field of 3D coatings.

#### **3.5.1 Deposition of $\text{Li}_4\text{Ti}_5\text{O}_{12}$ on silicon micropillars via the CSD method**

##### **3.5.1.1 Strategy**

For the generalization of the newly developed method, the first material that was investigated is  $\text{Li}_4\text{Ti}_5\text{O}_{12}$ . As shown in chapter II, this material has the potential to have a high capacitance. The deposition in 3D should result in a further increase of the capacitance.

##### **3.5.1.2 Experimental**

For the precursor, the same synthesis procedure was used as for the deposition of  $\text{Li}_4\text{Ti}_5\text{O}_{12}$  films on planar substrates, i.e. the mono-metal Ti (IV) and Li (I) ion solutions were prepared separately. The multi-metal ion Li/Ti precursor was then prepared by mixing the Ti (IV) and Li (I) solutions in the desired amounts (molar ratio = 5:4). Water and ethanol were added to the solution (Figure III-40) so that the total metal ion concentration and the volumetric ethanol:water ratio were set at, respectively, 0.05 M or 0.01 M and 0.9:1.

The Si micropillars, covered with 20 nm of TiN, were cleaned by a UV/O<sub>3</sub> process.[19] The deposition of the precursor on the pillars was performed via spray coating on the substrate set at a temperature of 180°C in a Exactacoat ultrasonic coating system. The nozzle was a AccuMist precision ultrasonic spray nozzle. The optimized spray coating parameters were used.

The deposited films were evaluated by means of scanning electron microscopy (SEM, FEI, NOVA 200), respectively, in a tilted view (45°) and cross-section view (90°).

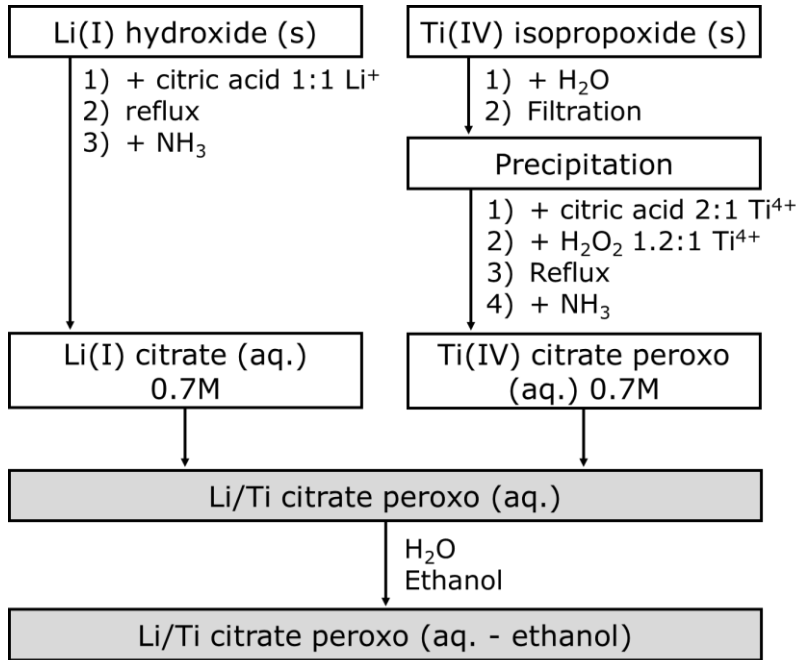


Figure III-40: Schematic representation of the synthesis of the aqueous/ethanol Li/Ti precursor.

### 3.5.1.3 Results and discussion

To illustrate the coating and thus the effectiveness of the process, a thick layer was deposited on the Si micropillars, via the use of the non-optimized process. Spray coating of the aqueous/ethanol Li/Ti precursor on the silicon micropillars at 180°C lead to the full coverage of the 3D substrate. In Figure III-41, the coating before post deposition anneal, thus before crystallization, is shown. The deposited film is very similar to the titanium oxide coating for which the process has been developed (Figure III-25). An appropriate post deposition anneal should lead to the crystallization of the deposited film, i.e. the spinel  $\text{Li}_4\text{Ti}_5\text{O}_{12}$  phase. Information of the research on 2D  $\text{Li}_4\text{Ti}_5\text{O}_{12}$  thin films (chapter II) can be used for this purpose. Furthermore, possible lithium loss during the deposition process should be taken into account (Chapter II). An excess of lithium in the precursor might be necessary.

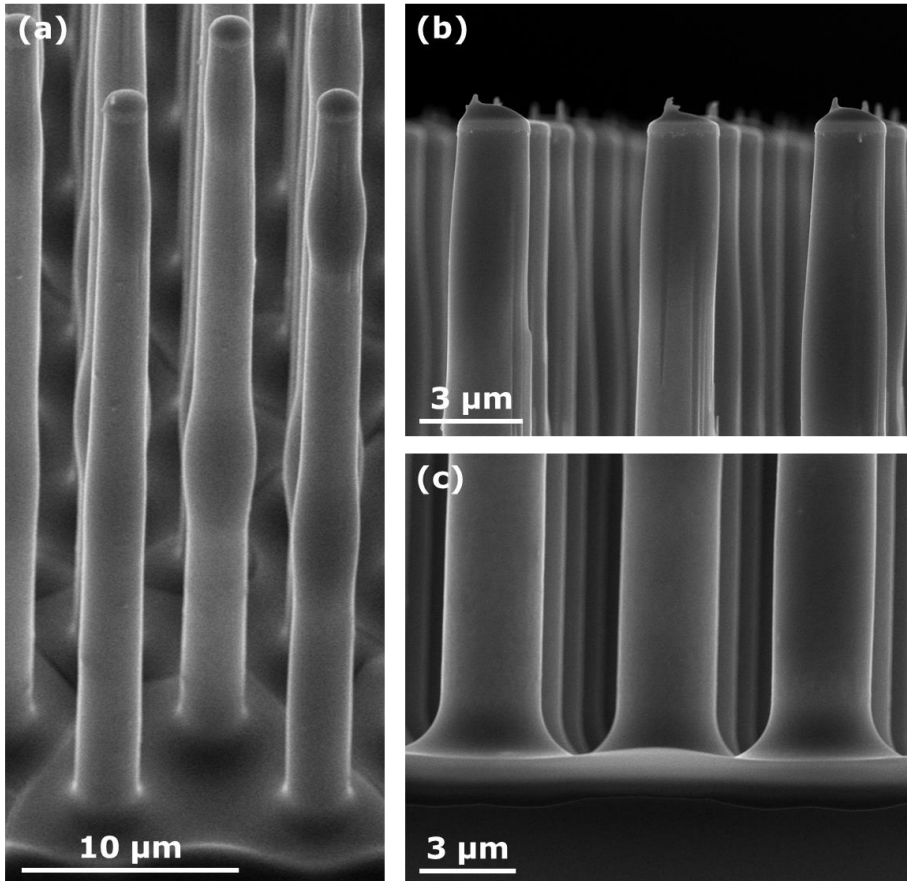


Figure III-41: SEM images of TiN coated Si micropillars, which were pre-treated by UV/O<sub>3</sub>, after spray coating (10 passes) with the aqueous/ethanol Li/Ti precursor, which has a total metal ion concentration of 50 mM. The deposition temperature, flow rate, path velocity and nozzle distance were, respectively, 180°C, 0.20 ml/min, 100 mm/s and 36 mm.

### 3.5.2 Deposition of LuFeO<sub>3</sub> on silicon micropillars via the CSD method

#### 3.5.2.1 Strategy

Since the process was only shown for TiO<sub>2</sub> and Li<sub>4</sub>Ti<sub>5</sub>O<sub>12</sub>, one could state that this method could only be applied to titanium containing precursors. To extend the potential of this novel method even more, it should be shown that also non-containing Ti precursors could be used. Therefore, the Lu/Fe precursor which was used to spin coat LuFeO<sub>3</sub> films on planar substrates, such as the Lu/Fe precursor was employed. As described before in this thesis, this precursor was successfully used to deposit phase-pure orthorhombic LuFeO<sub>3</sub> films on 2D substrates in view of thin-film capacitors. Deposition of this material on a 3D structured substrate would enable a higher surface area and thus a higher capacitance [25,26]:

$$C = \varepsilon \frac{A}{d}$$

(Equation III-8)

with  $\varepsilon$  and  $d$ , respectively, the absolute permittivity and the thickness of the dielectric material and  $A$  the geometric area of overlap of the plates.

#### 3.5.2.2 Experimental

For the precursor, the same synthesis procedure was used as for the deposition of LuFeO<sub>3</sub> films on planar substrates (Chapter II), i.e. the mono-metal Lu (III) and Fe (III) ion solutions were prepared separately. The multi-metal ion Lu/Fe precursor was then prepared by mixing the Lu (III) and Fe (III) solutions in the desired amounts (molar ratio = 1:1). Water and ethanol were added to the solution so that the total metal ion concentration and the volumetric ethanol:water ratio were set at, respectively, 0.01 M and 0.9:1 (Figure III-42).

The Si micropillars, covered with 20 nm of TiN, were cleaned by a UV/O<sub>3</sub> process.[19] The deposition of the precursor on the pillars was performed via spray coating on the substrate set at a temperature of 180°C in a Exactacoat ultrasonic coating system. The nozzle was a AccuMist precision ultrasonic spray nozzle. The optimized spray coating parameters were used. The substrate was

annealed on hot plates, first at 320°C (2 min) and then at 510°C (2 min) to remove the organic fractions.

The deposited films were evaluated by means of scanning electron microscopy (SEM, FEI, NOVA 200) in a tilted view (45°) and cross-section view (90°).

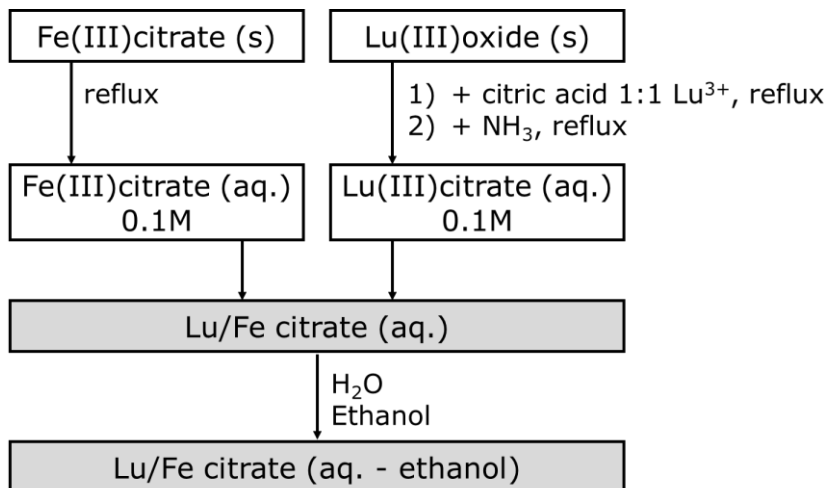


Figure III-42: Schematic representation of the synthesis of the aqueous/ethanol Lu/Fe precursor.

### 3.5.2.3 Results and discussion

The silicon micropillars were fully covered by spray coating of the Lu/Fe precursor at 200°C and a post deposition anneal on hot plates at resp. 320°C and 510°C for 2 minutes (Figure III-43). Once again, it is obvious that the coating is very similar to the titanium oxide coating for which the process has been developed (Figure III-25). The coating is not crystalline yet (cf. morphology of the deposited film). Based on the deposition of Lu/Fe oxide on planar films, earlier in this thesis (chapter II), it is clear that higher anneal temperatures are necessary to reach crystallization, thus to obtain the hexagonal or orthorhombic phase.

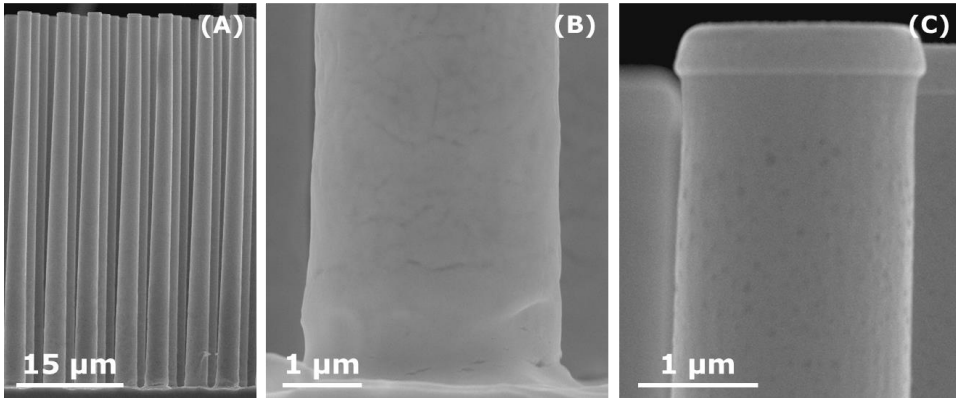


Figure III-43: SEM images of TiN coated Si micropillars, which were pre-treated by UV/O<sub>3</sub>, after spray coating (10 passes) with the aqueous/ethanol Lu/Fe precursor, which has a total metal ion concentration of 10 mM. The deposition temperature, flow rate, path velocity and nozzle distance were, respectively, 200°C, 0.20 ml/min, 100 mm/s and 36 mm. The substrate was annealed on hot plates, first at 320°C (2 min) and then at 510°C (2 min).

### 3.6 Determination of film thickness and conformality

The quantitative evaluation of the exact film thickness and conformality is of course of high value to characterize the deposited film, structurally and electrochemically. However, in contrary to 2D coatings, a cross-section SEM does not allow determination of those characteristics. When cleaving the sample, this will always be in between the pillars so that the thickness of the deposited layer cannot be visualized. One could then propose to estimate the layer thickness by measuring the silicon micropillar diameter before and after deposition. However, there is variation in pillar diameter as a function of pillar height (pillar diameter typically increases towards the bottom) and as a function of the pillar. Therefore, it is not possible to determine film thicknesses via this method.

Another way to determine the layer thickness is to perform a cross-section and look with X-SEM at the edge of area with the micropillars. As can be seen in Figure III-44, a typical substrate of silicon micropillars has a 1 cm<sup>2</sup> area in which micropillars are etched. However, the determination of film thicknesses at the edge of the sample is also not the way to perform. It is difficult to get a straight cleave of the substrate. Therefore, the pathway to the bottom of the pillars is mostly blocked. Furthermore, border effects probably have to be taken into

account when using spray coating as deposition technique. The dimension factor plays an important role in the formation of layers via spray coating. There is less surface area available for the same amount of sprayed material, so probably the deposition parameters have to be adjusted.

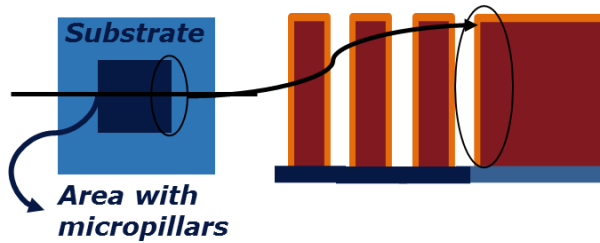


*Figure III-44: Proposed method to allow the determination of film thickness and conformity.*

Another method that can be used is based on a controlled cutting of the silicon micropillars. The space between the pillars is filled with an epoxy resin to allow additional mechanical stability. The embedded pillars are then cut by an abrasion process with specific angle for X-SEM. At that point, it is important that the deposited film has a good adhesion on the silicon pillars. The backscattered SEM mode should then allow to distinguish between the resin, pillar and coating. The deposited layer should consist of heavy metal ions to detect a clear separation in backscattered imaging. Therefore,  $\text{LiWO}_3$  coatings on micropillars were deposited via the described novel CSD method (deposition was done by van den Ham et al.) It was found that the mean thickness of the coating on the pillars was 59 nm. The conformity was determined to be 13% (standard deviation).

## 4 Summary

Atomic layer deposition is generally seen as the ideal method for conformal coating of three-dimensional structures. However if one could find a chemical solution deposition method, this would result in a high cost cut back, more flexibility and more possibility towards upscaling. In literature, some wet chemical methods are available. However those were mostly based on reactions with particular substrates and/or could not deliver a complete coverage on microstructured substrates. The knowledge from these experiments was further used to develop a novel chemical solution deposition (CSD) method for the deposition of (multi-)metal oxide coatings on 3D substrates, i.e. silicon micropillars coated with 20 nm TiN.

The CSD method was first shown for TiO<sub>2</sub>, a candidate anode material. As starting point, the aqueous citrate-peroxo Ti precursor was optimized, in particular by adding ethanol, to allow coating on high aspect ratio features. The whole was spray coated at elevated temperature (180°C) and by controlling all levels of the process, complete coverage of the silicon pillars with the Ti precursor was obtained. Since the deposition was performed at elevated temperature, it is believed that the drying process of the precursor is already induced before the spray touches the surface. Consequently, during the process, the solution is instantly transformed into a gel, consisting of coordinated complexes in which the Ti ions are immobilized. Moreover, because of the elevated temperature, this gel is already partly decomposed during the spray coat process. A further heat treatment of the pillars lead to the complete combustion of the gel and thus to titanium oxide formation, it also triggered the crystallization of the deposited layer. A thorough crystallization study indicated that phase-pure anatase TiO<sub>2</sub> films could be obtained by a well-defined post deposition anneal at 500°C. Lithium-ion insertion and extraction behavior was observed for the anatase film deposited on TiN-coated silicon pillars, indicating its application potential for 3D Li-ion batteries. Further electrochemical experiments are necessary to determine its exact potential towards the proposed application.

The presented technique was also successfully applied to deposit  $\text{Li}_4\text{Ti}_5\text{O}_{12}$  on the microstructured substrate. Because of its negligible volume change upon charge/discharge, this anode material seems best suited for thin-film applications. The method was also used for the deposition of  $\text{LuFeO}_3$ , as described earlier, a promising dielectric material for thin film capacitors. Further experiments should be defined to investigate their characteristics.

The determination of exact thickness and conformality of the resulting coatings is not straightforward. Focused ion beam technology (FIB), combined with SEM, could be the solution to counter this issue. However, on-going research shows that the reported novel method, which implies operational simplicity, low cost and relatively short deposition times, can deliver coatings with a conformality of ca. 13 % (standard deviation, determined by the embedding technology). Furthermore, the process could be successfully transferred to the more interesting 2 X 2 pillars, enabling the highest possible capacity, as discussed before. The technique is also being applied to achieve a series of other multi-metal oxide coatings (e.g. LLTO,  $\text{LiWO}_3$ ) on 3D substrates, bringing various novel applications such as commercial thin-film 3D Li-ion batteries one step closer to reality.

## 5 References

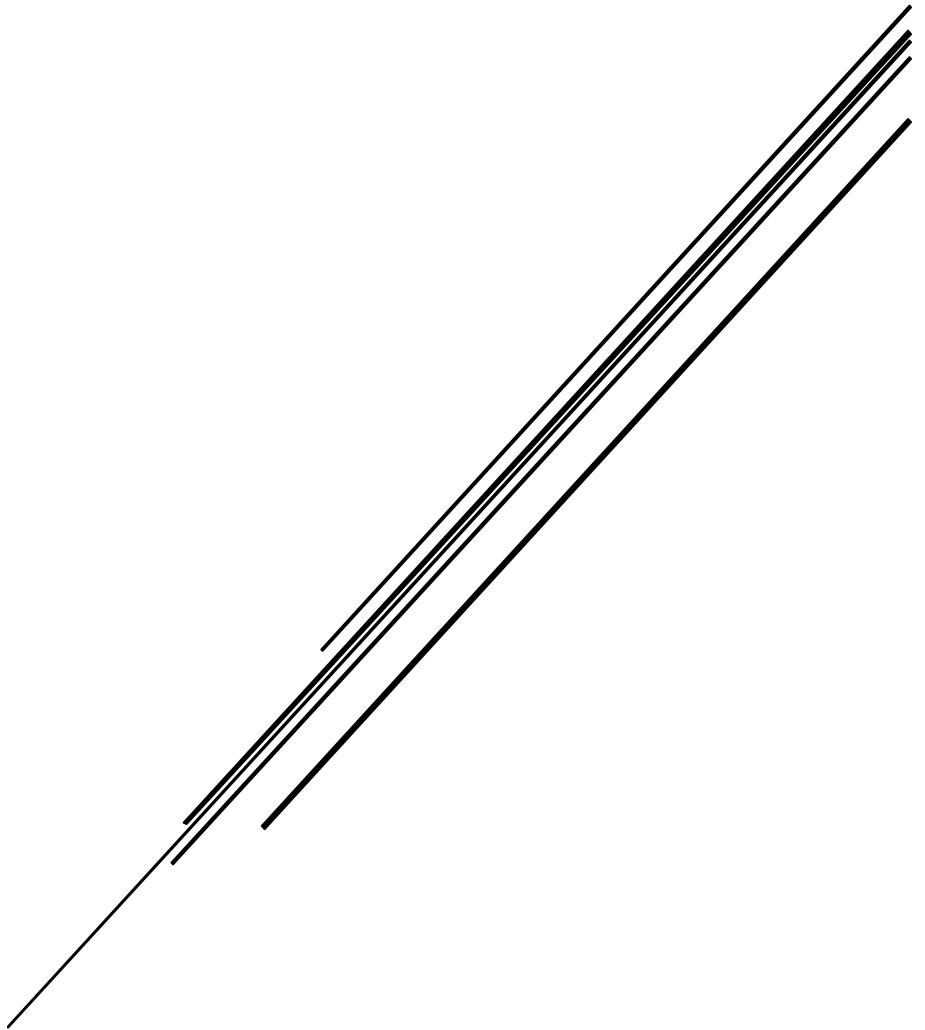
- [1] T.R.B. Foong, Y. Shen, X. Hu, A. Sellinger, Template-Directed Liquid ALD Growth of TiO<sub>2</sub> Nanotube Arrays: Properties and Potential in Photovoltaic Devices, *Adv. Funct. Mater.* 20 (2010) 1390–1396. doi:10.1002/adfm.200902063.
- [2] B.Y. Guo, J. Hu, H. Liang, L. Wan, C. Bai, TiO<sub>2</sub>-Based Composite Nanotube Arrays Prepared via Layer-by-Layer Assembly \*\*, *Adv. Funct. Mater.* 15 (2005) 196–2002. doi:10.1002/adfm.200305098.
- [3] J.H. Lee, I.C. Leu, M.C. Hsu, Y.W. Chung, M.H. Hon, Fabrication of aligned TiO<sub>2</sub> one-dimensional nanostructured arrays using a one-step templating solution approach, *J. Phys. Chem. B.* 109 (2005) 13056–13059. doi:10.1021/jp052203l.
- [4] K. Prabakar, M. Son, W.-Y. Kim, H. Kim, TiO<sub>2</sub> thin film encapsulated ZnO nanorod and nanoflower dye sensitized solar cells, *Mater. Chem. Phys.* 125 (2011) 12–14. doi:10.1016/j.matchemphys.2010.09.028.
- [5] J. Qiu, W. Yu, X. Gao, X. Li, Fabrication and Characterization of TiO<sub>2</sub> Nanotube Arrays Having Nanopores in Their Walls By Double-Template-Assisted Sol–Gel, *Nanotechnology.* 18 (2007) 295604. doi:10.1088/0957-4484/18/29/295604.
- [6] L. Zhang, Y. Zhu, Y. He, W. Li, H. Sun, Preparation and performances of mesoporous TiO<sub>2</sub> film photocatalyst supported on stainless steel, *Appl. Catal. B Environ.* 40 (2003) 287–292. doi:10.1016/S0926-3373(02)00154-6.
- [7] J. Qiu, Z. Jin, Z. Liu, X. Liu, G. Liu, W. Wu, et al., Fabrication of TiO<sub>2</sub> nanotube film by well-aligned ZnO nanorod array film and sol-gel process, *Thin Solid Films.* 515 (2007) 2897–2902. doi:10.1016/j.tsf.2006.08.023.
- [8] B.M.M. Shaijumon, E. Perre, B. Daffos, P. Taberna, J. Tarascon, P. Simon, Nanoarchitected 3D Cathodes for Li-Ion Microbatteries, (2010) 4978–4981. doi:10.1002/adma.201001922.
- [9] C.M. Ronconi, E.C. Pereira, Electrocatalytic properties of Ti/TiO<sub>2</sub> electrodes prepared by the Pechini method, *J. Appl. Electrochem.* 31 (2001) 319–323. doi:10.1023/A:1017544406347.
- [10] M.K. Van Bael, D. Nelis, A. Hardy, D. Mondelaers, K. Van Werde, J. D’Haen, et al., Integrated Ferroelectrics: An Aqueous Chemical Solution Deposition of Ferroelectric Thin Films, *Integr. Ferroelectr.* 45 (2002) 113–122. doi:10.1080/10584580215353.

- [11] The MEGlobal Group of Companies, Ethylene glycol: Product guide, 2008.
- [12] G. Vereecke, Internal discussion, imec, 2012.
- [13] H.T. Xue, Z.N. Fang, Y. Yang, J.P. Huang, L.W. Zhou, Contact angle determined by spontaneous dynamic capillary rises with hydrostatic effects: Experiment and theory, *Chem. Phys. Lett.* 432 (2006) 326–330. doi:10.1016/j.cplett.2006.10.017.
- [14] I. Truijen, M.K. Van Bael, H. Van Den Rul, J. D’Haen, J. Mullens, Synthesis of thin dense titania films via an aqueous solution-gel method, *J. Sol-Gel Sci. Technol.* 41 (2007) 43–48. doi:10.1007/s10971-006-0123-8.
- [15] A. Hardy, J. D’Haen, M.K. Bael, J. Mullens, An aqueous solution-gel citratoperoxo-Ti(IV) precursor: synthesis, gelation, thermo-oxidative decomposition and oxide crystallization, *J. Sol-Gel Sci. Technol.* 44 (2007) 65–74. doi:10.1007/s10971-007-1601-3.
- [16] D.R. Lide, *CRC Handbook of Chemistry and Physics*, 84th editi, CRC Press, New York, USA, 2003.
- [17] M. Aratono, T. Toyomasu, M. Villeneuve, Y. Uchizono, T. Takiue, K. Motomura, et al., Thermodynamic Study on the Surface Formation of the Mixture of Water and Ethanol, *J. Colloid Interface Sci.* 191 (1997) 146–53. doi:10.1006/jcis.1997.4929.
- [18] P.M. Vereecken, C. Huyghebaert, Conformal Deposition For 3D Thin-Film Batteries, *ECS Trans.* 58 (2013) 111–118. doi:10.1149/05810.0111ecst.
- [19] J.R. Vig, *Treatise on Clean Surface Technolgy - Volume 1*, 1st ed., Plenum Press, New York, 1987.
- [20] Sono-Tek, Spray coating, [Http://www.sono-Tek.com/](http://www.sono-Tek.com/). (2015).
- [21] R. Engle, Advantages of Ultrasonic Spray Coatings of Biomaterials onto Devices and Implantables (Sono-Tek), in: *Int. Coat. Sci. Technol. Symp.*, 2010: pp. 1–22.
- [22] L. Filipovic, S. Selberherr, G.C. Mutinati, E. Brunet, S. Steinhauer, A. Köck, et al., Methods of simulating thin film deposition using spray pyrolysis techniques, *Microelectron. Eng.* 117 (2014) 57–66. doi:10.1016/j.mee.2013.12.025.
- [23] J.F.M. Oudenhoven, L. Baggetto, P.H.L. Notten, All-Solid-State Lithium-Ion Microbatteries: A Review of Various Three-Dimensional Concepts, *Adv. Energy Mater.* 1 (2011) 10–33. doi:10.1002/aenm.201000002.

- [24] O. Frank, M. Zukalova, B. Laskova, J. Kürti, J. Koltai, L. Kavan, Raman spectra of titanium dioxide (anatase, rutile) with identified oxygen isotopes (16, 17, 18), *Phys. Chem. Chem. Phys.* 14 (2012) 14567–14572. doi:10.1039/c2cp42763j.
- [25] J. Bird, *Electrical and Electronic Principles and Technology*, Fourth edi, Newnes - Elsevier, 2010.
- [26] B.E. Conway, *Electrochemical Supercapacitors: Scientific Fundamentals and Technological Applications*, Kluwer Academic / Plenum Publishers, New York, USA, 1999.



# IV. SUMMARY, CONCLUSIONS AND OUTLOOK





Since the need for clean and efficient energy storage devices is expected to become immense, as the field of applications is constantly growing, the thesis did firstly focus on the synthesis of materials that can be used in those systems. Particularly, it was the intention to deposit functional multi-metal oxide films on planar substrates, interesting for thin-film capacitors or Li-ion thin-film batteries, and this via the use of chemical solution deposition. Aqueous "sol-gel" precursor chemistry was used, which is known to be cheaper, easier and more environmentally friendly compared to traditional sol-gel routes using organic solvents. Moreover, it allows the fabrication of complex multi-metal oxides due to the intimate mixing of metal ions and the resulting good homogeneity of the precursor.[1–3]

The first group of materials which is very attractive for energy storage devices and in particular for thin-film capacitors are ultra high-k materials. Due to their extremely high dielectric constant ( $k > 10000$ ), they can possibly be used for the miniaturization of the energy storage devices and the increase of their energy density. For orthorhombic  $\text{LuFeO}_3$  ceramics, a dielectric constant of 10000 (frequency  $\leq 1\text{kHz}$ ) had been reported at room temperature. [4] Nevertheless, research on the deposition of  $\text{LuFeO}_3$  thin films, indispensable for the thin film applications envisaged, was still very scarce, especially when it did come to wet chemical deposition.

A stable aqueous Lu/Fe multi-metal ion precursor was prepared by mixing citrate complex-based Fe and Lu solutions in the desired ratio. Prior to thin film deposition, the thermal decomposition of the precursor and the phase formation process towards bulk, crystalline  $\text{LuFeO}_3$  were studied. It was shown that phase-pure orthorhombic  $\text{LuFeO}_3$  could be formed at  $900^\circ\text{C}$ , indicating a high temperature requirement. These insights, combined with a profound study on the key deposition and process parameters, were successfully employed for the formation of orthorhombic  $\text{LuFeO}_3$  thin films on  $\text{Si}_3\text{N}_4$  via spin coating. Impedance spectroscopy analyses did confirm their associated ultra high dielectric constant ( $> 10000$ ) at room temperature for frequencies lower than or equal to  $1\text{kHz}$ , making them promising for the use in thin film capacitors. The downside of the material is that the dielectric loss is quite high at low frequencies.

Future work could focus on the deposition of orthorhombic  $\text{LuFeO}_3$  on a metallic substrate in order to create a thin-film capacitor. The characteristics of this device, and consequently the usefulness of the dielectric layer, could then be determined in a more direct way.

The further development of Li-ion batteries and specifically all-solid state Li-ion batteries would significantly improve battery safety and could bring a higher energy density at system level.

A new process was developed for the deposition of  $\text{Li}_4\text{Ti}_5\text{O}_{12}$  films. This material is known as a very stable high-performance electrode material.[5] While compensating for the lithium loss during the deposition process in the stable Li/Ti precursor, a phase-pure film could be achieved via spin coating after a post deposition anneal at  $700^\circ\text{C}$ . The phase-pure film was characterized by a very high capacity, particularly ca.  $800 \text{ mAh/cm}^3$  for the low C-rates (0.5C-1C), while a mixed  $\text{Li}_4\text{Ti}_5\text{O}_{12}$ /anatase film's capacity was  $500 \text{ mAh/cm}^3$  at 0.5C and 1C. Since  $800 \text{ mAh/cm}^3$  is higher than what is theoretical possible, probably the amount of active material was underestimated. However, it seems that this aqueous solution-gel process is able to deliver spinel  $\text{Li}_4\text{Ti}_5\text{O}_{12}$  films which can be incorporated in thin-film Li-ion batteries.

A more precise determination of the amount of active material and a more thorough electrochemical study should be performed to evaluate all electrochemical characteristics including the exact capacity and cycle life.

$(\text{Li}_x\text{Mg}_{1-2x}\text{Al}_x)\text{Al}_2\text{O}_4$  had been suggested as a novel Li-ion electrolyte with spinel structure and thus structurally compatible with the  $\text{Li}_4\text{Ti}_5\text{O}_{12}$  and  $\text{LiMn}_2\text{O}_4$  spinel electrodes.[6] A stable Li/Mg/Al multi-metal ion precursor was developed by mixing citrate-based Li, Mg and Al ion solutions in different ratios so that the theoretical x-value in  $(\text{Li}_x\text{Mg}_{1-2x}\text{Al}_x)\text{Al}_2\text{O}_4$  was varied ( $0 \leq x \leq 0.5$ ). Prior to film deposition, a crystallization study of the Li/Mg/Al powders showed that for  $x \leq 0.3$  phase-pure spinel  $(\text{Li}_x\text{Mg}_{1-2x}\text{Al}_x)\text{Al}_2\text{O}_4$  could be formed at  $600^\circ\text{C}$  in air. Crystalline spinel films could be achieved after a post deposition anneal at  $800^\circ\text{C}$ . A too high Li:Mg ratio for  $X=0.2$  lead to the formation of  $\text{LiAlO}_2$  as secondary phase, deteriorating the intrinsic film quality and morphology. Electrochemical impedance spectroscopy showed that none of the deposited films possess a decent ionic

conductivity. This is probably due to the formation of an amorphous  $\text{Al}_2\text{O}_3$  interface at the grain boundaries, caused by an excess of Al available in the films. Despite the potential good lattice matching between these spinel electrolyte films with spinel  $\text{Li}_4\text{Ti}_5\text{O}_{12}$ , the low ionic conductivity (much lower than  $10^{-6}$ - $10^{-8}$  S  $\text{cm}^{-1}$ ) tackles the potential use of these solid electrolyte films in thin-film Li-ion batteries. Future work should focus on the study of the grain boundaries, e.g. by HR-TEM/EDS characterization, to demonstrate or disprove the proposed hypothesis. It is believed that if the formation of  $\text{Al}_2\text{O}_3$  could be avoided, e.g. by a more elaborate tuning of the Li:Mg:Al ratio, this could result in a higher ionic conductivity. Then, the material could be stacked with  $\text{Li}_4\text{Ti}_5\text{O}_{12}$  as anode material to obtain Li-ion battery half-cell as proof-of-principle.

It is obvious that a similar process for deposition on a 3D substrate would take these materials even a step higher. Various known wet chemical methods were investigated. Those were mostly based on reactions with particular substrates and/or could not deliver a complete coverage on microstructured substrates. The knowledge from these experiments was further used to develop a novel chemical solution deposition (CSD) method for the deposition of (multi-)metal oxide coatings on 3D substrates, i.e. silicon micropillars coated with 20 nm TiN. The CSD method was shown first for  $\text{TiO}_2$ , a candidate anode material. As starting point, the aqueous citrate-peroxo Ti precursor was optimized, in particular by adding ethanol, to allow coating on high aspect ratio features. The whole was spray coated at elevated temperature ( $180^\circ\text{C}$ ) and by controlling all levels of the process, complete coverage of the silicon pillars with the Ti precursor was obtained. Since the deposition was performed at elevated temperature, the solution was instantly transformed into a gel, consisting of coordinated complexes in which Ti ions were immobilized. Further heat treatment of the pillars lead to the complete combustion of the gel and thus to titanium oxide formation, it also triggered the crystallization of the deposited layer. A thorough crystallization study did indicate that phase-pure anatase  $\text{TiO}_2$  films could be obtained by a well-defined post deposition anneal at  $500^\circ\text{C}$ . Lithium-ion insertion and extraction behavior was observed for the anatase film deposited on TiN-coated silicon pillars, further illustrating its application potential for 3D Li-ion batteries.

Further electrochemical experiments are necessary to determine its exact potential towards the proposed application.

The presented technique was also successfully applied to deposit  $\text{Li}_4\text{Ti}_5\text{O}_{12}$  on the microstructured substrate. Furthermore, the method was used for the deposition of Lu/Fe oxide films, as described earlier, promising as dielectric material for thin film capacitors. More experiments should be defined to investigate their characteristics.

The determination of exact thickness and conformality of the resulting coatings is not straightforward. Focused ion beam technology (FIB), combined with SEM, could be the solution to counter this issue. On-going research, using the "embedding technology", shows that the reported novel method, which implies operational simplicity, low cost and relatively short deposition times, can deliver coatings with a conformality of ca. 13 % (standard deviation). Furthermore, the process could be successfully transferred to the more interesting  $2\ \mu\text{m} \times 2\ \mu\text{m}$  pillars, enabling the highest possible capacity, as discussed before. The technique is also being applied to achieve a series of other multi-metal oxide coatings (e.g. LLTO,  $\text{LiWO}_3$ ) on 3D substrates, bringing various novel applications such as commercial thin-film 3D Li-ion batteries one step closer to reality.

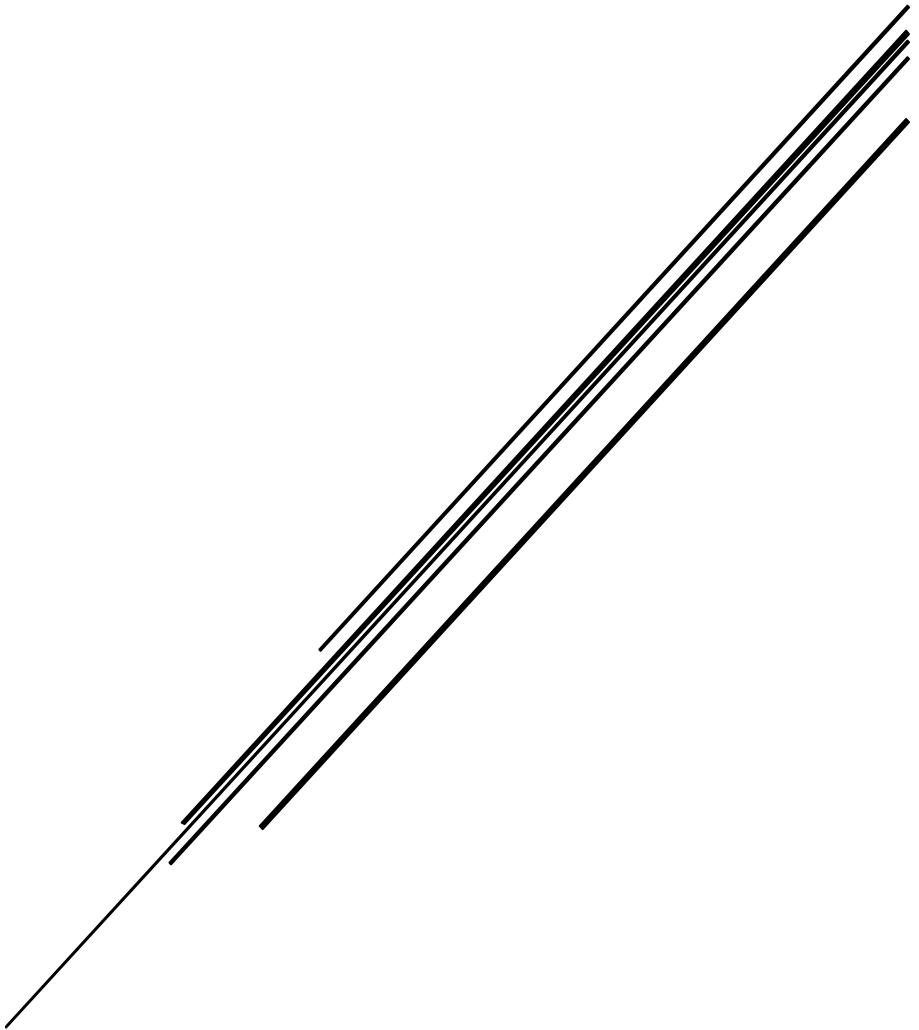
Since various other multi-metal oxide coatings on microstructured surfaces seem to be feasible (as long as ethanol can be added to the aqueous precursor solution), obviously, there are a lot of opportunities to exploit the novel CSD method even more. The ultimate goal, at the level of applications, is thus to develop a 3D all-solid state battery, consisting of an electrolyte film stacked between two electrode films, obtained via the described method. Furthermore more fundamental research could be performed to unravel the exact deposition mechanism of the spray coating technique. This requires an extra experimental study (e.g. by the use of a high-resolution camera) together with a profound modeling study.

## References

- [1] A. Hardy, S. Van Elshocht, C. Adelman, T. Conard, A. Franquet, O. Douhéret, et al., Aqueous solution-gel preparation of ultrathin ZrO<sub>2</sub> films for gate dielectric application, *Thin Solid Films*. 516 (2008) 8343–8351. doi:10.1016/j.tsf.2008.04.017.
- [2] S. Van Elshocht, A. Hardy, C. Adelman, M. Caymax, T. Conard, A. Franquet, et al., Impact of Process Optimizations on the Electrical Performance of High-k Layers Deposited by Aqueous Chemical Solution Deposition, *J. Electrochem. Soc.* 155 (2008) G91. doi:10.1149/1.2840628.
- [3] A. Hardy, S. Van Elshocht, W. Knaepen, J. D’Haen, T. Conard, B. Brijs, et al., Crystallization resistance of barium titanate zirconate ultrathin films from aqueous CSD: a study of cause and effect, *J. Mater. Chem.* 19 (2009) 1115. doi:10.1039/b816856c.
- [4] L. Zhang, X.M. Chen, Dielectric relaxation in LuFeO<sub>3</sub> ceramics, *Solid State Commun.* 149 (2009) 1317–1321. doi:10.1016/j.ssc.2009.05.036.
- [5] J.F.M. Oudenhoven, L. Baggetto, P.H.L. Notten, All-Solid-State Lithium-Ion Microbatteries: A Review of Various Three-Dimensional Concepts, *Adv. Energy Mater.* 1 (2011) 10–33. doi:10.1002/aenm.201000002.
- [6] F. Rosciano, P.P. Pescarmona, K. Houthoofd, A. Persoons, P. Bottke, M. Wilkening, Towards a lattice-matching solid-state battery: synthesis of a new class of lithium-ion conductors with the spinel structure., *Phys. Chem. Chem. Phys.* 15 (2013) 6107–12. doi:10.1039/c3cp50803j.



# V. SCIENTIFIC CONTRIBUTIONS





## 1 Patents

**S. Gielis**, A. Hardy, M. K. Van Bael, P. M. Vereecken, Conformal coating on three-dimensional substrates, PCT/EP2015/061133 (published on 2015/11/26: WO 2015/177221 A1).

## 2 Papers

### 2.1 Published

N. Peys, P. Adriaensens, S. Van Doorslaer, **S. Gielis**, E. Peeters, C. De Dobbelaere, S. De Gendt, A. Hardy, M. K. Van Bael, Aqueous citrato-oxovanadate(IV) precursor solutions for VO<sub>2</sub>: synthesis, spectroscopic investigation and thermal analysis, Dalton Transactions 43 (2014) 12614-12623. doi: 10.1039/c4dt01346h.

N. Peys, Y. Ling, D. Dewulf, **S. Gielis**, C. De Dobbelaere, D. Cuypers, P. Adriaensens, S. Van Doorslaer, S. De Gendt, A. Hardy, M. K. Van Bael, V<sub>6</sub>O<sub>13</sub> films by control of the oxidation state from aqueous precursor to crystalline phase, Dalton Transactions 42 (2013) 959-968. doi: 10.1039/c2dt31857a.

### 2.2 In preparation

**S. Gielis** et al., A novel solution-based process for the deposition of (multi-)metal oxide coatings on high aspect ratio features.

**S. Gielis** et al., Aqueous chemical solution deposition of high performance phase-pure Li<sub>4</sub>Ti<sub>5</sub>O<sub>12</sub> films for thin film Li-ion batteries.

**S. Gielis** et al., Aqueous chemical solution deposition of ultra high-k LuFeO<sub>3</sub> thin films.

### 3 Conference contributions

#### 3.1 Oral presentations

**S. Gielis**, N. Peys, S. Moitzheim, P. M. Vereecken, A. Hardy, M. K. Van Bael, Towards the 3D Thin-Film Li-Ion Battery: A Novel Solution-Based Process for the Deposition of (Multi-)Metal Oxide Coatings on High Aspect Ratio Features, 228<sup>th</sup> ECS meeting, Phoenix, Arizona, USA, October 11-15 2015.

**S. Gielis**, M. Ivanov, N. Peys, J. van den Ham, N. Pavlovic, P. Robaey, M. Nesladak, J. Banys, A. Hardy, M. K. Van Bael, (2015) Aqueous chemical solution deposition of  $\text{LuFeO}_3$  ultra high-k films, 39th International Conference and Exposition on Advanced Ceramics and Composites, Daytona Beach, Florida, USA, January 25-30 2015.

N. Peys, **S. Gielis**, J. van den Ham, G. Maino, A. Hardy, M. K. Van Bael, Aqueous solution processing of Li-based oxides as candidate electrode or electrolyte in solid-state Li-ion batteries, Materials Science and Technology (MS&T), Pittsburgh, Pennsylvania, USA, October 12-16 2014.

N. Labyedh, B. Put, **S. Gielis**, A. El Mel, M. Ksouri, A. Hardy, M. K. Van Bael, P. M. Vereecken, Lithium-Titanate Thin Films as Electrode Material for Solid State Lithium-ion Batteries, E-MRS spring meeting, Strasbourg, France, May 26-30 2014.

N. Peys, **S. Gielis**, C. De Dobbelaere, S. De Gendt, A. Hardy, M. K. Van Bael, An aqueous process for the formation of  $\text{VO}_2$  (M1) and  $\text{V}_6\text{O}_{13}$  films, Materials Science and Technology (MS&T), Montreal, Canada, October 27-31 2013.

N. Peys, **S. Gielis**, C. De Dobbelaere, S. Van Doorslaer, S. De Gendt, A. Hardy, M. K. Van Bael, Vanadium oxide nanostructure formation by an aqueous deposition route: from precursor solution to crystalline phase, MRS spring meeting, San Francisco, California, USA, April 1-5 2013.

N. Peys, **S. Gielis**, D. Dewulf, A. Hardy, S. De Gendt, M. K. Van Bael, Aqueous citrato-oxovanadate(IV) precursor for the deposition of VO<sub>x</sub> nanostructures. Chemistry Conference for Young Scientists (ChemCYS), Blankenberge, Belgium, March 1-2 2012.

**S. Gielis**, N. Peys, D. Dewulf, C. De Dobbelaere, N. Pavlovic, S. Van Elshocht, S. De Gendt, P. M. Vereecken, A. Hardy, M. K. Van Bael, Aqueous chemical solution deposition of LuFeO<sub>3</sub> thin films in view of energy storage applications, 9th Students' Meeting and 2nd ESR COST MP0904 Workshop, Novi Sad, Serbia, November 16-18 2011.

D. Dewulf, N. Peys, C. De Dobbelaere, **S. Gielis**, S. Van Elshocht, S. De Gendt, A. Hardy, M. K. Van Bael, Aqueous Chemical Solution Deposition as a tool for new high-k materials, E-MRS fall meeting, Warsaw, Poland, September 19-23 2011.

N. Peys, K. Schellens, C. De Dobbelaere, D. Dewulf, **S. Gielis**, P. Adriaensens, P. M. Vereecken, S. De Gendt, A. Hardy, M. K. Van Bael, New synthesis route for VO<sub>2</sub>(B) nanolayers by controlling the vanadium oxidation state throughout the entire process, E-MRS fall meeting, Warsaw, Poland, September 19-23 2011.

**S. Gielis**, M. van der Veen, S. De Gendt, P. M. Vereecken, Silver-assisted Electroless Etching of Si Nanowires, 218th ECS meeting, Las Vegas, Nevada, USA, October 10-15 2010.

### 3.2 Poster presentations

**S. Gielis**, B. Put, N. Peys, T. Vranken, F. Rosciano, P.M. Vereecken, A. Hardy, M. K. Van Bael, Aqueous chemical solution deposition of (Li<sub>x</sub>Mg<sub>1-2x</sub>Al<sub>x</sub>)Al<sub>2</sub>O<sub>4</sub> films as possible spinel electrolyte in all-solid-state Li- ion batteries, E-MRS spring meeting, Lille, France, May 26-30 2014.

**S. Gielis**, P. M. Vereecken, A. Hardy, M. K. Van Bael, Aqueous chemical solution deposition of  $(\text{Li}_x\text{Mg}_{1-2x}\text{Al}_x)\text{Al}_2\text{O}_4$  films as possible spinel electrolyte in all-solid-state Li-ion batteries, imec PhD days, Heverlee, Belgium, December 17-19 December 2013.

**S. Gielis**, N. Peys, N. Pavlovic, S. Van Elshocht, S. De Gendt, A. Hardy, M. K. Van Bael, Aqueous chemical solution deposition of  $\text{LuFeO}_3$  thin high-k films, Meeting of the Belgian Ceramic Society, Diepenbeek, Belgium, April 19 2013.

**S. Gielis**, N. Peys, D. Dewulf, N. Pavlovic, S. Van Elshocht, S. De Gendt, A. Hardy, M. K. Van Bael, Aqueous chemical solution deposition of  $\text{LuFeO}_3$  thin high-k films, WE Heraeus-Physics School on "Microelectronics for Society – More than Moore expands More Moore", Bad Honnef, Germany, June 10-16 2012.

N. Peys, **S. Gielis**, D. Dewulf, A. Hardy, S. De Gendt, M. K. Van Bael, Effect of the environmental  $\text{O}_2$  content and temperature on the formation of  $\text{VO}_x$  nanostructures in an Aqueous Chemical Solution Deposition process, WE Heraeus-Physics School on "Microelectronics for Society – More than Moore expands More Moore", Bad Honnef, Germany, June 10-16 2012.

**S. Gielis**, N. Peys, S. Van Elshocht, S. De Gendt, P. M. Vereecken, A. Hardy, M. K. Van Bael, Aqueous chemical solution deposition of  $\text{LuFeO}_3$  thin films for high energy density systems, imec PhD Days, Heverlee, Belgium, November 22-24 2011.

**S. Gielis**, N. Peys, D. Dewulf, C. De Dobbelaere, N. Pavlovic, H. Damm, S. Van Elshocht, S. De Gendt, P. M. Vereecken, A. Hardy, M. K. Van Bael, Aqueous chemical solution deposition of  $\text{LuFeO}_3$  thin films in view of energy storage applications, E-MRS fall meeting, Warsaw, Poland, September 19-23 2011.